Contemporary Concepts of Condensed Matter Science

SERIES EDITORS

E. BURSTEIN, M.L. COHEN, D.L. MILLS and P.J. STILES

CARBON NANOTUBES: QUANTUM CYLINDERS OF GRAPHENE

Volume Editors:

S. Saito and A. Zettl

Carbon Nanotubes

Quantum Cylinders of Graphene

This page intentionally left blank

Series: Contemporary Concepts of Condensed Matter Science
Series Editors: E. Burstein, M.L. Cohen, D.L. Mills and P.J. Stiles

Carbon Nanotubes

Quantum Cylinders of Graphene

S. Saito
Department of Physics, and
Research Center for Nanometer-Scale Quantum Physics
Tokyo Institute of Technology
Oh-okayama, Meguro-ku, Tokyo, Japan

A. Zettl
Department of Physics
University of California at Berkeley, and
Materials Sciences Division
Lawrence Berkeley National Laboratory
Berkeley, CA, USA

ELSEVIER

Amsterdam – Boston – Heidelberg – London – New York – Oxford
Paris – San Diego – San Francisco – Singapore – Sydney – Tokyo

Elsevier
Radarweg 29, PO Box 211, 1000 AE Amsterdam, The Netherlands
Linacre House, Jordan Hill, Oxford OX2 8DP, UK

First edition 2008

Library of Congress Cataloging-in-Publication Data
A catalog record for this book is available from the Library of Congress

British Library Cataloguing in Publication Data
A catalogue record for this book is available from the British Library

ISBN: 978-0-444-53276-3
ISSN: 1572-0934

Printed and bound in United Kingdom

08 09 10 11 12 10 9 8 7 6 5 4 3 2 1

CONTENTS

LIST OF CONTRIBUTORS

P. Avouris	IBM Research Division, T.J. Watson Research Center, Yorktown Heights, NY 10598, USA
P. G. Collins	Department of Physics and Astronomy, University of California, Irvine, CA 92697-4576, USA
G. Dresselhaus	Francis Bitter Magnet Lab, MIT, Cambridge, MA 02139, USA
M. S. Dresselhaus	Department of Physics and Department of Electrical Engineering and Computer Science, Massachusetts Institute of Technology, Cambridge, MA 02139, USA
L. Forró	Institute of Physics of Complex Matters, Ecole Polytechnique Federale de Lausanne, CH-1015 Lausanne, Switzerland
A. Jorio	Depto. de Fisica, Universidade Federal de Minas Gerais, Belo Horizonte-MG 30123-970, Brazil
C. L. Kane	Department of Physics and Astronomy, University of Pennsylvania, Philadelphia, PA 19104, USA
E. J. Mele	Department of Physics and Astronomy, University of Pennsylvania, Philadelphia, PA 19104, USA
R. Saito	Department of Physics, Tohoku University, and CREST, JST, Sendai 980-8578, Japan
S. Saito	Department of Physics and Research Center for Nanometer-Scale Quantum Physics, Tokyo Institute of Technology, 2-12-1 Oh-okayama, Meguro-ku, Tokyo 152-8551, Japan
J. W. Seo	Institute of Physics of Complex Matters, Ecole Polytechnique Federale de Lausanne, CH-1015 Lausanne, Switzerland
R. Bruce Weisman	Department of Chemistry, Center for Nanoscale Science and Technology, and Center for Biological and Environmental Nanotechnology, Rice University, 6100 Main Street, Houston, TX 77005, USA
A. Zettl	Department of Physics, University of California, Berkeley, CA 94708-7300, USA

This page intentionally left blank

SERIES PREFACE

CONTEMPORARY CONCEPTS OF CONDENSED MATTER SCIENCE

Contemporary Concepts of Condensed Matter Science, a new series of volumes, is dedicated to clear expositions of the concepts underlying theoretical, experimental, and computational research, and techniques at the advancing frontiers of condensed matter science. The term "condensed matter science" is central, because the boundaries between condensed matter physics, condensed matter chemistry, materials science, and biomolecular science are diffuse and disappearing.

The individual volumes in the series will each be devoted to an exciting, rapidly evolving subfield of condensed matter science, aimed at providing an opportunity for those in other areas of research, as well as those in the same area, to have access to the key developments of the subfield, with a clear exposition of underlying concepts and techniques employed. Even the title and the subtitle of each volume will be chosen to convey the excitement of the subfield.

The unique approach of focusing on the underlying concepts should appeal to the entire community of condensed matter scientists, including graduate students and post-doctoral fellows, as well as to individuals not in the condensed matter science community, who seek understanding of the exciting advances in the field.

Each volume will have a *Preface*, an *Introductory* section written by the volume editor(s) which will orient the reader about the nature of the developments in the subfield, and provide an overview of the subject matter of the volume. This will be followed by sections on the most significant developments that are identified by the volume editors, and that are written by key scientists recruited by the volume editor(s).

Each section of a given volume will be devoted to a major development at the advancing frontiers of the subfield. The sections will be written in the way that their authors would wish a speaker would present a colloquium on a topic outside of their expertise, which invites the listener to "come think with the speaker," and which avoids comprehensive in-depth experimental, theoretical, and computational details.

The overall goal of each volume is to provide an intuitively clear discussion of the underlying concepts that are the "driving force" for the high-profile developments of the subfield, while providing only the amount of theoretical, experimental, and computational detail that would be needed for an adequate understanding of the subject. Another attractive feature of these volumes is that each section will provide a guide to "well-written" literature where the reader can find more detailed information on the subject.

VOLUME PREFACE

The detailed geometric arrangement of atomic or molecular species constituting matter is central to the resulting physical properties. Indeed, this sensitivity is the very foundation of chemistry, biology, materials science, and solid-state physics. Materials in bulk form are often crystalline, where the atomic arrangement is periodic over large distances. This feature greatly simplifies theoretical calculations of the physical properties of materials, including the mechanical, electronic, thermal, and magnetic response. Using a variety of theoretical approaches it is possible to predict the properties of many materials knowing only the atomic number of the constituent atoms and the crystal structure. For example, it is predicted and experimentally confirmed that bulk silicon is a semiconductor in one packing configuration and a (superconducting) metal in another. Similarly, carbon is an ultra-hard insulator in one packing configuration and a seemingly very soft semimetal in another.

Reducing the size or dimensions of a bulk material can have a profound effect on its properties. Overall symmetries and even local atomic bonding configurations are often altered, and quantum confinement and surface energy terms become significant. Atomic or molecular energy states can dominate and physical properties can change dramatically, sometimes bearing little resemblance to those of the host bulk material. This transition, from bulk-like to surface-like, occurs at the nanoscale. Although nanoscale materials are ubiquitous in nature, of great interest are synthetic nanostructures not readily formed under "natural" conditions. These sometimes metastable materials are often produced under extreme nonequilibrium conditions, often with the assistance of tailor-made nanoscale catalytic particles.

This volume is devoted mostly to nanotubes, unique synthetic nanoscale quantum systems whose physical properties are often singular (i.e., record-setting). Nanotubes can be formed from a myriad of atomic or molecular species, the only requirement apparently being that the host material or "wall fabric" be configurable as a layered or sheet-like structure. Nanotubes with sp^2-bonded atoms such as carbon, or boron together with nitrogen, are the champions of extreme mechanical strength, electrical response (either highly conducting or highly insulating), and thermal conductance. Carbon nanotubes can be easily produced by a variety of synthesis techniques, and for this reason they are the most studied nanotubes, both experimentally and theoretically. Boron nitride nanotubes are much more difficult to produce and only limited experimental characterization data exist. Indeed, for boron nitride nanotubes, theory is well ahead of experiment. For these reasons this volume deals largely with carbon nanotubes. Conceptually, the

"building block" for a carbon nanotube is a single sheet of graphite, called graphene. Recently, it has become possible to experimentally isolate such single sheets (either on a substrate or suspended). This capability has in turn fueled many new theoretical and experimental studies of graphene itself. It is therefore fitting that this volume contains also a chapter devoted to graphene.

This volume is organized as follows:

Experimental and theoretical overviews are presented by the volume editors in Chapters 1 and 2. In the field of nanotube discovery, research, and development, theory and experiment have played key, intertwined roles. The discovery of the first carbon nanotube was strictly an experimental effort, yet the basic electrical, mechanical, and optical properties of carbon nanotubes were all theoretically established prior to laboratory measurement. In the case of boron nitride nanotubes, theoretical prediction of the material itself in fact preceded experimental synthesis of BN and B–C–N nanotubes.

One of the great promises of nanoscience and nanotechnology is enabling the continued rapid miniaturization of electronic devices. Alternate molecular scale electronics may be needed when silicon-based technologies hit a much-anticipated brick wall in the not-to-distant future. Nanotubes, which can be synthesized in both semiconducting and metallic forms, have appealing properties of high mechanical strength, resistance to oxidation and electromigration, and good thermal and electrical conductivity. These features, coupled to compatibility with conventional CMOS processing, make them attractive candidates for electronics elements including transistors, logic gates, memories, and sensors. Numerous high-technology companies, whose "bread and butter" microelectronics technology is based on silicon processing, are currently engaged in nanotube electronics research. Chapter 3, authored by Dr. P. G. Collins and Dr. P. Avouris, presents nanotube electronics from both an industrial and academic perspective.

The unusual geometrical confinement and boundary conditions, together with the relatively defect-free structure of nanotubes, makes for a rich vibrational system well-suited to vibrational and optical spectroscopy. Raman spectroscopy has played a critical experimental and theoretical role in nanotube development. Indeed, one of the most reliable methods used to ascertain the mean diameter of a nanotube sample is via Raman spectroscopy. Individual nanotubes can be interrogated using Raman studies, thus identifying the chiral indices specifying the unique tube geometry. Isolated nanotubes suspended in solution can also be examined via fluorescence methods. Excitation and decay signatures unique to different geometrical families of nanotubes can be used here to identity the semiconducting constituents of nanotube samples. Dr. M. S. Dresselhaus, Dr. G. Dresselhaus, Dr. R. Saito, and Dr. A. Jorio describe Raman spectroscopy as applied to nanotubes in Chapter 4, while Dr. R. B. Weisman describes in Chapter 5 the optical properties of nanotubes.

Carbon and boron nitride nanotubes are predicted to be, on a per-atom basis, the strongest and stiffest materials known. These predictions are borne out in experiment. These findings suggest nanotubes as obvious candidates for high frequency, high-Q oscillations. Furthermore, the concentric shells of multi-wall

nanotubes present an interesting geometry allowing inter-tube motion resulting in linear or rotational bearings for microelectromechanical systems (MEMS) or nanoelectromechanical systems (NEMS) applications, including nanoscale electric motors. Dr. J. W. Seo and Dr. L. Forró present in Chapter 6 the unusual structural properties of nanotubes and nanoelectromechanical systems applications.

Carbon nanotubes are sometimes described conceptually as rolled up sheets of graphene, and, as might be expected, many of the mechanical and electronic properties of nanotubes are derived from or closely related to corresponding properties of graphene. (Amusingly, graphene has recently been described by some as an opened-up and flattened nanotube!) The important intrinsic properties of, and rich theoretical constructs relevant to, graphene are covered in Chapter 7 by Dr. E. J. Mele and Dr. C. L. Kane.

Finally, it goes without saying that the study of nanoscale systems in general, and nanotubes and graphene in particular, would be unimaginably hampered were it not for high resolution microscopy techniques such as afforded by transmission electron microscopy (TEM), scanning tunneling microscopy (STM), atomic force microscopy (AFM), and scanning electron microscopy (SEM). The first nanotubes were in fact discovered in TEM investigations of carbonaceous materials. The elemental composition, geometrical structure and defect configuration, and even mechanical, electrical transport, electron field emission, and growth properties of nanotubes are now routinely examined using atomic force and electron microscopy tools, with many of the studies being conducted in situ. However, rather than attempting to combine the somewhat disparate microscopy studies into a single chapter, the volume editors have elected to distribute this work amongst relevant chapters of this volume.

S. Saito and A. Zettl

This page intentionally left blank

Chapter 1
NANOTUBES: AN EXPERIMENTAL OVERVIEW

A. Zettl

1. INTRODUCTION

The discovery in 1991 of carbon nanotubes [1], and the discovery of nanotubes formed from combinations of other elements soon thereafter [2,3], marked the beginning of highly intensified research into the science of nanostructures. Relevant research thrusts have been both experimental and theoretical in nature, with experimental findings often prompting subsequent theoretical modeling and analysis, and at the same time original theoretical predictions spurring experimental synthesis, characterization, and technological application. Progress in basic science and applications has been dramatic, due in large part to the relative ease by which carbon nanotubes can be synthesized, and the suitability of the materials to previously developed solid state experimental and theoretical characterization methods, including those originally tailored to low-dimensional materials.

The successful synthesis [4,5] in the 1970s and 1980s of quasi-one-dimensional inorganic and organic conductors such as potassium cyanoplatinate, polyacetylene, superconducting charge transfer salts, and charge density wave transition metal di- and tri-chalcogenides, along with sustained efforts in carbon fiber growth and application [6], led to the development of numerous specialized measurement techniques addressing the properties of low-dimensional systems, including transport coefficients (electrical and thermal conductivity, Hall effect, thermoelectric power, etc.), mechanical properties (Young's and shear modulus, velocity of sound), specific heat, compositional analysis (e.g., EELS), vibrational modes (Raman, infrared conductivity), and structure (TEM, X-ray diffraction, etc). Progress over the past two decades in the physics of quantum confined systems such as two-dimensional electron gases, quantum dots, and nanocrystals, together with technical advances in semiconductor lithographic techniques yielding submicron feature sizes, also helped set the stage for efficiently accessing nanotube properties.

Contemporary Concepts of Condensed Matter Science
Carbon Nanotubes: Quantum Cylinders of Graphene

ISSN: 1572-0934/doi:10.1016/S1572-0934(08)00001-2

2. SYNTHESIS

The ideal carbon nanotube has so many interdependent constraints that at first sight the successful laboratory synthesis of anything even resembling such a structure would appear hopelessly futile. The inherently very strong sp^2 carbon–carbon bond despises curvature, so a small-diameter tube-like geometry is metastable at best. Even a perfectly formed cylindrical tube is subject to collapse from internal wall–wall attraction [7]. Growing a single-wall nanotube (SWNT) to centimeter lengths implies unprecedented length-to-diameter aspect ratios of 10^7. Maintaining the same diameter and chirality along the tube is possible if only limited types of topological defects are allowed in the nanotube fabric. Well-nested multiwall nanotubes (MWNTs) are even more finicky, necessitating a highly restricted combination of diameters and chiralities such that each shell neatly matches the previous one with a near-ideal intershell van der Waals spacing of 3.4 Å.

Despite all these requirements apparently working against nanotube formation, carbon nanotubes are relatively easy to synthesize (Fig. 1). Indeed, a large number of different synthesis methods have proved highly successful. The original method [1,8], that of arc-plasma, is an adaptation of the Krätschmer–Huffman technique [9] first used to mass-produce the fullerene C_{60}. This method is still the preferred one for the production of very high quality, relatively long MWNTs. The method is also easily adapted to produce nanotubes filled with metals and carbides, or those of a chosen isotopic purity. Interestingly, catalysts are not needed to produce MWNTs when using the arc-plasma method. If transition metal or other catalysts are added to the arc-plasma feedstock, the resulting tubes may be nearly exclusively single wall [10,11]. In the Krätschmer–Huffman method, a nonequilibrium plasma is maintained by an electrical current. In a related synthesis technique, a laser-induced nonequilibrium plasma is used. This laser vaporization method was early on adapted to produce high-quality SWNTs within a fairly narrow diameter distribution (though the tubes produced were not all of a unique chirality [12]). High-pressure CO-based synthesis of SWNTs has been refined and scaled to industrial quantities [13], as have been various CVD techniques [14]. CVD, with or without rf or microwave enhancement, has proved to be especially useful in producing tubes of different morphology, including extremely long tubes, ''forests'' of aligned tubes, and tubes grown from one mounting post or electrical contact to another. CVD methods appear to be the most versatile for both SWNT and MWNT growth. Although a dream of many organic chemists, no SWNT or MWNT has yet been produced using strictly room temperature, wet chemistry methods.

Noncarbon nanotubes are more difficult to produce than pure carbon nanotubes. Transition-metal dichalcogenide- and oxide-based tubes [15] have been grown with some success using a variety of methods, but for the most part such tubes are not widely produced nor studied. The tubes do not have sp^2 bonding, so their mechanical, and perhaps electronic, properties are limited (though some may serve well in specific applications, such as ingredients in lubricants). It is well known that,

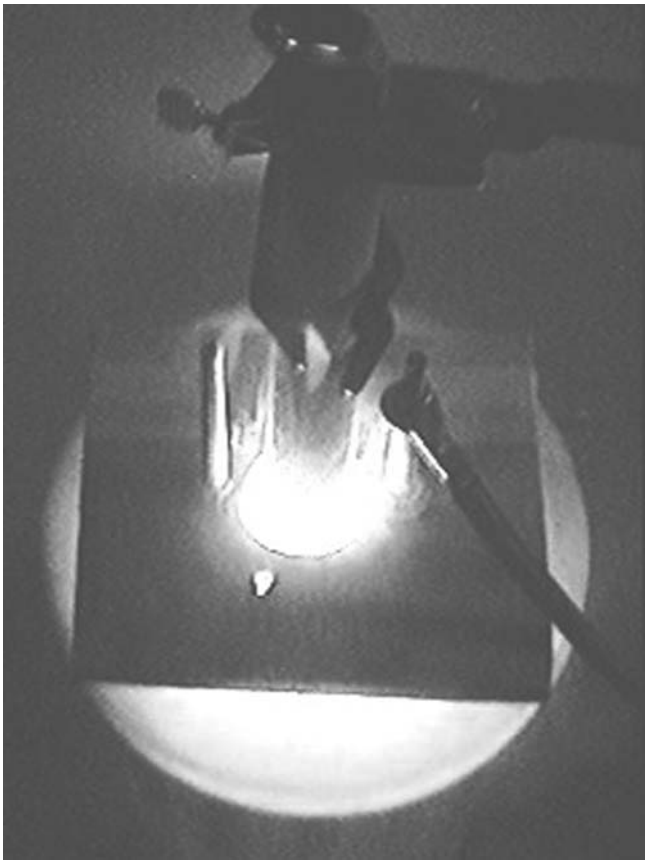

Fig. 1. Simplified method for nanotube production. An electric-current-induced arc between two electrodes immersed in liquid nitrogen produces a high-temperature plasma. Extremely high-quality nanotubes are immediately produced.

apart from carbon, boron and nitrogen also form robust sp^2 bonds. Shortly after the discovery of carbon nanotubes, various boron and nitrogen containing stable nanotube structures were predicted [16] and soon thereafter synthesized, including BC_3, BC_2N, and pure BN nanotubes [3,17,18]. BN nanotubes can be produced by arc-plasma, laser vaporization, CVD, and conversion of carbon or CN nanotubes. Though the supply of BN nanotubes has in the past been very restricted, they are now being mass-produced and the subject of much experimentation. Importantly, BN nanotubes have uniform (large-gap semiconductor) electrical properties relatively independent of tube diameter and chirality, making them less ''variable'' than carbon nanotubes. Theoretical predictions suggest that the band gap of BN nanotubes is *tunable*, via either mechanical deformation or the application of intense transverse electric fields [19,20]. The mechanical properties of carbon and BN nanotubes are comparable.

Although "pure" nanotubes are wonderful structures rich in basic science and applications potential, they also form intriguing building blocks for higher-order structures. One of the most common modifications of nanotubes is so-called functionalization, wherein the nanotube is purposefully modified to give it new chemical, electronic, magnetic, or even mechanical properties. Both "external" and "internal" functionalization is possible. External functionalization can be achieved by taking as-grown nanotubes and attaching chemical groups, nanoparticles, or other subsystems to the tube ends or sidewall. Such functionalization allows nanotubes to be attracted to other chemical species to which they might have been originally immune, or to assume new electrical characteristics [21]. It is suggested from experiment that simply adding oxygen to the end of a carbon nanotube greatly enhances the electron field emission capabilities of the nanotube [22]. One primitive but effective "functionalization" of carbon nanotubes is the addition of a surfactant to the nanotube exterior, whereby nanotube suspensions or solutions can be obtained. This allows controlled centrifuging of nanotubes, solution deposition, etc. Other external functionalizations include the addition of selected chemical groups, polymers, biologically relevant receptors, and sensor materials [23–26].

Nanotubes are easily filled with foreign species including simple gases, complex molecules, and nanocrystals. Such partially or completely filled nanotubes are effectively internally functionalized, since the internal filling can affect the "external" properties of the nanotube (via charge transfer, changes in vibrational modes, or magnetic interactions). Classic examples are carbon nanotubes filled with oxides, carbides, and salts [27]. Interestingly, fullerenes are attracted to the interior of carbon and BN nanotubes (where van der Waals forces yield a net lowering of energy), and hence nanotubes are rather easily filled by such species by simply exposing "end opened" tubes to fullerene vapor at elevated temperature. The resulting "peapod" [28] or "silocrystal" [29] structures are exceptionally stable. Indeed, if heated or irradiated, the internal fullerenes will not escape from the tube; rather they will coalesce into nanotubes themselves (this is one method for making double-wall carbon nanotubes, or carbon nanotubes encased in BN nanotubes).

3. CHARACTERIZATION

3.1. Electron Microscopy

The small lateral dimension of nanotubes makes them individually invisible to the naked eye. However, bulk amounts of carbon nanotubes are easily visible and they appear as black dust or soot, or, for tangled mats of tubes, as black rubbery felt. BN nanotubes are similar in appearance but white to light gray in color. To properly image small collections of tubes or individual tubes, microscopes with nanoscale resolution are necessary (thus ruling out all optical-based microscopes). Here, electron microscopes are invaluable. Scanning electron microscopes (SEMs) are

useful for obtaining an overall impression of the nanotube material (purity, typical length of tubes, etc.), or for imaging nanotube-containing devices such as transistors or nanomotors where larger scale device features are typically also of interest and must be simultaneously imaged. Individual SWNT's can just barely be resolved using the best SEMs, but even then it is difficult to distinguish a tight bundle of nanotubes from a true single nanotube.

For the imaging of individual nanotubes, either MWNTs or SWNTs, transmission electron microscopy (TEM) is king. Indeed, it is probably fair to say that without TEM, nanotubes might still be undiscovered. TEM imaging of nanotubes yields something akin to a cross-section of the tube [1] (Fig. 2). Hence, if the tube is oriented perpendicular to the direction of the imaging electron beam (the usual geometry), then each shell of the nanotube will appear as two parallel lines in the micrograph. The distance between the lines is the shell diameter. A SWNT will appear as just two parallel lines, while a three-wall MWNT, for

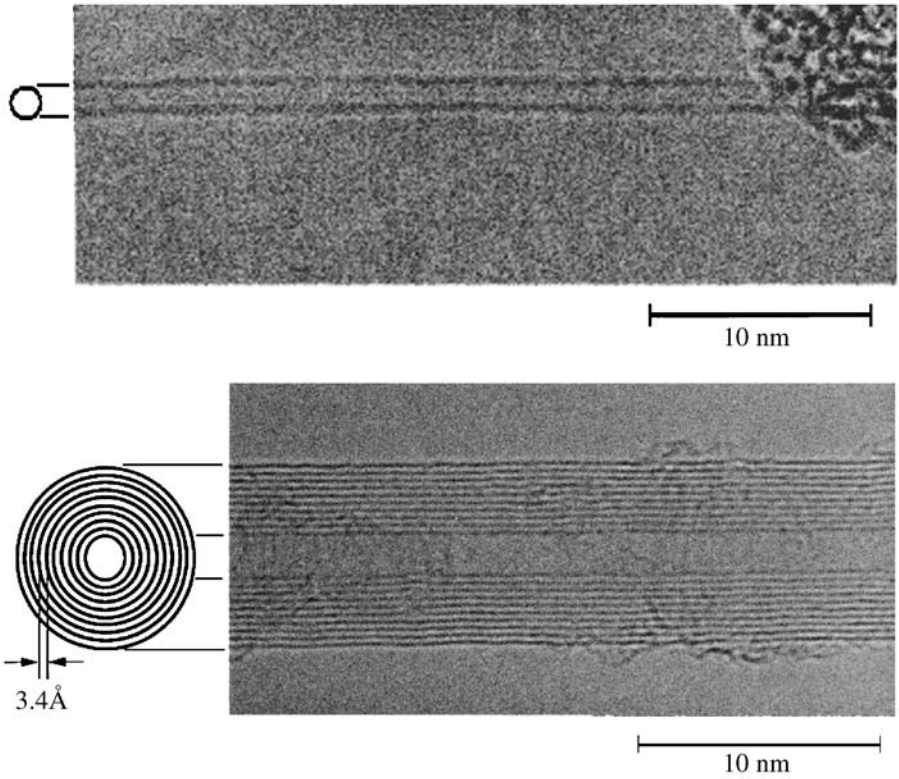

Fig. 2. High-resolution TEM images of a single-walled carbon nanotube (top) and a multiwalled carbon nanotube (bottom). The scales for the two images are the same. Single-walled nanotubes generally have a diameter smaller than even the innermost shell of multiwalled nanotubes.

example, will be represented by three sets of two parallel lines, the lines within a set separated by roughly 3.4 Å, the van der Waals separation for graphitic layering. TEM imaging immediately identifies the number of walls or shells, along with the overall perfection of the tube, the type of end-cap (if the ends of the tubes are within the field of view), and, most importantly, if foreign material (accidental or intentional) is present in the interior of the tube or on the outer surface of the tube. Collapsed nanotubes are easily identified via TEM [7], as are certain other kinds of gross defects, such as "bamboo-like" closures within the tube. Careful TEM imaging and analysis also allows the chirality of individual nanotubes to be determined, even if they constitute the concentric shells of a MWNT [30]. For BN nanotubes, for example (Fig. 3), there turns out to be a general correlation between the chiralities of successive shells in multiwall tubes [31,32].

Electron microscopy has proved to be extremely useful for the characterization of nanotube properties other than strictly structural. For example, the elastic Young's modulus and internal friction of MWNTs and SWNTs was first determined by

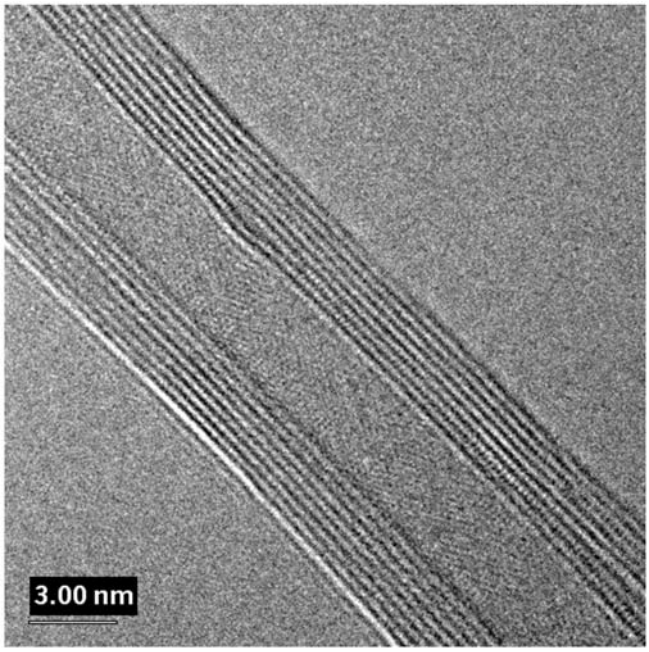

Fig. 3. High-resolution TEM image of a multiwalled BN nanotube. Note the exceptionally clean surfaces, both inside and outside the tube. The modulations along the tube shells are the atomic charge density corrugations. The pattern just discernable in the tube interior reflects electron interference from successive tube wall scatterings; a careful analysis of this pattern yields information about the shell chiralities. A minor structural defect affecting the innermost two shells is apparent just above and to the left of center.

TEM examination of vibration modes of cantilevered nanotubes, either thermally or electrostatically driven [33,34]. The advantage of these techniques is that individual tubes can be probed, and simultaneous TEM imaging makes known the geometrical properties of the tube in question.

One serious drawback to TEM imaging is that the imaging electrons can severely damage the nanotube. A 300 keV electron beam will fully destroy a MWNT within a minute or two, compromising the graphitized structure and leaving only amorphous carbon remnants behind. Fortunately, many high-resolution TEMs in use today yield sufficient resolution using only modest electron energies, say 100 keV or less. Under these irradiation conditions, a typical carbon nanotube can be imaged for many minutes or even tens of minutes with minimal structural damage. Of course, electron-beam damage can be used to advantage where the effects of controlled defect density on, say, structural, transport, or mechanical properties are of interest.

Rather recently, the power of electron microscopes has been greatly extended through the incorporation of nanomanipulators (Fig. 4). Nanomanipulators are essentially three-dimensional translation stages with ultrafine (atomic scale or better) adjustment capability, which are placed inside the SEM or TEM and mechanically manipulate the sample during imaging [35–37]. To achieve the necessary positional accuracy, both coarse (often detuned mechanical) and fine (often piezodriven) motion stages are utilized. Additional electrical feedthroughs allow simultaneous electrical excitations to be applied to the sample. In many ways, nanomanipulators resemble scanning tunneling or atomic force microscopes (AFMs) (indeed they can serve as such if properly configured). Early nanomanipulators were invariably home-made, but commercially produced systems, for incorporation into a variety of TEMs and SEMs, are now available. Noteworthy nanotube-related experiments that nanomanipulators have made possible include electron holography during field emission [38]; exploration of the mechanical properties of individual nanotubes [37]; the examination of ''sword and sheath'' failure modes of MWNTs under axial strain [39]; sharpening, peeling, and ''telescoping'' of nanotubes to form linear bearings and nanorheostats [37,40,41]; the creation of nanoscale mass conveyors, relaxation oscillators, and linear nanocrystal-powered nanomotors [42–44]; the construction and operation of tunable electromechanical resonators [45]; and examination of quantized conductance steps in nanotube–metal interfaces [46].

3.2. Scanning Tunneling and Atomic Force Microscopy

Under the most favorable imaging conditions TEMs just manage atomic resolution for light z elements (including, of course, carbon, boron, and nitrogen), but this is just the starting point for scanning tunneling microscopes (STMs). AFMs typically have lesser resolution than do STMs, but with the important benefit of being able to image on insulating substrates and having generally more straightforward mechanical manipulation features. With these capabilities in mind, is not surprising

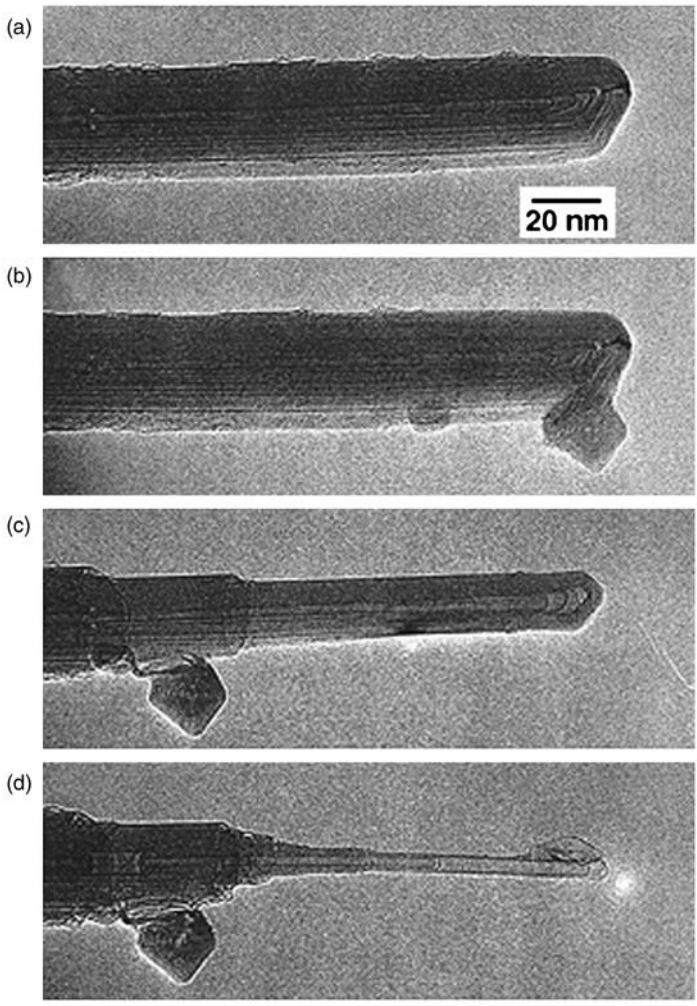

Fig. 4. Nanoscale surgery. A multiwall carbon nanotube is successively shaped by electrical current pulses supplied by a nanomanipulator operating inside a high-resolution TEM. Nanomanipulators make possible novel in situ mechanical and electrical experiments on individual nanotubes or other nanoscale objects.

that substantial experimental effort has been devoted to STM/AFM imaging of nanotubes.

Early theoretical calculations showed that the geometry of carbon nanotubes, coupled with the unusual ''Fermi point'' bandstructure of graphite, results in a strong dependence of the electronic properties on tube diameter and chirality. Testing these and related predictions provides a wonderful opportunity for STM imaging and spectroscopy. The difficulty here lies not in the necessity for any

particularly novel STM instrumentation or technique (established techniques are perfectly adequate), but rather in nanotube sample preparation. STM is a surface sensitive technique and, unlike TEM, it necessitates absolutely clean nanotube surfaces. Most STM sample preparation methods rely on deposition of a nanotube solution or suspension onto metal surfaces and simply letting the solvent evaporate, although some recent STM studies of carbon nanotubes indicate that "dry" contacting methods may be advantageous. Dramatic images of nanotubes have been obtained using both methods [47–49].

STM imaging is usually performed in vacuum, perhaps following a heating step to clean residual solvent or other contaminants from the tube and substrate. Understandably, success rates are low but on occasion atomic structure can be resolved. Important early successes were a determination of the diameter and chirality of carbon nanotubes determined via STM topographic images (Fig. 5), correlated to the electronic properties obtained at the same time via STM spectroscopy [47,48]. Tubes of different length have also been investigated for electronic quantum confinement effects [50], and nanotubes filled with fullerenes have been examined via STM spectroscopy [51]. The vibrational modes of nanotubes are also accessible via STM methods using specially fabricated nanotube devices [52].

Because STMs can yield "atomic resolution" it is often assumed that the true nanotube atomic "chicken wire" structure, with possible defects, is immediately obvious from an STM image. This is not so. STM generally maps integrated electronic density of states (DOS), and as such the recorded data may be extremely difficult to interpret, especially near defect sites. This is unfortunate, since one of the most interesting features of carbon nanotubes is possible defects. Geometrical defects can dramatically influence the local, and often global, electronic properties of nanotubes. For example, it is in principle possible to geometrically "graft" one chirality nanotube end-to-end onto another chirality nanotube using a suitable combination of defects (such as fivefold and sevenfold rings). The "junction" thus formed, which links tubes of different electronic structure, can be the source of a stable electronic device (such as a rectifier). Through an iterative theoretical analysis of experimental data, it is possible to deconvolute STM data to identify atomic defect structure in nanotubes. The method has been successfully applied to carbon nanotube junctions [53].

At first glance BN nanotubes would appear unlikely candidates for STM studies, primarily because of their rather large intrinsic electronic bandgap ($\sim 5\,\mathrm{eV}$). Nevertheless, individual BN tubes have been imaged (with atomic resolution) by STM methods, and in fact STM has proven to be an unexpectedly powerful tool for exploring BN nanotube electronic state structure. Unusual stripe patterns are obtained [54]. In addition, high local electric field afforded by a biased STM tip can be used to modify the local bandstructure. In the case of BN, this can result in a reduction of the bandgap [55]. It is predicted that, for sufficiently large applied transverse electric fields, the bandgap in BN nanotubes can be driven fully to zero, resulting in a metallic system [20].

Atomic force microscopy (AFM) generally lacks the ultrahigh resolution of STM, but the method affords many distinct advantages over SEM, TEM, and STM relevant to nanotube research. The primary use of AFM has been as a tool in device

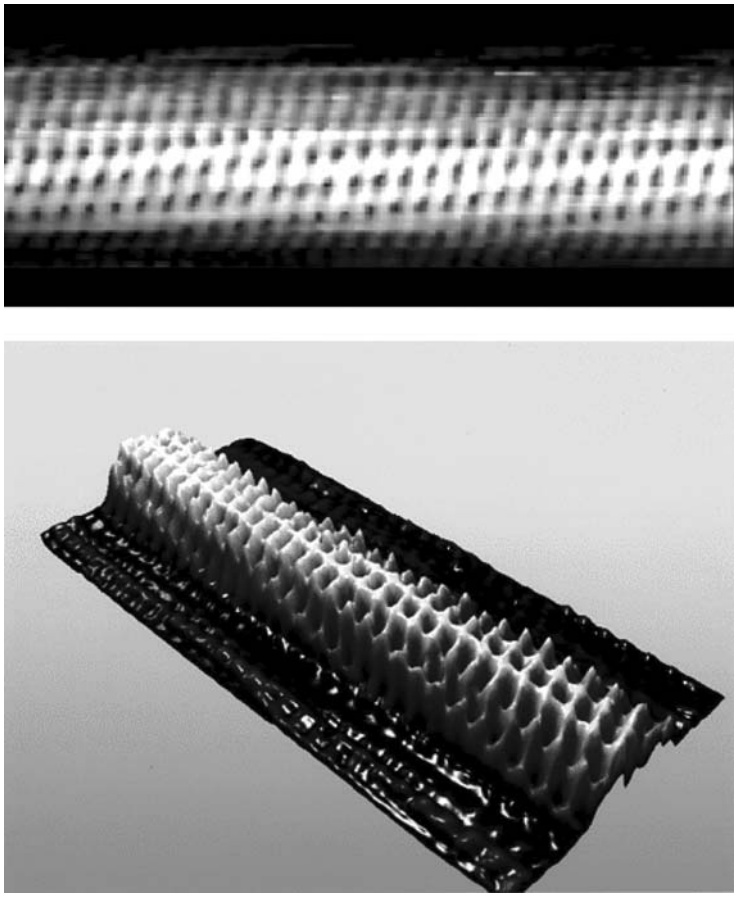

Fig. 5. Scanning tunneling microscope image of carbon nanotube, with two different data representations. From such images the nanotube geometrical indices can be deduced. Simultaneous STM spectroscopy yields experimentally the electronic density of states versus energy. Courtesy of C. Dekker Research Group.

fabrication. Often nanotubes are randomly dispersed on a silicon oxide surface, and an individual nanotube must then be ''wired up'' with electrical leads. AFM is an efficient method whereby a suitable nanotube is ''located'' [55]. The position coordinates thus obtained are used in the subsequent lithography process. Finished electronic and/or mechanical devices can also be imaged and further characterized via AFM. For example, the shear modulus of carbon nanotubes has been explored by AFM probing of torsional modes of suspended nanotubes, sometimes outfitted with deflection paddles [56,57]. Nanotubes, with their high stiffness and favorable aspect rations, have also been used as tip extensions for AFM cantilevers [58]. Enhanced AFM resolution is obtained, and the compound system also serves as a

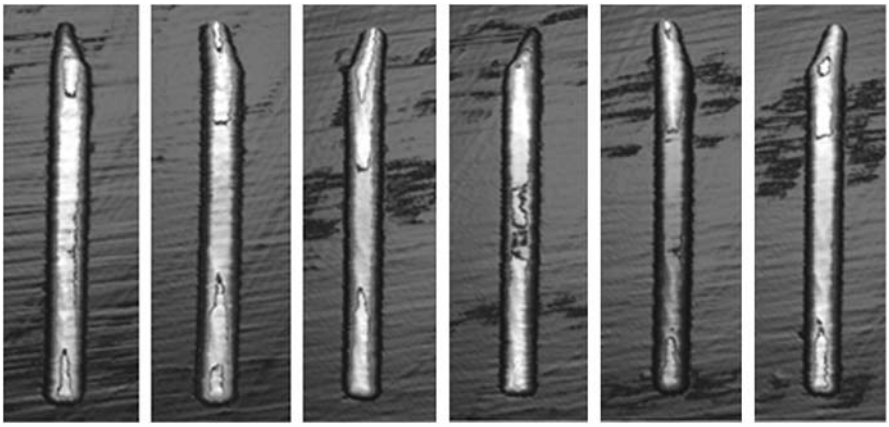

Fig. 6. Atomic force microscope images of a multiwall carbon nanotube in different orientations on a graphite surface. The tube was rolled with the AFM tip between images. The tube is 30 nm in diameter and 500 nm long. Courtesy of R. Superfine Research Group.

testing ground for the mechanical properties of the nanotube (including bending and buckling) [59].

An interesting application of AFM to MWNT characterization is to use the AFM tip as a ''finger'' with which to push and roll nanotubes around on a surface. This can be useful in the construction of nanotube-based devices, or simply as a means to study the properties of nanotubes. For example, MWNTs have been manipulated on cleaved graphite [60] (Fig. 6). Mechanical interactions of the MWNT with the substrate are thus elucidated, and simultaneous electrical measurements can also be made (the idea being that the indexing of the nanotube hexagonal pattern to the graphite below may affect the electronic conductance between the two systems).

3.3. Raman and Optical Spectroscopy

The unusual geometrical atomic structure of nanotubes leads naturally to a rich vibrational spectrum for both phonon and electronic excitations. Raman studies have been applied by many research groups to carbon nanotubes with important findings. A particularly useful result is the strong diameter dependence of the radial breathing mode (RBM) [61–63]. RBM analysis thus provides a relatively simple diagnostic for nanotube synthesis efforts, in that the diameter distribution of a bulk amount of nanotubes can be readily established. MWNTs are also here of interest, in particular double-wall tubes where an influence of one shell on the other is expected. Since Raman spectroscopy relies on light optics (with a focusing ability of about one micron), one might guess that a Raman study of a *single* nanotube is out of the question. However, by using sufficiently dilute depositions of nanotubes on substrates such that on average only one nanotube per square micron is present,

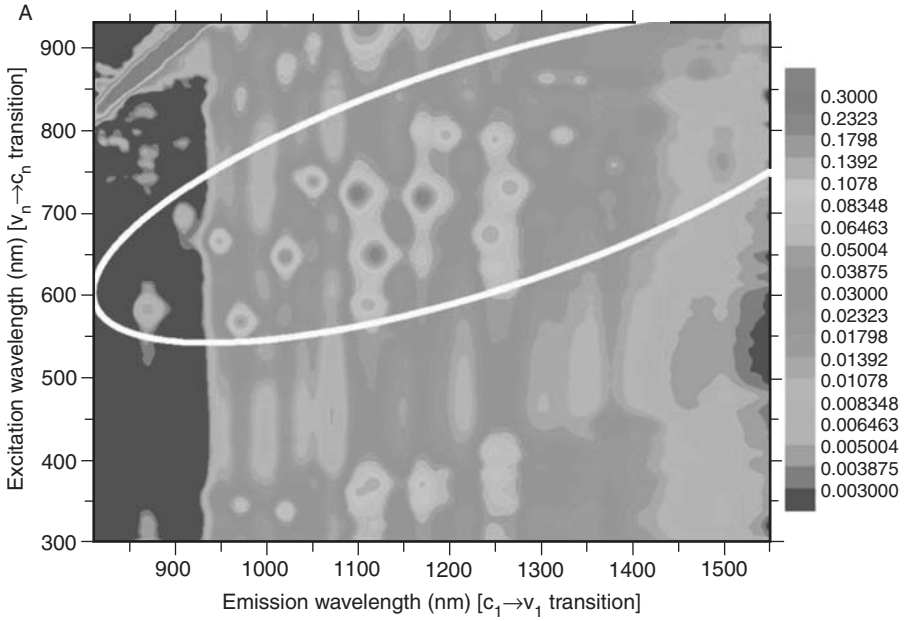

Fig. 7. Excitation wavelength versus emission wavelength for single-walled nanotubes isolated and in liquid suspension. These data identify the electronic transitions and thus structural indices for semiconducting tubes within the solution. Adapted from Ref. [65].

microRaman, with single-tube resolution, is possible. Using this method the diameter *and chirality* of individual SWNTs have been determined [64].

The low-dimensional electronic and phonon structure of nanotubes yields strong anomalies (van Hove singularities) in the excitation spectrum. In particular, sharp transitions are expected for optical absorption. Early optical studies of nanotubes were hampered by clustering of the tubes into ropes, but suitable dispersion methods have been developed that allow separation of individual tubes in stable liquid suspensions. The tubes thus suspended are coated by rather large surfactant molecules, but this does not appear to compromise to a large extent the intrinsic optical excitations. A wealth of information, including tube diameter and chirality (at least for semiconducting tubes) can be extracted using such optical excitation experiments [65] (Fig. 7). Indeed, the experiments have become sufficiently refined that the results have allowed the fine-tuning of theoretical models incorporating higher-order corrections for the electronic response.

3.4. Electronic and Thermal Transport

Nanotubes, with their small diameter, long length, and atomic perfection, appear to be physical realizations of the ideal quantum wire. It has been suggested that the

physics of diffusive carrier scattering (leading to Ohms law, etc.) is thus no longer applicable, but rather the concepts of quantum conductance channels and ballistic transport must be employed. But simply ''wiring up'' and measuring, say, the electrical conductance of a single nanotube, is nontrivial. Even the time-honored method of four-point conductivity measurements is of questionable utility, since added contacts may perturb the system so severely that the usual assumptions of ''nonperturbative contacts'' are invalid. From a theoretical viewpoint, one expects for a quantum wire an electrical conductance of e^2/h per perfectly transmitting channel. For two bands at the Fermi energy and two electron spin states, this yields four channels and hence a conductance of $4e^2/h$, or a resistance of approximately $6\,\mathrm{k}\Omega$. Such a low resistance is rarely measured in practice for isolated SWNTs, presumably due to poor contacts or defect-compromised transmission coefficients. The measurements are most often performed in a two-probe configuration. Some experiments have attempted to determine the voltage drop along the nanotube while it is carrying an electrical current [66]. For a uniformly diffusive conductor, one of course expects a continuous, linear drop in electrical potential. For a ballistic conductor, on the other hand, the potential drops stepwise, and then only at the contacts. There is some evidence that metallic SWNTs may behave more often as ballistic conductors than do semiconducting tubes [66]. Experiments show that the temperature dependence of the electrical conductance for carbon nanotubes is also unusual, and it has been suggested that the transport reflects Luttinger–Tomonaga correlated behavior rather than Fermi-liquid [67]. Luttinger liquids are most often characterized by power-law behavior in the temperature and electric field dependences with well-known exponents, and these have been observed in limited studies.

At low temperatures, carbon nanotubes appear to ''break up'' into a series of electronic domains or quantum dots (Fig. 8). The conductance is rich in structure if the nanotube charge is modulated by a third electrode (the ''gate'' electrode) capacitively coupled to the nanotube. The behavior is that of a usual Coulomb blockaded or multiply connected quantum dot system. Conductance experiments in this regime have extracted important length and energy scales for the nanotubes [68].

For collections of nanotubes in matt form, the electrical conductance is also interesting. Typically, the temperature dependence is that of a metal from room temperature until about 100 K, whereafter the resistance rises with decreasing temperature. In this low-temperature regime, the conductance is highly electric-field dependent. Here the temperature and field dependences have been interpreted in terms of carrier localization [69].

The electrical conductance of MWNTs is experimentally as well as theoretically challenging. Field emission experiments have proven without doubt that MWNTs are excellent conductors, capable of withstanding electrical current densities well in excess of $10^{10}\,\mathrm{A/cm^2}$, exceeding the current carrying capability of even superconducting wires [70–73]. However, the details of the conductance mechanism are complex. The typical MWNT is composed of nested concentric cylindrical shells, and for carbon there appears to be no general rule on the nesting of metallic versus semiconducting cylinders – in other words, the radial sequence is basically random.

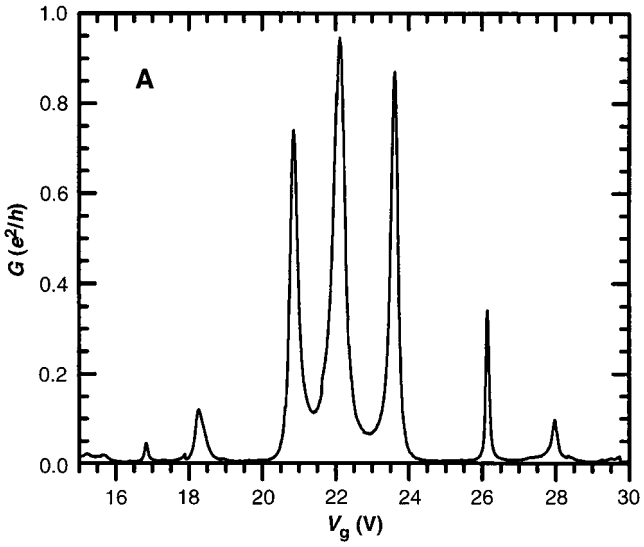

Fig. 8. Low-temperature conductance versus gate voltage for a single-wall nanotube wired up in a two-probe (source/drain) configuration on a silicon chip. The gate, coupled capacitively to the nanotube, controls the charge on the tube. The sharp conductance peaks are reminiscent of quantum dot behavior. Adapted from Ref. [68].

Hence, a MWNT is expected to have metallic as well as semiconducting tubes within it, in no particular order. However, the typical experimental contact to a MWNT is not uniformly through the end of the tube (contacting equally all shells), but rather is through only the sidewall of the outermost tube, making it unclear how the inner tubes are connected, if at all. Some experiments (such as Aharonov–Bohm type [74] and successive shell "blow out" [75] alterations) suggest that the outer shell, whatever its intrinsic electrical properties may be, primarily conducts the current. Other experiments suggest something akin to an anisotropic conductivity tensor, with weak intershell coupling [76]. Yet other experiments, performed in situ inside a TEM, suggest, at least in the high-field regime, that MWNTs behave much like *isotropic*, diffusive conductors (albeit very good ones).

Some interesting experiments have been designed to investigate explicitly intershell and length dependent nanotube conductance. For MWNTs dipped into liquid metals (such as mercury) there is evidence for unusual quantized conductance steps as a function of the depth the nanotube is immersed into the liquid [77], while for telescoped tubes the resistance between the outer shell on one end and the inner core on the other end suggests an exponential length dependence as the core is withdrawn [78,79].

Other transport coefficients of nanotubes (primarily carbon-based) have been investigated, including Hall effect (for collections of tubes) and thermoelectric power. Thermopower is a particularly useful probe in that it identifies the sign of the charge carrier. Interestingly, both positive and negative thermopower has been

observed for SWNTs [80]. This is believed to reflect extrinsic doping of the tubes (adsorbed oxygen, for example, may strip electrons from the tube and dope it to p-type). The thermal transport of nanotubes is of special interest, in part because nanotubes provide a near-ideal one-dimensional geometry for testing models of quantized thermal conductance, and also because carbon and BN nanotubes may (because of high phonon frequencies and low defect concentration) have exceptionally high absolute thermal conductances at room temperature. High metallic and insulating thermal has important implications for thermal management applications.

The thermal conductivity of mats of SWNTs decreases with decreasing temperature, and is linear in T at low temperature [81]. This is evidence for quantized thermal conductance (the quantum of thermal conductance is proportional to $k_B T$). At higher temperatures ($>30\,\mathrm{K}$) occupation of higher phonon subbands becomes apparent. From a mat-like geometry it is difficult to determine accurately the absolute value of the thermal conductivity, but single-tube experiments give values of order $3000\,\mathrm{W/mK}$ near room temperature [82]. Carbon nanotubes are exceptionally good thermal conductors. Thermal experiments on (isotopically impure) BN nanotubes have also been performed, and the results suggest that BN tubes have a thermal conductance somewhat less than that for carbon nanotubes [83]. It is yet unclear how much of the thermal conductance in carbon nanotubes is due to phonons and how much is due to electrons, but presumably most of the heat is carried by phonons.

4. APPLICATIONS

The unique mechanical, electronic, and thermal properties of nanotubes suggest many applications and disruptive technologies, ranging from space elevators to DNA sorting to ultra-fast, high-density electronic circuitry. Some nanotube-based devices have already entered the marketplace.

4.1. Composites

An appealing application for carbon and BN nanotubes is mechanical reinforcements and composites [84] (Fig. 9). The graphite-fiber industry is well established, and nanotubes in a way represent the ultimate graphite fiber. However, it is far from trivial to simply replace carbon fiber with nanotubes. In some applications, very long (meter-scale) fibers are required, and to date the longest laboratory nanotubes are but several centimeters long. Continuously grown nanotubes, of arbitrary length, are obviously of special interest and different synthesis methods are being tested. Interesting, methods have been developed to "spin" shorter nanotubes into longer fibers or cables, much like the spinning of yarn fibers [85]. In some composite applications, however, short fibers are in fact preferred. Despite the outstanding high elastic moduli of nanotubes, one must always address the problem

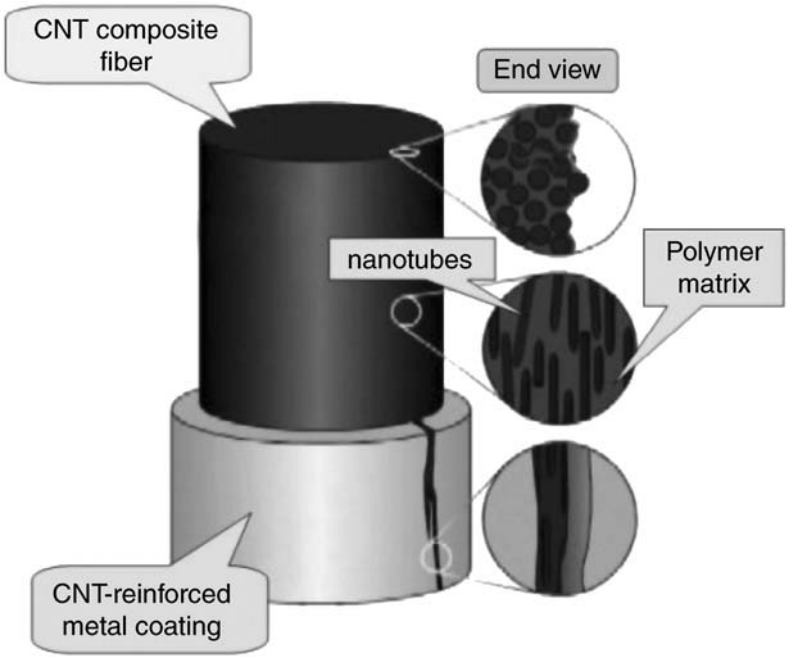

Fig. 9. Schematic illustration of a possible nanotube composite structure. Depending on application, long, aligned nanotubes may be preferred. The key to a useful composite is the interface between the nanotubes and the polymer matrix. Adapted from Nanopedia.

of adhesion between the surrounding matrix (say polymer) and the nanotube. Functionalization of the nanotube walls can be exploited, and some synthesis methods have in fact yielded high-quality nanotubes with "bumps" formed on their surfaces ("nanorebar" [86]). A number of composites have been produced using different forms of nanotubes, some with impressive performance enhancements. It must also be noted that nanotube-containing composites may have utilities beyond mechanical reinforcement. For example, the addition of nanotubes to certain plastics enhances the electrical conductance of the plastic and can make the material far more suitable for electrostatic painting processes (examples include automobile bumpers).

4.2. Electronic Devices

The good electrical conductance and high aspect ratio of carbon nanotubes suggests immediately another application: that of electron field emission. Electron field emission is useful for certain flat panel display technologies, high intensity lamps, and coherent electron sources such as those used in electron microscopes. Experiments on individual tubes, aligned arrays of tubes, and "matrix composites"

of tubes have demonstrated that carbon nanotubes are indeed excellent electron field emission sources [70–73]. A number of prototype devices employing nanotube field emitters have already been produced. Interestingly, BN nanotubes, despite their large electronic bandgap and supposed insulating properties, are found, under the right conditions, to display excellent field emission characteristics [87].

The application that has probably received the most attention for nanotubes is that of nanoscale electronic devices. It has even been suggested that nanotubes may play an important role in overcoming certain anticipated ''brick walls'' in the scaling of silicon-based devices to very small dimensions. Nanotubes are strong, withstand relatively high temperature, are highly electrically and thermally conducting, and are about 1 nm wide. These are all positive features for molecular-scale electronics. The first nanotube-based electronic device to be demonstrated was a rectifier [88], formed from SWNTs that contained a symmetry-breaking defect (Fig. 10). Identifying and characterizing the device was not trivial, and the process is summarized here to illustrate an intrinsic problem of nanotube electronics: scale-up. First, many high-quality SWNTs were grown by laser ablation. The ends were glued to a conducting substrate, and an STM tip was dragged over the tubes like a comb through hair, catching several tubes. The tip was then retracted, shedding nanotubes one by one, until only the longest tube remained attached. Further retraction resulted in the STM tip sliding along the tube length, probing it electrically as the nanotube remained in vacuum, suspended between the substrate and the STM tip (eliminating spurious substrate contamination effects). A small fraction of the tubes thus interrogated displayed device behavior. Unfortunately, although this method can be used to ''find'' tubes with desirable electronic characteristics, it is difficult if not impossible to reliably incorporate those nanotubes into a conventional chip-based device platform.

A goal for nanotube device experiments is to incorporate nanotubes directly into well-known silicon-based processing technology. The first nanotube-based field effect transistor consisted of a nanotube placed on a silicon oxide surface on top of degenerately doped silicon [89] (Fig. 11). Contacts (defined by electron-beam lithography) provided the source and drain terminals to the tube, while the doped silicon below served as the gate electrode. The device operated at room temperature. Many related carbon nanotube devices have been constructed and tested, with impressive performance specifications often exceeding the best conventional devices.

The ''all surface'' aspect of SWNTs is both good and bad. For one, it allows the nanotube to be used as an exceedingly gas or chemical sensor. Early experiments, for example, found that the electrical conductance (and thermoelectric power) of SWNTs is exceedingly sensitive to oxygen [80] (Fig. 12). Other experiments, including those employing tailored functionalization (both inorganic and that with biologically relevant receptors), have demonstrated that nanotubes may serve as low-power, sensitive gas detectors [90]. The drawback to this sensitivity is that nanotube electronics can be hypersensitive to ambient chemical species, necessitating extra protective measures. In addition, contact effects may play important roles

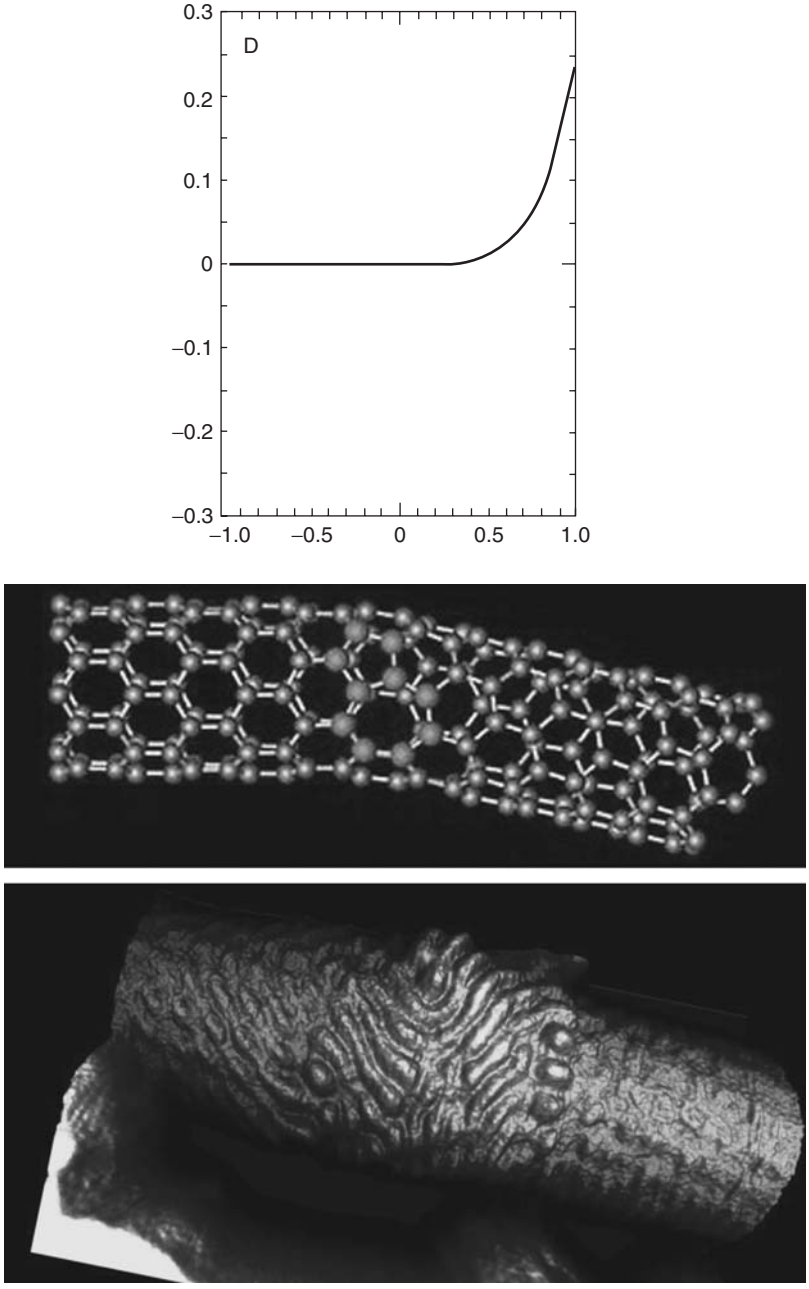

Fig. 10. Current (vertical axis, in μA) versus voltage (horizontal axis, in volts) for the first nanotube-based device fabricated: a single-walled carbon nanotube rectifier (upper graph). Rectification is possible when suitable defects (such as pentagon/heptagon pairs, as shown in the model in the lower image) occur on the nanotube wall, forming a junction between tube portions with differing electrical characteristics (center image). The lower illustration shows actual STM data for a nanotube junction with a pentagon/heptagon defect on its upper surface. Adapted from Refs. [53] and [88], and courtesy of S. Louie Research Group.

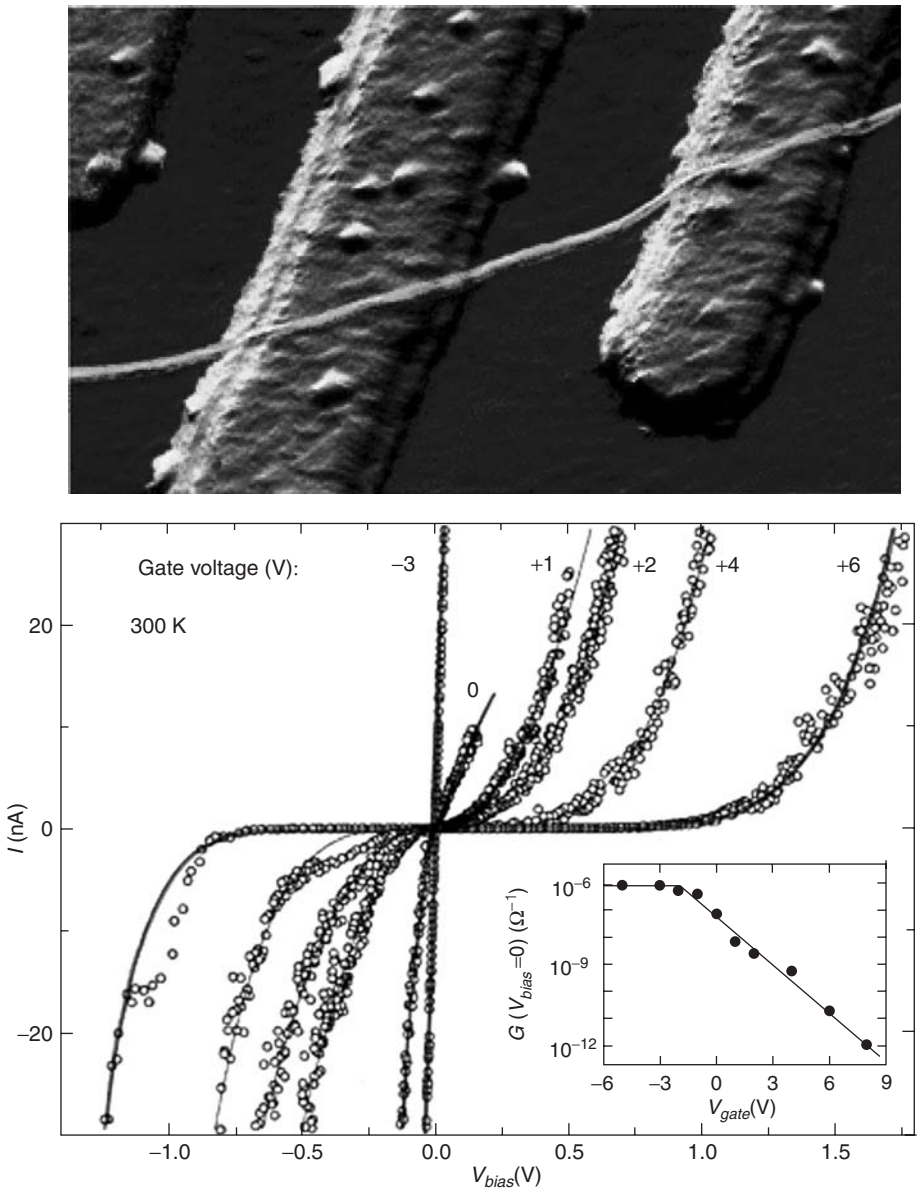

Fig. 11. Nanotube transistor AFM image (upper image), and typical current–voltage characteristics, obtained at room temperature. Adapted from Ref. [89].

(including doping) in many nanotube-based device architectures [91]. Nevertheless, an impressive collection of nanotube-based devices has been demonstrated, including higher-order devices with logic functions [92]. Some nanotube-based chemical sensors are in fact already in the market.

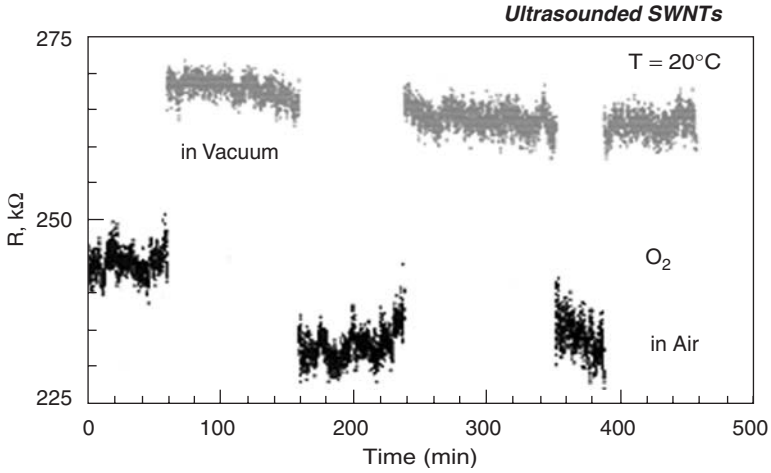

Fig. 12. Electrical resistance of a single-wall carbon nanotube exposed alternately to vacuum and oxygen. The resistance is consistently lower in the presence of oxygen (lower traces), suggesting charge transfer and demonstrating that nanotubes can be used as sensitive chemical gas sensors. Adapted from Ref. [80].

4.3. Nanoelectromechanical Systems (NEMS)

Nanotubes have mechanical and electronic properties that make them desirable candidates for a host of NEMS applications. The simplest of these rely on using the nanotube as an electromechanical switch. For example, two nanotubes touching each other may serve to close an electrical circuit. The mechanical contact may be facilitated by application of external or "internal" force. Sources of internal force are the van der Waals attraction between nanotubes or the stiction between nanotubes and substrate surfaces. The switching process has been demonstrated in the laboratory and attempts to commercialize it are underway [93] (Fig. 13).

The close fit and low friction between concentric shells of MWNTs is suggestive of linear and rotational bearings. Linear bearing motion has been demonstrated in TEM experiments where the end of a MWNT is opened up and the core tubes are telescoped back and forth using a nanomanipulator in a repeatable fashion [37]. Rotational motion has also been demonstrated in experiments where MWNTs serve as low-friction bearings in lithographically defined electrostatically driven rotational motors [94] (Fig. 14). Recent theoretical and experimental studies have attempted to quantify the magnitude of the frictional forces between nanotube shells in relative motion [95,96]. Experimentally, friction is absent within the resolution of the experiment, $<10^{-15}$ N/atom, and no evidence for atomic-scale wear or fatigue is observed. Nanotubes thus provide exceptionally low friction, virtually wear-free surfaces suitable for NEMS or MEMS application. Theoretically, dissipation occurs primarily at the open ends of the tube; two infinitely long

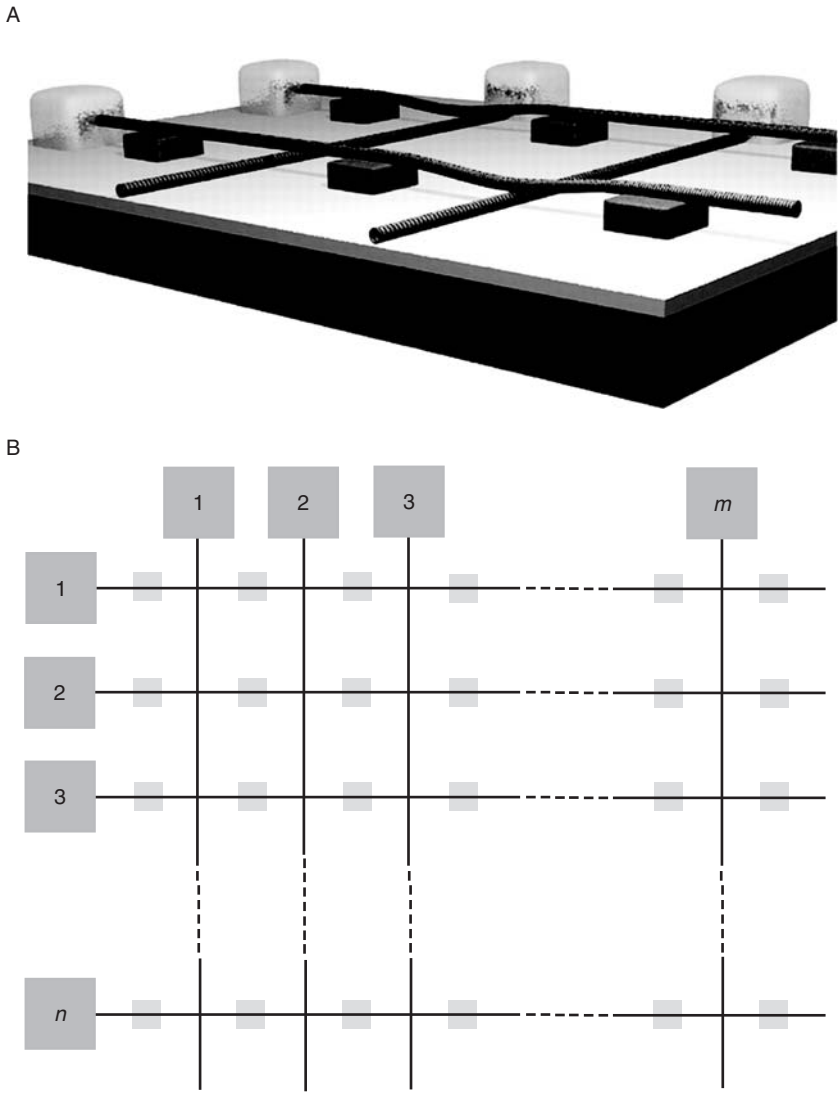

Fig. 13. Schematic of nanotubes in an electromechanical array configuration. Mechanical deformation allows physical (and electrical) contact between tubes. This could be useful in a memory device architecture. Adapted from Ref. [94].

nanotubes rotating or sliding one within the other apparently display no friction, at least at low velocity. Phonons generated by the motion are presumably readsorbed into the system with no net energy loss. At higher velocity, resonances with internal nanotube phonon modes may be encountered, which leads to dissipation resonances.

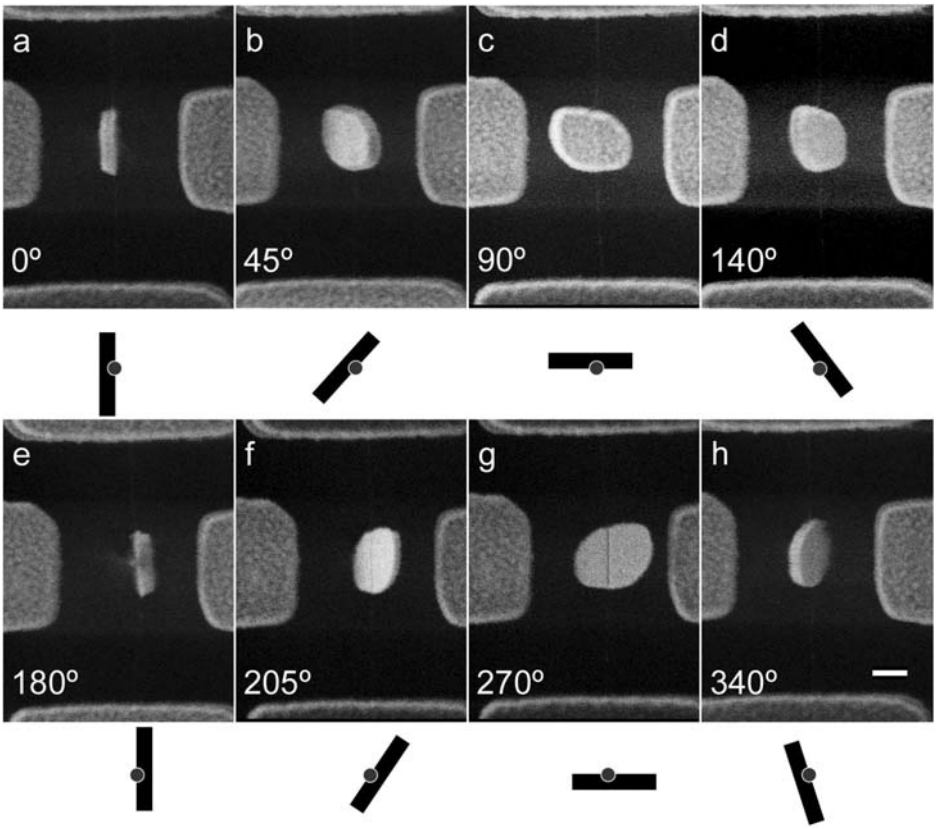

Fig. 14. Operational NEMS device. A multiwall carbon nanotube forms the rotational bearing in an electrostatically driven, rotational actuator. The nanotube is barely visible, running vertically through the center of each frame. The rotor is here photographed via SEM in different angular positions. Adapted from Ref. [93].

5. CONCLUSION

Experiments on nanotubes have established the basic mechanical and electronic properties. The majority of the experiments are consistent with theoretical models and predictions. Isolated tube experiments are now possible, allowing intrinsic tube properties to be separated from "extrinsic" tube–tube interaction or tube–substrate effects. Tubes of carbon, both single-wall and multiwall, are the most often studied experimentally, but important results have been obtained for BN and other noncarbon nanotubes as well. BN nanotubes share the same sp^2 structure of carbon nanotubes and thus many mechanical properties similarities exist. Nanotubes are being used to improve certain nanoscale instrumentation, including AFM and STM, and nanotubes are being mated with biologically relevant systems in a variety of ways. The rich basic

science afforded by nanotube systems is often complemented by an equally diverse and rich applications potential.

It should be emphasized that one of the key features of any condensed matter experimental science is the availability of high-quality samples. The mass production of the "buckyball" C_{60} had an enormous impact on the experimental (and theoretical) study of fullerenes, which led directly to the discovery of nanotubes. Single- and multiwall nanotubes would no doubt remain a modest theoretical curiosity if not for their ready availability in the laboratory. Along these lines, the recent isolation of single sheets of graphene [97] has spurred much new experimental and theoretical work in two-dimensional graphene. These studies are of direct relevance to nanotubes, as the effects of different boundary conditions, curvature, interlayer couplings, etc., are now directly accessible experimentally starting from an isolated sheet. In one sense the study of sp^2-bonded graphite has come full circle, and it is just the beginning of a wonderful age of nanoscale science exploration.

ACKNOWLEDGEMENTS

This work was supported in part by the US National Science Foundation and the US Department of Energy. Receipt of a Fellowship from the Miller Institute for Basic Research in Science is gratefully acknowledged.

REFERENCES

[1] S. Iijima, Helical microtubules of graphitic carbon, *Nature* **354**, 56 (1991).
[2] R. Tenne, L. Margulis, M. Genut and G. Hodes, Polyhedral and cylindrical structures of WS2, *Nature* **360**, 444 (1992).
[3] N.G. Chopra, R.J. Luyken, K. Cherrey, V.H. Crespi, M.L. Cohen, S.G. Louie and A. Zettl, Boron Nitride Nanotubes, *Science* **269**, 966 (1995).
[4] *Low-Dimensional Cooperative Phenomena*, edited by H.J. Keller (Plenum Press, New York, 1975).
[5] *Charge Density Waves in Solids*, edited by L.P. Gorkov and G. Gruner (North Holland, Amsterdam, 1989).
[6] M.S. Dresselhaus and G. Dresselhaus, *Graphite Fibers and Filaments*, Springer Series in Materials Science, vol. 5, (Springer-Verlag, Berlin, 1988).
[7] N. Chopra, L.S. Benedict, V.H. Crespi, M.L. Cohen, S.G. Louie and A. Zettl, Fully Collapsed Carbon Nanotubes, *Nature* **377**, 135 (1995).
[8] T.W. Ebbesen and P.M. Ajayan, Large-scale synthesis of carbon nanotubes, *Nature* **358**, 220 (1992).
[9] W. Krätschmer, L.D. Lamb, K. Fostiropoulos and D.R. Huffman, Solid C60: A new form of carbon, *Nature* **347**, 354 (1990).
[10] D.S. Bethune, C.H. Klang, M.S. de Vries, G. Gorman, R. Savoy, J. Vazquez and R. Beyers, Cobalt-catalysed growth of carbon nanotubes with single-atomic-layer walls, *Nature* **363**, 605 (1993).
[11] S. Iijima and T. Ichihasi, Single-shell nanotubes of 1-nm diameter, *Nature* **363**, 603 (1993).
[12] A. Thess, R. Lee, P. Nikolaev, H. Dai, P. Petit, J. Robert, C. Xu, Y.H. Lee, S.G. Kim, A.G. Rinzler, D.T. Colbert, G.E. Scuseria, D. Tomanek, J.E. Fischer and R.E. Smalley, Crystalline ropes of metallic carbon nanotubes, *Science* **273**, 483 (1996).

[13] H.J. Dai, A.G. Rinzler, P. Nikolaev, A. Thess, D.T. Colbert and R.E. Smalley, Single-wall nanotubes produced by metal-catalyzed disproportionation of carbon monoxide, *Chem. Phys. Lett.* **260**, 471 (1996).
[14] S. Fan, M.G. Chapline, N.R. Franklin, T.W. Tombler, A.M. Cassell and H.J. Dai, Self-oriented regular arrays of carbon nanotubes and their field emission properties, *Science* **283**, 512 (1999).
[15] R. Tenne and A. Zettl, Nanotubes from inorganic materials, in *Carbon Nanotubes*, edited by M.S. Dresselhaus, G. Dresselhaus, and P. Avouris (Springer-Verlag, Berlin, 2001), *Topics Appl. Phys.* **80**, 83.
[16] A. Rubio, J.L. Corkill and M.L. Cohen, Theory of graphitic boron nitride nanotubes, *Phys. Rev. B* **49**, 5081 (1994).
[17] Z. Weng-Shieh, K. Cherrey, N.G. Chopra, X. Blase, Y. Miyamoto, A. Rubio, M.L. Cohen, S.G. Louie and A. Zettl, Synthesis of $B_xC_yN_z$ nanotubules, *Phys. Rev. B* **51**, 11229 (1995).
[18] O. Stephan, P.M. Ajayan, C. Colliex, Ph. Redlich, J.M. Lambert, P. Bernier and P. Lefin, Doping graphitic and carbon nanotube structures with boron and nitrogen, *Science* **266**, 1683 (1994).
[19] Y.-H. Kim, K.J. Chang and S.G. Louie, Electronic structure of radially deformed BN and BC3 nanotubes, *Phys. Rev. B* **63**, 205408 (2001).
[20] K.H. Khoo, M.S.C. Mazzoni and S.G. Louie, Tuning the electronic properties of boron nitride nanotubes with transverse electric fields: A giant dc Stark effect, *Phys. Rev. B* **69**, 201401 (2004).
[21] S.B. Sinnot, Chemical functionalization of carbon nanotubes, *J. Nanosci. Nanotechnol.* **2**, 113 (2002).
[22] A. Maiti, J. Andzelm, M. Tanpipat and P. von Allmen, Effect of adsorbates on field emission from carbon nanotubes, *Phys. Rev. Lett.* **87**, 155502 (2001).
[23] J. Chen, M.A. Hamon, H. Hu, Y. Chen, A.M. Rao, P.C. Eklund and R.C. Haddon, Solution properties of single-walled carbon nanotubes, *Science* **282**, 95 (1998).
[24] A. Star, J.F. Stoddart, D. Steuerman, M. Diehl, A. Boukai, E.W. Wong, X. Yang, S.W. Chung, H. Choi and J.R. Heath, Preparation and properties of polymer-wrapped single-walled carbon nanotubes, *Angewandte Chemie* **40**, 1721 (2001).
[25] A. Star, J.-C. Gabriel, K. Bradley and G. Gruner, *Nano. Lett.* **3**, 459 (2003).
[26] W.-Q. Han and A. Zettl, Functionalized boron nitride nanotubes with a stannic oxide coating: A novel chemical route to full coverage. *J. Am. Chem. Soc.* **125**, 2062 (2003); W.-Q. Han and A. Zettl, Coating single-walled carbon nanotubes with tin oxide, *Nano. Lett.* **3**, 681 (2003).
[27] P.M. Ajayan and S. Iijima, Capillarity-induced filling of carbon nanotubes, *Nature* **361**, 333 (1993).
[28] B.W. Smith, M. Monthioux and D.E. Luzzi, Encapsulated C60 in carbon nanotubes, *Nature* **396**, 323 (1998).
[29] W. Mickelson, S. Aloni, W.-Q. Han, J. Cumings and A. Zettl, Packing C60 in boron nitride nanotubes, *Science* **300**, 467 (2003).
[30] R.R. Meyer, S. Friedrichs, A.I. Kirkland, J. Sloan, J.L. Hutchison and M.L.H. Green, A composite method for the determination of the chirality of single walled carbon nanotube. *J. Microsc.* **212**, 152 (2003); J.M. Zuo, I. Vartanyants, M. Gao, R. Zhang, and L.A. Nagahara, Atomic resolution imaging of a carbon nanotube from diffraction intensitites, *Science* **300**, 1419 (2003).
[31] D. Golberg and Y. Bando, Unique morphologies of boron nitride nanotubes, *Appl. Phys. Lett.* **79**, 415 (2001).
[32] B.G. Demczyk, J. Cumings, A. Zettl and R.O. Ritchie, Structure of boron nitride nanotubules, *Appl. Phys. Lett.* **78**, 2772 (2001).
[33] M.M.J. Treacy, T.W. Ebbesen and J.M. Gibson, Exceptionally high Youngs modulus observed for individual carbon nanotubes, *Nature* **381**, 678 (1996).
[34] P. Poncharal, Z.L. Wang, D. Ugarte and W.A. de Heer, Electrostatic deflections and electromechanical resonances of carbon nanotubes, *Science* **283**, 1513 (1999).
[35] H. Ohnishi, Y. Kondo and K. Takayanagi, Quantized conductance through individual rows of suspended gold atoms, *Nature* **395**, 780 (1998).
[36] E.A. Stach, T. Freeman, A.M. Minor, D.K. Owen, J. Cumings, M.A. Wall, T. Chraska, R. Hull, J.W. Morris, Jr., A. Zettl and U. Dahmen, Development of a nanoindenter for in-situ transmission electron microscopy, *Microsc. Microanal.* **7**, 507 (2001).

[37] J. Cumings and A. Zettl, Low-friction nanoscale linear bearing realized from multiwall carbon nanotubes, *Science* **289**, 602 (2000).
[38] J. Cumings, M.R. McCartney, J.C.H. Spence and A. Zettl, Electron holography of field-emitting carbon nanotubes, *Phys. Rev. Lett.* 88, 5 056804-1/4 (2002).
[39] M.F. Yu, O. Lourie, M.J. Dyer, K. Moloni, T.F. Kelly and R.S. Ruoff, Strength and breaking mechanism of multiwalled carbon nanotubes under tensile load, *Science* **287**, 637 (2000).
[40] J. Cumings, P.G. Collins and A. Zettl, Peeling and sharpening multiwall nanotubes, *Nature* **406**, 586 (2000).
[41] J. Cumings and A. Zettl, Localization and nonlinear resistance in telescopically extended nanotubes, *Phys. Rev. Lett.* **93**, 086801-1-4 (2004).
[42] B.C. Regan, S. Aloni, R.O. Ritchie, U. Dahmen and A. Zettl, Carbon nanotubes as nanoscale mass conveyors, *Nature* **428**, 924 (2004).
[43] B.C. Regan, S. Aloni, K. Jensen and A. Zettl, Surface-tension-driven nanoelectromechanical relaxation oscillator, *Appl. Phys. Lett.* **86**, 123119 (2005).
[44] B.C. Regan, S. Aloni, K. Jensen, R.O. Ritchie, U. Dahmen and A. Zettl, Nanocrystal Powered Nanomotor, *Nano. Lett.* **5**, 1730 (2005).
[45] K. Jensen, C. Girit, W. Mickelson and A. Zettl, Tunable nanoresonators constructed from telescoping nanotubes, *Phys. Rev. Lett.* **97**, 215503 (2006).
[46] S. Frank, P. Poncharal, Z.L. Wang and W.A. deHeer, Carbon nanotube quantum resistors, *Science* **280**, 1744 (1998).
[47] J.W.G. Wildoer, L.C. Venema, A.G. Rinzler, R.E. Smalley and C. Dekker, Electronic structure of atomically resolved carbon nanotubes, *Nature* **391**, 59 (1998).
[48] T.W. Odom, J.-L. Huang, P. Kim and C.M. Lieber, Atomic structure and electronic properties of single-walled carbon nanotubes, *Nature* **391**, 62 (1998).
[49] P.M. Albrecht and J.W. Lyding, Ultrahigh-vacuum scanning tunneling microscopy and spectroscopy of single-walled carbon nanotubes on hydrogen-passivated Si(100) surfaces, *Appl. Phys. Lett.* **83**, 5029 (2003).
[50] L.C. Venema, J.W.G. Wildöer, J.W. Janssen, S.J. Tans, H.L.J. Temminck Tuinstra, L.P. Kouwenhoven and C. Dekker, Imaging electron wave functions of quantized energy levels in carbon nanotubes, *Science* **283**, 52 (1999).
[51] D.J. Hornbaker, S.J. Kahng, S. Misra, B.W. Smith, A.T. Johnson, E.J. Mele, D.E. Luzzi and A. Yazdani, Mapping the one-dimensional electronic states of nanotube peapod structures, *Science* **295**, 828 (2002).
[52] B.J. LeRoy, S.G. Lemay, J. Kong and C. Dekker, Electrical generation and absorption of phonons in carbon nanotubes, *Nature* **432**, 371 (2004).
[53] M. Ishigami, H.J. Choi, S. Aloni, S.G. Louie, M.L. Cohen, and A. Zettl, Identifying defects in nanoscale materials, *Phys. Rev. Lett.* 93 19 196803-1/4 (2004).
[54] M. Ishigami, S. Aloni and A. Zettl, Scanning tunneling microscopy and spectroscopy of boron nitride nanotubes, in *Molecular Nanostructures*, vol. 685, edited by H. Kuzmany, J. Fink, M. Mehring and S. Roth, *AIP Conference Proceedings*, (2003), p. 389.
[55] M. Ishigami, J.D. Sau, S. Aloni, M.L. Cohen and A. Zettl, Observation of the giant Stark effect in boron-nitride nanotubes, *Phys. Rev. Lett.* **94**, 056804 (2005).
[56] A.J. Kulik, A. Kis, G. Gremaud, S. Hengsperger and L. Forró, Nanoscale mechanical properties using SPM, in *Techniques and Applications in Nanotechnology Handbook*, edited by B. Bushan (Springer-Verlag, Heidelberg, 2004).
[57] P.A. Williams, S.J. Papadakis, A.M. Patel, M.R. Falvo, S. Washburn and R. Superfine, Fabrication of nanometer-scale mechanical devices incorporating individual multiwalled carbon nanotubes as torsional springs, *Appl. Phys. Lett.* **82**, 805 (2003).
[58] G. Nagy, M. Levy, R. Scarmozzino, R.M. Osgood, H. Dai, R.E. Smalley, C.A. Michaels, G.W. Flynn and G.F. McLane, Carbon nanotube tipped atomic force microscopy for measurement of <100 nm Etch morphology on semiconductors, *Appl. Phys. Lett.* **73**, 529 (1998).
[59] E.W. Wong, P.E. Sheehan and C.M. Lieber, Nanobeam mechanics: Elasticity, strength and toughness of nanorods and nanotubes, *Science* **277**, 1971 (1997).

[60] M.R. Falvo, R.M. Taylor II, A. Helser, V. Chi, F.P. Brooks Jr., S. Washburn and R. Superfine, Nanometre-scale rolling and sliding of carbon nanotubes, *Nature* **397**, 236 (1999).
[61] A.M. Rao, E. Richter, S. Bandow, B. Chase, P.C. Eklund, K.A. Williams, S. Fang, K.R. Subbaswamy, M. Menon, A. Thess, R.E. Smalley, G. Dresselhaus and M.S. Dresselhaus, Diameter-selective Raman scattering from vibrational modes in carbon nanotubes, *Science* **275**, 187 (1997).
[62] F. Simon, Ch. Kramberger, R. Pfeiffer, H. Kuzmany, V. Zólyomi, J. Kürti, P.M. Singer and H. Alloul, Isotope engineering of carbon nanotube systems, *Phys. Rev. Lett.* **95**, 017401 (2005).
[63] S. Bandow, G. Chen, G.U. Sumanasekera, R. Gupta, M. Yudasaka, S. Iijima and P.C. Eklund, Diameter-selective resonant Raman scattering in double-wall carbon nanotubes, *Phys. Rev. B* **66**, 075416 (2002).
[64] A. Jorio, R. Saito, J.H. Hafner, C.M. Lieber, M. Hunter, T. McClure, G. Dresselhaus and M.S. Dresselhaus, Structural (*n*, *m*) determination of isolated single-wall carbon nanotubes by resonant Raman scattering, *Phys. Rev. Lett.* **86**, 1118 (2001).
[65] S.M. Bachilo, M.S. Strano, C. Kittrell, R.H. Hauge, R.E. Smalley and R.B. Weisman, Structure-assigned optical spectra of single-walled carbon nanotubes, *Science* **298**, 2361 (2002).
[66] A. Bachtold, M.S. Fuhrer, S. Plyasunov, M. Forero, E.H. Anderson, A. Zettl and P.L. McEuen, Scanned probe microscopy of electronic transport in carbon nanotubes, *Phys. Rev. Lett.* **84**, 6082 (2000).
[67] M. Bockrath, D.H. Cobden, J. Lu, A.G. Rinzler, R.E. Smalley, L. Balents and P.L. McEuen, Luttinger-liquid behaviour in carbon nanotubes, *Nature* **397**, 598 (1999).
[68] M. Bockrath, D.H. Cobden, P.L. McEuen, N.G. Chopra, A. Zettl and R.E. Smalley, Single-electron transport in ropes of carbon nanotubes, *Science* **275**, 1922 (1997).
[69] M.S. Fuhrer, M.L. Cohen, A. Zettl and V. Crespi, Localization in single-walled carbon nanotubes, *Solid State Comm.* **109**, 105 (1999).
[70] A.G. Rinzler, J.H. Hafner, P. Nikolaev, L. Lou, S.G. Kim, D. Tomanek, P. Nordlander, D.T. Colbert and R.E. Smalley, Unraveling nanotubes-field-emission from an atomic wire, *Science* **269**, 1550 (1995).
[71] W.A. de Heer, A. Châtelain and D. Ugarte, A carbon nanotube field-emission electron source, *Science* **270**, 1179 (1995).
[72] P.G. Collins and A. Zettl, A simple and robust electron beam source from carbon nanotubes, *Appl. Phys. Lett.* **69**, 1969 (1996).
[73] G.Z. Yue, Q. Qiu, B. Gao, Y. Cheng, J. Zhang, H. Shimoda, S. Chang, J.P. Lu and O. Zhou, Generation of continuous and pulsed and diagnostics imaging X-ray radiation using a carbon-nanotube-based field-emission cathode, *Appl. Phys. Lett.* **81**, 355 (2002).
[74] A. Bachtold, C. Strunk, J.-P. Salvetat, J.-M. Bonard, L. Forró, T. Nussbaumer and C. Schönenberger, Aharonov–Bohm oscillations in carbon nanotubes, *Nature* **397**, 673 (1999).
[75] P.G. Collins, M.S. Arnold and P. Avouris, Engineering carbon nanotubes and nanotube circuits using electrical breakdown, *Science* **292**, 706 (2001).
[76] T.D. Yuzvinsky, W. Mickelson, S. Aloni, S.L. Konsek, A.M. Fennimore, G.E. Begtrup, A. Kis, B.C. Regan and A. Zettl, Imaging the life story of nanotube devices, *Appl. Phys. Lett.* **87**, 083103 (2005).
[77] S. Frank, P. Poncharal, Z.L. Wang, and W.A. deHeer, Carbon nanotube quantum resistors, *Science* **280**, 1744 (1998); H.J. Choi, J. Ihm, Y.-G. Yoon, and S.G. Louie, Possible explanation for the conductance of a single quantum unit in metallic carbon nanotubes, *Phys. Rev. B* **60**, R14009 (1999).
[78] J. Cumings and A. Zettl, Resistance of telescoping nanotubes, in structural and electronic properties of molecular nanostructures, *American Institute of Physics Conference Proceedings* (Melville, NY, 2002), vol. 633, pp. 227–230.
[79] S. Akita and Y. Nakayama, Nanoscale variable resistance using interlayer sliding of multiwall nanotube, *Jpn. J. Appl. Phys.* **43**, 3796 (2004).
[80] P.G. Collins, K. Bradley, M. Ishigami and A. Zettl, Extreme oxygen sensitivity of electronic properties of carbon nanotubes, *Science* **287**, 1801 (2000).
[81] J. Hone, M. Whitney, C. Piskoti and A. Zettl, Thermal conductivity of single-walled carbon nanotubes, *Phys. Rev. B* **59**, R2514 (1999).

[82] P. Kim, L. Shi, A. Majumdar and P.L. McEuen, Thermal transport measurements of individual multiwalled nanotubes, *Phys. Rev. Lett.* **87**, 215502 (2001).
[83] C.W. Chang, W-.Q. Han and A. Zettl, Thermal Conductivity of B-C-N and BN Nanotubes, *Appl. Phys. Lett.* **86**, 173102 (2005).
[84] H.Z. Geng, R. Rosen, B. Zheng, H. Shimoda, L. Fleming, J. Liu and O. Zhou, Fabrication and properties of composites of poly(ethylene-oxide) and functionalized carbon nanotubes, *Adv. Mater.* **14**, 1387 (2002).
[85] M. Zhang, K.R. Atkinson and R.H. Baughman, Multifunctional carbon nanotube yarns by downsizing an ancient technology, *Science* **306**, 1358 (2004).
[86] N.G. Chopra and A. Zettl (unpublished)
[87] J. Cumings and A. Zettl, Field emission and current–voltage properties of boron nitride nanotubes, *Solid State Commun.* **129**, 661 (2004).
[88] P.G. Collins, A. Zettl, H. Bando, A. Thess and R.E. Smalley, Nanotube nanodevice, *Science* **278**, 100 (1997).
[89] S.J. Tans, A.R.M. Verschueren and C. Dekker, Room-temperature transistor based on a single carbon nanotube, *Nature* **393**, 49 (1998).
[90] J. Kong, N. Franklin, C. Chou, S. Pan, K.J. Cho and H. Dai, Nanotube molecular wires as chemical sensors, *Science* **287**, 622 (2000).
[91] P. Avouris, J. Appenzeller, R. Martel and S.J. Wind, Carbon nanotube electronics, *Proc. IEEE* **91**, 1772 (2000).
[92] A. Bachtold, P. Hadley, T. Nakanishi and C. Dekker, Logic circuits with carbon nanotube transistors, *Science* **294**, 1317 (2001).
[93] A.M. Fennimore, T.D. Yuzvinsky, W.-Q. Han, M.S. Fuhrer, J. Cumings and A. Zettl, Rotational actuators based on carbon nanotubes, *Nature* **424**, 408 (2003).
[94] T. Rueckes, K. Kim, E. Joselevich, G.Y. Tseng, C.L. Cheung and C.M. Lieber, Carbon nanotube-based nonvolatile random access memory for molecular computing, *Science* **289**, 94 (2000).
[95] P. Tangney, S.G. Louie and M.L. Cohen, Dynamic sliding friction between concentric carbon nanotubes, *Phys. Rev. Lett.* **93**, 065503 (2004).
[96] A. Kis, K. Jensen, S. Aloni, W. Mickelson and A. Zettl, Interlayer forces and ultralow sliding friction in multiwalled carbon nanotubes, *Phys. Rev. Lett.* **97**, 025501 (2006).
[97] K.S. Novoselov, A.K. Geim, S.V. Morozov, D. Jiang, Y. Zhang, S.V. Dubonos, I.V. Grigorieva and A.A. Firsov, Electric field effect in atomically thin carbon films, *Science* **306**, 666 (2004).

This page intentionally left blank

Chapter 2
QUANTUM THEORIES FOR CARBON NANOTUBES

S. Saito

1. INTRODUCTION

Carbon is a fascinating element. One can construct in principle an infinite number of different one-dimensional (1D) crystalline geometries as well as zero-dimensional clusters consisting entirely of carbon. The former are carbon nanotubes and each nanotube has hexagonal sp^2 covalent bond network with distinct diameter and chirality (Fig. 1) [1]. The latter are called fullerenes having pentagon–hexagon network [2]. Actually in the case of fullerenes, many different kinds of fullerenes, from C_{60} to around C_{100} with various isomers, have already been extracted from soot in macroscopic amounts and have been chromatographically *purified*, giving rise to many kinds of new crystalline carbon phases [3].

In the case of carbon nanotubes, existence of many kinds of nanotubes in various samples has also been confirmed experimentally using Raman spectroscopy, photoexcitation spectroscopy, scanning probe microscopies, and, most importantly, the transmission electron microscopy, which enabled Sumio Iijima to *discover* the material itself and simultaneously to clarify its rich geometries, i.e., the chiral nature of nanotubes [1]. On the other hand, unlike fullerenes, a geometrically homogeneous macroscopic sample of *any* carbon nanotube has not been produced yet. Therefore, *predictive* quantum mechanical theories have played and will continue to play a role of essential importance in the field of carbon nanotubes as will be reviewed in this chapter, in which an overview of theories applied to carbon nanotubes is presented and the advantages of each theory are summarized.

Contemporary Concepts of Condensed Matter Science
Carbon Nanotubes: Quantum Cylinders of Graphene

ISSN: 1572-0934/doi:10.1016/S1572-0934(08)00002-4

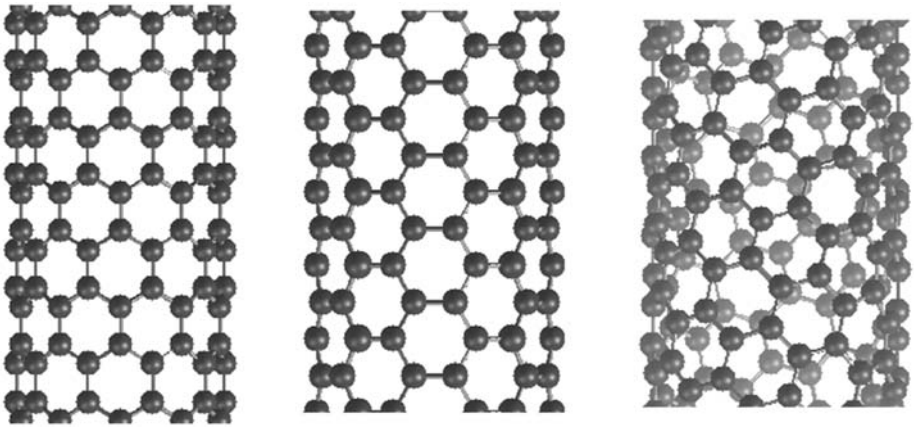

Fig. 1. Carbon nanotubes. There are two kinds of achiral nanotubes called "zigzag nanotubes" (left) and "armchair nanotubes" (center). The remaining nanotubes are called "chiral nanotubes" (right). Courtesy of Y. Akai.

2. TIGHT-BINDING MODELS

In the traditional tight-binding model, transfer matrix elements of the Hamiltonian between atomic orbits on the nearest-neighbor sites are considered, and their values are so assumed that they reproduce the experimental band structure of the crystalline material of interest. Then, one can discuss and understand the basic physical properties that the valence electrons show [4]. In many "modern" tight-binding models, on the other hand, several kinds of generalizations have been devised and a more quantitative analysis of the electronic properties of known materials is now possible. In some tight-binding models, even the atomic geometries as well as the energetics of various materials to be given by the first-principles theories are now being discussed with a high degree of accuracy. Especially for carbon, many kinds of tight-binding models have been constructed for various purposes. They have been applied to carbon nanotubes, and many important predictions including their rich electronic transport properties depending on the bond network topology have been made.

2.1. $\pi-\sigma$ Tight-Binding Model

Most important electronic properties of carbon nanotubes, i.e., the chirality dependence of their electronic transport properties, were first systematically studied and clarified by using the tight-binding model that deals not only with π states but also with σ states by Hamada et al. [5]. One of two kinds of achiral nanotubes, now so-called armchair nanotubes, are found to be metallic, while other nanotubes are either moderate-gap or narrow-gap semiconductors depending on the network topology as far as the order of its diameter is 1 nm (Fig. 2).

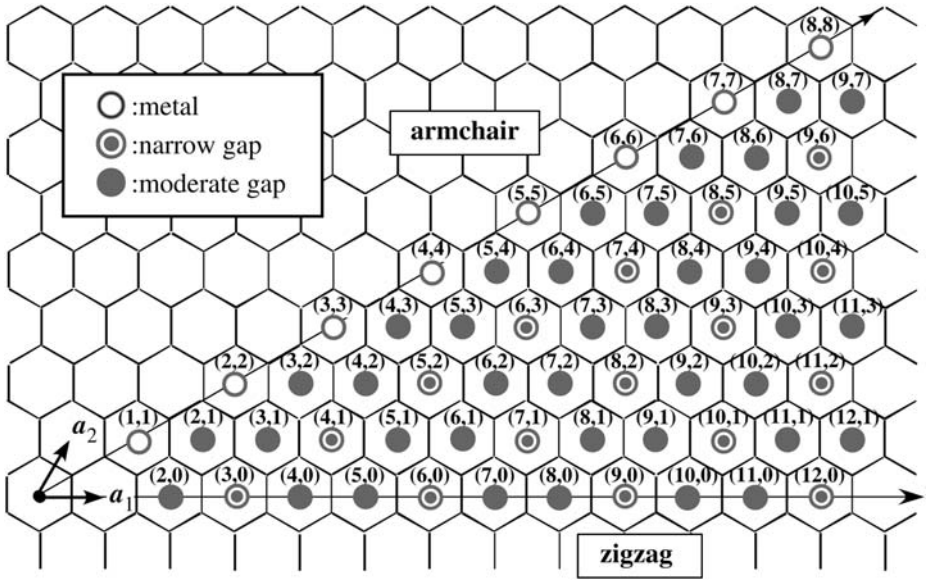

Fig. 2. Circumferential vector map of carbon nanotubes and their electronic transport properties. Courtesy of T. Matsumoto.

Opening of the moderate gap can be understood by considering the π states of the planar graphene with the periodic boundary condition whose periodicity is the circumferential length of the corresponding nanotube [5–7]. Although graphene is a two-dimensional (2D) material and there are electronic states at the Fermi level, it does not have ''Fermi lines'' but two ''Fermi points'' in its 2D first Brillouin zone. This peculiar electronic property of graphene gives rise to a whole variety of transport properties of carbon nanotubes. Opening of the narrow gap can also be understood from the graphene electronic structure if one takes into account a curvature effect on cylindrical nanotube geometry [5]. In a planer hexagonal network of graphene, each C atom possesses only one kind of C–C bonds with its three neighbors. Therefore, not only atoms but also chemical bonds are all equivalent on graphene. However, although all the C atoms are equivalent in *any* nanotube, each C atom on achiral and chiral nanotubes possesses two and three kinds of C–C bonds, respectively, on the nonplanar nanotube surface. The transfer matrix element for a tilted $\pi-\pi$ pair should be different from that for a parallel pair on a planer surface. In addition, π states on curved nanotube surface are no longer pure C 2p states but should retain some C 2s component also. These curvature effects are known to be responsible for the opening of narrow gap in the electronic structure of otherwise metallic nanotubes. These effects can be fully taken into account in the tight-binding model with C 2s and 2p orbitals, which gives rise to both π and σ states of the system studied ($\pi-\sigma$ tight-binding model). In the $\pi-\sigma$ tight-binding model used by Hamada et al. [5,8], moreover, not only transfer matrix

elements but also the overlap matrix elements are considered, and geometry dependences of both matrix elements have been adjusted so as to reproduce well the electronic structure of graphite and solid C_{60} given by the density functional theory (DFT). It is now one of the most reliable tight-binding models to study quantitatively the electronic structure of various carbon-based materials with given atomic geometry.

2.2. π Tight-Binding Model

Although the $\pi-\sigma$ tight-binding model can give fairly accurate electronic states of the system, most of the low-energy excitations of carbon nanotubes involve only π states. Hence, the tight-binding model, which deals only with π states (π tight-binding model), has been a very useful model in this field from the beginning [7]. The electronic density of states (DOS) reported by using the π tight-binding model showed many spiky peaks in the DOS curve as well as the constant DOS value around the Fermi level in metallic nanotubes. These specific electronic properties clearly indicate the importance of the dimensionality in such nanotube systems. Heretofore, the π tight-binding model has been used to understand not only qualitatively but also quantitatively a variety of electronic properties in carbon nanotubes as will be given in other chapters of this volume.

2.3. Tight-Binding Model for Geometries and Energetics

In the case of carbon, the $\pi-\sigma$ tight-binding model combined with short-range interatomic repulsive force has been used to discuss the geometries of many kinds of condensed phases [9–11]. The model has many parameters not only in the transfer matrix elements but also in the repulsive force term. Both terms are given as functions of atomic geometries. Most widely used parameters in this model have been so adjusted that the energetics of chemical bonds given in the DFT for both sp^2- and sp^3-network materials, i.e., graphene and diamond, can be reproduced well [9]. As for nanostructured materials, the model has been used to discuss the relative stabilities as well as the geometries of fullerene isomers [12]. More importantly, the model played an essential role in analyzing the X-ray diffraction patterns of new phases of solid C_{60} produced under external pressure, and three distinct polymerized C_{60} phases were identified [13,14]. In the work the formation of four-membered rings with interfullerene covalent bonds was successfully predicted.

Details of the nanotube geometries, on the other hand, have scarcely been discussed unlike fullerenes, since the hexagonal network is often considered to be rather rigid. However, as will be shown in the following section, it is found in the framework of the DFT that geometrical details are very important for relatively thin nanotubes produced well under some experimental conditions [15,16]. Hence, it is an interesting challenge to discuss the details of nanotube geometries and

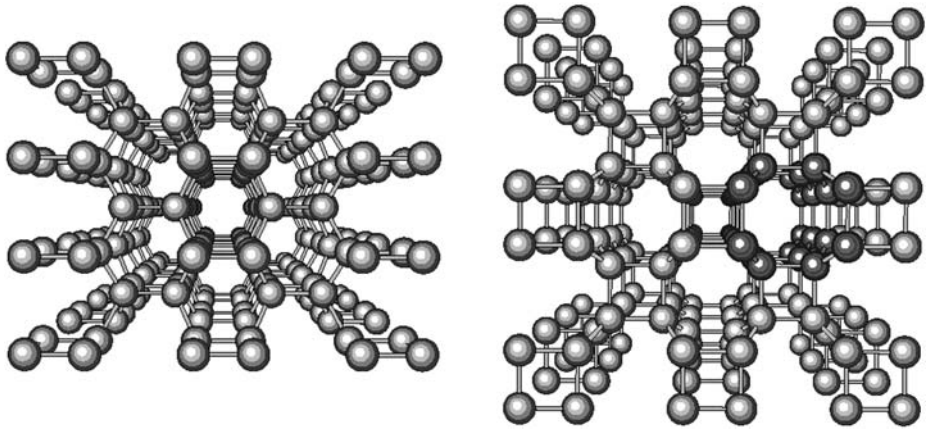

Fig. 3. Side view (left) and the top view (right) of the body-centered tetragonal C_4 lattice. As can be seen from the top view, the lattice consists of polymerized (2,2) armchair nanotubes. Courtesy of M. Sakurai.

energetics, which depend on the diameter and the chirality of the nanotube using the tight-binding model.

In addition to isolated individual carbon nanotubes, condensed phases of nanotubes, i.e., bundles of single-walled carbon nanotubes and concentric multi-walled carbon nanotubes, are very important phases to be discussed. In these condensed phases of nanotubes, not only chemical bonds but also the interlayer interaction between sp^2 carbon layers is very important. To describe this long-range interlayer interaction properly in the tight-binding model, a completely new set of parameters with the interaction range of 7 Å has been constructed and applied to nanotubes to discuss and predict the pressure-induced structural phase transformation of the crystalline nanotube phase [11]. As a result, the pressure-induced phase transformation of crystalline (10,10) nanotube solid into new sp^3 network solid carbon, the body-centered tetragonal C_4 phase, has been predicted (Fig. 3). Interestingly, this new phase can be considered as a polymerized phase of thin (2,2) armchair nanotubes, and therefore this pressure-induced phase transformation is a process in which the nanotube diameter decreases and simultaneously the polymerization via the formation of the intertube four-membered rings takes place.

3. DENSITY FUNCTIONAL THEORY

As has been discussed in the preceding section, the DFT [17,18] is considered to give very accurate electronic and structural properties of various nanostructured materials. Especially for the materials with s and p valence electrons including carbon-based materials, results obtained in this framework have been used as standards to construct various kinds of tight-binding models and interatomic model potentials for many elements.

In the DFT, the quantum mechanical many-body effects are all incorporated in the exchange-correlation functional, although its exact form is not known yet. In practice, however, there are several approximate but accurate ways to treat the functional. Most widely used approximation for the functional is the local-density approximation (LDA) where it is assumed that the exchange-correlation energy of the inhomogeneous interacting electron gas is to be given as a sum of the exchange-correlation energy of infinitesimal small spatial regions over the entire system, and that the contribution of each region is computed from the exchange-correlation energy of the uniform electron gas with the same density [18]. In the systems with spin polarization, the local-spin-density approximation (LSDA) can be used instead [19]. Also, the generalized gradient approximation (GGA) is used widely [20]. In GGA, the contribution of each region depends not only on the electron (spin) density but also on its gradient, and some of GGA functional forms are known to give more accurate energetics than those in LDA and LSDA in many systems, especially in magnetic systems. On the other hand, in the case of carbon, if well-extended basis functions such as plane waves are used, LDA is known to give accurate interlayer distance as well as the stacking sequence of graphite, i.e., "AB" stacking with the interlayer distance of 3.35 Å [11], while GGA fails to give the graphite interlayer distance. For the study of nanostructured carbon materials with sp^2-based geometries including carbon nanotubes, therefore, LDA should be a reasonable and yet highly accurate method to be adopted in the framework of the DFT. In this section, some important results for carbon nanotubes obtained in LDA are reviewed.

3.1. Geometries and Electronic States

It is known that there are only two kinds of C–C bonds in the icosahedral-symmetry C_{60} (Fig. 4a). Thirty bonds shared by two hexagons are shorter than other sixty bonds on twelve pentagons [21]. Experimental lengths of these two kinds of bonds are 1.401 and 1.458 Å, respectively, in gas phase [22]. Their small difference of 0.057 Å is found to be very important when predicting its electronic structure from first principles. The relative energy differences of the electronic states in C_{60} change considerably if one ignores this bond length difference. For example, the width of the gap between the highest-occupied state and the lowest-unoccupied state obtained in LDA for the C_{60} with the graphite bond length of 1.421 Å for all 90 bonds is 1.38 eV, which is smaller by as much as 0.25 eV than the gap value of 1.64 eV for the C_{60} having the experimental geometry with the bond length difference of 0.057 Å. The optimized geometry of C_{60} in LDA with the same methodology as has been used for carbon nanotubes to be discussed below is found to have a bond length difference of 0.055 Å, which is very close to the experimental difference value [23]. Accordingly, its gap width in LDA, 1.67 eV, is also very close to that for the experimental-geometry C_{60}.

This strong dependence of the electronic structure on geometries observed in C_{60} should be generally the case in nanostructured carbon materials including carbon nanotubes since the interaction between valence electrons and the lattice should be

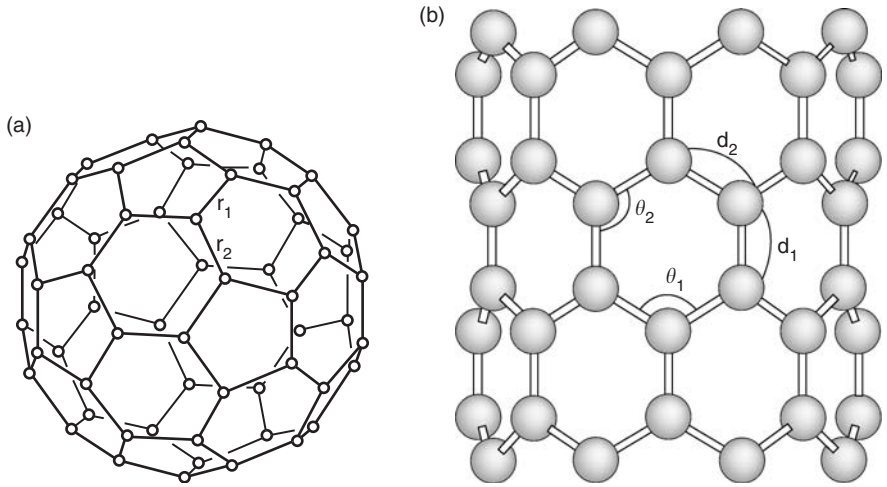

Fig. 4. (a) Two kinds of bonds in C_{60} (longer on-pentagon bond r_1 and shorter bond r_2 shared by hexagons) and (b) those in the zigzag nanotube. From Ref. [15].

much stronger in stiff C–C covalent-bond materials than in metallic-bond materials. Actually, the electronic structure of the so-called zigzag nanotubes is found to be modified upon the geometry optimization in LDA from the initial "graphite geometries" [15]. In this study, the Troullier–Martins pseudopotentials [24] with separable approximation by Kleinman and Bylander [25] are adopted, and plane wave basis functions with the cutoff energy of 50 Ry are used. Also, the LDA exchange-correlation functional by Ceperley and Alder is applied [26,27]. For the geometry optimization as well as the diagonalization of the Kohn-Sham Hamiltonian, the conjugate gradient procedure is used [28].

As for the geometry of zigzag nanotubes, there are two kinds of bonds as in the case of C_{60} (Fig. 4b) [15,29]. Their lengths are found to be different from each other, and there appear two long bonds and one short bond around each atom. The latter bond, which is parallel to the tube axis, should possess more double-bond character than the former. Interestingly, the length difference in two kinds of bonds is found to be inversely proportional to the diameter squared, and therefore it turns out to be important in thin nanotubes when considering their electronic properties. In Fig. 5, the electronic band structure of a few zigzag nanotubes is shown. It is evident that the geometry optimization can have large effects on the electronic structure of thin nanotubes [15].

3.2. Energetics

Graphene, a single-layer graphite sheet, is energetically the most stable sp^2-carbon network geometry because of its flatness. Total energies per atom should be higher in nanostructured sp^2-carbon materials with larger average curvature due to the energy cost for the bond bending from their ideal sp^2 angle. Accordingly, carbon

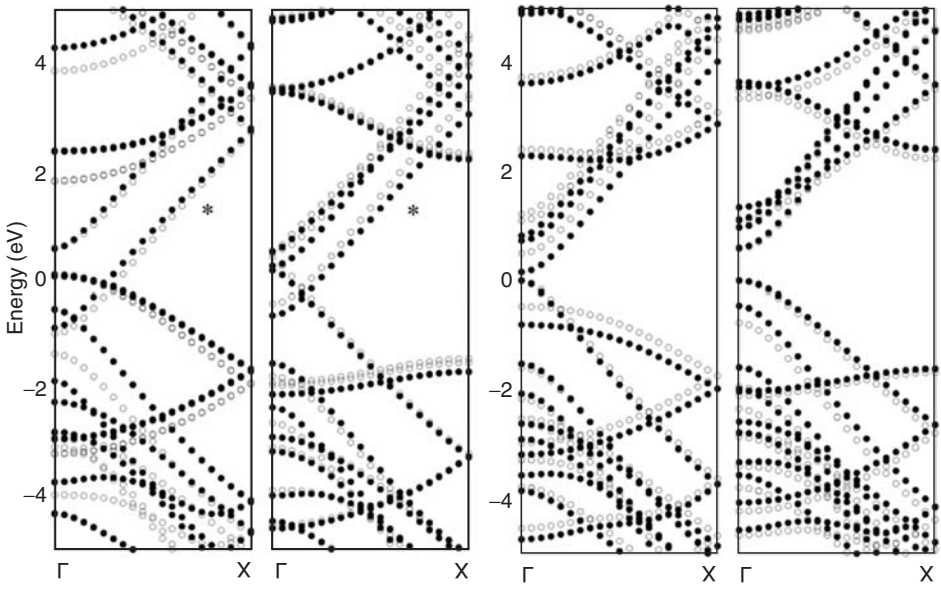

Fig. 5. Electronic band structure of zigzag nanotubes, (5,0), (6,0), (7,0), and (8,0) (from left to right). Electronic states labeled with asterisk are hybridized with nearly free electron states as well as with σ states. Courtesy of K. Kanamitsu.

nanotubes with smaller diameters should have higher total energies per atom. Graphene, in this context, is classified as the most stable carbon nanotube with an infinite diameter. An accurate quantitative analysis of the energetics of carbon nanotubes in the DFT has shown that the total energy per atom in the zigzag nanotube measured from that for graphene is proportional to the inverse diameter squared (Fig. 6) [15], which is the relationship expected from the elasticity theory for continuum flat sheet [30]. The total energy per atom in several kinds of chiral nanotubes is also known to show very similar diameter dependence [31]. However, the detailed chirality dependence of the total energy in carbon nanotubes is an interesting and important issue to be addressed systematically in the future.

In nanostructured carbon materials, on the other hand, the total energy per atom may not be the most important factor to be considered in analyzing geometries of newly produced materials as well as in designing new materials. In the case of fullerenes, for example, C_{60} is by far the most abundant fullerene in soot, and the second most abundant fullerene is C_{70}. The larger fullerenes such as C_{76}, C_{78}, and C_{84} are much less abundant. However, the total energy per atom in C_{60} is highest among all the fullerenes [12,32,33]. Similarly, C_{70} is energetically higher than fullerenes that are larger than C_{70}. This "mystery of relative abundance" is closely related to another long-standing mystery, i.e., a microscopic growth mechanism of icosahedral C_{60} and other fullerenes. In the case of carbon nanotubes, even the presence of the relatively abundant nanotubes itself is a controversial subject [34]. The importance of the total

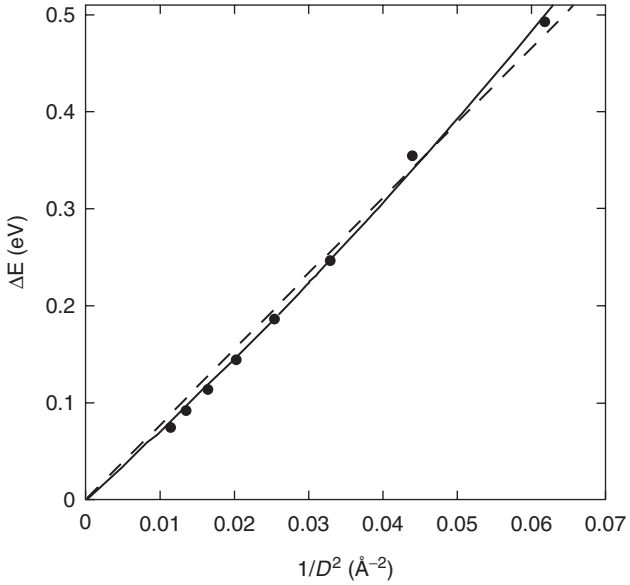

Fig. 6. Total energy per atom measured from that in graphene as a function of the $1/D^2$ where D is a nanotube diameter. A dashed line is the linear fitting line, while a solid curve shows the parabola fitting. From Ref. [15].

energy per atom in the relative abundance of various carbon nanotubes should be addressed in relation with their microscopic growth mechanism as in the case of fullerenes. In addition, it should be noted from the energetics of zigzag nanotubes that the total energy per atom in a carbon nanotube measured from that for graphene is expected to be much lower than that from fullerenes with the similar diameter [15,35]. The (9,0) carbon nanotube, having the same diameter as that of C_{60}, is, for example, nearly three times lower in energy than C_{60}. This high stability of even thin carbon nanotubes adds to their importance as materials of rich potential applications.

3.3. Electronic Structure of Chiral Carbon Nanotubes

First-principles electronic structure studies of chiral carbon nanotubes other than achiral zigzag and armchair nanotubes have scarcely been reported so far because the translational unit cell of achiral nanotubes is very long and hence their systematic study using the usual first-principles computational program for crystalline materials can be very expensive. For example, the number of atoms per translational unit cell of the achiral (10,10) nanotube is 40, while that of the chiral (10,9) nanotube is as large as 1048.

However, as has been mentioned previously, all the C atoms in any carbon nanotube are equivalent to each other. This high symmetry of carbon nanotubes can be fully utilized by considering the additional symmetry operations, rotations

and screw-symmetry operations [36]. These symmetry operations are not considered in a usual electronic-structure computational program for crystalline materials but can be taken into account if present in the case of 1D systems. If both operations are fully taken into account, there are only two atoms per "unit cell" in any carbon nanotube, and also in any boron-nitride nanotube. These two atomic sites are equivalent to each other in carbon nanotubes if one further considers the two-fold symmetry with the rotation axis perpendicular to the tube axis.

In Fig. 7, this *chiral unit cell* with threefold rotational symmetry is shown for the (6,3) nanotube [37]. The (m,l) carbon nanotube has the N-fold rotational symmetry where

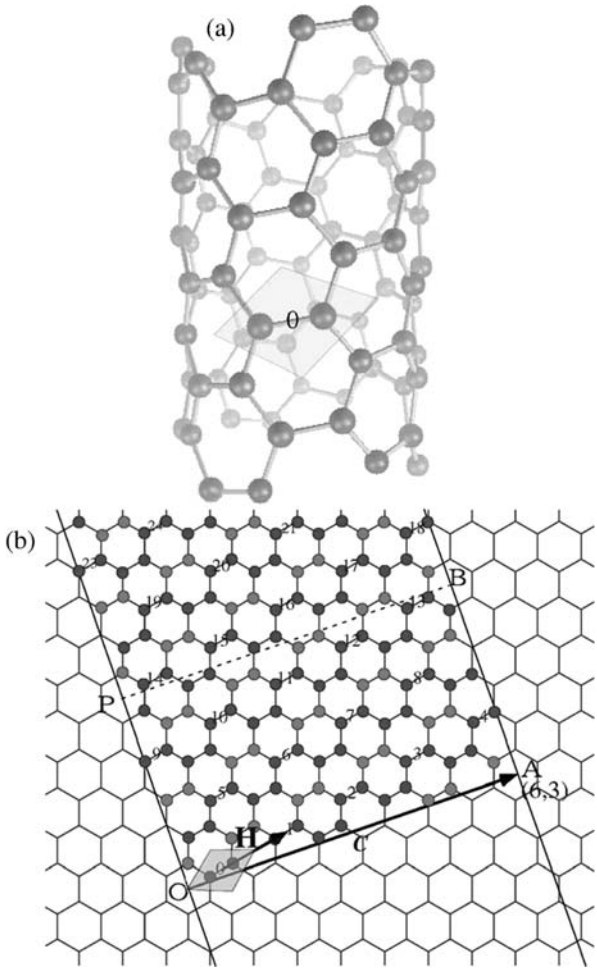

Fig. 7. (a) Chiral unit cell of the (6,3) nanotube having two atoms and (b) unfolded translational unit cell having 84 atoms with the cell dimension of OP. From Ref. [37], and Courtesy of Y. Akai.

N is the greatest common divisor of m and l. The corresponding rotational operation $\hat{C}_N$ to the wavefunction of the system, $\psi(\mathbf{r})$, should generate the phase factor as follows:

$$\hat{C}_N\psi(\mathbf{r}) = \exp\left(\frac{2\pi i\, n}{N}\right)\psi(\mathbf{r}), \quad (n = 0, 1, 2, \ldots, N-1)$$

where n is the rotational quantum number. Similarly, the helical operation, $\hat{S}$, to the wavefunction generates the phase factor:

$$\hat{S}\psi(\mathbf{r}) = \exp(i\kappa)\,\psi(\mathbf{r}), \quad (0 \le \kappa < 2\pi)$$

where κ is the helical quantum number and is closely related to the wave number associated with the 1D translational unit cell [36,38]. Accordingly, one can consider the electronic band structure in carbon nanotubes and draw dispersion curves of electronic states as a function of κ as is shown in Fig. 8 for the case of the (6,3) nanotube [37]. Hence, each quantum state in carbon nanotubes is to be labeled by a set of quantum numbers (j,n,κ) as $\psi_{jn\kappa}(\mathbf{r})$ where j is the principle quantum number classifying the quantum states with the same rotational and helical quantum numbers.

By considering these rotational and screw-symmetry operations for 1D systems, the size of the unit cell is no longer remains an obstacle for the electronic-structure

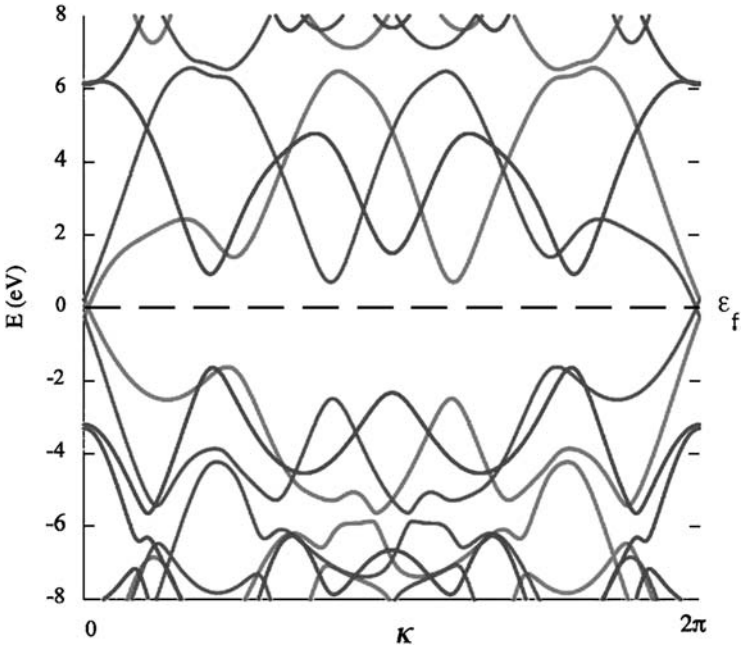

Fig. 8. Electronic structure of the (6,3) nanotube shown as a function of helical quantum number κ. From Ref. [37], and Courtesy of Y. Akai.

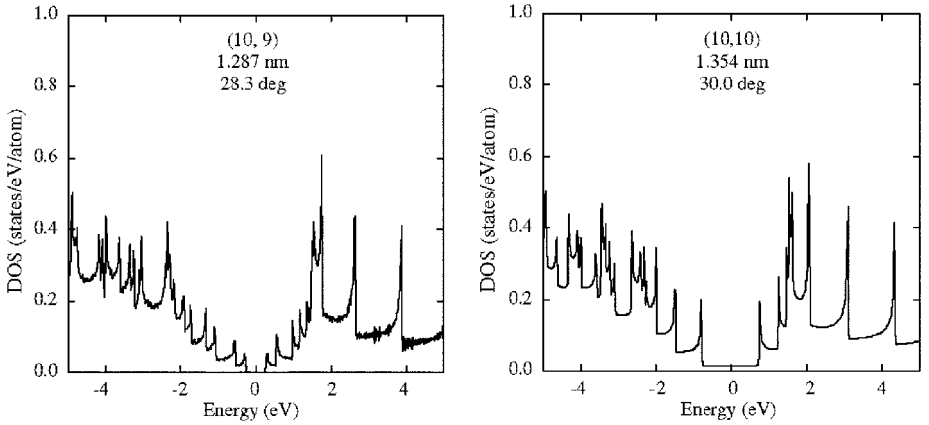

Fig. 9. Electronic density of states (DOS) of the chiral (10,9) nanotube and that of armchair (10,10) nanotube. From Refs. [37,40].

study of nanotubes. On the other hand, one needs to introduce suitable basis functions that are compatible with these operations. Obviously, plane waves, which are the most common basis functions in the electronic structure study of crystalline materials from first principles, are not suitable basis functions here. Atomic orbitals can be one of suitable basis sets. However, the most systematic first-principles electronic structure study of chiral as well as achiral nanotubes utilizing the rotational and screw-symmetry operations has been done using the real-space grid method with higher-order finite-difference pseudopotentials [39], and as many as 178 carbon nanotubes with diameters from 0.8 to 2.0 nm have been studied [31]. In Fig. 9, the electronic DOS of the (10,9) nanotube is shown together with that of the (10,10) nanotube [37,40]. It is found that the electronic structure from first principles shows interesting differences compared with that from not only the π tight-binding model but also the $\pi-\sigma$ tight-binding model, especially in its unoccupied-state energy regions above the Fermi level [31]. These DOSs obtained for 178 kinds of nanotubes should serve as a database to be compared with the experimental results such as scanning tunneling spectroscopy measurements, and to be used in designing nanotube-based device materials in the future.

3.4. Narrow-Gap Semiconductor Nanotubes

As has been mentioned, it has been predicted by using the highly accurate $\sigma-\pi$ tight-binding model that two-thirds of carbon nanotubes are moderate-gap semiconductor nanotubes and that the remaining one-third of carbon nanotubes are narrow-gap semiconductor nanotubes except (n,n) armchair nanotubes, which are metallic [5]. Also, it has been discussed in the effective-mass approximation [41].

The gap value of these narrow-gap semiconductor nanotubes is an interesting issue to be addressed using the chiral LDA method because the gap value might be of the same order as the difference between the LDA and tight-binding electronic state energies. Whether the gap value is larger or smaller than the tight-binding value would be of high importance. If it would be smaller, one may consider the nanotubes as metallic nanotubes at least at room temperature. On the other hand, if it would be larger, one should consider them not as metallic nanotubes but as semiconducting nanotubes.

In Fig. 10, the LDA gap values for narrow-gap nanotubes having the diameter between 0.7 and 1.5 nm, obtained by utilizing the rotational and screw-symmetry operations, are shown [39]. It is interesting to note that, according to the LDA results, more than half of these nanotubes should be considered as semiconductor nanotubes. If one further considers the many-body corrections to LDA gap values as will be discussed in the next section, most of these "narrow-gap nanotubes" are expected to behave as semiconductors even at room temperature, and only very thick nanotubes having a relatively large chiral angle may behave as metal.

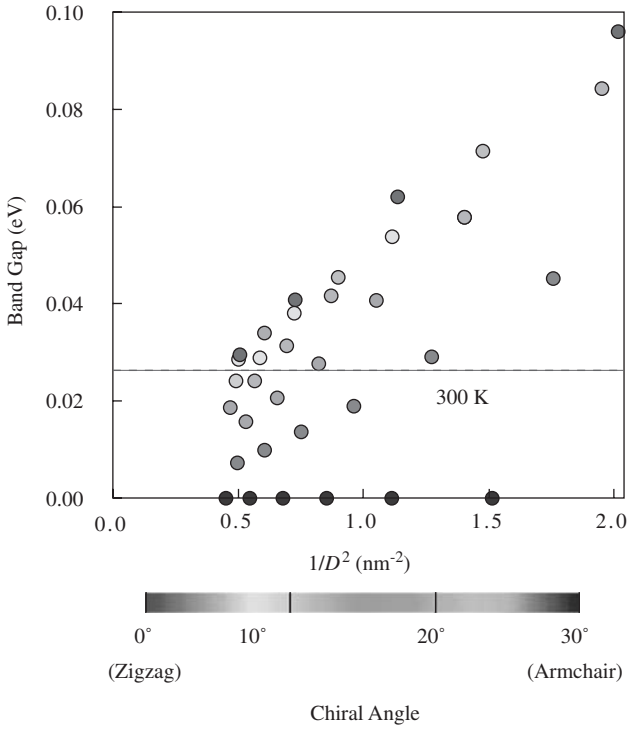

Fig. 10. Fundamental gap values of narrow-gap semiconductor nanotubes obtained by using the chiral LDA method. From Ref. [37], and Courtesy of Y. Akai.

4. MANY-BODY THEORIES

One can expect that the LDA electronic structure and the DOS for nanostructured carbon materials should show good accord with experiments, as has been confirmed for fullerenes. Not only for C_{60} but also for C_{70} and larger fullerenes, the occupied-state DOS and the unoccupied-state DOS demonstrate good agreement with photoemission and inverse-photoemission spectra, respectively [32,33]. The LDA electronic structure for carbon nanotubes, discussed in the previous section, should also show good accord with these experiments, although one has to wait for a future production of the homogeneous-geometry sample of carbon nanotubes to confirm this accordance. On the other hand, in the case of semiconducting carbon nanotubes, the value of the fundamental gap itself is expected to be underestimated in the LDA electronic structure. Although the LDA takes into account the electron correlation beyond the Hartree–Fock treatment and actually its fundamental-gap value for semiconductors is generally much better than the Hartree–Fock value, it is known that the LDA fundamental gap value is usually smaller than the experimental gap value. In this section, the many-body theory, which is known to give a more accurate fundamental gap value than the LDA and applied to carbon nanotubes, is reviewed. Also, theories to give a response of a quantum system to the external field are introduced.

4.1. Band Gap and GW Approximation

In semiconducting nanostructured materials, the value of the fundamental gap is one of the most important physical quantities to be discussed. The gap value can be defined as an energy difference between the highest-occupied quasiparticle state and the lowest-unoccupied quasiparticle state of the system. Although the LDA electronic state energies systematically underestimate the fundamental gap of semiconductors, a systematic improvement of the LDA electronic state energies within the framework of the DFT should be very difficult because an improvement of the exchange-correlation functional itself has been a hard task and, moreover, the improvement of the total energy of the system, and not of the electronic state energies, has usually been considered.

In order to describe the quasiparticle states of interacting electrons more accurately than the LDA treatment, one should explicitly treat the one-particle Green function, which gives quasiparticle energies as far as the quasiparticle picture holds in the interacting many-electron system [42]. Hedin's GW approximation [43] is one of such treatments in the framework of the many-body theory and is known to give much better fundamental gap values than the LDA [44]. In the GW approximation, the self-energy operator is given by the product of the one-particle Green function (G) and the screened Coulomb interaction (W). This corresponds to the first-order term of the perturbation series with respect to a rather weak interaction, W, and should be much better than the Hartree–Fock approximation, which is known to correspond to the first-order approximation in the perturbation series with respect to a strong bare Coulomb interaction. Although the superiority

of the *GW* approximation over the LDA is not a priori clear and even within the *GW* approximation there are several different ways to treat *G* as well as *W*, it is known that in many semiconducting and insulating systems the fundamental gap value obtained in the *GW* approximation is generally much better than the LDA value. In the case of silicon, for example, the *GW* gap values obtained so far are within the range of 0.2 eV difference from the experimental value of 1.17 eV, while that of the LDA is 0.6 eV and the Hartree–Fock gap value is much worse, larger than 6 eV [45]. As for diamond, the *GW* gap value is 5.54 eV [46], being very close to the experimental value of 5.5 eV.

The *GW* treatment is, on the other hand, computationally much more expensive than the LDA. In the case of carbon nanotubes, in addition, the translational unit cell in chiral nanotubes becomes large as has been mentioned previously. Therefore, the *GW* approximation has been applied only to very thin nanotubes or to relatively thin achiral nanotubes [47–49]. For (7,0) and (8,0) zigzag nanotubes which are predicted to be moderate-gap semiconductor nanotubes in the $\pi-\sigma$ tight-binding model, the LDA gap values after the geometry optimization are 0.2 and 0.6 eV, respectively. The *GW* gap values are found to be much larger, 0.6 and 1.2 eV for (7,0) and (8,0) nanotubes, respectively [37,48]. This increase of gap values in the *GW* approximation from the LDA values in 1D systems follows the same trend as in three-dimensional (3D) materials as well as in zero-dimensional clusters [50].

Although the above (7,0) and (8,0) nanotubes might be slightly thinner than the abundant nanotubes being present in single-walled carbon nanotube samples produced so far, the next zigzag nanotube, (9,0), has almost the same diameter as the C_{60} fullerene and should be one of the abundant single-walled carbon nanotubes in various samples. This (9,0) nanotube is to be classified as narrow-gap semiconductor nanotube according to the $\pi-\sigma$ tight-binding model although the π tight-binding model classifies it as metallic nanotube. For these narrow-gap semiconductor nanotubes, the LDA gap values are found to be rather large as discussed in the previous section. Hence, the many-body effect is of high importance because it may open up the gap value further. The *GW* study of the (9,0) nanotube actually confirmed the importance of the many-body effect and, including the geometry-optimization effect, the gap value is predicted to be as large as 0.17 eV. In Fig. 11, the DOS of the (9,0) nanotube obtained using the *GW* approximation is shown [49]. It is interesting to note that, in such thin nanotubes, the electron-hole symmetry does not hold any more because unoccupied π states are hybridized with the nearly free electron states as well as with σ states [48,51].

4.2. Excitons and Optical Spectra

It was pointed out theoretically in 1997 by Ando [52] that the excitonic effects in 1D carbon nanotubes should be sizable. It took a few more years for experimentalists to discuss the optical properties of carbon nanotubes [53]. Especially to discuss the details of excitonic effects from optical measurements, production of a sample with individual nanotubes surrounded by a surfactant was necessary [54,55]. Because of the excitonic

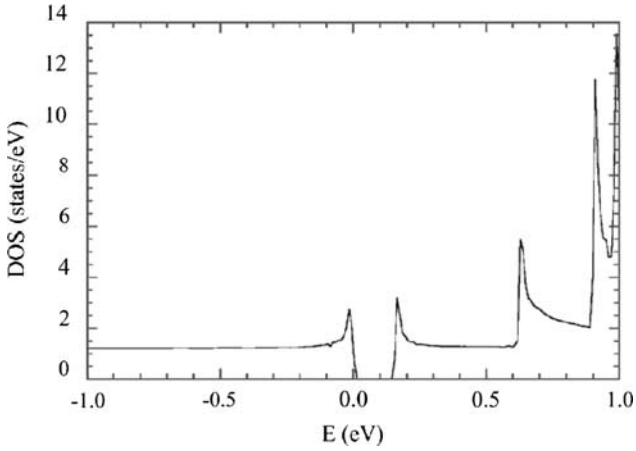

Fig. 11. Electronic DOS of the (9,0) nanotube obtained by using the *GW* approximation. From Ref. [49].

effects, peaks of optical spectra may not correspond to the energy differences between occupied and unoccupied quasiparticle states. Quasiparticle energies correspond to the excitation energies from the N-body ground state to the $N+1$ or $N-1$ eigenstates, while the exciton state is the excited state having the same particle number as the ground state. The former quasiparticle states can be given by the one-particle Green function as has already been shown previously, while the latter excitonic effects and optical spectra should be discussed by analyzing the effective interaction, or the density–density response function. In such analysis in the standard many-body theory starting from the one-particle Green function, so-called Bethe–Salpeter equation can be used [56]. An application of this analysis to carbon nanotubes has been well summarized by Louie in the preceding volume of this series [57].

In the framework of the DFT, the electron density is the key quantity to be discussed, and therefore the density–density response function can be addressed within its framework [58,59]. The formalism is called the time-dependent DFT, and in practice the LDA is often adopted and the method is called time-dependent LDA (TDLDA) [60]. The real-time version of the TDLDA has already been applied to carbon nanotubes to discuss the excited carrier dynamics [61]. Also, the optical spectra of thin nanotubes have been discussed in the framework of the TDLDA [62]. More realistic, thicker carbon nanotubes will be discussed in this framework in the future.

5. EFFECTIVE-MASS APPROXIMATION

Electronic properties of carbon nanotubes given in the tight-binding model have been well reproduced in a $\boldsymbol{k}\cdot\boldsymbol{p}$ method, which is also classified as the effective-mass approximation [63]. The theory first considers the electronic structure of graphene, and then discusses the electronic states around two Fermi points, usually called K and K′ points

in the 2D Brillouin zone after the name of the symmetry point, K, in the 3D Brillouin zone for the hexagonal lattice. In carbon nanotubes, not only the periodicity but also the curvature effects can be incorporated in this method. Because of the simplicity of the formalism, this $\boldsymbol{k \cdot p}$ method has successfully been applied to many important physical aspects of carbon nanotubes including magnetic properties, excitons and optical properties, impurity effects, and phonon effects. A thorough review of these successful applications to carbon nanotubes has been given by Ando [41].

6. PERSPECTIVES

As has been reviewed in this chapter, theoretical predictions for the physical properties of carbon nanotubes, 1D carbon cylinders with the diameter of the order of 1 nm, have motivated extensive experimental research on these "tinny" materials ever since their discovery by Iijima in 1991 [1]. Similarly, the experimental findings such as so-called peapods [64] have motivated theoretical research on these "large" unit cell systems as well [65]. This fruitful collaboration of theory and experiment will continue to be a source of new physics in the field of carbon nanotubes and other nanostructured carbon-based materials in the future. Also from the technological viewpoint, carbon nanotube is the most important material to be studied for the post-silicon era, and the predictive theoretical methods reviewed in this chapter as well as the methodologies to be applied to the electronic transport properties of nanostructured systems [66] will be of higher importance in the future.

In general, materials can behave differently in the nanometer-scale world from their bulk phase due to quantum size effects. In the case of carbon, combined with the peculiar electronic structure of the mother material graphene, and with the very strong C–C covalent bonding that stabilizes many distinct network geometries, one can obtain various nanostructured carbon phases with rich properties. This has given importance but also difficulties to the research of carbon nanotubes. In the case of fullerenes, C_{60} is highly abundant and many interesting compounds as well as C_{60} polymers have been produced using the high-purity C_{60} sample. In the case of carbon nanotubes, on the other hand, many different kinds of nanotubes are present in most samples. The next experimental breakthrough awaited in the materials science of carbon nanotubes is, therefore, the production of homogeneous-geometry samples. It will lead to many new nanotube-based crystalline compounds, which in turn will give new challenge to the theory of carbon nanotubes.

ACKNOWLEDGMENTS

This work was supported by the 21st Century Center of Excellence Program by Ministry of Education, Science, and Culture of Japan through the Nanometer-Scale Quantum Physics Project of the Tokyo Institute of Technology. The author also acknowledges the support from the Asahi Glass Foundation and the Grants-in-Aid for Scientific Research from the Ministry of Education, Science, and Culture of Japan.

REFERENCES

[1] S. Iijima, Helical microtubules of graphitic carbon, *Nature* **354**, 56 (1991).
[2] H.W. Kroto, J.R. Heath, S.C. O'Brien, R.F. Curl and R.E. Smalley, C_{60} – Buckminsterfullerene, *Nature* **318**, 162 (1985).
[3] K. Kikuchi, N. Nakahara, T. Wakabayashi, S. Suzuki, H. Shiromaru, Y. Miyake, K. Saito, I. Ikemoto, M. Kainosho and Y. Achiba, NMR characterization of isomers of C_{78}, C_{82}, and C_{84} fullerenes, *Nature* **357**, 142 (1992).
[4] W.A. Harrison, *Elementary Electronic Structure* (World Scientific, Singapore, 1999).
[5] N. Hamada, S. Sawada and A. Oshiyama, New one-dimensional conductors: Graphitic microtubules, *Phys. Rev. Lett.* **68**, 1579 (1992).
[6] K. Tanaka, K. Okahara, M. Okada and T. Yamabe, Electronic properties of bucky-tube model, *Chem. Phys. Lett.* **191**, 469 (1992).
[7] R. Saito, M. Fujita, G. Dresselhaus and M.S. Dresselhaus, Electronic structure of chiral graphene tubules, *Appl. Phys. Lett.* **60**, 2204 (1992).
[8] S. Okada and S. Saito, Electronic structure of C_{78} and C_{78}-graphite cointercalation compound, *J. Phys. Soc. Jpn.* **64**, 2100 (1995).
[9] C.H. Xu, C.Z. Wang, C.T. Chan and K.M. Ho, A transferable tight-binding potential for carbon, *J. Phys. Condens. Matter* **4**, 6047 (1992).
[10] D. Tomanek and M.A. Schluter, Growth regimes of carbon clusters, *Phys. Rev. Lett.* **67**, 2331 (1991).
[11] Y. Omata, Y. Yamagami, K. Tadano, T. Miyake and S. Saito, Nanotube nanoscience: A molecular-dynamics study, *Physica E* **29**, 454 (2005).
[12] B.L. Zhang, C.H. Xu, C.Z. Wang, C.T. Chan and K.M. Ho, Systematic study of structures and stabilities of fullerenes, *Phys. Rev. B* **46**, 7333 (1992).
[13] C.H. Xu and G.E. Scuseria, Theoretical predictions for a 2-dimensional rhombohedral phase of solid C_{60}, *Phys. Rev. Lett.* **74**, 274 (1995).
[14] M. Nunez-Regueiro, L. Marques, J.-L. Hodeau, O. Bethoux and M. Perroux, Polymerized fullerite structures, *Phys. Rev. Lett.* **74**, 278 (1995).
[15] K. Kanamitsu and S. Saito, Geometries, electronic properties, and energetics of isolated single walled carbon nanotubes, *J. Phys. Soc. Jpn.* **71**, 483 (2002).
[16] V. Zolyomi and J. Kurti, First-principles calculations for the electronic band structures of small diameter single-walled carbon nanotubes, *Phys. Rev. B* **70**, 085403 (2004).
[17] P. Hohenberg and W. Kohn, Inhomogeneous electron gas, *Phys. Rev.* **136**, B864 (1964).
[18] W. Kohn and L.J. Sham, Self-consistent equations including exchange and correlation effects, *Phys. Rev.* **140**, A1133 (1965).
[19] U. von Barth and L. Hedin, A local exchange-correlation potential for the spin polarized case: I, *J. Phys. C: Solid State Phys.* **5**, 1629 (1972).
[20] J.P. Perdew, K. Burke and M. Ernzerhof, Generalized gradient approximation made simple, *Phys. Rev. Lett.* **77**, 3865 (1996).
[21] M.D. Newton and R.E. Stanton, Stability of buckminsterfullerene and related carbon clusters, *J. Am. Chem. Soc.* **108**, 2469 (1986).
[22] K. Hedberg, L. Hedberg, D.S. Bethune, C.A. Brown, H.C. Dorn, R.D. Johnson and M. Devries, Bond lengths in free molecules of buckminsterfullerene, C_{60}, from gas-phase electron-diffraction, *Science* **254**, 410 (1991).
[23] T. Miyake and S. Saito, Geometry and electronic structure of rhombohedral C_{60} polymer, *Chem. Phys. Lett.* **380**, 589 (2003).
[24] N. Troullier and J.L. Martins, Efficient pseudopotentials for plane-wave calculations, *Phys. Rev. B* **43**, 1993 (1991).
[25] L.M. Kleinman and D.M. Bylander, Efficacious form for model pseudopotentials, *Phys. Rev. Lett.* **48**, 1425 (1982).
[26] D.M. Ceperley and B.J. Alder, Ground state of the electron gas by a stochastic method, *Phys. Rev. Lett.* **45**, 566 (1980).

[27] J.P. Perdew and A. Zunger, Self-interaction correction to density-functional approximations for many-electron systems, *Phys. Rev. B* **23**, 5048 (1981).
[28] O. Sugino and A. Oshiyama, Vacancy in Si: Successful description within the local-density approximation, *Phys. Rev. Lett.* **68**, 1858 (1992).
[29] O. Gulseren, T. Yildirim and S. Ciraci, Systematic *ab initio* study of curvature effects in carbon nanotubes, *Phys. Rev. B* **65**, 153405 (2002).
[30] S. Sawada and N. Hamada, Energetics of carbon nanotubes, *Solid State Commun.* **83**, 917 (1992).
[31] Y. Akai and S. Saito, Electronic structure, energetics, and geometric structure of carbon nanotubes: A density-functional study, *Physica E* **29**, 555 (2005).
[32] S. Saito and A. Oshiyama, Electronic and geometric structures of C_{70}, *Phys. Rev. B* **44**, 11532 (1991).
[33] S. Saito, S. Sawada and N. Hamada, Electronic and geometric structures of C_{76} and C_{84}, *Phys. Rev. B* **45**, 13845 (1992).
[34] K. Hirahara, M. Kociak, S. Bandow, T. Nakahira, K. Itoh, Y. Saito and S. Iijima, Chirality correlation in double-wall carbon nanotubes as studied by electron diffraction, *Phys. Rev. B* **73**, 195420 (2006).
[35] S. Okada and S. Saito, Electronic structure and energetics of pressure-induced two-dimensional C_{60} polymers, *Phys. Rev. B* **59**, 1930 (1999).
[36] J.W. Mintmire, D.H. Robertson and C.T. White, Properties of fullerene nanotubes, *J. Phys. Chem. Solids* **54**, 1835 (1993).
[37] Y. Akai, Electronic and geometric structure of carbon nanotubes: A systematic first-principles study, Ph.D. Thesis, Department of Physics, Tokyo Institute of Technology, 2006.
[38] J.W. Mintmire, B.I. Dunlap and C.T. White, Are fullerene tubules metallic? *Phys. Rev. Lett.* **68**, 631 (1992).
[39] J.R. Chelikowsky, N. Troullier, K. Wu and Y. Saad, Higher-order finite-difference pseudopotential method: An application to diatomic molecules, *Phys. Rev. B* **50**, 11355 (1994).
[40] Y. Akai and S. Saito, Local-density-approximation density of states of single-wall carbon nanotubes, http://www.stat.phys.titech.ac.jp/saito/ldados.html
[41] T. Ando, Theory of electronic states and transport in carbon nanotubes, *J. Phys. Soc. Jpn.* **74**, 777 (2005).
[42] A.L. Fetter and J.D. Walecka, *Quantum Theory of Many-Particle Systems* (McGraw-Hill, New York, 1971).
[43] L. Hedin and S. Lundqvist, Effects of electron-electron and electron-phonon interactions on the one-electron state of solids, in *Solid State Physics*, vol. 23, edited by H. Ehrenreich, F. Seitz and D. Turnbull (Academic, Boston, 1969), p. 2.
[44] S.G. Louie, Quasiparticle theory of electron excitations in solids, in *Quantum Theory of Real Materials*, edited by J.R. Chelikowsky and S.G. Louie (Kluwer Academic, Boston, 1996), p. 83.
[45] N. Hamada, M. Hwang and A.J. Freeman, Self-energy correction for the energy-bands of silicon by the full-potential linearized augmented-plane-wave method – Effect of the valence-band polarization, *Phys. Rev. B* **41**, 3620 (1990).
[46] S. Saito, T. Maeda and T. Miyake, Energetics, electronic properties, and geometries of B-doped diamond: A first-principles study, in *Diamond Electronics – Fundamentals to Applications*, edited by P. Bergonzo, R. Gat, R.B. Jackman and C.E. Nebel (Mater. Res. Soc. Symp. Proc. **956**, Warrendale, PA, 2007), 0956-J14-03.
[47] C.D. Spataru, S. Ismail-Beigi, L.X. Benedict and S.G. Louie, Excitonic effects and optical spectra of single-walled carbon nanotubes, *Phys. Rev. Lett.* **92**, 077402 (2004).
[48] T. Miyake and S. Saito, Quasiparticle band structure of carbon nanotubes, *Phys. Rev. B* **68**, 155424 (2003).
[49] T. Miyake and S. Saito, Band-gap formation in $(n,0)$ single-walled carbon nanotubes ($n = 9,12,15,18$): A first-principles study, *Phys. Rev. B* **72**, 073404 (2005).
[50] S. Saito, S.B. Zhang, S.G. Louie and M.L. Cohen, Quasiparticle energies in small alkali-metal clusters, *J. Phys. Condens. Matter* **2**, 9041 (1990).
[51] X. Blasé, L.X. Benedict, E.L. Shirley and S.G. Louie, Hybridizations effects and metallicity in small radius carbon nanotubes, *Phys. Rev. Lett.* **72**, 1878 (1994).

[52] T. Ando, Excitons in carbon nanotubes, *J. Phys. Soc. Jpn.* **66**, 1066 (1997).
[53] H. Kataura, Y. Kumazawa, Y. Maniwa, I. Umezu, S. Suzuki, Y. Ohtsuka and Y. Achiba, *Synthetic Metals* **103**, 2555 (1999).
[54] M.J. O'Connell, S.M. Bachilo, C.B. Huffman, V.C. Moore, M.S. Strano, E.H. Haroz, K.L. Rialon, P.J. Boul, W.H. Noon, C. Kittrell, J. Ma, R.H. Hauge, R.B. Weisman and R.E. Smalley, Band gap fluorescence from individual single-walled carbon nanotubes, *Science* **297**, 593 (2002).
[55] S.M. Bachilo, M.S. Strano, C. Kittrell, R.H. Hauge, R.E. Smalley and R.B. Weisman, Structure-assigned optical spectra of single-walled carbon nanotubes, *Science* **298**, 2361 (2002).
[56] E.K. Chang, M. Rohlfing and S.G. Louie, Excitons and optical properties of α-quartz, *Phys. Rev. Lett.* **85**, 2613 (2000).
[57] S.G. Louie, Predicting materials and properties: Theory of the ground and excited state, in *Conceptual Foundations of Materials*, edited by S.G. Louie and M.L. Cohen (Contemporary Concepts of Condensed Matter Science Series, edited by E. Burstein, M.L. Cohen, D.L. Mills and P.J. Stiles, Elsevier, Amsterdam, 2006), p. 9.
[58] M.J. Stott and E. Zaremba, Linear-response theory within the density-functional formalism: Application to atomic polarizabilities, *Phys. Rev. A* **21**, 12 (1980).
[59] A. Zangwill and P. Soven, Density-functional approach to local-field effects in finite systems: Photoabsorption in the rare gases, *Phys. Rev. A* **21**, 1561 (1980).
[60] W. Ekardt, Size-dependent photoabsorption and photoemission of small metal particles, *Phys. Rev. B* **31**, 6360 (1985).
[61] Y. Miyamoto, A. Rubio and D. Tomanek, Real-time *ab initio* simulations of excited carrier dynamics in carbon nanotubes, *Phys. Rev. Lett.* **97**, 126104 (2006).
[62] F. Sottile, F. Bruneval, A.G. Marinopoulos, L.K. Dash, S. Botti, V. Olevano, N. Vast, A. Rubio and L. Reining, TDLDA from molecules to solids: The role of long-range interactions, *Int. J. Quantum Chem.* **102**, 684 (2005).
[63] H. Ajiki and T. Ando, Electronic states of carbon nanotubes, *J. Phys. Soc. Jpn.* **62**, 1255 (1993).
[64] B.W. Smith, M. Monthioux and D.E. Luzzi, Encapsulated C_{60} in carbon nanotubes, *Nature* **396**, 323 (1998).
[65] S. Okada, S. Saito and A. Oshiyama, Energetics and electronic structures of encapsulated C_{60} in a carbon nanotube, *Phys. Rev. Lett.* **86**, 3835 (2001).
[66] M. Buttiker, Y. Imry, R. Landauer and S. Pinhas, Generalized many-channel conductance formula with application to small rings, *Phys. Rev. B* **31**, 6207 (1985).

Chapter 3
THE ELECTRONIC PROPERTIES OF CARBON NANOTUBES

P. G. Collins and P. Avouris

1. INTRODUCTION

Following the early work of Endo [1,2] on multiwalled carbon structures, Iijima was first to image and clearly elucidate the structure of carbon nanotubes [3]. Almost immediately, theoretical models started appearing which predicted unusual electronic properties for this novel class of material. Unlike other materials known at the time, carbon nanotubes were predicted to be either metals or semiconductors based on the exact arrangement of their carbon atoms [4,5]. At that time, the idea of testing such predictions seemed fanciful – imaging these wires required the highest resolution transmission electron microscopes (TEMs), after all, and researchers joked about nanometer-scale alligator clips making the necessary electrical connections.

The jokes were short-lived, of course, as a number of enabling technologies matured and proliferated throughout the 1990s and ushered in the new "nanoscience" field. Scanned probe microscopes (SPMs) became standard laboratory equipment, field-emission scanning electron microscopes (SEMs) made nanoscale imaging easier than ever before, and electron-beam lithography brought ultrasmall electronic device fabrication to hundreds of university campuses. By taking advantage of the long length of nanotubes, research groups rapidly demonstrated electrical connections to individual nanotubes and a flood of interesting measurements began.

Historically, the first electrical measurements were performed on multiwalled nanotubes (MWNTs) [6], nanotubes composed of multiple concentric graphitic shells. However, the electrical characterization of nanotubes began in earnest in 1996, following the distribution of single-walled carbon nanotubes (SWNTs) grown by Andreas Thess in Richard Smalley's group at Rice University [7]. The simpler, single-walled morphology is more theoretically tractable, and electronic devices composed of SWNTs turn out to be sufficiently complicated without any additional shells of conducting carbon.

Contemporary Concepts of Condensed Matter Science
Carbon Nanotubes: Quantum Cylinders of Graphene

ISSN: 1572-0934/doi:10.1016/S1572-0934(08)00003-6

2. SEMIMETALLIC GRAPHITE

Graphite is a semimetal, a highly unusual electronic material with a unique Fermi surface. As a result, the additional quantization present in nanoscale graphitic fragments is a fascinating subject, resulting in electronic properties which cannot be duplicated by nanowires composed of normal metals or semiconductors.

Graphite has layered structure composed of parallel planes of sp^2-bonded carbon atoms called "graphene" layers. These layers are 0.34 nm apart and only interact via weak, van der Waals forces. The quantum electronic states of a graphene sheet are purely 2D, with nearly continuously varying momenta in the plane (k_x, k_y), but with only a single allowed value for k_z. This 2D confinement does not in itself lead to deviations from the standard Fermi liquid model. A nearly free-electron system in 2D has the same parabolic energy dispersions as a 3D system, though the surfaces of constant energy will be circles or curved lines instead of the more familiar spheres and spheroids.

Fig. 1 depicts the 2D bandstructure of a graphene sheet. Many of the constant energy surfaces in graphene are circular lines, but a notably different geometry occurs at the high-symmetry corners $k = \mathbf{K}$ of the first Brillouin zone. At each corner, two bands[1] cross each other with almost perfectly linear dispersion, and the constant-energy surface shrinks to a discrete point. Quasiparticles on linear bands have no "effective mass" by standard definitions and may be treated with the Dirac equation for massless fermions. Because of the crystal symmetry, exactly six points in k-space exhibit this unusual effect, all having the same magnitude of momentum $|k| = \sqrt{k_x^2 + k_y^2} = \pi/a$, where a is the hexagonal lattice constant of 0.25 nm. While

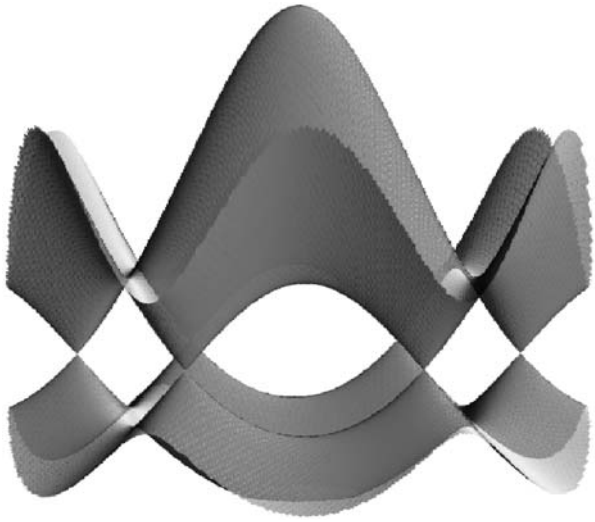

Fig. 1. The electronic bandstructure of a graphene sheet has band crossings at the high-symmetry corners **K** and **K′** of the Brillouin zone. The Fermi level E_F intersects these crossings, resulting in the semimetallic properties of graphene and graphite.

band-edge states are typically immobile standing waves centered on the atomic lattice, the graphene states have a nonzero and nearly energy-independent velocity $v_F = 8 \times 10^5$ m/s.

These unusual features would be easily overlooked if not for the fact that they lie directly at graphene's Fermi energy E_F, the principal energy of interest for nearly all electronic properties. Both carbon atoms in the unit cell contribute one delocalized p_z electron to the crystal, so it is perfectly natural for the p_z-derived band to each be exactly filled to the band edge **K**. This filling sets E_F exactly at the band intersection where the number of available quantum states shrinks to a point. Whereas normal metals might have spherical Fermi surfaces with many available quantum states, graphene has a Fermi "surface" composed of only six allowed momenta – more accurately, the surface is a sparse collection of Fermi points. It can be considered either a very poor metal or a zero-gap semiconductor.

This low number of states accounts for many of the unusual properties in graphene-based materials. 3D graphite is categorized as a semimetal [8,9] and exhibits a relatively high resistivity $\rho \sim 10\,\text{m}\Omega\,\text{cm}$, a nonlinear current–voltage dependence, and an unusual cusp in the electronic density of states $D(E)$ at $E = E_F$.

3. SINGLE-WALLED CARBON NANOTUBES

3.1. Further Quantization of the Graphene System

The valence and conduction bands of all materials are drawn as continuous but are actually composed of closely spaced, discrete states. These states have a regular separation Δk inversely proportional to L, the macroscopic length of the sample, and for large L (compared to the atomic lattice spacing) the states are effectively continuous. For nanometer-scale materials, Δk can increase to the point where very few k values are allowed and the bands of states become quite sparse. Under these conditions, electrons no longer freely hop from one state to another – the change in either momentum or energy becomes too great for the available thermal fluctuations – and the material is considered to be strongly quantized.

Of course, a sample can be quantized in one of its dimensions and not another. A suitably thin film will retain a continuum of allowed states k_x and k_y in the plane of the film, even if only a few, well-separated wavevectors k_z remain accessible perpendicular to the plane. In a nanowire, one of the wavevectors remains quasi-continuous while the two wavevectors perpendicular to the wire's longitudinal axis become strongly quantized. To visualize the available electronic states for a nano-scale 2D film or 1D wire, it often suffices to extract a plane or a line, respectively, out of the material's 3D bandstructure. For a typical metal or semiconductor, this extra quantization rarely results in dramatic electronic effects: bulk metals tend to produce metallic nanowires, and bulk semiconductors produce semiconducting nanowires, though with possibly modified bandgaps.

Graphene begins as a 2D material, but it too may be further quantized by slicing a narrow strip from the sheet. In this case, the allowed electronic states constitute a

line of points, or "band," sliced from the graphene 2D bandstructure. If the width of the strip is N atoms, then N parallel subbands constitute the complete set of allowed states. Each subband corresponds to a different wavevector in the strip's narrow dimension, analogous to the different transverse modes of a waveguide.

As depicted in Fig. 2, it is possible to extract slices from graphene's bandstructure with remarkably different properties. A slice in the direction of a **K** point will include two of the graphene Fermi points and be metallic, but a slice in a different direction may not. Accurately describing a 1D graphene strip therefore requires two independent parameters: both the width of the strip as well as the angle of the strip with respect to the atomic lattice. Only with both parameters can the electronic properties of the strip be completely specified.

Fundamentally, the SWNT is isoelectronic with this narrow graphene strip with only minor differences. The edges of the narrow strip dictate boundary conditions of a hard-wall potential; the cylindrical SWNT, on the other hand, merely requires single-valuedness around the circumference. This more relaxed boundary condition does not impose any additional energy cost and, as a result, the SWNT's electronic subbands will have almost identical energy dispersions as the parent graphene. In other words, the graphical construction of "slices" from the graphene bandstructure is even more accurate for the SWNT than it is for the flat strip.[2]

Two constructions of this sort are depicted in Fig. 2. It is convenient to specify the circumference of a SWNT as a vector composed of the two primitive lattice vectors,

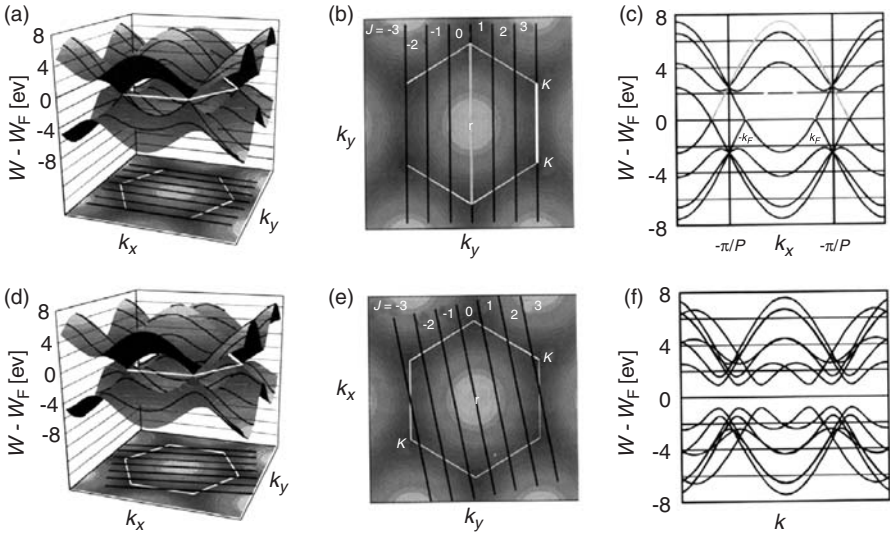

Fig. 2. 1D quantization of the graphene bandstructure for different nanotube symmetries. The top row corresponds to an "armchair" nanotube in which a subband directly intersects the **K** symmetry points (a, b) and results in a metallic bandstructure (c). In the bottom row, a chrial nanotube's subbands miss all of the **K** points (d, e) and the bandstructure is semiconducting. Reproduced from Dresselhaus et al. [85].

$\overrightarrow{c} = \overrightarrow{na}_1 + \overrightarrow{ma}_2$. In this scheme, the two parameters specifying the SWNT are the vector indices (n, m) instead of the magnitude of the circumference and an angular orientation. For all SWNTs with $n = m$, one of the allowed subbands of states runs directly from $k = 0$ to $k = \mathbf{K}$, making all such SWNTs metallic conductors. For SWNTs with $n \neq m$, the subband intersecting $k = 0$ will not cross the **K** point. Nevertheless, one of the other, parallel subbands may intersect **K**. A geometric construction proves that when the difference between n and m is divisible by 3 (e.g., $n - m = 3j$, with $j = 1,2,3\ldots$), one of the various allowed subbands intersects the **K** point and causes the SWNT to be metallic. This leads to the result that 1/3 of all possible carbon SWNTs are metallic and 2/3 are semiconducting. It is believed that the effects of curvature may introduce very small electronic gaps in the metallic SWNTs with $n \neq m$, but these gaps have energies well below room temperature [10].

The SWNTs that are not metallic have direct semiconducting bandgaps E_g, the magnitude of which follows a straightforward rule. Because graphene's energy dispersion near E_F is linear in k, the energy gap between the states closest to **K** is directly proportional to the separation Δk between subbands. Δk is itself solely determined by the width of the graphene strip (or of an unrolled SWNT) and the lattice constant a. So all SWNTs of a given diameter D will have the same semiconducting bandgap E_g, regardless of the precise values of n and m, and the value will be $E_g = (0.85\,\text{eV nm})/D$. Typical experimental SWNT diameters of 1.0, 1.4, and 2.0 nm give optical bandgaps of approximately 0.85, 0.60, and 0.43 eV, respectively.

3.2. Electronic Properties of Metallic Nanotubes

Metallic SWNTs are those that have a subband intersecting the symmetric Fermi points $k = \pm\mathbf{K}$. Each Fermi point contributes one "forward moving" wavevector with $v_g > 0$ and one "backward moving" wavevector with $v_g < 0$. Including the spin degeneracy there are exactly four forward moving electron states and four backward moving ones at zero temperature.

Each of these states carries current and, in the absence of any scattering, will contribute one quantum of conductance $G_0 = e^2/h = 39\,\mu\text{S}$. Elastic scattering may be included in this Landauer model [11,12] as a nonunity transmission coefficient T, in which case the total conductance of all four states can be simply stated as

$$G = G_0 \sum T_i.$$

An idealized metal SWNT with four parallel, unity-transmission channels will have a conductance of 155 μS or a resistance $R = 1/G = 6.5\,\text{k}\Omega$. This idealized value is not temperature-dependent.

In a traditional metal, inelastic electron–phonon scattering from acoustic phonons is the dominant limitation to electrical conductivity, and this scattering limits the applicability of the Landauer model above. In SWNTs, however, electron–phonon scattering is strongly suppressed. The 1D electron states of a SWNT can only scatter into a very limited number of empty electronic states and such events require a large

momentum transfer [13]. The resulting suppression produces long inelastic mean free paths l_{e-ph}, on the order of 0.5 μm at room temperature. For submicron-scaled devices, this means that electron–phonon scattering is essentially absent. In order to experimentally measure l_{e-ph}, on the other hand, devices have been fabricated using millimeter-length SWNTs [14]. As shown in Fig. 3, these lengths conclusively demonstrate the diffusive limit of conduction.

Electron–phonon scattering becomes particularly important at high applied bias (high fields). As the SWNT bias V is increased, additional scattering mechanisms turn on and the SWNT resistance increases as shown in Fig. 4. This increase is almost perfectly linear in V, so that the device I–V curve has an apparent current saturation at high bias. The experimental result is quite counter-intuitive: not only does a metallic SWNT break Ohm's law, but it also deviates from the stepwise conductance behavior normally associated with quantum wires [15]. Nevertheless, the behavior is captured by a simple model of optical-phonon emission [16]. The suppression of

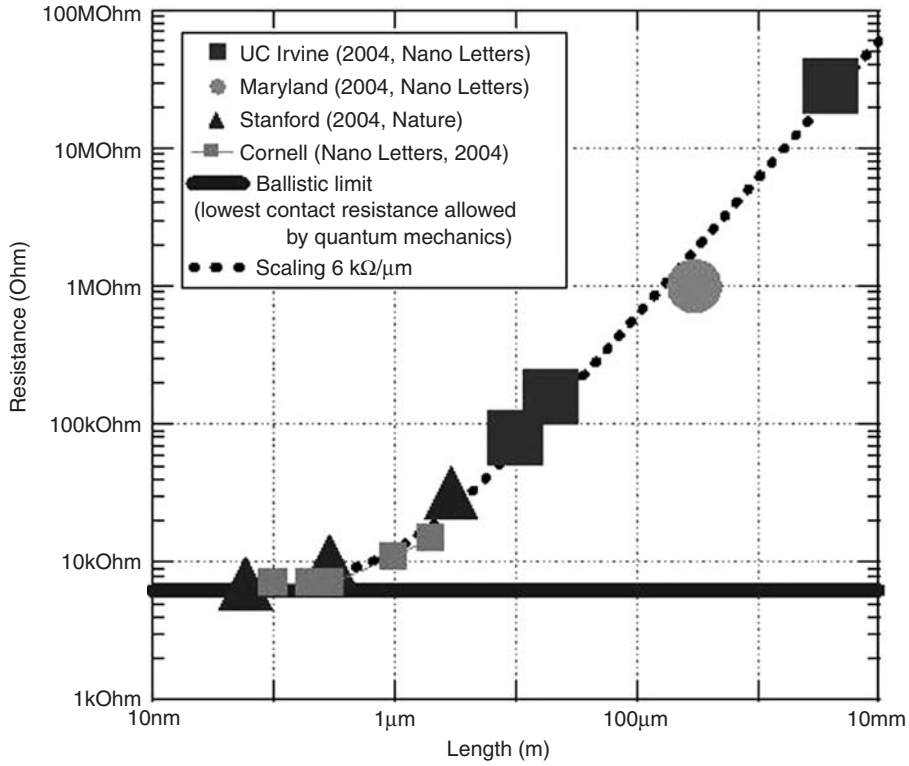

Fig. 3. SWNT resistance versus device length. At very short lengths, a metallic SWNT is quasi-ballistic and the device resistance can approach the fundamental minimum of 6.5 kΩ. As device lengths exceed the mean free path for acoustic-phonon scattering, the resistance becomes diffusive with a resistivity of approximately 6 kΩ/μm. Reproduced from Li et al. [14]

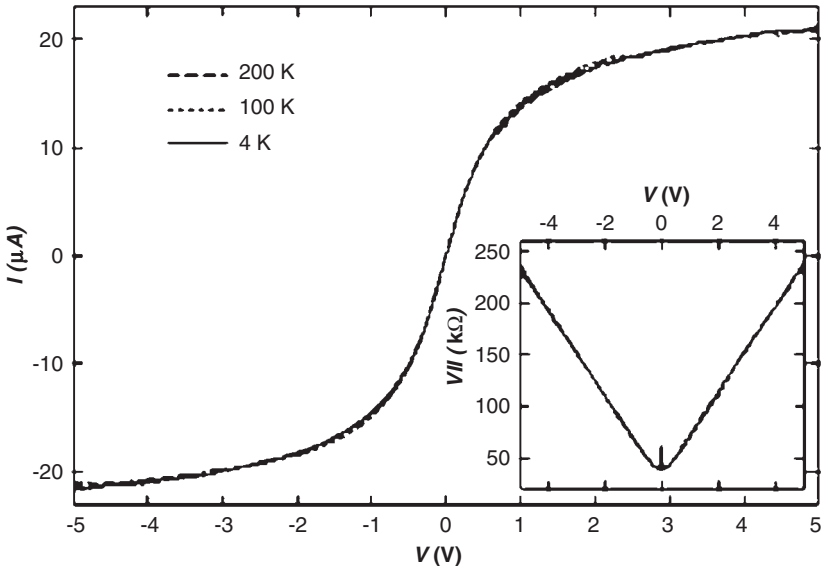

Fig. 4. SWNT current and resistance (inset) versus applied bias V. Over a wide bias range, the resistance increases linearly with V and is relatively insensitive to temperature. The behavior matches a model in which low-energy, acoustic-phonon scattering is nearly absent and the resistance is predominantly due to high-energy, optical-phonon emission. Note that this device, which is approximately 1 μm in length, has a small but nonnegligible contact resistance. Reproduced from Yao et al. [16]

electron scattering and thermalization by acoustic phonons allows electrons to accumulate energy in an applied electric field. Once the energy of an optical phonon is exceeded (approximately 0.18 eV), spontaneous emission can occur. This dissipative mechanism becomes more active proportional to increases in V.

The direct observation of optical-phonon emission is rarely observed in metals. Because of the high fields and associated current densities required, most materials will suffer self-heating and electromigration degradation before a clear phonon emission regime can be reached. In SWNTs, on the other hand, quasi-ballistic transport is nearly dissipationless and the covalently bonded carbon atom lattice is impervious to electromigration. SWNTs readily carry currents of 20 μA, corresponding to current densities exceeding 10^8 A/cm^2, without degradation. At these currents, the I–V curve becomes nearly horizontal: the current saturates as all bias increases are efficiently converted to optical-phonon emissions. Higher currents can only be reached by suppressing this emission, for example by using extremely short devices. The mean free path for electron–optical-phonon scattering in metallic nanotubes has been experimentally measured to be approximately 10 nm [17,18], and devices fabricated on this length scale can carry many times more current.

In experimental SWNT devices, other mechanisms can also play significant roles and result in low-bias conductances much smaller than $4G_0$. Contact resistance

plagued early SWNT measurements, limiting measured conductances to 1–10% of the theoretical value. Organic residues from solution-deposited SWNTs and polymer residues from lithographic processing were two common contaminants at contact interfaces. Processing improvements have allowed contact resistances to drop dramatically, with many research groups now using Pd metal to achieve low-resistance contacts to SWNTs [19]. However, a simplistic model of a metal–metal interface, even one which incorporates the differing metal work functions, does not necessarily capture the complexity of the SWNT electronic contact. Empirically, good contacts can only be obtained using metals with good wetting properties (at least for SWNTs with diameters larger than 1.5 nm) and across interfacial boundaries extending a few hundred nm along the SWNT itself. These characteristics may indicate the difficulty of establishing adiabatic equilibrium between the few quantum states of the SWNT and the large number of bulk states in the connecting electrodes.

Various other elastic scattering mechanisms can also decrease the SWNT conductance G. Point defects, with their associated localized states and high fields, contribute to elastic scattering. And the mere presence of an underlying substrate, with its associated contaminants or trapped charges, presents the SWNT with a modulated potential energy landscape. Both mechanisms reduce the transmission coefficients T_i within the Landauer model and, in the low temperature limit, can induce localization [20]. An active area of ongoing SWNT research is focused on freely suspended SWNTs, in which substrate effects can be eliminated.

In addition to decreasing G, these mechanisms make SWNTs sensitive to external electric fields. An applied field, as from a third gate electrode, can move a localized electronic state in and out of resonance with the conduction electrons at E_F and make G gate-dependent. Because of a prevailing conception of SWNTs as being structurally perfect, many researchers have used the presence or absence of transconductance dG/dV_g to identify a SWNT as having a metallic or semiconducting bandstructure. Indeed, the number of current-carrying states in the energy band of a metallic SWNT is not sensitive to small changes in E_F, so metallic SWNTs should normally have $dG/dV_g = 0$. But in the presence of defects, even metallic SWNTs will exhibit transconductance and can be gated to zero conductance at low source–drain bias. Underestimating this mechanism leads to the misattribution of metallic SWNTs as semiconducting. Furthermore, the possibility of defect-induced barriers severely compromises the ability to conclusively identify small-energy bandgaps from three-terminal conductance measurements.

When both contact resistance and elastic scattering are limited, metallic SWNTs can behave like ballistic conductors. In fact, SWNTs today are routinely measured having 6.5–15 kΩ resistances. In this limit, delocalized electrons are coherent along the entire length of a SWNT device, especially at low temperatures. Reflections at the SWNT ends result in electronic standing wave oscillations, directly analogous to those in an optical Fabry–Perot cavity. These electronic oscillations have been directly imaged by scanning tunneling microscopy (STM) [21] and indirectly observed in the two-terminal conductance [22], as shown in Fig. 5.

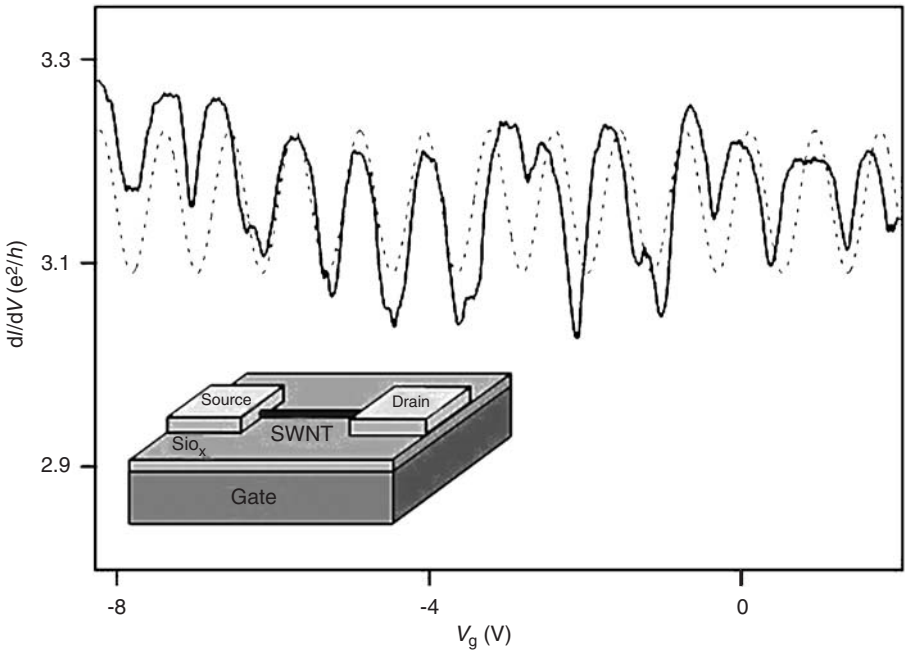

Fig. 5. Differential conductance of a metallic SWNT 200 nm in length. With sufficiently good contacts, the SWNT conductance approaches the theoretical limit of $4e^2/h$. The periodic oscillations with gate bias V_g correspond to Fabry–Perot interferences of electrons reflecting off the source and drain electrodes. This measurement is performed at $T = 4\,K$. From Liang et al. [22]

3.3. Electronic Properties of Semiconducting Nanotubes

Two-thirds of all possible SWNTs are expected to have semiconducting bandstructures with direct bandgaps. As with conventional semiconductors, these SWNTs can have majority hole or electron carriers depending on the position of E_F within the bandgap. Unlike bulk semiconductors, however, it is not straightforward to substitutionally dope a SWNT.

Nevertheless, E_F is easily shifted higher or lower in energy by applied electric fields. The entire carrier population resides on the SWNT surface and is exquisitely sensitive to fields – there is little opportunity for effective screening among 1D-confined charges. In the device geometry of a field-effect transistor (FET), a nearby, capacitatively coupled gate electrode is used to reversibly shift the SWNT E_F to different energies. Other sources of electric fields can include adsorbed chemical species and charge modulations on the supporting substrate. These mechanisms will be discussed after a brief introduction to SWNT FET characteristics.

3.3.1. Intrinsic Semiconducting SWNTs

The field sensitivity of semiconducting SWNTs is the most desirable property of conducting channels in a FET. In fact, enhancing sensitivity and reducing shielding length scales are among the difficulties faced in improving modern CMOS devices.[3] In the most commonly used, "backgated" SWNT device architecture, degenerately doped Si wafer serves as a supporting substrate and global gate electrode. SWNT circuits are then fabricated on top of a thin, thermally grown SiO_2 film and gated by the Si through the oxide. Individual devices can be patterned using electron-beam lithography, but the availability of micron-length SWNTs permits the use of optical lithography, and many research groups have demonstrated wafer-scale device fabrication.

Fig. 6 depicts typical transport characteristics of an intrinsic, semiconducting SWNT in a backgated FET geometry. The conductance at negative gate voltages V_g is attributed to hole carriers, and the sharp drop in conductance at the gate threshold V_t corresponds to a shifting of E_F higher into the bandgap of the SWNT. At still higher V_g, E_F enters the conduction band and electron transport dominates. The conductance change, shown here spanning five orders of magnitude, constitutes the primary attribute of a FET – an electronically controlled switch – and is a key performance metric. One desires a high conductance "On" state and a low conductance "Off" state. Alternately, low conductance in the "On" state limits achievable drive

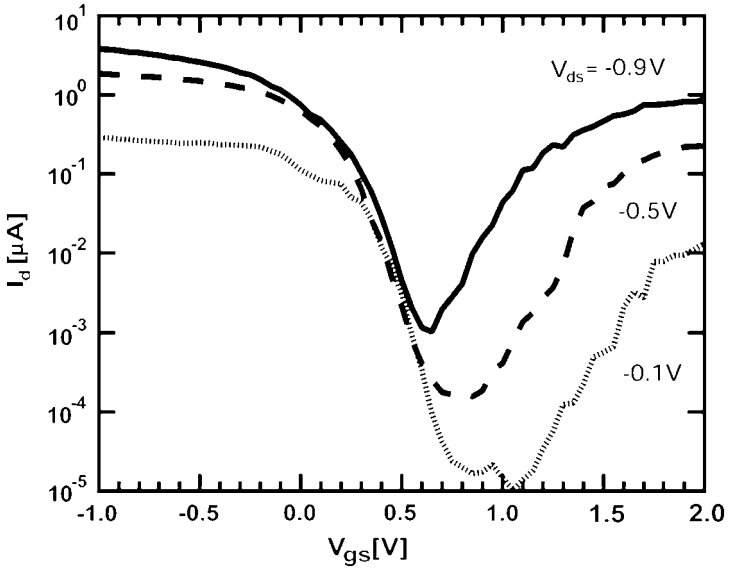

Fig. 6. Gate dependence of an ambipolar SWNT FET. At positive gate bias, the conductance is primarily due to electron carriers, while at negative gate the carriers are holes. Near the threshold voltage, the Schottky barriers for holes and electrons are approximately equal and both carriers can be injected when the source–drain bias is large. Alternately, small biases maximize the achievable on–off ratio. From Lin et al. [86].

currents and requires high voltages in cascaded devices. High residual conductance in the "Off" state leads to unacceptable quiescent power dissipation.

Additional important device metrics include the width of the transition region, the effective carrier mobility, and a wide range of other performance parameters, which are beyond the scope of this review. To summarize briefly, prototype SWNT FETs exhibit performance that is very competitive or exceeds the properties of modern Si technologies [23]. By improving on the rudimentary architecture shown above, SWNT FETs have been demonstrated with high mobilities and transconductances, low turn-on voltages, and subthreshold slopes near the thermal limit [23,24]. Some of the most important of these characteristics will be treated below.

First, however, it must be noted that SWNT FETs behave differently from conventional FETs in fundamental ways. Conventional FET technologies form source and drain electrodes from degenerately doped semiconductors in order to eliminate Schottky barriers at the interfaces of the semiconductor channel. In SWNTs, such materials are unavailable and metal contact electrodes are usually employed, with Schottky barriers forming at the metal–semiconductor interfaces. Fortunately, Schottky barriers are less consequential in a 1D system than in planar geometries. In particular, the electrostatics of a 1D SWNT contacting a 3D metal electrode allow the depletion widths to vary considerably with applied biases [25]. Furthermore, interface states do not pin the Fermi level very effectively, the way they do in planar interfaces, because of the lack of screening in 1D. As a result of these differences, SWNT Schottky barriers are quite sensitive to local electric fields and, in general, the switching in a SWNT FET can be attributed to Schottky-barrier modulation [25,26].

Much of the literature on SWNT FETs can be fit by a simple model dominated by Schottky-barrier switching. Near $V_g = 0$, an intrinsic SWNT will be insulating with a midgap Fermi level E_F. Small, negative V_g values shift E_F toward the valence band, but conduction remains limited by a large-width Schottky barrier. As V_g becomes more negative, the barrier width decreases and hole conductance increases exponentially. The same occurs for electron carriers at positive V_g. When a work-function mismatch is present at the interface, the bands have additional curvature at zero gate, which can exponentially favor one carrier type over another. A review of SWNT Schottky barriers has been presented by Heinze et al. [27].

Some hope exists of preparing low-resistance contacts to semiconducting SWNTs using appropriate metals. Materials-related concerns of the semiconductor industry, however, limit the choices of metals that may be used. Using Pd, experiments have demonstrated a decrease in SWNT Schottky barriers for increasing diameters, to the point that large-diameter (e.g., >2.0 nm) SWNTs exhibit negligible barriers [28] as shown in Fig. 7. Unfortunately, large-diameter nanotubes also have small bandgaps, which limits the achievable "Off" conductance of a device. Ideally, optimal devices would have nearly perfect, low-resistance contacts and also small-diameter SWNTs (e.g., <1.5 nm) having larger bandgaps.

To further emphasize the consequences of Schottky barriers, consider the device transconductance g and carrier mobility μ. These two parameters are common metrics for comparing conventional FETs and they may be extracted from SWNT

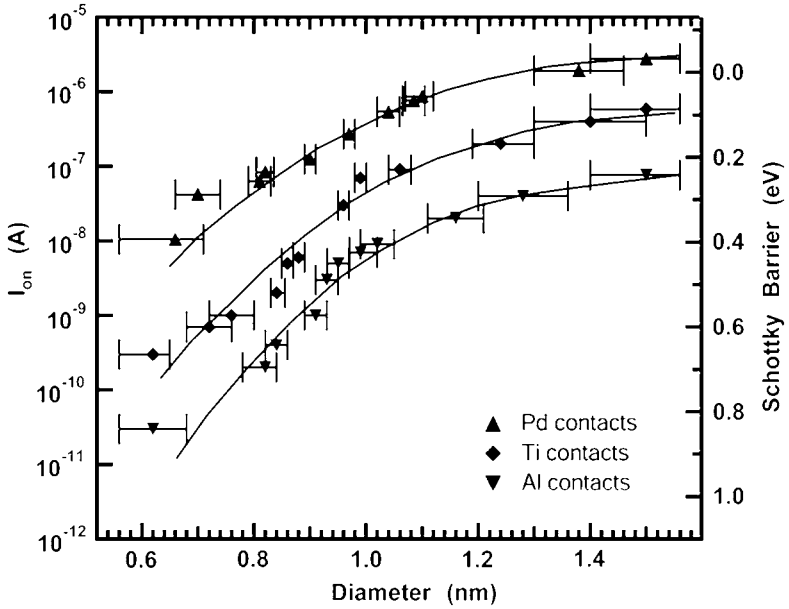

Fig. 7. Schottky barrier contacts limit the maximum possible drive current in a SWNT FET. The barrier height is sensitive to both the SWNT diameter and the contact metal. For low work-function metals like Pd contacting small gap (large diameter) SWNTs, the effective barrier is minimized and maximum currents are achieved. The data points shown here are measured with a 0.5 V source–drain bias at a gate voltage $V_g - V_T = -0.5$ V. From Chen et al. [28].

device characteristics. The transconductance $g = dI_{SD}/dV_g$ is a measure of the sensitivity of the source–drain current to changes in gate voltage, and this parameter determines the width of the switching transition. In conventional devices, g directly measures the capacitive coupling between the gate electrode and carriers in the transistor channel, but in a quasi-ballistic, Schottky-barrier FET g is wholly determined by the gate's modification of the barrier width. Therefore, the measured SWNT transconductance of 10–20 μS [24,29] misrepresents the device physics if it is interpreted conventionally. Similarly, the mobility μ is a measure of the conductivity per individual charge carrier, and in conventional FETs it is a measure of the carrier velocity (per unit of applied field). In a quasi-ballistic FET the SWNT mobility is an "effective mobility" in the sense that it does not merely reflect carrier velocity but also the tunneling characteristics of the Schottky barriers. In long SWNTs where the bulk scattering dominates and the transport is diffusive, the mobility has its conventional meaning and values as high as $\mu \sim 100\,000\,cm^2/Vs$ have been reported at low fields and room temperature. Theory predicts a temperature- and diameter-dependence of the low-field mobility [30].

The high performance of SWNT FETs is therefore both an opportunity and a challenge, since device development must account for their unusual physics.

Already, there is a growing appreciation that these FETs exhibit different scaling rules with respect to channel length and oxide thickness than traditional devices. Novel architectures have demonstrated a variety of performance improvements [24,29,31,32], and investigations of high-frequency behavior indicate that SWNTs may operate at competitive switching speeds exceeding 100 GHz.

3.3.2. Doping and Chemical Variability in Semiconducting SWNTs

Throughout the early years of silicon transistor research, the presence of unintentional contaminants and dopants complicated and confused experimental efforts. It is not surprising, then, that similar effects have occurred in the SWNT field. Throughout the early literature on SWNT FETs, for example, researchers observed only p-type conduction and no conduction at large, positive V_g [33,34].

Substitutional doping of the SWNTs seemed unlikely, so other mechanisms were proposed to explain this p-type behavior. Ultimately, the SWNT devices were understood to be very sensitive to weakly adsorbed species at or near the Schottky barrier contact, to the extent that simple air exposure was sufficient to cause the apparent SWNT doping. Through a gradual discovery process, a wide range of doping experiments and theoretical calculations were performed. As a result, the remarkable chemical sensitivity and variability of SWNT circuits is now widely appreciated.

Early doping experiments focused on common graphite intercalants such as iodine and alkali metals, partly in hope of finding superconductivity like in the carbon fullerenes. Instead of superconductivity, though, researchers found irreversible electronic behaviors, which seemed strongly dependent on sample history [35]. The onset of n-type conduction, which might be attributed to alkali metal intercalation, was not reversible in vacuum but immediately disappeared upon exposure to air. Subsequently, it was found that a vacuum treatment alone was sufficient to change the majority carrier type, even in the absence of intentional dopants [36–39].

The net result is that SWNT FETs prepared in air will generally exhibit p-type behavior, and that vacuum degassing produces n-type behavior. Using intermediate temperatures, ambipolar behaviors (with E_F near the middle of the semiconducting gap) are also readily obtained. Encapsulation of the devices inside a passivation layer does not interfere with this thermal treatment, so air-stable devices with either carrier type can be selected. The effect is shown in Fig. 8 for a sample contacted by Au electrodes, and can be explained in terms of the differing Schottky barrier heights for electron and hole conduction. The work function of Au, like many metals, is very sensitive to molecular adsorbates, and these can raise or lower the effective barriers to carriers in a particular band. The observed p-type behavior is not, therefore, due to hole doping; instead, it arises from a nearly transparent Schottky barrier to holes and an insurmountable one for electrons.

This variability can be considered as either an advantage or a disadvantage for electronic devices. On one hand, the possibility for simultaneous electron and hole injection at opposite ends of a SWNT enables a range of electro-optic behaviors to

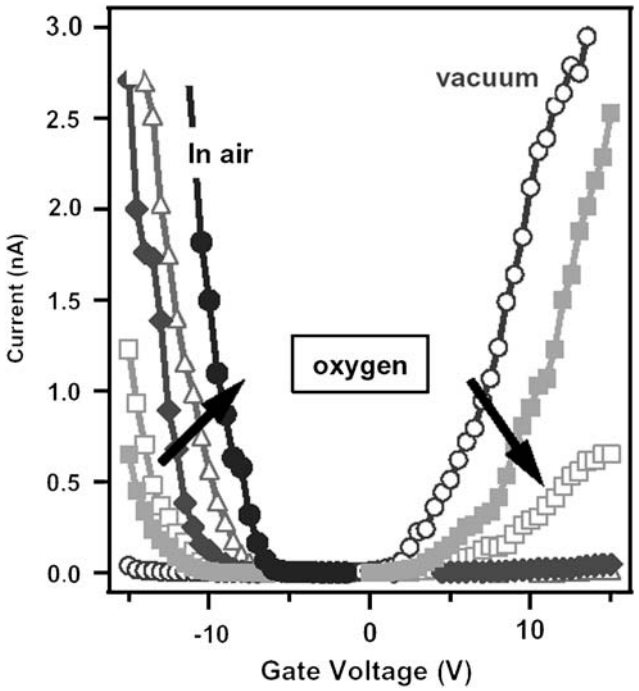

Fig. 8. The apparent majority carrier in SWNT FETs changes from electrons in air to holes in vacuum, with a strong dependence on the presence of oxygen. This effect is due to a shift in the work function of the connective Au electrodes. In air, the work-function mismatch to the SWNT results in a smaller Schottky barrier for holes than for electrons. In vacuum, the Au work function increases and the reverse becomes true. From Derycke et al. [39].

be described further below. The sensitivity to processing conditions, however, also suggests a variability that poses difficulties for device manufacturing. One solution to this variability is to better match the SWNT's work function with that of the connecting electrodes [19,38]. In this case, E_F is most likely to be midgap and neither carrier is preferentially selected by processing. A second solution is to use smaller bandgap SWNTs so that the Schottky barrier effects are minimized [28]. SWNTs with 2 nm diameters and even MWNTs are much more likely to exhibit ambipolar conduction than SWNTs with 1 nm diameters. While bandgap reduction can produce low, symmetric Schottky barriers, it also results in high FET "Off" currents. To achieve acceptable, reproducible characteristics, the most effective SWNT devices may ultimately employ a combination of novel architectures, SWNT diameter selectivity, and choice of materials. Fig. 9 depicts one such architecture in which the ends of the SWNT are degenerately doped using $SbCl_6^-$ ions to minimize interfacial barriers.

In addition to these Schottky barrier effects, different molecular species have also been observed to shift the turn-on threshold V_T of SWNT FETs. In this

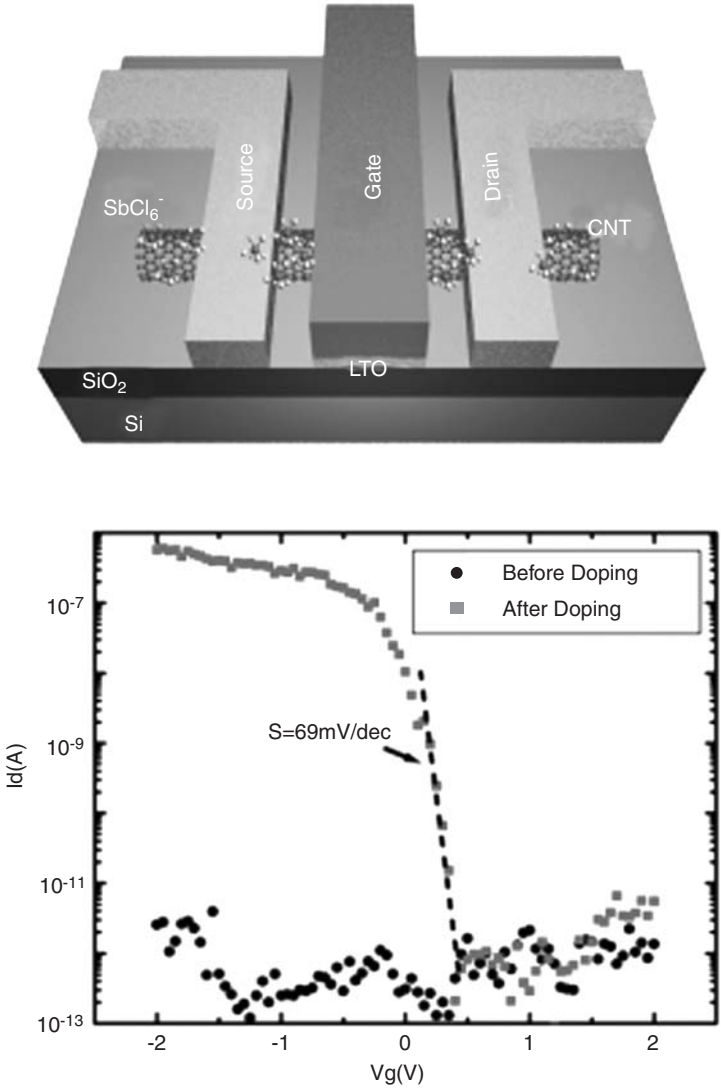

Fig. 9. In traditional semiconductor devices, degenerately doped semiconductors form the source and drain contacts to the semiconducting channel. Similar effects in SWNT FETs can minimize Schottky barrier effects. Here, a partly exposed SWNT is oxidized by $SbCl_6^-$ ions in order to degenerately dope the portions, which contact the source and drain electrodes. The resulting FET characteristics exhibit a sharp conductance transition and very small subthreshold swing S, both of which may be attributed to switching by the SWNT body. From Chen et al. [24].

case, the effect is similar to traditional doping in which E_F is shifted higher or lower within the bandgap: electron donors increase E_F and lower the necessary V_T for n-type conduction, and electron acceptors do the opposite. This is most strikingly observed for strong oxidants and reducing agents like NO_2 and amines [40], but it also occurs for a wide range of reactants including polymers, aromatics, and biomolecules.

The sensitivity of SWNTs is particularly high because these conductors have no shielded bulk atoms. A single monolayer of adsorbed charge donors approaches a 1:1 atomic ratio with the SWNT carbon atoms, allowing for remarkable dopant concentrations. Alternately, charge transfer to the substrate and interfaces can also account for the V_T behaviors observed experimentally. A molecule that chemisorbs to the underlying substrate will produce a local dipole field and partially gate the SWNT. Since SWNTs have no bulk carriers and are not particularly effective at electrostatic shielding, this electrostatic local gating is functionally equivalent to the chemical doping of a particular site. In fact, distinguishing between local electrostatic "doping" and true charge transfer to a SWNT is experimentally quite difficult. Different chemical species may interact with SWNTs through either mechanism.

It is important again to note that this variability has both positive and negative consequences. Because of the sensitivity of V_T to molecular adsorption, SWNT FETs have been demonstrated as remarkably sensitive chemical sensors. Small, reversible shifts in V_T can lead to orders-of-magnitude change in the FET's source–drain conductance at fixed gate bias. On the other hand, before SWNT FETs may be used as digital logic circuits, this V_T variability must be reliably controlled. Recently, progress has been made developing air-stable dopants that allow even degenerate doping of semiconducting nanotubes and thus make possible new device structures that minimize parasitic capacitances and improve device speed [24].

3.4. Many-Electron Effects in Carbon Nanotubes

Up to this point, the discussion of the ground state electronic structure and electrical properties of carbon nanotubes has been based on a single-particle, tight-binding model. While this simple description has been found to be quite successful overall, it fails to explain many important aspects of nanotube behavior.

Ando and co-workers [41,42] discussed the role of e–e Coulomb interactions early on and suggested that they can significantly enlarge the single-particle bandgaps in semiconducting nanotubes, a prediction that was later confirmed by first-principles calculations [43]. The strong e–e interactions, taken in combination with the linear dispersion near E_F in metallic nanotubes, produce a model system for the formation of a state of matter referred to as a Tomonaga–Luttinger liquid [44,45]. This state is characterized by unique properties including spin-charge separation and a set of power laws governing current injection through tunneling contacts.

Experimentally, power law dependences of the differential conductance on temperature and voltage have been observed in both bundles [46] and individual metallic SWNTs [47]. Furthermore, the power law exponent was found to depend on the geometry of the contacting electrodes as expected theoretically. The spectral function and the temperature dependence of the intensity at the Fermi level exhibit power law dependences with the appropriate exponents when nanotube aggregates are measured by angle-integrated photoemission [48]. All of this evidence supports the Luttinger liquid model, though conclusive, direct proof awaits future experiments.

Another inadequacy of the single-particle, tight-binding model is an appropriate description of the excited states of SWNTs. When an electron is promoted to an excited state, an overall attractive interaction develops between it and the hole left behind to form a bound state called an exciton. In a perfect 1D system, the electron–hole (e–h) attraction will be infinite [49]. While SWNTs are not quite 1D, e–h attraction leads to the formation of strongly bound, quasi-1D excitons. The predicted exciton binding energies range from $\sim 1\,\text{eV}$ for small diameter ($<1\,\text{nm}$), semiconducting SWNTs, to a few tenths of an eV for larger ($\sim 2\,\text{nm}$) diameter SWNTs [50], with still smaller binding energy excitons occurring even in metallic SWNTs [50]. Another theoretical prediction is that nearly all of the oscillator strength of the band-to-band transition should be transferred to the exciton, making the interband transition nearly invisible to optical absorption experiments [50].

Three effects have combined to delay the recognition of these important many-body effects. First, essentially all oscillator strength is concentrated into the excitonic transition so that only one transition is experimentally observed. Second, the strong e–e repulsion is partially cancelled by the attractive e–h interaction, so that experimentally measured excitation energies have reasonably corroborated bandgaps predicted by the simple, single-particle model. Third, the sharp peaks in photoluminescence spectra have been favorably compared to the joint density of states arising from van Hove singularities in the single-particle bandstructure. In fact, these peaks arise from excitonic transitions, not interband transitions. Only recently has two-photon excitation spectroscopy been used to confirm the predicted strong excitonic binding in carbon nanotubes [51]. The most important implication of many-body effects is therefore that the optical absorption (optical bandgap) does not equal the electrical bandgap in semiconducting nanotubes. This necessitates new types of measurements and the reinterpretation of a number of transport and optical studies.

An outstanding issue that remains to be addressed in future research involves the effect of the SWNT's environment on the above many-body effects. The screening of e–e and e–h interactions is greatly influenced by the dielectric constant of the surrounding environment, since the long-range Coulomb fields are primarily transmitted through the surrounding medium rather than the SWNT body [50]. Because of this sensitivity, both the electrical and the optical bandgaps become environment-dependent. In fact, any electronic or optoelectronic properties influenced by many-body effects might exhibit environmental sensitivities.

3.5. Optoelectronic Devices

The combination of electronic and optical properties in semiconductor devices comprises a broad and important technological subfield. This section deviates from strictly electronic properties in order to address the promise of SWNTs for optoelectronic devices. It is a mere introduction to a complex and fast-moving field in which many novel materials have recently attracted attention.

Confined electron and hole carriers can recombine by a variety of different mechanisms. In most cases, the energy will be released as heat (phonon emission), but a fraction of the recombination events can result in the radiative emission of a photon. This process is termed "electroluminescence" and is widely used to produce solid-state light sources such as light emitting diodes (LEDs). In order to fabricate LEDs or any other electroluminescent device, one must recombine significant populations of electrons and holes. Conventionally, this is achieved at an interface between a hole-doped and an electron-doped material (e.g., a "p–n junction").

Unlike conventional semiconductors, SWNTs can form ambipolar FETs in which both electrons and holes contribute to the conduction. Using a large source–drain bias, electrons and holes can be simultaneously injected at the opposite ends of a SWNT channel. This allows electroluminescence to occur, as first demonstrated by Misewich et al. [52]. While the emission mechanism is exactly the same as from p–n junctions, ambipolar SWNTs do not require chemical doping and formation of metallurgical interfaces.

Experimentally, SWNT electroluminescence exhibits a variety of interesting properties. The emitted light is strongly polarized along the tube axis. The radiation also has a characteristic energy that depends on the diameter and chirality of the excited SWNT, just as the optical bandgap does. As discussed above, the electronic bandgap is not necessarily the same as the optical bandgap, since the free electron and hole may first form a bound exciton before recombining radiatively. Finally, the geometric length of the electroluminescent region is observed to cover approximately 1 μm. This length may be interpreted as an effective e–h recombination scale, regardless of whether intermediary excitonic binding is first occurring.

Because this recombination length is relatively long, SWNT devices may be fabricated either shorter or longer than it. In short SWNT devices, the light emission encompasses the entire SWNT. In long devices, on the other hand, the emission will be localized wherever the concentrations of electrons and holes overlap most strongly. This overlapped region can be physically moved using a gate electrode, since the relative contributions of electrons and holes to the total current is strongly gate-dependent. As a consequence, a SWNT LED is a moveable light source – an electronic signal V_g can smoothly and continuously position the site of emission [53]. Fig. 10 demonstrates this effect for four different gate voltages. One can immediately envision combining such an LED with an aperture to produce fast electro-optic switches, or electronically moveable light emitters.

In addition to this translatable emission, localized electroluminescence is also observed from particular spots on a SWNT under *unipolar* transport conditions. In this case, the current is exclusively carried by only one type of carrier, but at certain

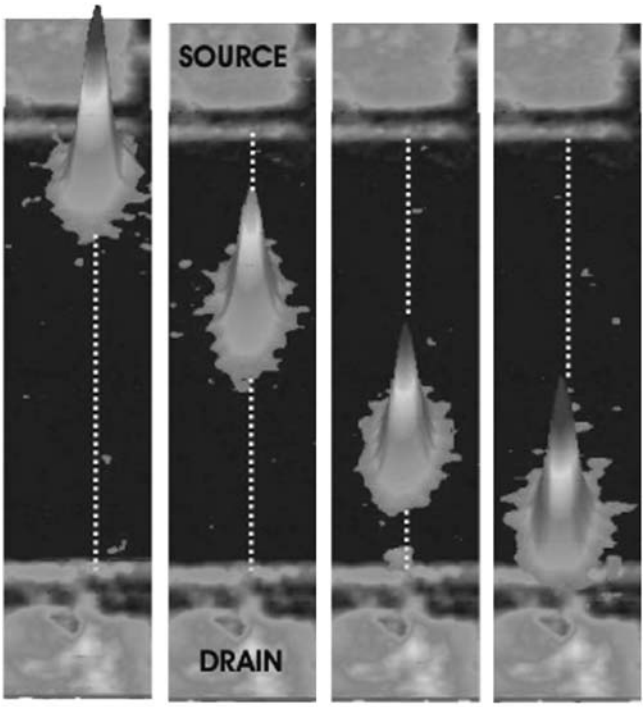

Fig. 10. Electroluminescence from a long, single SWNT in a FET configuration. The electron–hole recombination length is short ($\sim 1\ \mu m$) compared to the length of the device, so the point of highest luminescence is easily resolved within the electrodes. Furthermore, this site can be controlled by varying the gate voltage V_g. This figure depicts the luminescence at four different values of V_g. From Freitag et al. [53].

randomly positioned sites light emission is nevertheless observed. Since both types of carriers are necessary to produce light, these sites must be actively generating e–h pairs. This process could occur, for example, around SWNT defects, trapped charges in the insulator, or any other inhomogeneities, which produce large, local electric fields. The monitoring of localized electroluminescence thus provides a potential new tool for detecting defects in SWNT devices or even large-area device arrays.

Photoconductivity is the reverse process of electroluminescence, with optical radiation producing electron and hole carriers. An example of a photoconductivity measurement is shown in Fig. 11. The resonant excitation of a SWNT generates measurable electric currents with a reasonable photocurrent yield of approximately 10% [54]. Alternately, in the open-circuit configuration the SWNT generates a photovoltage, which is then limited in magnitude to the SWNT bandgap [54].

Thus, a single-SWNT FET device can be used as a transistor, a light emitter, or a light detector. Choosing among these different modes of operation only requires changing the bias conditions and does not require separately tailoring the chemical

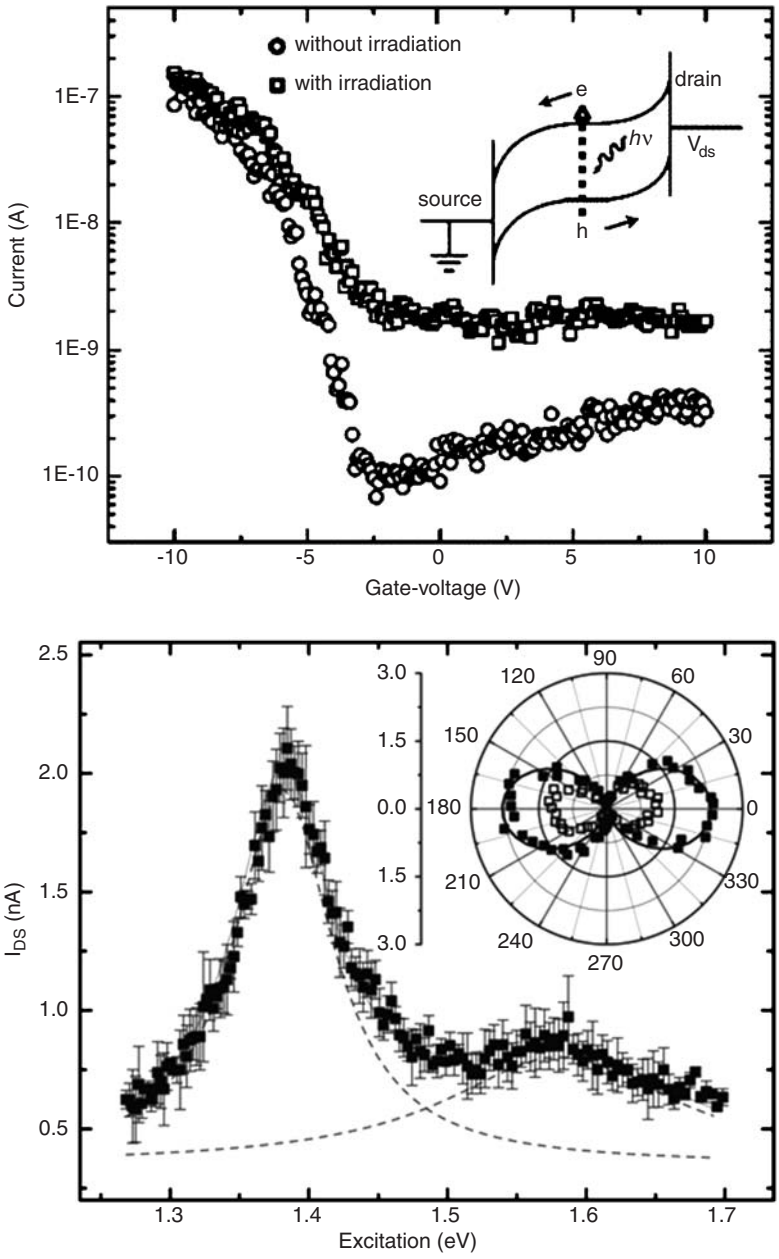

Fig. 11. Photoconductivity from an individual SWNT in a FET configuration. Incident radiation produces a large increase in conductivity if it is resonantly tuned to form electron–hole pairs (top). The effect is sensitive to both photon energy (bottom) and polarization (bottom, inset), with polarizations parallel to the SWNT generating the largest photocurrents. The primary resonance near 1.4 eV is due to the creation of excitons (the "E_{22}" transition), and the higher energy peak is a sideband attributed to exciton–phonon coupling. Adapted from Qiu et al. [87]

doping or the device architecture. This flexibility suggests new avenues for SWNT electronics research, since straightforward fabrications may be able to produce complex, SWNT-based circuitry with both digital logic and optoelectronic capabilities.

4. CARBON NANOTUBE AGGREGATES

4.1. SWNT Ropes

While individual SWNTs have now been widely studied, much of the preliminary nanotube literature from the 1990s investigated the properties of SWNT "ropes." These agglomerations of SWNTs became widely available for electronics research following the synthesis of Thess et al. [7]. Because the SWNTs had similar diameters, they close-packed like threads in a rope and were even briefly considered to be SWNT crystals. The packing took maximum advantage of van der Waals cohesion and, as a result, made individual SWNTs quite difficult to experimentally isolate.

Even SWNTs of identical diameter have varied electronic properties due to the different possible chiralities. A SWNT rope is therefore most simply modeled as a weakly interacting bundle of metallic and semiconducting SWNTs in parallel. In reality, the properties of a rope are somewhat more complex. In large-diameter bundles, only a fraction of the SWNTs directly contact the connective electrodes, and metallic SWNTs partially electrostatically shield the semiconducting SWNTs. When the constituent SWNTs are shorter than the rope itself, conduction must be assisted by intertube transport. Moreover, the interstitial sites in SWNT ropes can host a wide range of chemical species. While intercalation may be commercially useful for the storage of methane gas or lithium ions, both intentional and unintentional doping complicated the interpretation of early experimental results.

Despite these numerous obstacles, the availability of SWNT ropes accelerated initial nanotube research. In particular, atomic imaging and spectroscopy by STM confirmed the field's underpinnings [55,56]. Theoretical models were also refined, with SWNT interactions leading to an additional pseudogap in $D(E_F)$ [10]. However, the synthesis of isolated SWNTs by chemical vapor deposition (CVD) techniques helped overcome many of these materials problems, so that CVD-grown SWNTs were rapidly adopted as an alternative to SWNT ropes.

4.2. SWNT Films

By spin-coating or spraying a SWNT suspension onto a substrate, macroscopic films of SWNTs may be easily fabricated. The primary advantage of these films is their size, which enabled the earliest attempts to electrically characterize SWNTs. More recently, interest in both thick and dilute SWNT films has seen a resurgence. Thick SWNT films generally behave like graphitic conductors, albeit with high-surface area and mechanical flexibility. As described in the next section, they have shown particular promise as electromechanical actuators [57] and as porous

electrochemical electrodes [58] and commercialization efforts are underway using them as microelectromechanical relays for nonvolatile memory.

Dilute films form percolation networks which, like SWNT ropes, can have complex electronic properties. Of special interest are networks of *sparse* SWNTs, which can be grown using CVD following the dilute dispersal of catalyst particles onto a substrate. This technique produces a loosely connected film composed of semiconducting and metallic SWNTs, each of which retains its individual electronic character. Locally, the electronic properties of such films reflect a parallel combination of the individual SWNTs. Over large areas, however, the films behave as percolation networks dependent on SWNT density and length distributions and on the electronic properties of intertube junctions.

Because semiconducting SWNTs typically outnumber metallic ones by a factor of two, a regime exists above the percolation threshold in which metallic SWNTs do not fully interconnect. For films in this regime, every conduction path includes one or more semiconducting segments. These films exhibit remarkably good transistor and chemical sensor behaviors [59,60] considering the presence of metallic components. In practice, the window for fabricating film transistors is not restrictively narrow because SWNT defects and intertube junctions are also sensitive to electric fields. These additional transconductance mechanisms relax the restriction on the metallic number density and have made SWNT film transistors relatively straightforward to fabricate.

Dilute SWNT films have a number of properties that distinguish them from single-SWNT circuits. They do not have the optimum mobility and subthreshold characteristics of individual SWNTs, but as large-area transistors the films exhibit larger drive currents and have greater tolerance for individual SWNT failures. As demonstrated in Fig. 12, they have been incorporated onto plastic substrates as active electronic devices, which are both flexible and transparent [61,62]. And the element size is well suited for pixellated displays and whole cell biosensors. Thus, while individual SWNT sizes may allow a breakthrough in scaling transistor dimensions

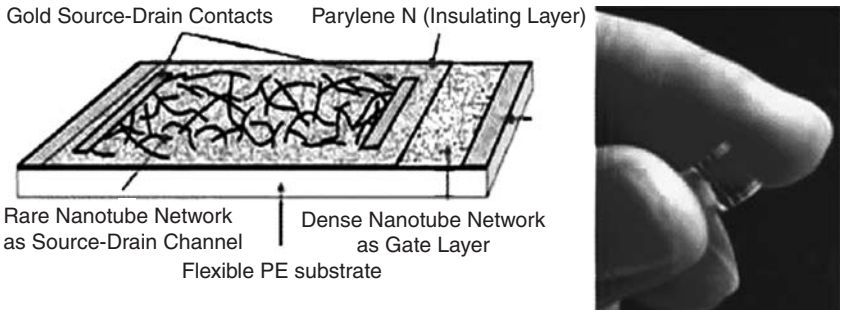

Fig. 12. A film of nanotubes on a flexible, transparent substrate can be used as a field-effect transistor (FET). Similar technologies may enable large area flat panel displays or low cost, printable active circuits. From Artukovic et al. [62]

downwards, the other unique properties of SWNTs enable a wider range of electronics opportunities, and research on SWNT films is likely to remain quite active.

4.3. Multiwalled Carbon Nanotubes

MWNT consists of individual carbon nanotubes concentrically nested around each other. Unlike the SWNT aggregates described above, MWNTs can have a very high degree of order and three-dimensional crystallinity. Each cylinder, or shell, of the MWNT nests perfectly in the structure with a spacing similar to the interplanar distance in crystalline graphite. Remarkably, however, the electronic communication between these shells is minimal. As in graphite, the physical spacing between layers is 0.34 nm, too large for any significant overlap between the delocalized π orbitals of adjacent layers. Only defects substantially increase the interlayer coupling, and interior MWNT layers are believed to have very low defect densities.[4]

As a result, the individual layers in a MWNT may be modeled as parallel, independent SWNTs with the properties described above. A rich literature exists on the possible corrections to this simple model, but to first order it is accurate. Nevertheless, MWNTs are exceptionally complex wires. The nesting imposes tight restrictions on the diameter of a particular shell but not on its chirality. Each shell will therefore randomly alternate between semiconducting and metallic [63], producing something like a coaxial cable but with many more alternating layers. This effect is shown in Fig. 13. The diameter-dependence of SWNT bandgaps is believed to be preserved, so that in the absence of metallic chiralities MWNTs exhibit a radial bandgap variation from shell to shell. A typical MWNT might have

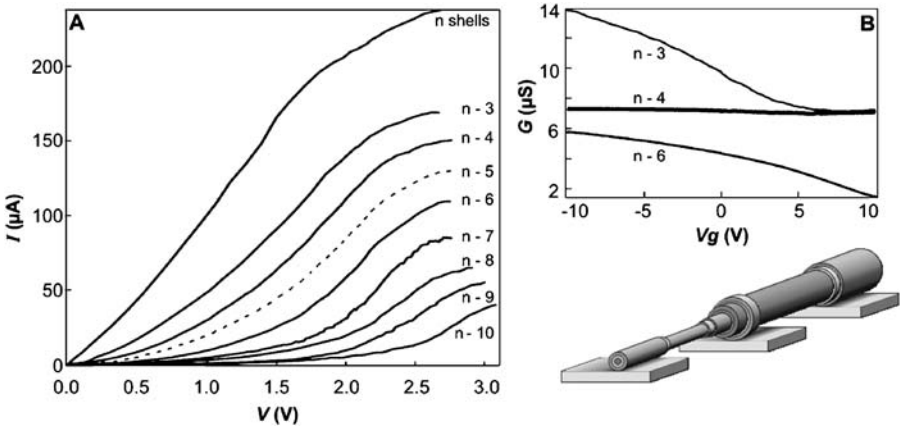

Fig. 13. A crystalline MWNT is composed of many nested SWNTs. By peeling away one carbon layer at a time, characteristics of different inner shells may be investigated. Here, the current–voltage characteristics (A) and gate dependence of the conductance (B) are both measured on different layers of a MWNT. Adapted from Collins et al. [63].

shell diameters ranging from 2 to 20 nm, corresponding to electronic bandgaps of 0.3 eV at the inner diameter and 0.03 eV at the outer surface. At room temperature, therefore, the outer shells of a MWNT conduct regardless of chirality, since thermal excitations exceed the small bandgaps (i.e., $kT > E_g$).

A second electronic complication in MWNTs is the existence of closely spaced electronic subbands above and below E_g. As depicted in Fig. 2, these subbands have energy spacings of the order of E_g. In SWNTs, E_g is sufficiently large that the subbands only play a role in optical properties. In MWNTs, on the other hand, these subbands are merely 10's of meV apart, so that multiple subbands may be thermally populated at room temperature. Furthermore, small amounts of chemical doping [64] can shift E_F and ensure that it crosses multiple subbands.

A final complication for MWNT devices is the proper description of their electrical contacts. For a pristine MWNT physically connected to a metal electrode, only the outermost carbon shell is truly connected in an electrical sense. Inner shells are not ohmically connected but may communicate via tunneling, coulomb drag, diffusive scattering, and a range of other mechanisms. At low temperatures and low bias, these mechanisms can be minimized and the measured conductance will be exclusively due to the properties of the outermost shell. Under these conditions, MWNTs behave very much like large-diameter SWNTs, with quasi-ballistic conduction, coulomb blockade charging effects, and even Aharonov–Bohm-like interferences from circumferential states [65,66].

At high bias, on the other hand, electron injection at the contacts helps to equilibrate multiple shells, all of which contribute to conduction with one or more subbands. Room temperature measurements clearly indicate the contributions of multiple shells, even in the low bias limit [67]. For example, a MWNT composed of an outer semiconducting shell and an inner metallic shell can be partially gated by electrostatic fields, but never turned off because of leakage through the metallic component. More complete characterizations can individually measure every shell's contribution and sensitivity to electrostatic gating [63]. Despite this facility, the precise behavior of a given MWNT is difficult to generalize because of the many different types of variability.

Under exceptional conditions, MWNTs can exhibit conductance quantization, even at room temperature. A series of experiments performed with suspended MWNTs dipped into liquid mercury contacts has demonstrated characteristics of single-shell ballistic transport [68,69]. These effects are not observed in planar, lithographically fabricated devices, however, even ones in which the MWNT is suspended across an air or vacuum gap. It may be that unique properties of mercury, combined with a special preparation that eliminates surface scattering, allows the quantization steps to be observed.

To take full advantage of their inner carbon shells, it is possible to modify a MWNT in various ways. By chemically etching the ends, all of the MWNT shells can be exposed and a metal electrode will then contact each one, albeit with a vanishingly small contact area. Alternately, energetic beams of electrons or atoms can be used to introduce defects and electrically crosslink the shells [70]. At very low dosages, MWNTs become better conductors due to the contributions of multiple

inner shells, but generally the simultaneous loss of crystallinity degrades the conductivity and introduces disorder scattering. Such samples then exhibit unusual bias- and temperature-dependences.

4.4. Disorder in the Nanotube Nomenclature

Because of the rapidly growing literature on nanotube electronics, it is important to point out that variations exist in carbon nanotube nomenclature. A wide variety of material morphologies exist, especially given the large number of research groups investigating nanotube synthesis. The electronic properties described above are unique to isolated, sp^2-bonded planes of graphitic carbon and do not necessarily apply to more disordered carbonaceous materials.

Two particularly subtle errors frequently mislead researchers unfamiliar with the historical development of the field. First, a wide range of hollow-core materials have been called MWNTs. The earliest MWNTs were grown at very high temperatures in arc furnaces designed for the production and study of fullerenes. High temperatures assist the annealing of sp^2-bonded networks and much of the structural carbon in these nanotubes was believed to be defect-free, making the graphene bandstructure relevant. In such materials, the intershell coupling is indeed minimized and the individual shells can be quasi-ballistic. Theoretical models of MWNTs exclusively refer to such materials. Experimentally, less crystalline carbon wires such as those synthesized at lower temperatures can be highly defective and rarely consist of perfectly nested shells, much less electronically independent ones. These materials generally have the electronic properties of graphitized carbon fibers, which cannot be reasonably compared to the single-conducting-shell results [65,68] described above. A wide range of hollow carbon wires are called MWNTs only by convenience, even though they may clearly lack the mechanical, chemical, and electronic properties associated with SWNTs and the MWNTs of theoretical models.

A second comment regards the existing literature on SWNTs. The early synthesis of SWNTs was achieved by incorporating transition metal catalysts into carbon plasmas. During the popularization of CVD synthesis, it was therefore widely accepted that catalyst-promoted nanotube growth resulted in SWNTs. Many experimental results have been attributed to SWNTs without any structural characterization other than a measurement of the outer diameter. Subsequently, careful microscopy [71] and shell-counting experiments have determined that diameter is a very poor predictor of the number of shells in a CVD-grown nanotube, especially for diameters larger than 2 nm. True SWNTs with diameters of 1, 2, 3 nm, and higher have indeed been observed by high-resolution microscopy, but double-walled and triple-walled nanotubes are far more common at the larger diameters and accurate wall counting requires patience and skill. The unintentional experimental confusion on this issue indicates the lack of techniques originally available for characterizing nanotubes integrated into electronic circuits. Today, techniques such as Raman spectroscopy can clearly distinguish between circuits have single- or double-walled nanotubes.

5. ELECTRONIC APPLICATIONS OF CARBON NANOTUBES

Because nanotubes exhibit many interesting electronic properties, a wide range of electronic applications have been proposed and investigated. Various prototype devices have been demonstrated with excellent, commercially competitive properties.

However, a primary obstacle to many applications remains the variability in electronic characteristics. Chiral variability is a widely acknowledged problem with SWNTs, but there is hope that it may be solved through specially designed catalysts or selective wet chemistry [72]. An equally serious but less well-documented problem is the sensitivity of SWNTs to small chemical, mechanical, and electronic variations present on substrates, at metal electrodes, and in the SWNTs themselves. Researchers who have produced 4″ and 6″ wafers full of SWNT devices have sidestepped the chirality problem by manually selecting the subgroups of semiconducting or metallic SWNTs. Even among these subgroups, electrical properties vary by an *order of magnitude* from device to device, perhaps due to surface contaminants or nanoscale geometric variations. When the SWNT diameter is not precisely controlled, the variations are even larger.

Thus, even if the chirality issue were immediately resolved, consistent specifications for nanotube circuitry would remain elusive. SWNT transistors and memory elements for digital logic can be individually demonstrated but not yet manufactured, and many additional processing techniques remain to be discovered and developed before SWNT devices will have reliable data sheets. In this sense, nanotube electronics resembles early Si research of the 1950s and 1960s. Variability remains a primary challenge for nanoelectronics applications in which SWNTs assist downscaling to ultrasmall or ultradense circuitry.

Larger circuits and devices incorporating many nanotubes can be much less sensitive to small fluctuations on individual SWNTs. For example, the thin-film SWNT FETs described above are not particularly small, but their flexibility, reasonable performance, and low-cost fabrication suggest particular application niches. Similar electronic devices that rely only on nanotube ensemble properties can be produced more dependably than single-nanotube devices, and some of these are closer to successful commercialization. The remainder of this section provides a short tour of potential applications enabled by the electronic properties of nanotube ensembles. One must consider, however, whether the performance of these large nanotube ensembles is distinguishable from that of films of carbon fibers, a more traditional and much lower cost material.

5.1. Conductive Composites

Because of their extreme aspect ratios, nanotubes can form conductive percolation networks at very small volume fractions. By embedding nanotubes into a polymer matrix, antistatic and electrically conductive plastics are readily produced. In fact, such products are the earliest-known commercial applications of carbon nanotubes.

The volume fraction of nanotubes can be as small as 0.1% [73], allowing the intrinsic properties of the matrix, which might include transparency, flexibility, and strength, to be retained. At still higher densities, the nanotubes can also begin to tailor the matrix's mechanical properties.

When not confined within a matrix, conductive nanotube films exhibit large surface areas and significant mechanical flexibility. These properties enable electrochemical and electromechanical applications [74]. For example, nanotube "supercapacitors" exhibit very large capacitances for their size, because even a compressed nanotube film remains porous to most electrolytes. A nanotube electrode with a macroscopic area A has an effective surface area hundreds of times larger than A and exhibits capacitances exceeding 100 F/g of nanotube material [74]. Furthermore, nanotube supercapacitors can charge and discharge at power rates of 20–30 W/g, sufficient for high power applications such as hybrid-electric vehicles [75]. The chemical inertness of nanotubes is critical to this type of application: nanotubes do not readily degrade with repeated cycling the way that other high-surface-area materials do. Of course, some electrolytes are more chemically active than others, and the application of nanotubes to lithium ion storage has been hampered by large, irreversible capacitances [76]. Nevertheless, nearly all lithium ion batteries manufactured today include a small percentage of lifetime-enhancing carbon nanotubes. Both capacitative and chemical energy storage using nanotube electrodes remain active research topics, with products successfully deployed in both areas. However, these applications are quite sensitive to the high costs of nanotube materials and will benefit from ongoing research in bulk nanotube synthesis.

Nanotube films have also been investigated as electronically controlled mechanical actuators and switching elements. In an electrolyte, the capacitive charging of a nanotube film leads to swelling and mechanical deformation [57], which can be employed as a type of actuator. In air or vacuum, electrostatics alone are sufficient to deform nanotubes [77], since despite their high tensile strength nanotubes are relatively floppy and bendable. The deformation of individual nanotubes has been imaged by SEM and TEM, and using high-frequency fields a nanotube's mechanical resonances can be directly measured [78,79].

Visionaries imagine mechanical work at the nanoscale being accomplished by nanotube actuators and positioners. In the shorter term, electromechanical actuation has been employed to build simpler electronic switches [80]. These devices resemble relays with nanotube films as the flexible armature contact. Unlike relays, these mechanical switches do not require magnetic fields or power-hungry solenoids, so they can be lithographically fabricated in large arrays and potentially used for nonvolatile memory applications.

5.2. Electron Emitters

As chemically inert wires with high aspect ratios, carbon nanotubes exhibit all of the properties desired in a good field emitter [81]. Both SWNTs and MWNTs exhibit emission at low threshold electric fields of 1–2 V/μm, indicating that their sharp tips

geometrically enhance local electric fields by factors of 1000 or more. The tolerance of nanotubes for extraordinary current densities further allows these emitters to operate at high power densities.

Individual field emitters constitute a small commercial market, but arrays of emitters can be used for general lighting, flat panel displays, and high power electronics. In each of these applications, the nanotube emission exceeds the minimum performance specifications to be competitive; the primary barriers to commercialization involve other issues such as fabrication, compatibility, and product complexity. In lighting, these barriers are relatively small and high-brightness, high-efficiency lighting products exist. Alternately, flat panel displays are highly complex products with interrelated technical, economic, and practical specifications. Display technologies demand thousands of identical pixels, a stringent requirement on emitter variability. In this field, multiple demonstration prototypes by companies including Samsung and Motorola have not yet resulted in consumer products.

Field emission is intrinsically a nondissipative, energy-efficient tunneling process. Emission devices are therefore useful in a variety of high power density applications, such as the frequency modulation of very large currents or surge protection for power and telecommunications substations. In the past, potential power devices such as these have been severely limited by the available field emission materials, and nanotubes have made new performance levels possible.

Additionally, a field emission beam is very energetic, and when directed at a metal target it can generate X-rays [82]. Before nanotubes, field emission sources lacked the current densities necessary to produce high flux X-ray sources for medical imaging or scientific equipment. As a result, X-ray equipment has depended on power-hungry, water-cooled, thermal electron sources. The advent of nanotube-based X-ray sources allows low weight, low power, portable devices, with the added advantage of higher spatial resolution and longer lifetimes compared to thermal sources [82]. These devices are currently being developed for multiple applications including biomedical scanning, airport security, and space exploration, as depicted in Fig. 14.

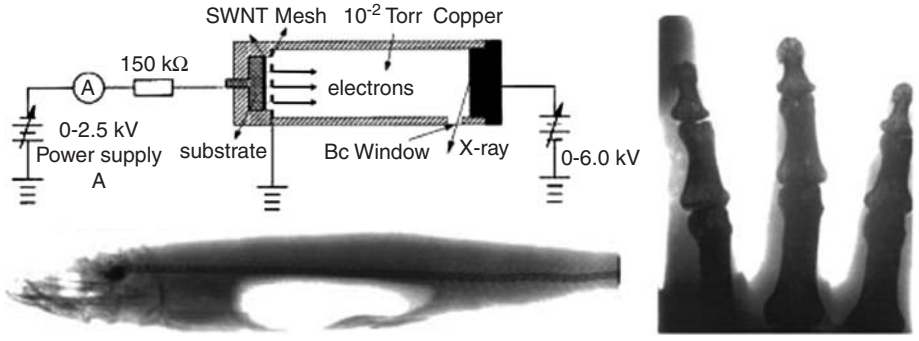

Fig. 14. A SWNT cathode is a very effective field emitter, with turn-on fields as low as 1 V/μm. The emitted electron beam can be used to light a phosphor or, as shown here, to generate X-rays medical imaging. Adapted from Yue et al. [82].

5.3. Chemical and Biological Sensors

Chemical and biological sensing constitute a broad market fragmented into many niches and served by a wide variety of transduction mechanisms – optical, electrochemical, mechanical, and electronic. Electronic sensors have generally competed poorly because of the difficulty of interfacing solid-state circuits with chemically specific functional molecules, and doing so without inducing temperature, humidity, and temporal variabilities.

In principle, SWNTs are ideal for electronic chemical sensors. Charge carriers are exclusively confined to the conductor's surface and the measured resistance can be sensitive to individual scattering sites. Even though applications requiring large numbers of identical FETs remain out of reach for SWNT electronics, a chemical sensor demands only a few individual circuits. Put another way, a chemical sensor can exploit one of the biggest weaknesses of SWNT circuits, namely their sensitivity to chemical perturbations. Nevertheless, the very possibility of chemical sensitivity was not appreciated in the early years of SWNT research. Attempts to intentionally dope individual SWNTs led researchers to uncover unexpected sensitivities to air exposure and reevaluate the p-type behavior of SWNT FETs [36]. Subsequent experiments found sensitivities spanning from reagents like NH_3 and NO_2 [40] to inert gases [83].

The field of chemical sensing continues to be unique among the electronic applications described here because it remains poorly understood on a fundamental level. No single explanation can account for all of the experimental evidence of chemical sensitivity in SWNT circuits. Active hypotheses include chemical doping of SWNTs by charge transfer, electrostatic doping via charge transfer to the supporting substrate, modulation of interfacial (Schottky) barriers due to adsorption on the metal electrodes, chemical modification of defect sites, mechanical impingement and deformation of the SWNT structure, and simple van der Waals interactions.

Nevertheless, the development of SWNT chemical sensors is progressing remarkably quickly considering that so little has been confirmed regarding the transduction mechanisms. Experimentalists have confirmed the effect, tailored its usefulness, and sensor products are now commercially available. Prototype sensors exist which can test for dilute toxic gases, hydrogen gas leaks, traces of explosives, and specific analytes in medical patients' breath (Fig. 15). By extending the principle to SWNT devices coated with proteins or antibodies, simple biochemical sensors have also been demonstrated [84]. Similar progress with a variety of noncarbon nanowires provide researchers significant latitude to choose an appropriate surface chemistry for a particular analyte. The carbon SWNT, however, may provide an optimum starting point for leveraging organic chemistry. Direct linkages of carbon SWNT circuits into biomolecular processes is a new research opportunity which is only beginning to be explored, and the field is likely to grow rapidly in coming years. The concept captures the broad premise of nanotechnology and suggests that the highest impact applications of SWNT electronics may result from innovation at the boundaries between solid-state electronics, chemistry, and life sciences.

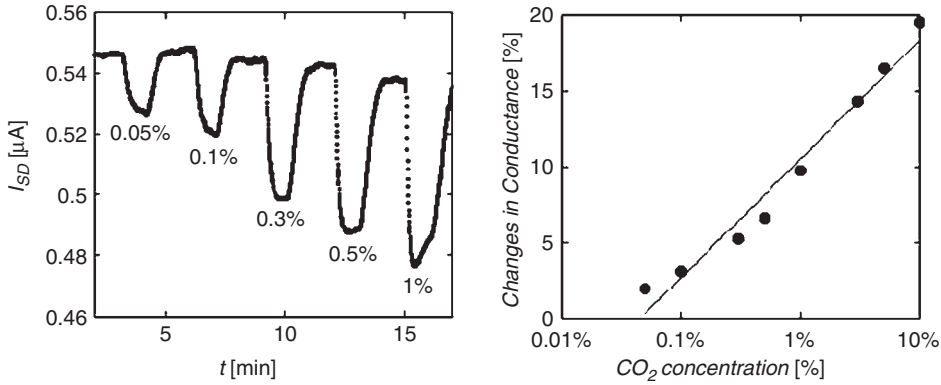

Fig. 15. The chemical sensitivity of SWNT FETs may be directed toward different analytes by coating or chemically functionalizing the devices in different ways. Using this approach, sensors selective to various gases and liquids have been demonstrated. Here, a starch-based polymer coating makes an n-type SWNT device sensitive to different concentrations of CO_2 gas. The measurement at left is performed under fixed bias conditions ($V_g = +6$, $V_{SD} = 0.2\,V$). Similar devices are under development for capnography, the monitoring of patient respiration, in which the desired dynamic range is the 0–10% CO_2 range. Adapted from Star et al. [88].

NOTES

1. The two bands derive from the π states of sp^2-bonded carbon. Two π states, one occupied and one unoccupied, result from having two atoms per unit cell.
2. An exception occurs when the nanotube is sufficiently small that curvature-induced strain modifies the electronic states. For nanotube diameters of 1.0 nm and larger, these effects can generally be ignored, but smaller nanotubes or nanotubes with mechanical kinks will exhibit rehybridized bonds due to curvature effects.
3. Solutions such as the double-gated FET and finned-channel FET are enabling current performance increases in CMOS devices, but at the cost of complexity.
4. Graphite crystals invariably incorporate line and point defects, which account for almost all of the *c*-axis thermal and electrical conductivity, as well as the sample-to-sample variation in these properties.

REFERENCES

[1] A. Oberlin, M. Endo and T. Koyama, Filamentous growth of carbon through benzene compounds, *J. Crystal Growth* **32**, 335 (1976).
[2] M. Endo, *Chem. Tech.* **18**, 568 (1988).
[3] S. Iijima, Helical microtubules of graphitic carbon, *Nature* **354**, 56 (1991).
[4] R. Saito, G. Dresselhaus and M.S. Dresselhaus, Magnetic energy bands of carbon nanotubes, *Phys. Rev. B* **50**, 14698 (1994).
[5] N. Hamada, S. Sawada and A. Oshiyama, New one-dimensional conductors: graphitic microtubules, *Phys. Rev. Lett.* **68**, 1579 (1992).

[6] L. Langer, L. Stockman, J.P. Heremans et al., Electrical resistance of a carbon nanotube bundle, *J. Mater. Res.* **9**, 927 (1994).
[7] A. Thess, R. Lee, P. Nikolaev et al., Crystalline ropes of metallic carbon nanotubes, *Science* **273**, 483 (1996).
[8] B.T. Kelly, *Physics of Graphite* (Applied Science, London, 1981).
[9] K.S. Novoselov, A.K. Geim, S.V. Morozov et al., Electric field effect in atomically thin carbon films, *Science* **306**, 666 (2004).
[10] P. Delaney, H.J. Choi, J. Ihm, S.G. Louie and M.L. Cohen, Broken symmetry and pseudogaps in ropes of carbon nanotubes, *Nature* **391**, 466 (1998).
[11] Y. Imry and R. Landaur, Conductance viewed as transmission, *Rev. Mod. Phys.* **71**, S306 (1999).
[12] S. Datta, *Electronic Transport in Mesoscopic Systems* (Cambridge University Press, Cambridge, 1995).
[13] P.L. McEuen, M. Bockrath, D.H. Cobden, Y.G. Yoon and S.G. Louie, Disorder, pseudospins, and backscattering in carbon nanotubes, *Phys. Rev. Lett.* **83**, 5098 (1999).
[14] S.D. Li, Z. Yu, C. Rutherglen and P.J. Burke, Electrical properties of 0.4 cm long single-walled carbon nanotubes,, *Nano Lett.* **4**, 2003 (2004).
[15] B.J. vanWees, H. van Houten, C.W.J. Beenakker et al., Quantized conductance of point contacts in a two-dimensional electron gas, *Phys. Rev. Lett.* **60**, 848 (1988).
[16] Z. Yao, C.L. Kane and C. Dekker, High-field electrical transport in single-wall carbon nanotubes, *Phys. Rev. Lett.* **84**, 2941 (2000).
[17] A. Javey, J. Guo, M. Paulsson et al., High-field quasiballistic transport in short carbon nanotubes, *Phys. Rev. Lett.* **92** (2004).
[18] J.Y. Park, S. Rosenblatt, Y. Yaish et al., Electron-phonon scattering in metallic single-walled carbon nanotubes, *Nano Lett.* **4**, 517 (2004).
[19] D. Mann, A. Javey, J. Kong, Q. Wang and H.J. Dai, Ballistic transport in metallic nanotubes with reliable Pd ohmic contacts, *Nano Lett.* **3**, 1541 (2003).
[20] S.J. Tans and C. Dekker, Molecular transistors: Potential modulations along carbon nanotubes, *Nature* **404**, 834 (2000).
[21] L.C. Venema, J.W.G. Wildoer, J.W. Janssen et al., Imaging electron wave functions of quantized energy levels in carbon nanotubes, *Science* **283**, 52 (1999).
[22] W. Liang, M. Bockrath, D. Bozovic et al., Fabry–Perot interference in a nanotube electron waveguide, *Nature* **411**, 665 (2001).
[23] P. Avouris, M. Radosavljevic and S.J. Wind, in *Applied Physics of Carbon Nanotubes*, edited by S.V. Rotkin and S. Subramoney (Springer, Berlin, 2005).
[24] J. Chen, C. Klinke, A. Afzali and P. Avouris, Self-aligned carbon nanotube transistors with charge transfer doping, *Appl. Phys. Lett.* **86** (2005).
[25] S. Heinze, M. Radosavljevic, J. Tersoff and P. Avouris, Unexpected scaling of the performance of carbon nanotube Schottky-barrier transistors, *Phys. Rev. B* **68** (2003).
[26] S. Heinze, J. Tersoff, R. Martel et al., Carbon nanotubes as Schottky barrier transistors, *Phys. Rev. Lett.* **89** (2002).
[27] S. Heinze, J. Tersoff and P. Avouris, in *Introducing Molecular Electronics*, vol. 680, edited by G. Cuniberti (Springer, Berlin, 2005).
[28] Z. Chen, J. Appenzeller, J. Knoch et al., The role of metal-nanotube contact in the performance of carbon nanotube field-effect transistors, *Nano Lett.* **5**, 1497 (2005).
[29] A. Javey, J. Guo, D.B. Farmer et al., Carbon nanotube field-effect transistors with integrated ohmic contacts and high-k gate dielectrics, *Nano Lett.* **4**, 447 (2004).
[30] V. Perebeinos, J. Tersoff and P. Avouris, Electron–phonon interaction and transport in semiconducting carbon nanotubes, *Phys. Rev. Lett.* **94**, 086802 (2005).
[31] A. Javey, P.F. Qi, Q. Wang and H.J. Dai, Ten- to 50-nm-long quasi-ballistic carbon nanotube devices obtained without complex lithography, *Proc. Natl. Acad. Sci. U. S. A.* **101**, 13408 (2004).
[32] Y.M. Lin, J. Appenzeller, J. Knoch and P. Avouris, High-performance carbon nanotube field-effect transistor with tunable polaritie, *IEEE Trans. Nanotech.* **4**, 481 (2005).

[33] S.J. Tans, A.R.M. Verschueren and C. Dekker, Room-temperature transistor based on a single carbon nanotube, *Nature* **393**, 49 (1998).
[34] R. Martel, T. Schmidt, H.R. Shea, T. Hertel and P. Avouris, Single- and multi-wall carbon nanotube field-effect transistors, *Appl. Phys. Lett.* **73**, 2447 (1998).
[35] M. Bockrath, J. Hone, A. Zettl et al., Chemical doping of individual semiconducting carbon-nanotube ropes, *Phys. Rev. B* **61**, 10606 (2000).
[36] P.G. Collins, K. Bradley, M. Ishigami and A. Zettl, Extreme oxygen sensitivity of electronic properties of carbon nanotubes, *Science* **287**, 1801 (2000).
[37] K. Bradley, S.H. Jhi, P.G. Collins et al., Is the intrinsic thermoelectric power of carbon nanotubes positive? *Phys. Rev. Lett.* **85**, 4361 (2000).
[38] R. Martel, V. Derycke, C. Lavoie et al., Ambipolar electrical transport in semiconducting single-wall carbon nanotubes, *Phys. Rev. Lett.* **87**, 6805 (2001).
[39] V. Derycke, R. Martel, J. Appenzeller and P. Avouris, Controlling doping and carrier injection in carbon nanotube transistors, *Appl. Phys. Lett.* **80**, 2773 (2002).
[40] J. Kong, N.R. Franklin, C.W. Zhou et al., Nanotube molecular wires as chemical sensors, *Science* **287**, 622 (2000).
[41] T. Ando, Excitons in carbon nanotubes, *J. Phys. Soc. Jpn.* **66**, 1066 (1997).
[42] H. Sakai, H. Suzuura and T. Ando, Effective-mass theory of electron correlations in band structure of semiconducting carbon nanotubes, *J. Phys. Soc. Jpn.* **72**, 1698 (2003).
[43] C.D. Spataru, S. Ismail-Beigi, L.X. Benedict and S.G. Louie, Excitonic effects and optical spectra of single-walled carbon nanotubes, *Phys. Rev. Lett.* **92** (2004).
[44] R. Egger, Luttinger liquid behavior in multiwall carbon nanotubes, *Phys. Rev. Lett.* **83**, 5547 (1999).
[45] C. Kane, L. Balents and M.P.A. Fisher, Coulomb interactions and mesoscopic effects in carbon nanotubes, *Phys. Rev. Lett.* **79**, 5086 (1997).
[46] M. Bockrath, D.H. Cobden, J. Lu et al., Luttinger-liquid behaviour in carbon nanotubes, *Nature* **397**, 598 (1999).
[47] H.W.C. Postma, M. de Jonge, Z. Yao and C. Dekker, Electrical transport through carbon nanotube junctions created by mechanical manipulation, *Phys. Rev. B* **62**, 10653 (2000).
[48] H. Ishii, H. Kataura, H. Shiozawa et al., Direct observation of Tomonaga-Luttinger-liquid state in carbon nanotubes at low temperatures, *Nature* **426**, 540 (2003).
[49] R. Loudon, Infinite binding energy of a truly 1d exciton, *Am. J. Phys.* **27**, 649 (1959).
[50] V. Perebeinos, J. Tersoff and P. Avouris, Scaling of excitons in carbon nanotubes, *Phys. Rev. Lett.* **92**, 257402 (2004).
[51] F. Wang, G. Dukovic, L.E. Brus and T.F. Heinz, The optical resonances in carbon nanotubes arise from excitons, *Science* **308**, 838 (2005).
[52] J.A. Misewich, R. Martel, P. Avouris et al., Electrically induced optical emission from a carbon nanotube FET, *Science* **300**, 783 (2003).
[53] M. Freitag, J. Chen, J. Tersoff et al., Mobile ambipolar domain in carbon-nanotube infrared emitters, *Phys. Rev. Lett.* **93**, 076803 (2004).
[54] M. Freitag, Y. Martin, J.A. Misewich, R. Martel and P. Avouris, Photoconductivity of single carbon nanotubes, *Nano Lett.* **3**, 1067 (2003).
[55] T.W. Odom, H. Jin-Lin, P. Kim and C.M. Lieber, Atomic structure and electronic properties of single-walled carbon nanotubes, *Nature* **391**, 62 (1998).
[56] J.W.G. Wildoer, L.C. Venema, A.G. Rinzler, R.E. Smalley and C. Dekker, Electronic structure of atomically resolved carbon nanotubes, *Nature* **391**, 59 (1998).
[57] R.H. Baughman, C.X. Cui, A.A. Zakhidov et al., Carbon nanotube actuators, *Science* **284**, 1340 (1999).
[58] K.H. An, W.S. Kim, Y.S. Park et al., Supercapacitors using single-walled carbon nanotube electrodes, *Adv. Mater.* **13**, 497 (2001).
[59] E.S. Snow, J.P. Novak, P.M. Campbell and D. Park, Random networks of carbon nanotubes as an electronic material, *App. Phys. Lett.* **82**, 2145 (2003).
[60] E.S. Snow, J.P. Novak, M.D. Lay et al., Carbon nanotube networks: Nanomaterial for macroelectronic applications, *J. Vac. Sci. Technol., B* **22**, 1990 (2004).
[61] K. Bradley, J.C.P. Gabriel and G. Gruner, Flexible nanotube electronics, *Nano Lett.* **3**, 1353 (2003).

[62] E. Artukovic, M. Kaempgen, D.S. Hecht, S. Roth and G. Gruner, Transparent and flexible carbon nanotube transistors, *Nano Lett.* **5**, 757 (2005).
[63] P.C. Collins, M.S. Arnold and P. Avouris, Engineering carbon nanotubes and nanotube circuits using electrical breakdown, *Science* **292**, 706 (2001).
[64] M. Kruger, I. Widmer, T. Nussbaumer, M. Buitelaa and C. Schonenberger, Sensitivity of single multiwalled carbon nanotubes to the environment, *New J. Phys.* **5** (2003).
[65] A. Bachtold, C. Strunk, J.P. Salvetat et al., Aharonov–Bohm oscillations in carbon nanotubes, *Nature* **397**, 673 (1999).
[66] A. Bachtold, M. de Jonge, K. Grove-Rasmussen et al., Suppression of tunneling into multiwall carbon nanotubes, *Phys. Rev. Lett.* **87**, 6801 (2001).
[67] P.G. Collins and P. Avouris, Multishell conduction in multiwalled carbon nanotubes, *Appl. Phys. A: Mater. Sci. Process.* **74**, 329 (2002).
[68] S. Frank, P. Poncharal, Z.L. Wang and W.A. de Heer, Carbon nanotube quantum resistors, *Science* **280**, 1744 (1998).
[69] P. Poncharal, C. Berger, Y. Zi, Z.L. Wang and W.A. de Heer, Room temperature ballistic conduction in carbon nanotubes, *J. Phys. Chem. B* **106**, 12104 (2002).
[70] T.W. Ebbesen, H.J. Lezec, H. Hiura et al., Electrical conductivity of individual carbon nanotubes, *Nature* **382**, 54 (1996).
[71] J. Cumings, W. Mickelson and A. Zettl, Simplified synthesis of double-wall carbon nanotubes, *Solid State Commun.* **126**, 359 (2003).
[72] S. Banerjee, T. Hemraj-Benny and S.S. Wong, Covalent surface chemistry of single-walled carbon nanotubes, *Adv. Mater.* **17**, 17 (2005).
[73] M.J. Biercuk, M.C. Llaguno, M. Radosavljevic et al., Carbon nanotube composites for thermal management, *Appl. Phys. Lett.* **80**, 2767 (2002).
[74] R.H. Baughman, A.A. Zakhidov and W.A. de Heer, Carbon nanotubes-the route toward applications, *Science* **297**, 787 (2002).
[75] C.S. Du, J. Yeh and N. Pan, High power density supercapacitors using locally aligned carbon nanotube electrodes, *Nanotechnology* **16**, 350 (2005).
[76] G.T. Wu, C.S. Wang, X.B. Zhang et al., Structure and lithium insertion properties of carbon nanotubes, *J. Electrochem. Soc.* **146**, 1696 (1999).
[77] P. Kim and C.M. Lieber, Nanotube nanotweezers, *Science* **286**, 2148 (1999).
[78] M.M.J. Treacy, T.W. Ebbesen and J.M. Gibson, Exceptionally high Young's modulus observed for individual carbon nanotubes, *Nature* **381**, 678 (1996).
[79] P. Poncharal, Z.L. Wang, D. Ugarte and W.A. de Heer, Electrostatic deflections and electromechanical resonances of carbon nanotubes, *Science* **283**, 1513 (1999).
[80] T. Rueckes, K. Kim, E. Joselevich et al., Carbon nanotube-based nonvolatile random access memory for molecular computing, *Science* **289**, 94 (2000).
[81] J.M. Bonard, H. Kind, T. Stockli and L.A. Nilsson, Field emission from carbon nanotubes: the first five years, *Solid-State Electron.* **45**, 893 (2001).
[82] G.Z. Yue, Q. Qiu, B. Gao et al., Generation of continuous and pulsed diagnostic imaging X-ray radiation using a carbon-nanotube-based field-emission cathode, *Appl. Phys. Lett.* **81**, 355 (2002).
[83] G.U. Sumanasekera, C.K.W. Adu, S. Fang and P.C. Eklund, Effects of gas adsorption and collisions on electrical transport in single-walled carbon nanotubes, *Phys. Rev. Lett.* **85**, 1096 (2000).
[84] A. Star, J.C.P. Gabriel, K. Bradley and G. Gruner, Electronic detection of specific protein binding using nanotube FET devices, *Nano Lett.* **3**, 459 (2003).
[85] M.S. Dresselhaus and P. Avouris, in *Carbon Nanotubes*, vol. 80, edited by M.S. Dresselhaus and P. Avouris (Springer-Verlag, Berlin, 2001), pp. 1–9.
[86] Y.-M. Lin, J. Appenzeller, Z.H. Chen et al., High-performance dual-gate carbon nanotube FETs with 40-nm gate length, *IEEE Electron Device Lett.* **26**, 823 (2005).
[87] X.H. Qiu, M. Freitag, V. Perebeinos and P. Avouris, Photoconductivity spectra of single-carbon nanotubes: Implications on the nature of their excited states, *Nano Lett.* **5**, 749 (2005).
[88] A. Star, T.R. Han, V. Joshi, J.C.P. Gabriel and G. Gruner, Nanoelectronic carbon dioxide sensors, *Adv. Mater.* **16**, 2049 (2004).

This page intentionally left blank

Chapter 4
RAMAN SPECTROSCOPY OF CARBON NANOTUBES

M. S. Dresselhaus, G. Dresselhaus, R. Saito and A. Jorio

1. INTRODUCTION

Raman spectroscopy has been widely used by most carbon nanotube researchers to characterize their samples broadly, from their basic synthesis and purification processes all the way to their ultimate use in nanotube modifications and device applications. The broad interest from the carbon nanotube research community in Raman spectroscopy comes from the capability of this technique to easily and nondestructively characterize carbon nanotube samples with respect to diameter and chirality distribution, population of specific (n, m) species in a sample, sample purity, doping, functionalization, as well as temperature, pressure and strain effects. To achieve such a characterization capability, research has focused on understanding the basic physical properties of carbon nanotubes, primarily by advancing our knowledge of their electronic, vibrational and geometric structure, and of the interrelation between these properties.

The unique optical and spectroscopic properties observed in single wall carbon nanotubes (SWNTs) are largely due to the one-dimensional (1D) confinement of electronic and phonon states and due to the so-called resonance Raman process. Because of this 1D confinement, the resonance effect is both strongly enhanced relative to graphite and highly selective of the SWNT geometric structure, namely its diameter and chirality. Thus Raman spectroscopy has become not only a spectroscopic tool, but also has become a structural characterization tool for SWNTs. In this article we show how carbon nanotubes are a unique system for the study of the rich Raman spectra of 1D systems, and at the same time Raman spectroscopy has provided an exceedingly powerful tool for the detailed characterization of SWNTs.

Raman scattering refers to the inelastic scattering of light in molecules and solids. By exciting (or absorbing) an elementary excitation of the material (usually a phonon, the quantum of lattice vibration), the scattered light loses (or gains) the

Contemporary Concepts of Condensed Matter Science
Carbon Nanotubes: Quantum Cylinders of Graphene

ISSN: 1572-0934/doi:10.1016/S1572-0934(08)00004-8

characteristic energy of the excitation ΔE relative to the energy of the incident light (E_{laser}). Raman spectra refer to the spectral intensity of the scattered light as a function of energy shift ΔE, usually measured in units of $\text{cm}^{-1} = (1/8065)\,\text{eV}$. These spectra are observed by using a laser, a monochromator, a spectrometer, and a detector. A monochromator (or some optical filter) is needed for removing the strong elastically scattered Rayleigh light, appearing near $\Delta E = 0$.

Fig. 1a gives a general view of the Raman spectra from a typical SWNT bundle sample taken with different laser excitation lines (E_{laser}) and Fig. 1b shows spectra taken at the individual nanotube level. There are two dominant Raman signatures that distinguish a SWNT from other forms of carbon. The first relates to the low frequency feature, usually in the range 100–300 cm^{-1}, arising from scattering by the radial breathing modes (RBM) which correspond to symmetric in-phase

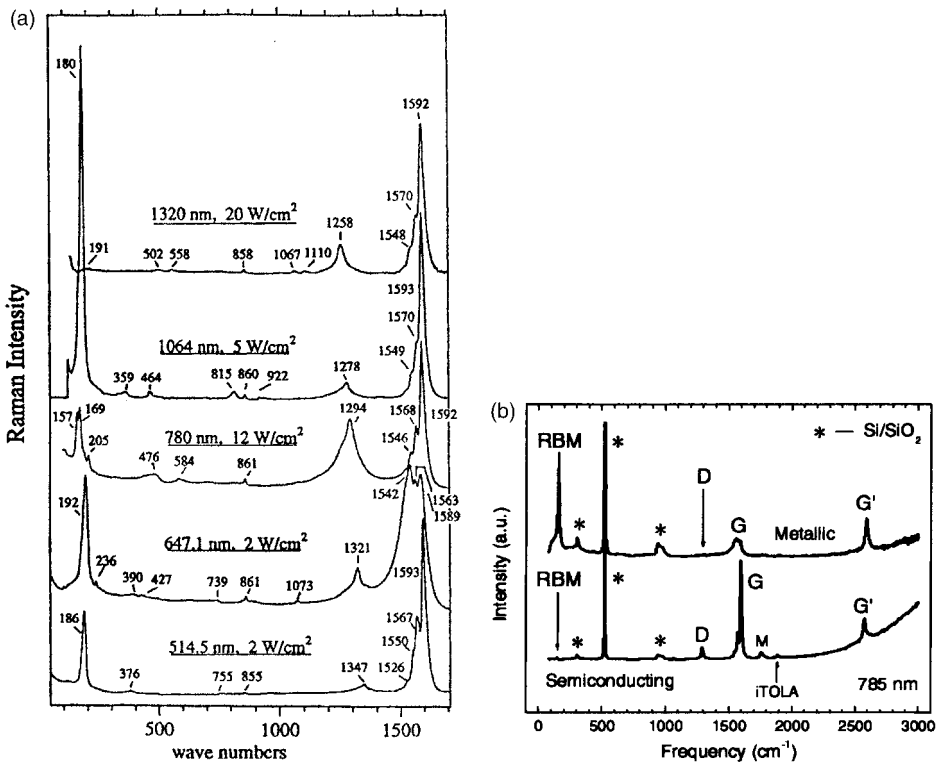

Fig. 1. (a) Room temperature Raman spectra from SWNT bundles grown by the laser vaporization method, excited at five different laser energies (wavelengths) [1], as indicated along with the power density and the vibrational frequencies (in cm^{-1}). (b) Raman spectra from a metallic (top) and a semiconducting (bottom) SWNT at the single nanotube level. The dominant spectral features are indicated and are discussed in this chapter. The Raman features denoted by "*" come from the Si/SiO_2 substrate [2].

displacements of all the carbon atoms in the SWNT in the radial direction. The second signature relates to the multiple higher frequency features (around 1500–1600 cm^{-1}) associated with the tangential (*G*-band) vibrational modes. Neither the RBM feature nor the *multiple* *G*-band features are observed in any other sp^2 bonded carbon material, which shows a characteristic *single* *G*-band (Lorentzian shape) Raman peak at 1582 cm^{-1} (discussed in Section 3.3.2). These two first-order Raman features (the RBM and the multi *G*-band) are, therefore, the spectral signatures of SWNTs and have been used to characterize nanotube samples from their earliest stage of identification [3,4].

From an historical perspective, the use of Raman spectroscopy to characterize carbon materials [5] generally motivated researchers to apply this technique also to SWNTs shortly after the early synthesis of SWNTs in 1993 [6,7]. Even though only $\sim$1% of the carbonaceous material in the sample was estimated to be due to SWNTs [3], a unique Raman spectrum was observed, different from any other previously observed spectrum for a carbon material, thereby motivating further development of this noninvasive characterization technique for SWNTs.

The power of this technique to study and characterize carbon nanotube samples and nanotube properties became evident in 1997, when the process was shown to be highly selective not only of SWNTs embedded in a sample containing other carbonaceous species, but of specific (n, m) SWNTs due to the resonance Raman effect [1]. Since the resonance Raman intensity depends on the density of electronic states (DOS) available for the optical transitions, and this resonance property is especially important for 1D systems where quantum confinement effects give rise to singularities in the DOS. Fig. 1a shows that when E_{laser} is varied, the Raman spectra change dramatically, because different laser excitation energies are in resonance with different SWNTs depending on their tube diameters d_t and chiral angles θ. Resonance Raman spectroscopy (RRS) has thus become a very powerful tool to study the vibrational and electronic properties of SWNTs. The next breakthrough came in 2001 with the observation of the Raman spectrum from one isolated SWNT sitting on a SiO_2 substrate [2] (see Fig. 1b), greatly advancing our understanding of Raman spectroscopy in 1D materials generally, since SWNT properties could now be measured in great detail at the single nanotube level from an object only $\sim$1 nm in diameter with a well-defined geometrical structure [1].

To understand the very special Raman spectra of carbon nanotubes, the physics we learn from SWNTs, and how to use this technique to characterize SWNT samples [8,9], some basic concepts of the Raman scattering effect are introduced in Section 2. This is followed by a discussion of how resonance Raman scattering has been used to study and characterize (Section 3) carbon nanotubes.

2. BASIC CONCEPTS OF RESONANCE RAMAN SCATTERING

In this section the constituent optical processes in Raman scattering are introduced, and resonant processes are distinguished from nonresonant processes. Resonance

with both the incident and scattered photon are considered, along with first-order and higher-order scattering processes for phonon emission (Stokes process) and phonon absorption (anti-Stokes process).

A Raman scattering event consists of three basic optical processes: (1) photon absorption to excite an exciton (an electron bound to the hole that is simultaneously created by the photon), (2) phonon emission from an exciton, and (3) finally photon emission by the exciton. We measure the emitted photons as a Raman spectrum in which the Raman scattering intensity is plotted vs. energy shift ΔE (see Section 1 and Fig. 1). In light scattering, the photon absorption process generally occurs even though the energy separation between the ground and excited states is not equal to the photon energy, in which case we call the transition a *virtual* or *nonresonant* transition.

It is easy to understand a nonresonant transition for a mechanical system, consisting of a spring and a ball. Even though we force this system to vibrate with a frequency which is not a natural eigen-frequency of the system, the vibration will still have some vibrational amplitude. When the vibrational frequency is close to an eigen-frequency of the system, the vibrational amplitude becomes singularly large. This enhancement in intensity is identified with a resonance phenomenon.

A similar effect occurs for the Raman process, and it is called RRS. Here the scattered amplitude becomes very large when E_{laser} is close to the transition energy for light absorption or emission (E_{ii}). There are two possible conditions for resonance, and these are called, the incident and scattered resonance conditions in which either the incident or scattered photons, respectively, have the same energy as the energy level separation of the system. For photon absorption, where the incident light resonance condition is:

$$E_{\text{laser}} = E_{ii} \qquad \text{(incident light resonance)} \tag{1}$$

all Raman features will be resonantly enhanced. However, for the scattered light resonance condition for the creation of a phonon with frequency ω_i,

$$E_{\text{laser}} = E_{ii} + \hbar\omega_i \qquad \text{(Stokes scattered light resonance)} \tag{2}$$

the resonance condition depends on the phonon energy $\hbar\omega_i$. Inelastic scattering of light is also possible by absorbing a phonon, which is called anti-Stokes Raman scattering. Anti-Stokes Raman spectra can be seen relative to $\Delta E = 0$ on the opposite side of the spectrum for phonon emission (Stokes Raman spectra). In order to absorb a phonon, the phonon should be present in the Bose–Einstein distribution at thermal equilibrium. Thus anti-Stokes Raman spectra will have a very low intensity for high energy phonons and at low temperatures. The resonance condition for the anti-Stokes Raman spectra for the incident light resonance condition is the same as that of the Stokes spectra. As for the scattered light resonance, the condition is given by

$$E_{\text{laser}} = E_{ii} - \hbar\omega_i \qquad \text{(anti-Stokes scattered light resonance)} \tag{3}$$

Thus by comparing the Stokes with the anti-Stokes spectra, we can know whether the resonance condition is for the incident resonance or scattered resonance.

The number of emitted phonons before relaxation of the lattice can be one, two, and so on, which we call, respectively, one-phonon, two-phonon, and multi-phonon Raman processes. The order of a scattering event is defined as its number in the sequence of all the scattering events, including both phonon inelastic scattering and elastic scattering by an imperfection (such as a defect or edge) of the crystal. The lowest order process is the first-order Raman scattering process which involves one-phonon emission, such as the RBM, or the *G*-band feature shown in Fig. 1 for SWNTs. A scattering event with only elastic scattering, i.e., change of photon direction but no frequency shift, corresponds to Rayleigh scattering.

Finally, incident and scattered light polarization is an important issue for Raman scattering, because optical absorption and emission usually exhibit a polarization dependence. The so-called selection rules, which depend on light polarization, tell us whether or not a given set of electronic levels that can be coupled by light.

3. RESONANCE RAMAN SPECTROSCOPY OF CARBON NANOTUBES

In this section we focus on the various features appearing in the resonance Raman spectra of SWNTs. The spectra observed from SWNT bundle samples and at the single nanotube level are discussed, focusing on the complementary information provided by ensembles of SWNTs and by a single nanotube.

3.1. 1D van Hove Singularities and the Kataura Plot

In the case of a SWNT, the energy separation which is relevant to RRS corresponds to the transition energies which appear as singularities [called van Hove singularities (vHSs)] in the electronic density of states (DOS). These singularities in the DOS (see Fig. 2) come from the energy maxima or minima of 1D energy subbands of an individual SWNT. The electronic structure of an (n, m) SWNT has many 1D energy subbands, and therefore many vHSs. However, despite the large number of vHSs, only a small number of electronic levels can be connected by light due to the symmetry selection rules. Electrons (and phonons) in carbon nanotubes are characterized by their 1D wave vectors (k for electrons and q for phonons) and by their symmetries, that relate to nothing else than the number of nodes for their wave functions around the circumferential direction. The totally symmetric A states for electrons (and phonons) have no nodes, while the various harmonics usually exhibit double degenerate symmetries E_μ, so that for levels labeled by $\mu = 1, 2, 3, \ldots$ the eigenvectors have 2, 4, 6, … nodes [10,11]. It is known that light can be strongly absorbed when the polarization of the electric field is parallel to the nanotube axis. In this case, valence and conduction electrons having the same symmetry ($E_\mu^v \rightarrow E_\mu^c$) are coupled by light. On the other hand, when the polarization vector is

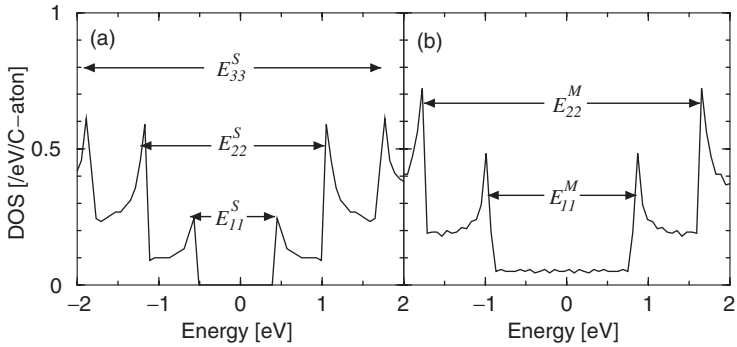

Fig. 2. Electronic density of states for (a) a semiconducting SWNT and (b) a metallic SWNT. The Fermi energy (E_F) is located at $E = 0$. An optical transition is possible between vHS peaks in the valence and conduction bands. Energy separations between two vHS peaks are labeled from smallest to largest for semiconducting tubes by E_{11}^S, E_{22}^S, E_{33}^S, …, and for metallic tubes by E_{11}^M, E_{22}^M, … .

perpendicular to the nanotube axis, the absorption vanishes [12,13] in accordance with polarization selection rules which further tell us that the resonance energies for perpendicular polarization of the light couple $E_\mu^v \rightarrow E_{\mu\pm1}^c$.

Therefore, because of the selection rules for optical transitions [12,13], optical transitions occur between two peaks which are approximately symmetrically placed with respect to the Fermi energy E_F, as shown in Fig. 2. These transitions are labeled E_{11}, E_{22}, E_{33} and so on, according to how close in energy they are to E_F. Like a fingerprint, each carbon nanotube labeled by (n, m) has different E_{ii} values. We further note in Fig. 2, that the DOS at E_F for metallic tubes is nonzero and constant between the highest valence band vHS and the lowest conduction band vHS. The actual transition energies E_{ii} are excitonic in nature because the excited electron is bound to the hole that is left behind in the excitation process, giving rise to what is called a bound electron–hole pair or an exciton. The actual E_{ii} are further perturbed by electron–electron repulsion effects and it is these perturbed excitonic transition energies E_{ii} that are observed experimentally and calculated theoretically. These electron–hole and electron–electron interactions are specially important in 1D systems, since the electrons and holes are highly confined in 1D space.

To analyze the resonance Raman spectra of SWNTs, it is useful to have a plot of these resonant transition energies E_{ii} as a function of tube diameter d_t for all (n, m) SWNTs, and we call such a plot a Kataura plot (see Fig. 3). This plot was first proposed in 1999 by H. Kataura [14], and subsequent optical and Raman spectroscopic measurements had a large influence on the detailed development of this plot. From the Kataura plot in Fig. 3, we see that the resonant transition energies E_{ii} are approximately inversely proportional to d_t, and each E_{ii} band has some width due to the chirality dependence of E_{ii} [15]. For a given d_t, the sequence of E_{ii} is in the order E_{11}^S, E_{22}^S, E_{11}^M, E_{33}^S, etc. starting from the lowest energy. One typical use of a Kataura plot would be to tell a researcher that for a sample with a diameter

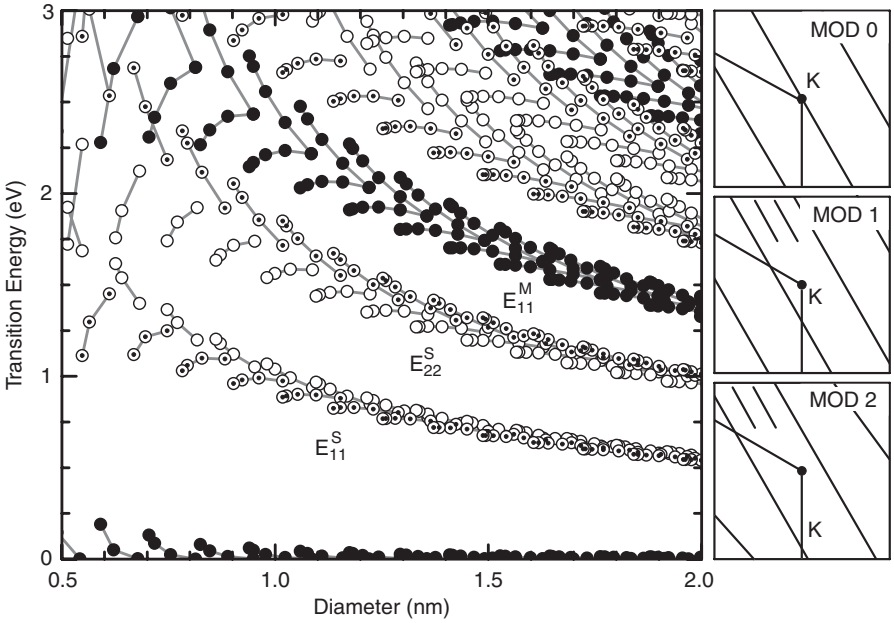

Fig. 3. Plot of the transition energies E_{ii} vs. d_t for all (n, m) values occurring for $0.5 < d_t < 2.0$ nm (Kataura plot) where S and M denote semiconducting, and metallic nanotubes, respectively. On the right, cutting lines are shown for M tubes (MOD0), and S tubes of two types, MOD1 and MOD2, for open and open-dot circles respectively (see text).

distribution of, for example, $d_t = 1.4 \pm 0.1$ nm, a Raman signal from semiconducting (S) and metallic (M) SWNTs would be expected for $E_{laser} \sim 1.4$ eV (E_{22}^{S}) and 1.9 eV (E_{11}^{M}), respectively. Note that when we rotate the polarization of the light away from parallel to the SWNT axis, the resonance condition obtained for parallel polarization for a given E_{laser} (Fig. 3) will no longer apply [16].

3.2. Family Patterns

SWNTs are metallic when $(n-m)$ or equivalently when $(2n+m)$ is divisible by 3 (MOD0) and are semiconducting otherwise [10,17,18]. This fundamental result can be understood from the diagrams in Fig. 3 to the right of the Kataura plot, where the cutting lines, denoting allowed states for wave vectors in the circumferential direction of SWNTs, are shown to only pass through the K point in the 2D graphene Brillouin zone (BZ) for the case of MOD0, where the K point is the point in reciprocal space of 2D graphite, where the valence and conduction bands cross E_F to form a zero gap semiconductor [10]. For semiconducting SWNTs we distinguish the case where the remainder of the division of $(2n+m)/3$ is 1 or 2 by MOD1 (open circles in Fig. 3) and MOD2 (open-dot circles), respectively. We thus see that the energies E_{ii}^{S} follow a similar pattern (the so-called family behavior), according to the

$2n+m$ value of a SWNT (which labels its family) and whether the SWNT is MOD1 or MOD2 [19,20]. Thus, a (6,5) SWNT would be designated by MOD2 and family $2n+m=17$. Each metallic SWNT has two vHSs in its DOS for each E_{ii}^{M}, except for armchair SWNTs. The occurrence of two vHSs for each E_{ii}^{M} is due to the so-called trigonal warping effect of the electronic structure [15], and the energy separation between the two vHSs for a metallic tube generally increases as the chiral angle decreases. Family patterns are observed in Fig. 3 for both S and M SWNTs. We note that each (n, m) nanotube in the long tube length limit has a unique set of E_{ii} values and can in this sense be considered as a unique molecule. The connection between the resonance Raman spectra and the Kataura plot is further discussed below.

3.3. Raman Spectroscopy for Isolated Individual SWNTs

Because of the strong resonance process in 1D systems, a large enhancement in the Raman signal occurs, allowing the identification of the structure (diameter d_t and chiral angle θ) of individual SWNTs to be made, which in turn allows nanotube properties to be determined as a function of d_t and θ.

3.3.1. The RBM (n, m) Assignment and the Resonance Window

In this subsection we show how measurements at the single nanotube level allow a determination to be made of the d_t and θ nanotube chirality, which is usually denoted in terms of the (n, m) indices of the SWNT [10]. In addition, single nanotube spectroscopy allows measurements to be made of the resonant window of an individual SWNT, if a suitable "tunable" laser source is available.

In the process of measuring the Raman spectra from isolated SWNTs on a Si/SiO_2 substrate using a fixed laser energy E_{laser}, the laser spot is focused on the substrate surface (micro Raman spectroscopy) and is scanned over the sample until the Raman signal from an isolated SWNT is observed. The Raman intensity from SWNTs is usually buried under the noise, except for a few (n, m) SWNTs, which have E_{ii} values within the resonance window of a given E_{laser}. Fig. 4b shows the Raman spectra from three isolated SWNTs in resonance with an excitation laser $E_{laser}=1.58\,eV$, taken from different spots on the Si/SiO_2 substrate shown in Fig. 4a. From knowledge of both the RBM frequency ω_{RBM} and $E_{ii}\sim E_{laser}$, the (n, m) geometrical structure can be defined, making use of the Kataura plot (Fig. 3) and a relation between ω_{RBM} and d_t. The ω_{RBM} is known to depend linearly on the number of carbon atoms around the SWNT circumference, and therefore ω_{RBM} depends on $1/d_t$. In this work [2] the relation used to relate ω_{RBM} to d_t for SWNTs in the diameter range $1.2<d_t<1.8$ nm was found to be $\omega_{RBM}=248/d_t$. This assignment with $\omega_{RBM}=248/d_t\,cm^{-1}$ works well for $d_t>1$ nm. However, for small diameter SWNTs ($d_t<1$ nm), we need to consider in detail the curvature effect of the cylindrical surface of a SWNT on E_{ii} and ω_{RBM}. The Kataura plot itself has been established by making resonance Raman (see Section 3.4) and photoluminescence (PL) [20] measurements on many tubes so that the family patterns in Fig. 3 could be firmly established.

By using a tunable laser, it is also possible to study the resonance window of *one* isolated SWNT, giving the E_{ii} value with a precision better than 5 meV, as shown in

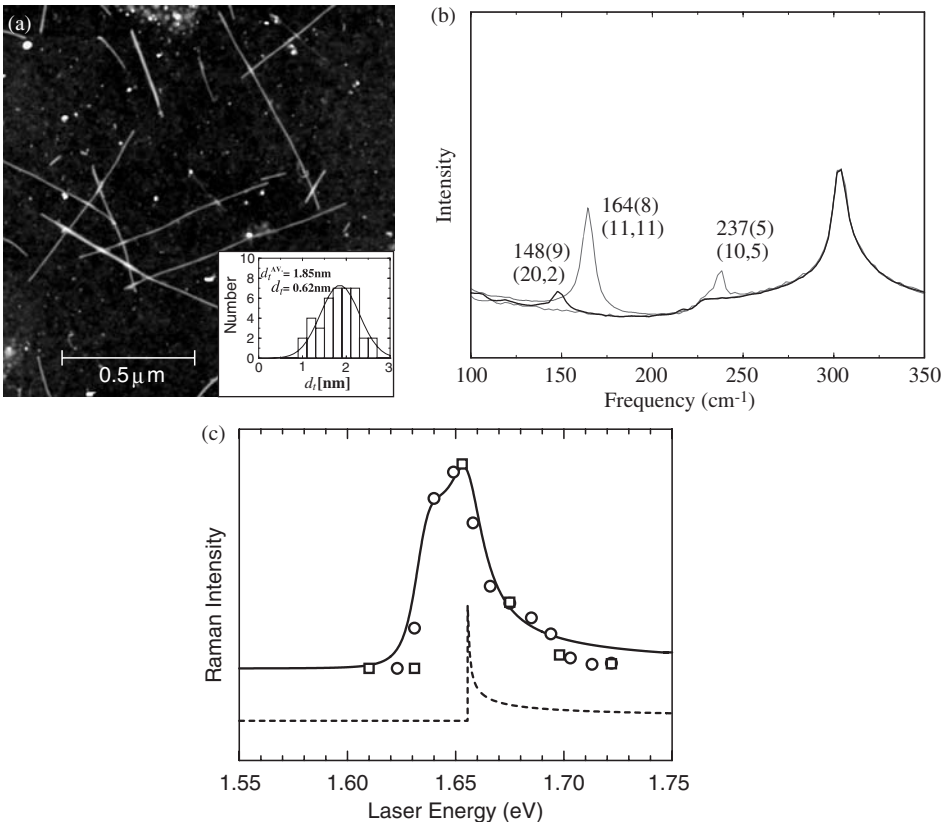

Fig. 4. (a) AFM image of SWNTs on a Si/SiO_2 substrate. The inset shows the SWNT diameter distribution of the sample. (b) Raman spectra from three different spots in (a). The RBM frequencies (widths) and the (n, m) assignment for each resonant SWNT are displayed [2]. The 303 cm^{-1} feature comes from the Si substrate and is used for calibration purposes. (c) Raman intensity vs. E_{laser} for the anti-Stokes RBM feature at the 173.6 cm^{-1} assigned to an isolated (18,0) SWNT on a Si/SiO_2 substrate [21]. The predicted resonant window (solid curve) and the vHS at 1.655 eV (dashed curve) are shown, based on the tight binding model.

Fig. 4c [21]. Here the resonance window for the anti-Stokes process is shown to have a full width at half maximum intensity of only 8 meV and to be asymmetric in lineshape, reflecting the asymmetric lineshape of the van Hove singularity (dotted curve in Fig. 4c). To observe the asymmetry in the resonance window, its linewidth must be small. The appearance of spiky vHS peaks in the DOS is a general effect of quantum confined 1D energy bands, but this effect is enhanced in SWNTs because of their small d_t values.

3.3.2. The G-Band Raman Spectra at the Single Nanotube Level

The *G*-band refers to the in-plane optic phonon modes which are Raman-active in sp^2 graphitic materials. Since graphite is not an ionic material, the longitudinal (LO)

and transverse (TO) optic phonon modes are degenerate at the Γ point (zone center) of the Brillouin Zone (BZ). Because of the curvature of the cylindrical surface of SWNTs, their LO and TO phonon modes are split into higher and lower frequencies, G^+ and G^-, respectively. While the LO frequency ω_{G^+}, for vibrations along the tube axis for semiconducting tubes, is almost independent of d_t, the TO frequency ω_{G^-}, for vibrations in the circumferential direction, is downshifted because of its mode softening due to tube curvature.

RRS at the single nanotube level allows detailed measurements to be made of both diameter and chirality effects and polarization effects, as summarized below. Such detailed studies are not possible for ensemble samples. The difference in the lineshape for the *G*-band for graphite, which consists of a single simple Lorentzian line, and for SWNTs is dramatically shown in Fig. 5a. For both semiconducting and metallic SWNTs, two dominant features are seen in Fig. 5a, corresponding to fully symmetric modes. For semiconducting SWNTs (Fig. 5b) the LO (or G^+) mode has a stronger intensity, and the weaker mode is the TO (or G^-) mode discussed above, with an LO–TO splitting induced by tube curvature effects. This splitting increases as $1/d_t^2$, as shown in Fig. 5c. Whereas the TO (or G^-) mode for semiconducting SWNTs has a Lorentzian lineshape, Fig. 5a shows that the lineshape for the G^- mode for metallic tubes is very different and follows a Breit–Wigner–Fano lineshape, with a $1/d_t^2$ mode frequency dependence that is approximately twice as strong as for the semiconducting SWNTs [22]. Fig. 5b shows that the LO–TO splitting can be used in addition to ω_{RBM} to characterize the nanotube diameter.

In the case of isolated SWNTs, the polarization of the light relative to the nanotube axis is important for studies of the Raman intensity. Absorption and/or emission of light perpendicularly polarized with respect to the nanotube axis is responsible for the observation of Raman modes with E_1 and E_2 group theoretical symmetry [10], while only phonons with A symmetry can be observed for parallel polarized light [11]. E_1 and E_2 phonons have indeed been seen in the *G*-band of both isolated [23,24] and bundled [25] SWNTs, and their polarization dependence confirms the selection rules for this 1D system. However, the most general polarization behavior for the optical properties of SWNTs is a strong angular dependence of the polarization, where the general Raman intensity drops for light perpendicular to the nanotube axis [23,26], and this behavior is understood by the antenna effect of electromagnetic theory [27]. Such polarization effects could be important for potential optical communications applications of SWNTs.

3.4. Setting up the Kataura Plot

In setting up the Kataura plot (Fig. 3) we use information from the *G*-band spectra to give the general placement of the E_{ii}^M and E_{ii}^S bands, and we use E_{ii} vs. ω_{RBM} in the RBM spectra to yield a specific point on the Kataura plot for each (n, m) SWNT [28]. Measurements on many SWNTs allow ω_{RBM} to be related to d_t [28] and these relations are further supported by theoretical calculations [29]. PL measurements can only be made on semiconducting SWNTs [20] and for these

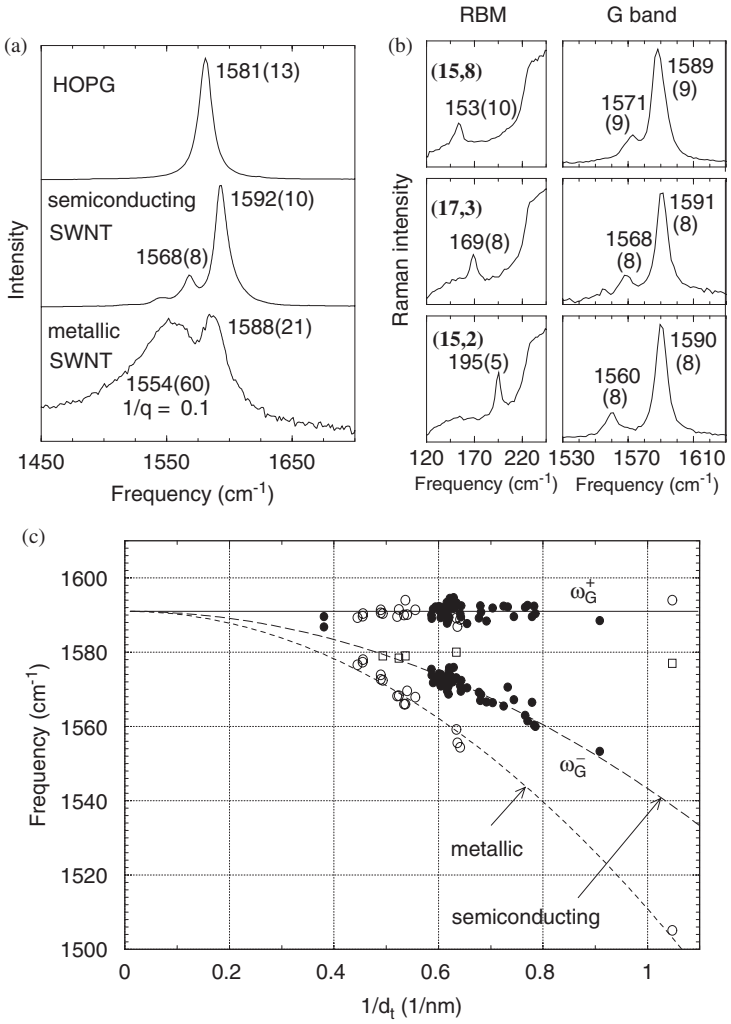

Fig. 5. (a) *G*-band Raman spectra for highly oriented pyrolytic graphite (HOPG), and for semiconducting and metallic SWNTs. (b) RBM and *G*-band spectra of isolated SWNTs for larger (top) to smaller (bottom) diameters. (c) *G*-band frequencies ω_{G^+} and ω_{G^-} for 62 isolated SWNT are plotted vs. $1/d_t$ [22].

SWNTs, the PL data yield points for the Kataura plot in agreement with the RRS data [20,28].

3.4.1. The G-Band and the Subband Positions

The determination of the relative subband positions utilizes the different lineshapes of M and S SWNTs, as shown in Figs. 5a and 6a. This difference in lineshape is best

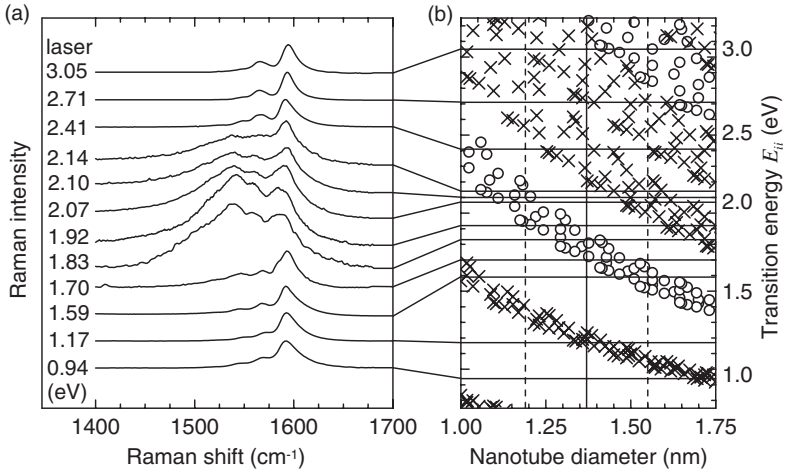

Fig. 6. (a) Raman spectra of the tangential G-band modes of SWNT bundles measured with several different laser lines, on a sample with $d_t = 1.37 \pm 0.18$ nm [32]. (b) Resonant transition energies E_{ii} vs. d_t. The vertical solid line is the average d_t and the vertical dashed lines denote the d_t distribution width. Crosses are for S SWNTs and open circles for M SWNTs.

observed in SWNT bundle samples since the coupling of the conduction electrons to phonons through a plasmon excitation is enhanced by intertube interactions [30,31]. By measuring the Raman spectra of nanotube bundles through varying E_{laser}, as shown in Fig. 6a, different E_{ii} for M and S tubes are probed at different E_{laser} values [32], and this information is used to identify M and S SWNTs in Fig. 6b. Based on the lineshape fits of the G^- feature for S and M SWNTs, the various traces in Fig. 6a are identified in Fig. 6b with the resonant E_{ii} for semiconducting and metallic SWNTs contained within the sample.

3.4.2. The RBM and the Kataura Plot

By using a Raman system with many laser lines, it is possible to obtain the E_{ii} energies for many tubes, as shown in Fig. 7a where Raman intensity contours vs. ω_{RBM} are shown. These data were obtained from resonance Raman spectra [28] taken from a sample by high pressure CO method with a diameter distribution $d_t = 1.0 \pm 0.2$ nm where the individual tubes were wrapped with sodium dodecyl sulfate (SDS) [33]. A wrapping agent is used to isolate one SWNT from another to enable PL measurements to be made [33]. In this way Raman spectroscopy (RRS) and PL measurements could be carried out on the same sample [28].

In order to avoid use of an empirical fitting procedure in implementing the Kataura plot, we plot E_{ii} vs. ω_{RBM} (Fig. 7b) directly from the experimental values in Fig. 7a for each (n, m) resonant SWNT [28]. Black circles and squares represent, respectively, S and M SWNTs. Using 76 values of E_{laser} for $1.52 \leq E_{laser} \leq 2.71$ eV, a 2D plot is made from the RBM spectra obtained from Stokes resonance Raman

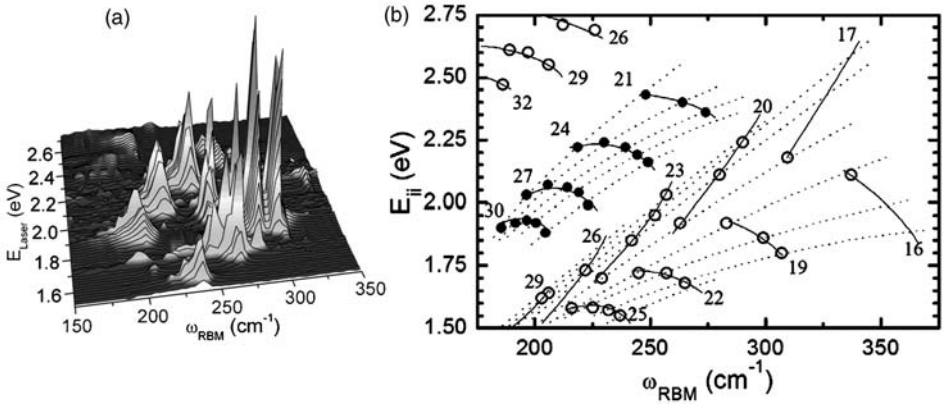

Fig. 7. (a) RBM resonance Raman measurements of HiPco SWNT nanotubes, wrapped in SDS and dispersed in an aqueous solution [33], taken with 76 different laser lines E_{laser} between 1.52 and 2.71 eV [28]. (b) The points denote 47 electronic transition energies E_{ii} vs. ω_{RBM} for 41 different (n, m) SWNTs in (a). Solid and open circles, respectively, denote metallic and semiconducting SWNTs. Each family is denoted by its $(2n + m) =$ constant value, allowing family patterns to be clearly seen.

measurements as a function of E_{laser}. Each RBM peak in Fig. 7a can be assigned to a (n, m) SWNT with the idea of family patterns (see Section 3.2). The family patterns of E_{ii} $(2n+m =$ constant) for semiconducting (E_{22}^{S} and E_{33}^{S}) and metallic (E_{11}^{M}) tubes are clearly seen in Fig. 7b, where we also show the values of $(2n+m)$. The different behaviors of the MOD1 and MOD2 semiconducting SWNTs (see Section 3.2) in the Kataura plot are clearly seen.

The $(E_{ii}, \omega_{\text{RBM}})$ results (Fig. 7b) can be compared with a theoretical model that considers in detail the distortion of the C–C bonds due to the curvature of the graphene sheet when it is rolled up to form a SWNT [18,29]. The model also considers the effects of the excitonic binding of the excited electron–hole pair and the Coulomb repulsion of electrons. Both of these phenomena are referred to as many-body effects. The comparison between this theoretical model and the RRS experimental results leads to a clear (n, m) assignment for each tube.

From the (n, m) assignment for both metallic and semiconducting SWNTs through Fig. 7b, a simple relation $\omega_{\text{RBM}} = 218/d_{\text{t}} + 16\,\text{cm}^{-1}$ is obtained to correlate ω_{RBM} with d_{t} for the small diameter tubes (d_{t} from 0.7 to 1.2 nm) for SWNTs wrapped with SDS in aqueous solution [28]. This relation between ω_{RBM} and d_{t} is needed to connect the RRS experiments and the Kataura plot (Fig. 3). This relation also makes connections to prior theoretical works studying the effect of the deformation of the C–C bond angles and bond lengths on ω_{RBM} on other Raman features [34]. For actual samples, a variety of expressions have been used to relate the connection between the radial breathing mode frequency and the nanotube diameter, and this topic is discussed further in Section 3.4.4 dealing with environmental effects.

Efforts have been made to observe of the electronic transition energies for light polarized perpendicular to the nanotube axis [35,36]. For SWNT bundle samples, some special RBM spectra have been observed, and these spectra can be explained by a Kataura plot not for E_{ii}, but for $E_{i,i\pm1}$ transitions [12]. This change in the polarization seen by a particular SWNT (suppression of the antenna effect) is attributed to fields from neighboring SWNTs [35]. A general picture corresponding to that shown in Fig. 7b for the $E_{i,i\pm1}$ transitions will be important for gaining a deeper understanding of the electronic properties of SWNTs.

3.4.3. Raman Intensity and Characterization of the (n, m) Population

As the (n, m) dependence of the resonance Raman spectra becomes well established, very important information that can be obtained from RRS is the amount of each specific (n, m) species in a bulk sample and the metal vs. semiconductor population ratio. Such information is very important for advancing both the synthesis and separation processes aimed at producing carbon nanotube samples for applications, depending on their electronic properties.

The method for quantifying the (n, m) population by using resonance Raman scattering is based on the assumption that the intensity for the fully resonant Raman signal depends on the scattering efficiency (or Raman cross-section) of each specific (n, m) nanotube species and its population in the sample. Therefore, by measuring the fully resonant Raman intensity for each specific nanotube in the sample (see Fig. 7a), and by correcting for the (n, m) dependent Raman cross-section for each (n, m), the amount of each (n, m) species in the sample is obtained.

Since the electron–phonon coupling exhibits a strong (n, m) dependence [37], in order to characterize the population of specific (n, m) SWNTs in a sample, the RBM resonance intensities must be analyzed considering the (n, m) dependence of the RBM Raman cross-section. We expect the ratio $P = I_{\mathrm{RBM}}^{\mathrm{EXP}}/I_{\mathrm{RBM}}^{\mathrm{CALC}}$ to give the population P of each specific (n, m) SWNT within the samples. The first-order Raman intensity $I(\omega, E_{\mathrm{laser}})$ as a function of phonon energy, $\hbar\omega$, and incident laser energy, E_{laser} is calculated by [38,39]

$$I(\omega, E_{\mathrm{laser}}) = \sum_j \left| \sum_b \frac{M^d(k-q, jb) M^{\mathrm{ep}}(q, ba) M^d(k, aj)}{\Delta E_{aj}(\Delta E_{aj} - \hbar\omega)} \right|^2 \tag{4}$$

in which $\Delta E_{aj} \equiv E_{\mathrm{laser}} - (E_a - E_j) - i\gamma$, and j, a, and b denote, respectively, the initial state, the excited states, and the scattered states of an electron, while γ denotes the broadening factor of the resonance event. Such an analysis has been applied to quantify the (n, m) population in SWNTs grown by the so-called CoMoCAT process [40]. This growth process has been considered the most successful in producing samples with a very narrow d_t distribution. By analyzing the P obtained by RRS from CoMoCAT SWNTs [41], it is clear that the semiconducting (6, 5) SWNT is the most abundant species, representing about 2/5 of the sample. By summing up all the

P for semiconducting and metallic tubes, a S:M ratio of 11:1 is obtained, showing a large dominance of S species in this growth process.

3.4.4. Characterization of Environmental Effects

Another application of Raman spectroscopy research is to quantify the effect of the SWNT environment on their electronic and vibrational properties. Because of the environment (wrapped by DNA or SDS, bundled, in suspension, or temperature and pressure) seen by a (n, m) SWNT, the E_{ii} values can shift by up to 80 meV.We call these shifts in E_{ii} environmental effects. Effects of the environment generally have a smaller influence on ω_{RBM}.

The environment is observed to asymmetrically broaden and even to split the RBM feature observed from one single (n, m) tube wrapped by DNA [42]. The E_{ii} of the SWNT are perturbed by changing the dielectric constant, temperature, and pressure. One illustration of an environmental effect is shown in Fig. 8 where the dependence of the RBM spectra on the laser intensity for a fixed $E_{\mathrm{laser}} = 1.72$ eV is shown, indicating that the relative intensities of the RBM peaks change with increasing laser power [28]. The transition energies E_{22}^{S} in Fig. 8b also vary with the laser power density, for each of the eight SWNTs with (n, m) assignments in Fig. 8a. Here the E_{22}^{S} move in opposite directions when the laser power increases for S SWNTs of the MOD1 type (dotted lines) and of the MOD2 type (solid lines). The E_{22}^{S} undergo a downshift for MOD1 SWNTs and an upshift for MOD2 SWNTs (similar to the recently reported uniaxial strain-enhanced effect observed in SWNT

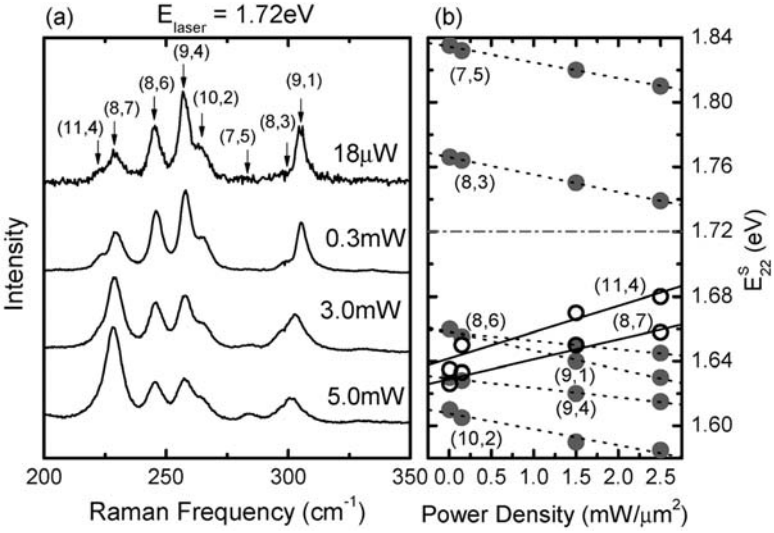

Fig. 8. (a) Dependence of the RBM spectra for HiPco SWNTs in bundles on the laser excitation power for a fixed $E_{\mathrm{laser}} = 1.72$ eV. (b) Dependence of the transition energies E_{22}^{S} on the laser power density for specific (n, m) SWNTs. Gray dots and open circles are for MOD1 and MOD2 nanotubes, respectively.

bundles [43]), thus explaining the changes in the relative intensities for the RBM peaks observed from a single E_{laser} (Fig. 8a). The changes in E_{ii} due to sample heating show that control of the laser power is important when analyzing the RRS of a nanotube sample.

3.5. Double Resonance Second-Order and Defect-Induced Modes

Many features in addition to the RBM and *G*-band features are also observed in the Raman spectra in Fig. 1. In this section we focus our attention on defect-induced modes and double resonance (DR) second-order features. Of these, the so-called *D* band (around 1200–1400 cm^{-1}) is the most extensively studied feature [44] and is a well-known example of a disorder-induced band, that has been widely used to characterize disorder in many kinds of graphitic materials [45], including SWNTs. Furthermore, a rich set of spectral features is observed for the intermediate frequency range between 600 and 1100 cm^{-1} [46], and several multi-phonon bands can be observed above 1700 cm^{-1} [47], the best known being the so-called G'-band (overtone of the *D* band) observed in the range 2400–2800 cm^{-1} [47,48].

In general, the observation of overtones and combination modes in condensed matter systems is rare because of dispersion effects which make these features too weak and broad to pick out from the noisy background. The enhanced intensity caused by the DR process in graphite-like materials and the intensity enhancement caused by the vHSs in SWNTs, however, allow such overtones and combination modes to be quite clearly observed. These DR features usually exhibit changes in their excited electronic states with changing E_{laser}, thereby providing new information about SWNT properties. To understand the physics related to overtones and combination modes, the basic physics for higher order scattering events for SWNTs are discussed here.

3.5.1. Double Resonance Scattering

In second-order Raman scattering (see Fig. 9b and c), the $\mathbf{q}$ and $-\mathbf{q}$ scattering wave vectors are involved, so that an electron can return to its original k position after scattering. Second-order Raman scattering consists of either (b) one-phonon and one-elastic scattering event, or (c) two-phonon scattering events. In the case of two-phonon scattering events, we can have involvement of either the same phonon modes (overtone mode) or different phonon modes (combination modes).

In second-order DR processes for carbon materials (see Fig. 9b and c), the electron (1) absorbs a photon at a $\mathbf{k}$ state, (2) scatters to $\mathbf{k}+\mathbf{q}$ states, (3) scatters back to a $\mathbf{k}$ state, and (4) emits a photon by recombining with a hole at a $\mathbf{k}$ state. The two scattering processes consist of either elastic scattering by the defects of the crystal or inelastic scattering by emitting a phonon, as shown in Fig. 9. Thus (1) one-elastic and one-inelastic scattering event (Fig. 9b) and (2) two-inelastic scattering events (Fig. 9c) are relevant to 2nd order Raman spectroscopy. Hereafter we call them, respectively, one-phonon and two-phonon DR Raman spectra [49]. In a DR Raman process, two resonance conditions for three intermediate states should be satisfied, in which the intermediate $\mathbf{k}+\mathbf{q}$ state is always a real electronic state (solid circles in

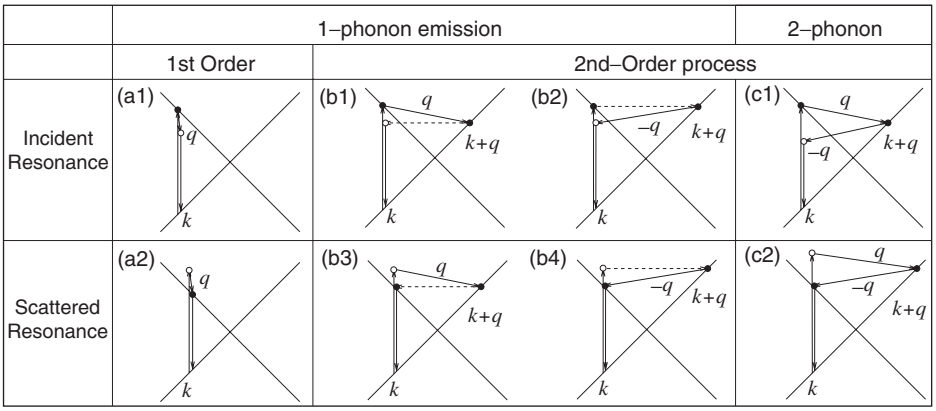

Fig. 9. (a) First-order and (b) one-phonon second-order, (c) two-phonon second-order, resonance Raman spectral processes: (top) incident photon resonance and (bottom) scattered photon resonance conditions. For one-phonon, second-order transitions, one of the two scattering events is an elastic scattering event (dashed lines). Resonance points are shown as solid circles. See text for details.

Fig. 9) and either the initial or the final k states is a real electronic state. The Raman intensity of a DR process is, in principle, comparable to that of a first-order process obeying a single resonance condition. In order to satisfy energy–momentum conservation in one-phonon DR Raman spectroscopy (see Fig. 9b1 and b2), the inelastic scattering process gives a shorter phonon $\mathbf{q}$ vector from the initial $\mathbf{k}$ state than the elastic scattering process.

The electronic structure of 2D graphite near the Fermi energy E_F is linear in wave vector $\mathbf{k}$, which is expressed by the crossed solid lines in Fig. 9. The crossing point corresponds to E_F located at the K point. When the laser energy E_{laser} increases, the resonance k vector for the electron moves away from the K point. In the DR process, the corresponding $\mathbf{q}$ vector for the phonon increases with increasing $\mathbf{k}$, measured from the K point. Thus by changing E_{laser}, we can observe the phonon energy $\hbar\omega(q)$ along the phonon dispersion relations (Fig. 10). This effect is observed experimentally as a dispersion of the phonon energy as a function of E_{laser} [49]. A tunable laser system can directly measure this dispersive behavior for a dispersive feature, such as the D-band or the G'-band in the Raman spectrum (see Fig. 1).

When we consider the energy and momentum conservation for $\mathbf{k}$ and $\mathbf{q}$, we need to introduce two other concepts to describe the scattering processes: intravalley and intervalley scattering, respectively, associated with $\mathbf{q} = 0$ and $\mathbf{q} = 2\mathbf{k}$ phonons where the value of $\mathbf{k}$ is measured from the K (or K′) point [50,51]. Since E_F is located at two inequivalent K and K′ points in the 2D Brillouin zone, we can consider the scattering not only in the vicinity of K (or K'), as shown in Fig. 9, but also in scattering from K to K′ (or from K' to K). The corresponding $\mathbf{q}$ vector for intravalley and intervalley scattering is, respectively, near the Γ and K points, as measured from the Γ point. Only $\mathbf{q} = 2\mathbf{k}$ modes show a large dispersive behavior for the Raman frequency vs. E_{laser}.

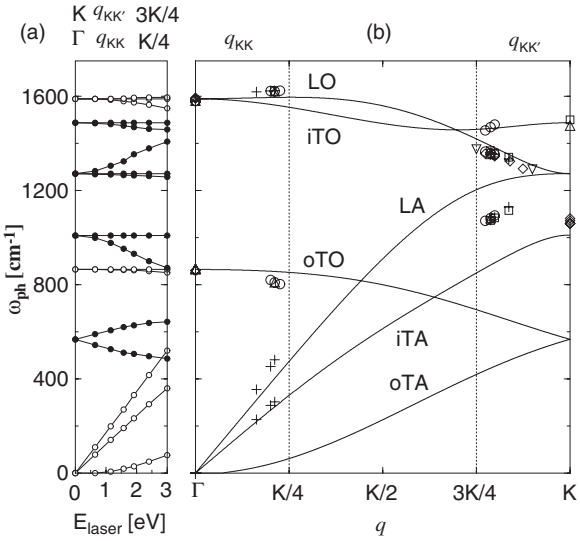

Fig. 10. (a) Calculated Raman frequencies for the double resonance (DR) condition vs. E_{laser} (bottom axis) and vs. q vector along Γ−K (top axis). Solid and open circles correspond to phonon modes near the K and Γ points, respectively. (b) The six graphite phonon dispersion curves (lines) and experimental Raman data (symbols) [50].

Both in graphite and in SWNTs, the D-band at 1350 cm^{-1} and the G'-band at 2700 cm^{-1} (for $E_{laser} = 2.41$ eV) are, respectively, due to one-phonon and two-phonon, 2nd order Raman intervalley scattering processes. Thus for graphite, the D-band spectra appearing at 1350 cm^{-1} (one-phonon DR) can be fitted to two Lorentzians, while the G'-band feature at 2700 cm^{-1} (two-phonon DR) can be fitted to one Lorentzian [51]. The disorder-induced D band is observed in disordered graphite-like materials, including carbon nanotubes, while its second-order harmonic, the G'-band is observed even in the absence of defects. Typically ω_D and $\omega_{G'}$ would be measured for $E_{laser} = 2.41$ eV and their dispersion would be 53 cm^{-1}/eV and 106 cm^{-1}/eV, respectively, for SWNTs. Although the ω_D and $\omega_{G'}$ dependences on E_{laser} are linear for most disordered graphite-like materials, ω_D and $\omega_{G'}$ in SWNTs exhibit an anomalous oscillatory dispersive effect, since the resonance condition for SWNTs occur at their 1D vHSs [48,52,53].

Many weak features in the Raman spectra for SWNTs can be assigned to one-phonon or two-phonon, 2nd order DR processes. These are listed in Table 1 together with their frequencies and dispersion $d\omega/dE_{laser}$. Also of importance is the variation of their mode frequencies with tube diameter d_t [54].

3.5.2. Characterizing Doping from the D and G′ bands

The D and G' bands provide a sensitive tool for characterizing carbon nanotube defects, functionalization, and doping [8,9]. While high resolution TEM and EELS techniques were not sensitive enough to detect boron in SWNTs, such doping could

Table 1. Properties of the various Raman features in graphite and SWNTs[a].

Name	ω (cm^{-1})	Res.[b]	$d\omega/dE$[c]	Notes
iTA	288	DR1-AV	129	iTA mode, $\mathbf{q} = 2\mathbf{k}$
LA	453	DR1-AV	216	LA mode, $\mathbf{q} = 2\mathbf{k}$
RBM	$248/d_t$	SR	0	Nanotube only, vibration of radius
oTO	860	DR1-AV	0	IR-active mode in graphite
D	1350	DR1-EV	53	LO or iTO mode, $\mathbf{q} = 2\mathbf{k}$
G	1582	SR	0	Raman-active mode of graphite
M^-	1732	DR2-AV	–26	Overtone of oTO mode, $\mathbf{q} = 2\mathbf{k}$
D^*	1620	DR1-AV	0	Defect oriented peak $\mathbf{q} = 2\mathbf{k}$
M^+	1755	DR2-AV	0	Overtone of oTO mode, $\mathbf{q} = 0$
iTOLA	1950	DR2-AV	230	Combinational mode of iTO and LA
G'	2700	DR2-EV	106	Overtone of D mode
$2D^*$	3240	DR2-AV	0	Overtone of D^*
2G	3180	DR2-AV	0	Overtone of *G* mode

[a]Dispersive mode frequencies ω are given at $E_{laser} = 2.41$ eV.
[b]The notation used here to classify resonance Raman scattering processes is: SR: 1st order, single resonance; DR1: 1 phonon, double resonance; DR2: 2 phonon, double resonance. AV: intravalley scattering; EV: intervalley scattering.
[c]$d\omega/dE$ denotes the change ω in cm^{-1} produced by changing $E = E_{laser}$ by 1 eV.

be detected in their Raman spectra taken for B concentrations up through 3 atomic % B in the target. The effect of doping MWNTs (multiwall carbon nanotubes) and SWNTs of large and small d_t, is observed as an increase in the intensity of the disorder-induced *D*-band in the Raman spectra [55–57]. Upon boron doping, the *D*-band intensity increases for higher doping levels [56,57], and in addition other changes to the spectra occur (see Fig. 11), such as bringing the RBM feature into better resonance with E_{laser} by shifting E_{ii} values and bringing more semiconducting tubes into resonance as can be seen in Fig. 11 by the change in the G'-band lineshape. Furthermore, ω_D and $\omega_{G'}$ are observed to downshift with boron doping, consistent with an increase in the in-plane lattice constant and a weakening of the B–C in-plane bond strength relative to that of the C–C bond, which is also observed in boron doped graphite [58]. One remarkable effect is a relatively larger downshift observed in $\omega_{G'}$ for metallic SWNTs compared to semiconducting SWNTs because of the larger occupation of states at E_F in M SWNTs. Thus the effect of hole addition through boron doping moves down E_F slightly from approximately mid-gap, in contrast to S SWNTs for which E_F drops all the way down to the highest lying vHS in the valence band.

3.5.3. Other Double Resonance Features

Interesting examples of overtone features are the features between 1700 and 2100 cm^{-1} shown in Fig. 12a, for SWNT bundles [47] and for several laser lines (E_{laser}). The two features near 1740 cm^{-1} (*M* band) are attributed to overtones of the out-of-plane (oTO), infrared-active mode at 867 cm^{-1} in graphite. Here the M^+ feature is identified with a nondispersive (intravalley $\mathbf{q} = 0$ scattering) DR process, and the M^- with a dispersive (intervalley $\mathbf{q} = 2b$) DR process (see Fig. 12a) [47]. The

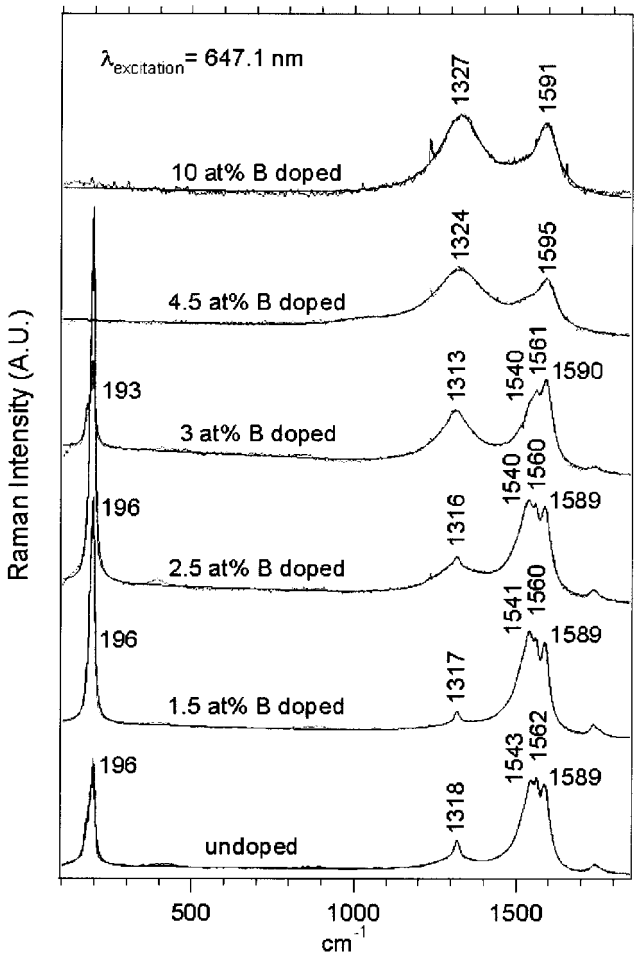

Fig. 11. First-order room temperature Raman spectra of SWNT bundle samples generated from targets with the indicated boron concentrations. All Raman spectra were excited using $E_{\text{laser}} = 1.96$ eV (647.1 nm) excitation energy. The spectra for the 4.5 and 10 at.% samples correspond to spectra for disordered graphite [57].

second-order *M*-band features are also interesting as an example of an overtone mode near $\mathbf{q} = 0$ whose fundamental (oTO) is not Raman-active (but is IR active) in the first-order spectrum of graphite, but can be observed in second order through the DR process. The *M*-band modes are further enhanced in SWNTs by van Hove singularity effects, and by symmetry-breaking effects associated with SWNT curvature.

The iTOLA, assigned as a combination mode not seen in graphite, is a highly dispersive DR-derived mode, upshifting from 1864 to 2000 cm^{-1} as E_{laser} varies from 1.58 to 2.71 eV [47]. To account for its large observed dispersion with E_{laser},

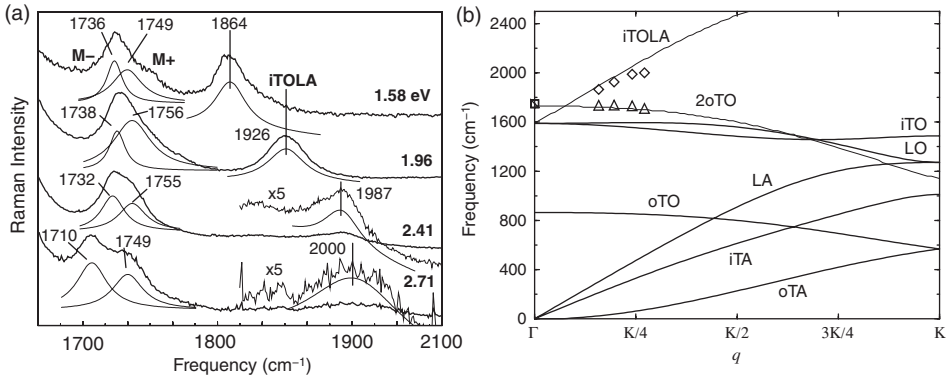

Fig. 12. (a) Lorentzian fits of the Raman spectra taken at several E_{laser} values for the M-bands near 1750 cm^{-1} and the highly dispersive iTOLA feature observed at 1950 cm^{-1} in SWNT bundles [47,59]. (b) Phonon dispersion for 2D graphite along the $\Gamma - K$ direction, including the dispersion for 2oTO (M-band) and iTO + LA (iTOLA). Squares, up-triangles, and diamonds denote experimental values for the M ($q = 0$ and $q = 2k$) and iTOLA ($q = 2k$) bands [47].

this so-called iTOLA band is attributed to a combination of two intravalley phonons, iTO + LA, one from the in-plane transverse optical branch (iTO) and the second phonon from the longitudinal acoustic (LA) branch, where the acoustic LA phonon is responsible for the large dispersion (see Fig. 12a) that is observed experimentally [47]. Fig. 12b shows the relation of the iTOLA mode dispersion to phonon branches in 2D graphite.

3.5.4. Step-Like Behavior of Dispersive Raman Spectra

From 700 to 1100 cm^{-1}, strongly dispersive Raman spectra are found for the so-called intermediate frequency modes (IFM) in tube bundle samples [60]. Fig. 13a plots the E_{laser} dependence of the IFM features shown in Fig. 13b for four E_{laser} values [46]. Interestingly, the use of a tunable laser system with a small energy spacing between E_{laser} lines, brings into focus a new and very unusual effect for Raman spectroscopy in general. When E_{laser} is varied, individual Raman peaks first increase and then decrease in intensity, while remaining approximately constant in phonon frequency. This behavior can be seen clearly by observing some of the well-resolved sharp peaks (see arrows in Fig. 13a). The dispersive behavior is not monotonic, as observed for many features in graphite-like materials due to energy-selective DR Raman scattering processes [50,61], but the dispersive behavior rather occurs in "steps."

In the 2D graphite parent material, the IFM spectral region contains an out-of-plane (o) optical (O) branch, with $\omega_O(q = 0)$ approximately 860 cm^{-1} for the oTO mode and by acoustic (A) branches [10]. In a second-order scattering process, these modes can become Raman-active, and the sum and difference of phonon frequencies can be observed. Such an effect is common in molecular spectroscopy, but is very unusual for solid state spectroscopy, where too many combinations are possible, and

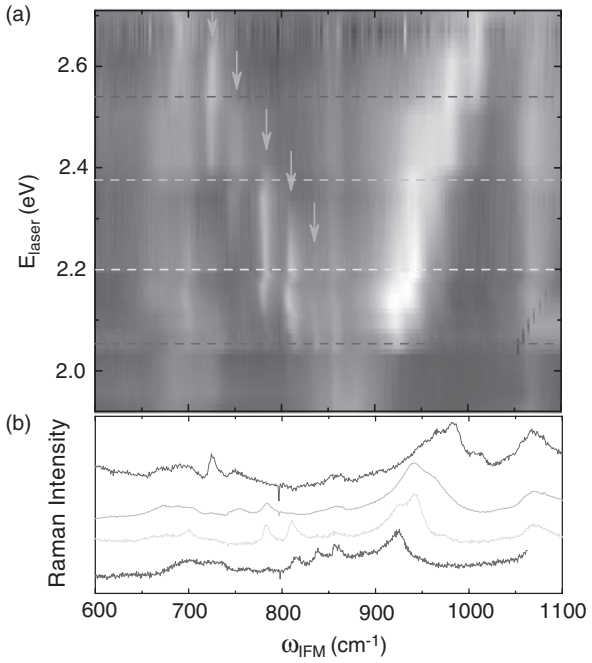

Fig. 13. (a) Two-dimensional plot for the E_{laser} dependence for the Raman spectra of SWNT bundles in the IFM range. The illuminated areas indicate high Raman intensity. Arrows point to five well-defined ω^{-}_{IFM} features. (b) IFM Raman spectra with $E_{\text{L}} = 2.05$ (top), 2.20, 2.34, and 2.54 eV (bottom) [46].

the averaging over many wave vector-allowed processes gives rise to just a broad background rather than to observable peaks with well-defined frequencies. The IFMs in SWNTs arise from such an effect and can be related to a vHS for each (n, m) SWNT and to the combination of two phonons, one optical and one acoustic to give the sum $\omega^{+}_{\text{IFM}} = \omega_{\text{O}} + \omega_{\text{A}}$ (creation of two phonons) and the difference $\omega^{-}_{\text{IFM}} = \omega_{\text{O}} - \omega_{\text{A}}$ (creation of an O phonon and the annihilation of an A phonon). The ω^{+}_{IFM} and ω^{-}_{IFM} thus give rise to the positively and negatively dispersive IFMs shown in Fig. 13a, respectively.

4. SUMMARY

Each of the many spectral features appearing in the Raman spectra of SWNTs provide important characterization information about SWNTs, with complementary information provided by ensembles of SWNTs in SWNT bundle samples and by isolated (n, m) SWNTs at the single nanotube level. Emphasis is given both to Raman spectroscopy for 1D systems and to the use of Raman spectroscopy to characterize the (n, m) structure, defects, and the various environmental effects encountered by

SWNTs. Raman spectroscopy is also closely connected to PL spectroscopy of semiconducting SWNTs, since both experimental techniques are strongly sensitive to the transition energies of individual SWNTs, to their electronic density of states, and to their interactions. Combination of transport and other experiments with Raman spectroscopy will be highly desirable to further our understanding of the electronic and vibrational structure of SWNTs.

ACKNOWLEDGMENTS

A.J acknowledges financial support by PRPq-UFMG, FAPEMIG, and CNPq, Brazil. R.S. acknowledges a Grant-in-Aid (No. 16076201) from the Ministry of Education, Japan. G.D and M.S.D. acknowledge support under NSF Grant DMR 04-05538.

REFERENCES

[1] A.M. Rao, E. Richter, S. Bandow, B. Chase, P.C. Eklund, K.W. Williams, S. Fang, K.R. Subbaswamy, M. Menon, A. Thess, R.E. Smalley, G. Dresselhaus and M.S. Dresselhaus, Diameter-selective Raman scattering from vibrational modes in carbon nanotubes, *Science* **275**, 187 (1997).

[2] A. Jorio, R. Saito, J.H. Hafner, C.M. Lieber, M. Hunter, T. McClure, G. Dresselhaus and M.S. Dresselhaus, Structural (n, m) determination of isolated single-wall carbon nanotubes by resonant Raman scattering, *Phys. Rev. Lett.* **86**, 1118 (2001).

[3] J.M. Holden, P. Zhou, X.-X. Bi, P.C. Eklund, S. Bandow, R.A. Jishi, K. Das Chowdhury, G. Dresselhaus and M.S. Dresselhaus, Raman scattering from nanoscale carbons generated in a cobalt-catalyzed carbon plasma, *Chem. Phys. Lett.* **220**, 186 (1994).

[4] K. Tohji, T. Goto, H. Takahashi, Y. Shinoda, N. Shimizu, B. Jeyadevan, I. Matsuoka, Y. Saito, A. Kasuya, T. Ohsuna, K. Hiraga and Y. Nishina, Purifying single walled nanotubes, *Nature* **383**, 679 (1996).

[5] M.S. Dresselhaus, G. Dresselhaus, A.M. Rao, A. Jorio, A.G. Souza Filho, Ge.G. Samsonidze and R. Saito, Resonant Raman scattering on one-dimensional systems, *Indian J. Phys.* **77B**, 75 (2003).

[6] S. Iijima and T. Ichihashi, Single shell carbon nanotubes of 1-nm diameter, *Nature (Lond.)* **363**, 603 (1993).

[7] D.S. Bethune, C.H. Kiang, M.S. de Vries, G. Gorman, R. Savoy, J. Vazquez and R. Beyers, Cobalt-catalysed growth of carbon nanotubes with single atomic layer walls, *Nature (Lond.)* **363**, 605 (1993).

[8] M.S. Dresselhaus, G. Dresselhaus, A. Jorio, A.G. Souza Filho and R. Saito, Raman spectroscopy on isolated single wall carbon nanotubes, *Carbon* **40**, 2043 (2002).

[9] M.S. Dresselhaus, G. Dresselhaus, R. Saito and A. Jorio, Raman spectroscopy of carbon nanotubes, *Phys. Rep.* **409**, 47 (2005).

[10] R. Saito, G. Dresselhaus and M.S. Dresselhaus, *Physical Properties of Carbon Nanotubes* (Imperial College Press, London, 1998).

[11] Ge.G. Samsonidze, R. Saito, A. Jorio, M.A. Pimenta, A.G. Souza Filho, A. Grüneis, G. Dresselhaus and M.S. Dresselhaus, The concept of cutting lines in carbon nanotube science, *J. Nanosci. Nanotechnol.* **3**, 431 (2003).

[12] H. Ajiki and T. Ando, Aharonov–Bohm effect in carbon nanotubes, *Physica B Condens. Matter* **201**, 349 (1994).

[13] H. Ajiki and T. Ando, Carbon nanotubes: Optical absorption in Aharonov–Bohm flux, *Jpn. J. Appl. Phys. Suppl.* **34-1**, 107 (1995).

[14] H. Kataura, Y. Kumazawa, N. Kojima, Y. Maniwa, I. Umezu, S. Masubuchi, S. Kazama, X. Zhao, Y. Ando, Y. Ohtsuka, S. Suzuki, and Y. Achiba, in *Proceedings of the International Winter School on Electronic Properties of Novel Materials (IWEPNM'99)*, American Institute of Physics, Woodbury, NY, 1999, AIP Conference Proceedings, 486 (1999) pp. 328–332.
[15] R. Saito, G. Dresselhaus and M.S. Dresselhaus, Trigonal warping effect of carbon nanotubes, *Phys. Rev. B* **61**, 2981 (2000).
[16] Ge.G. Samsonidze, A. Grüneis, R. Saito, A. Jorio, A.G. Souza Filho, G. Dresselhaus and M.S. Dresselhaus, Interband optical transitions in left-, right-handed single-wall carbon nanotubes, *Phys. Rev. B* **69**, 205402(1) (2004).
[17] R. Saito, M. Fujita, G. Dresselhaus and M.S. Dresselhaus, Electronic structures of carbon fibers based on C_{60}, *Phys. Rev. B* **46**, 1804 (1992).
[18] A. Jorio, C. Fantini, M.A. Pimenta, R.B. Capaz, Ge.G. Samsonidze, G. Dresselhaus, M.S. Dresselhaus, J. Jiang, N. Kobayashi, A. Grüneis and R. Saito, Resonance Raman spectroscopy (n, m) dependent effects in small diameter single-wall carbon nanotubes, *Phys. Rev. B* **71**, 075401 (2005).
[19] S.M. Bachilo, M.S. Strano, C. Kittrell, R.H. Hauge, R.E. Smalley and R.B. Weisman, Structure-assigned optical spectra of single walled carbon nanotubes, *Science* **298**, 2361 (2002).
[20] R.B. Weisman and S.M. Bachilo, Dependence of optical transition energies on structure for single-walled carbon nanotubes in aqueous suspension: An empirical Kataura plot, *Nanoletters* **3**, 1235 (2003).
[21] A. Jorio, A.G. Souza Filho, G. Dresselhaus, M.S. Dresselhaus, R. Saito, J.H. Hafner, C.M. Lieber, F.M. Matinaga, M.S.S. Dantas and M.A. Pimenta, Joint density of electronic states for one isolated single-wall carbon nanotube studied by resonant Raman scattering, *Phys. Rev. B* **63**, 245416-1 (2001).
[22] A. Jorio, A.G. Souza Filho, G. Dresselhaus, M.S. Dresselhaus, A.K. Swan, M.S. Ünlü, B. Goldberg, M.A. Pimenta, J.H. Hafner, C.M. Lieber and R. Saito, G-band resonant Raman study of 62 isolated single wall carbon nanotubes, *Phys. Rev. B* **65**, 155412 (2002).
[23] A. Jorio, A.G. Souza Filho, V.W. Brar, A.K. Swan, M.S. Ünlü, B.B. Goldberg, A. Righi, J.H. Hafner, C.M. Lieber, R. Saito, G. Dresselhaus and M.S. Dresselhaus, Polarized resonant Raman study of isolated single-wall carbon nanotubes: Symmetry selection rules, dipolar, multipolar antenna effects, *Phys. Rev. B Rapid* **65**, R121402 (2002).
[24] A. Jorio, M.A. Pimenta, A.G. Souza Filho, Ge.G. Samsonidze, A.K. Swan, M.S. Ünlü, B.B. Goldberg, R. Saito, G. Dresselhaus and M.S. Dresselhaus, Resonance Raman spectra of carbon nanotubes by cross-polarized light, *Phys. Rev. Lett.* **90**, 107403 (2003).
[25] A. Jorio, G. Dresselhaus, M.S. Dresselhaus, M. Souza, M.S.S. Dantas, M.A. Pimenta, A.M. Rao, R. Saito, C. Liu and H.M. Cheng, Polarized Raman study of single-wall semiconducting carbon nanotubes, *Phys. Rev. Lett.* **85**, 2617 (2000).
[26] G.S. Duesberg, I. Loa, M. Burghard, K. Syassen and S. Roth, Polarized Raman spectroscopy on isolated single-wall carbon nanotubes, *Phys. Rev. Lett.* **85**, 5436 (2000).
[27] Y. Wang, K. Kempa, B. Kimball, J.B. Carlson, G. Benham, W.Z. Li, T. Kempa, J. Rybcznski, A. Herczynski and Z.F. Ren, Receiving and transmitting light-like radio waves: Antenna effect in arrays of aligned carbon nanotube, *Appl. Phys. Lett.* **85**, 2607 (2004).
[28] C. Fantini, A. Jorio, M. Souza, A.J. Mai, Jr., M.S. Strano, M.S. Dresselhaus and M.A. Pimenta, Optical transition energies, radial breathing modes for HiPco carbon nanotubes from Raman spectroscopy, *Phys. Rev. Lett.* **93**, 147406 (2004).
[29] Ge.G. Samsonidze, R. Saito, N. Kobayashi, A. Grüneis, J. Jiang, A. Jorio, S.G. Chou, G. Dresselhaus and M.S. Dresselhaus, Family behavior of the optical transition energies in single-wall carbon nanotubes of smaller diameters, *Appl. Phys. Lett.* **85**, 5703 (2004).
[30] H. Kataura, Y. Kumazawa, Y. Maniwa, I. Umezu, S. Suzuki, Y. Ohtsuka and Y. Achiba, Optical properties of single-wall carbon nanotubes, *Synth. Metals* **103**, 2555 (1999).
[31] S.D.M. Brown, A. Jorio, P. Corio, M.S. Dresselhaus, G. Dresselhaus, R. Saito and K. Kneipp, Origin of the Breit–Wigner–Fano lineshape of the tangential G-band feature of metallic carbon nanotubes, *Phys. Rev. B* **63**, 155414 (2001).

[32] M.A. Pimenta, A. Marucci, S. Empedocles, M. Bawendi, E.B. Hanlon, A.M. Rao, P.C. Eklund, R.E. Smalley, G. Dresselhaus and M.S. Dresselhaus, Raman modes of metallic carbon nanotubes, *Phys. Rev. B Rapid* **58**, R16016 (1998).
[33] M.J. O'Connell, S.M. Bachilo, X.B. Huffman, V.C. Moore, M.S. Strano, E.H. Haroz, K.L. Rialon, P.J. Boul, W.H. Noon, C. Kittrell, J. Ma, R.H. Hauge, R.B. Weisman and R.E. Smalley, Band gap fluorescence from individual single walled carbon nanotubes, *Science* **297**, 593 (2002).
[34] J. Kürti, V. Zólyomi, M. Kertesz and G.Y. Sun, The geometry, the radial breathing mode of carbon nanotubes: Beyond the ideal behaviour, *New J. Phys.* **5** (2003) Art. 125
[35] A. Grüneis, R. Saito, J. Jiang, Ge.G. Samsonidze, M.A. Pimenta, A. Jorio, A.G. Souza Filho, G. Dresselhaus and M.S. Dresselhaus, Resonant Raman spectra of carbon nanotube bundles observed by perpendicularly polarized light, *Chem. Phys. Lett.* **387**, 301 (2004).
[36] S. Maruyama, A molecular dynamics simulation of heat conduction of a finite length single-walled carbon nanotube, *Microscale Thermophys. Eng.* **7**, 41 (2003).
[37] J. Jiang, R. Saito, A. Grüneis, S.G. Chou, Ge.G. Samsonidze, A. Jorio, G. Dresselhaus, and M.S. Dresselhaus, Intensity of the resonance Raman excitation spectra of single-wall carbon nanotubes, *Phys. Rev. B* **71**, 205420 (2005); see also J. Jiang, R. Saito, K. Sato, J.S. Park, Ge. G. Samsonidze, A. Jorio, G. Dresselhaus and M.S. Dresselhaus, Exciton-photon, exciton-phonon matrix elements, and resonant Raman intensity of single-wall carbon nanotubes, *Phys. Rev. B* **75**, 035405 (2007).
[38] M. Cardona, Light scattering in solids II, in *Topics in Applied Physics*, edited by M. Cardona and G. Guntherodt (Springer, Berlin, 1982), vol. 50, chap. 2, pp. 19–176.
[39] R.M. Martin and L.M. Falicov, Light scattering in solids I, in *Topics in Applied Physics*, edited by M. Cardona (Springer, Berlin, 1983), vol. 8, chap. 3, pp. 79–145.
[40] B. Kitiyanan, W.E. Alvarez, J.H. Harwell and D.E. Resasco, Controlled production of single-wall carbon nanotubes by catalytic decomposition of Co on bimetallic Co–Mo catalysts, *Chem. Phys. Lett.* **317**, 497 (2000).
[41] A. Jorio, A.P. Santos, H.B. Ribeiro, C. Fantini, M. Souza, J.P.M. Vieira, C.A. Furtado, J. Jiang, R. Saito, L. Balzano, D.E. Resasco and A. Pimenta, Quantifying carbon nanotube species with resonance Raman scattering, *Phys. Rev. B* **72**, 075207 (2005).
[42] A. Jorio, C. Fantini, L.G. Cancado, H.B. Ribeiro, A.P. Santos, C.A. Furutado, M.S. Dresselhaus, G. Dresselhaus, Ge. G. Samsonidze, A. Gruneis, J. Jiang, N. Kobayashi, R. Saito and M.A. Pimenta, Spectroscopy of small diameter single-wall carbon nanotubes, in *Proceedings of the XVIII International Winterschool/Euroconference on the Electronic Properties of Novel Materials*, vol. 786, edited by H. Kuzmany, J. Fink, M. Mehring and S. Roth (American Institute of Physics, Woodbury, NY, 2005), p. 406.
[43] M. Lucas and R.J. Young, Effect of uniaxial strain deformation upon the Raman radial breathing modes of single-wall carbon nanotubes in composites, *Phys. Rev. B* **69**, 085405 (2004).
[44] M.J. Matthews, M.A. Pimenta, G. Dresselhaus, M.S. Dresselhaus and M. Endo, Origin of dispersive effects of the Raman *D*-band in disordered carbon materials, *Phys. Rev. B* **59**, R6585 (1999).
[45] M.S. Dresselhaus and R. Kalish, *Ion Implantation in Diamond, Graphite and Related Materials*, vol. 22 (Springer-Verlag, Berlin, 1992); [Springer Series in Materials Science].
[46] C. Fantini, A. Jorio, M. Souza, L.O. Ladeira, M.A. Pimenta, A.G. Souza Filho, R. Saito, Ge.G. Samsonidze, G. Dresselhaus and M.S. Dresselhaus, One-dimensional character of combination modes in the resonance Raman scattering of carbon nanotubes, *Phys. Rev. Lett.* **93**, 087401 (2004).
[47] V.W. Brar, Ge.G. Samsonidze, G. Dresselhaus, M.S. Dresselhaus, R. Saito, A.K. Swan, M.S. Ünlü, B.B. Goldberg, A.G. Souza Filho and A. Jorio, Second-order harmonic, combination modes in graphite, single-wall carbon nanotube bundles, isolated single-wall carbon nanotubes, *Phys. Rev. B* **66**, 155418 (2002).
[48] M.A. Pimenta, E.B. Hanlon, A. Marucci, P. Corio, S.D.M. Brown, S.A. Empedocles, M.G. Bawendi, G. Dresselhaus and M.S. Dresselhaus, The anomalous dispersion of the disorder-induced, the second-order Raman bands in carbon nanotubes, *Braz. J. Phys.* **30**, 423 (2000).

[49] R. Saito, A. Grüneis, Ge.G. Samsonidze, V.W. Brar, G. Dresselhaus, M.S. Dresselhaus, A. Jorio, L.G. Cançado, C. Fantini, M.A. Pimenta and A.G. Souza Filho, Double resonance Raman spectroscopy of single wall carbon nanotubes, *New J. Phys.* **5**, 157.1 (2003).
[50] R. Saito, A. Jorio, A.G. Souza Filho, G. Dresselhaus, M.S. Dresselhaus and M.A. Pimenta, Probing phonon dispersion relations of graphite by double resonance Raman scattering, *Phys. Rev. Lett.* **88**, 027401 (2002).
[51] L.G. Cançado, M.A. Pimenta, R. Saito, A. Jorio, L.O. Ladeira, A. Grüneis, A.G. Souza Filho, G. Dresselhaus and M.S. Dresselhaus, Stokes, anti-Stokes double resonance Raman scattering in two-dimensional graphite, *Phys. Rev. B* **66**, 035415 (2002).
[52] S.D.M. Brown, A. Jorio, G. Dresselhaus and M.S. Dresselhaus, The *D*-band feature of carbon nanotubes, *Phys. Rev. B* **64**, 073403 (2001).
[53] A. Grüneis, M. Hulman, Ch. Kramberger, H. Peterlik, H. Kuzmany, H. Kataura, and Y. Achiba, in *Proceeding of the International Winter School on Electronic Properties of Novel Materials*, vol. 591, p. 319, AIP Conference Proceedings (Kirchberg, Austria, 2001).
[54] A.G. Souza Filho, A. Jorio, Ge.G. Samsonidze, G. Dresselhaus, M.A. Pimenta, M.S. Dresselhaus, A.K. Swan, M.S. Ünlü, B.B. Goldberg and R. Saito, Competing spring constant versus double resonance effects on the properties of dispersive modes in isolated single wall carbon nanotubes, *Phys. Rev. B* **67**, 035427-1 (2003).
[55] W.K. Hsu, S. Firth, P. Redlich, M. Terrones, H. Terrones, Y.Q. Zhu, N. Grobert, A. Schilder, R.J.H. Clark, H.W. Kroto and D.R.M. Walton, Boron-doping effects in carbon nanotubes, *J. Mater. Chem. Lett.* **10**, 1425 (2000).
[56] J. Maultzsch, S. Reich, C. Thomsen, H.S. Webster, R. Czerw, D.L. Carroll, S.M.C. Vieira, P.R. Birkett and C.A. Rego, Raman characterization of boron-doped multiwalled carbon nanotubes, *Appl. Phys. Lett.* **81**, 2647 (2002).
[57] K. McGuire, N. Gothard, P.L. Gai, M.S. Dresselhaus, G. Sumanasekera and A.M. Rao, Synthesis, Raman characterization of boron-doped single walled carbon nanotubes, *Carbon* **43**, 219 (2005).
[58] B.T. Kelly, Physics of graphite, *Appl. Sci. Publ.* (London and New Jersey), (1981).
[59] S.D.M. Brown, P. Corio, A. Marucci, M.A. Pimenta, M.S. Dresselhaus and G. Dresselhaus, Second-order resonant Raman spectra of single-walled carbon nanotubes, *Phys. Rev. B* **61**, 7734 (2000).
[60] L. Alvarez, A. Righi, T. Guillard, S. Rols, E. Anglaret, D. Laplaze and J.-L. Sauvajol, Resonant Raman study of the structure and electronic properties of SWNTs, *Chem. Phys. Lett.* **316**, 186 (2000).
[61] C. Thomsen and S. Reich, Double resonant Raman scattering in graphite, *Phys. Rev. Lett.* **85**, 5214 (2000).

Chapter 5
OPTICAL SPECTROSCOPY OF SINGLE-WALLED CARBON NANOTUBES

R. Bruce Weisman

1. INTRODUCTION

It has long been known that careful study of the light wavelengths absorbed or emitted from atoms and molecules offers deep insights into their electronic structures. In fact, such optical spectroscopy formed the experimental foundation for the development of quantum mechanics, and it continues to provide precise experimental data essential for understanding the electronic properties of a wide variety of materials. In addition to its central role in basic atomic, molecular, and condensed matter physics, optical spectroscopy has been widely applied in a variety of powerful analytical techniques. These applied spectroscopic methods can sensitively and selectively detect and identify a wide range of chemical substances in varied environments. They currently serve as essential tools in the chemical and pharmaceutical industries, in forensics, in environmental research and safety monitoring, and in medical laboratories. In view of these precedents, researchers in both basic and applied science should take special interest in the optical spectroscopy of novel artificial nanomaterials.

Perhaps the most intensely studied new family of nanomaterials is single-walled carbon nanotubes (SWNT) [1,2]. These are tubular structures of carbon atoms having typical diameters near 1 nm and lengths larger by factors of 100 to 1 000 000. Their extremely high aspect ratios give SWNT some unique and remarkable physical properties. The high aspect ratios also suggest the need for multi-disciplinary approaches in SWNT research: when viewed in cross-section, these nanotubes resemble organic molecules that can be described using concepts and methods of molecular physics; but as viewed along the tube axis, they are extended periodic structures suitable for treatment within condensed matter physics.

Contemporary Concepts of Condensed Matter Science
Carbon Nanotubes: Quantum Cylinders of Graphene

ISSN: 1572-0934/doi:10.1016/S1572-0934(08)00005-X

Although SWNTs are not produced directly from graphite, they can be envisioned as sections of single graphene sheets that have been rolled up to form seamless cylinders capped at the ends with hemifullerenes. This rolling up process can generate a large number of discrete transverse structures which differ in tube diameter and chiral (or roll-up) angle. As illustrated in Fig. 1, each of these distinct structures can be described and labeled by the relative position of hexagonal cells in the graphene sheet that become superimposed after roll-up. If one cell is arbitrarily chosen as the origin, then any other can be uniquely identified by two integers, denoted n and m, describing its displacement in primitive lattice vectors from the origin cell. The length of the "roll-up" vector connecting two cells in the graphene sheet equals the circumference of the resulting nanotube, and the angle between that vector and the "zigzag" axis noted in Fig. 1 defines the nanotube's chiral angle. The long axis of the tube lies perpendicular to the roll-up vector. Chiral angles between 0 and 30° encompass all unique SWNT structures, if enantiomers are neglected.

Each carbon atom in such a single-walled nanotube structure is covalently linked to three neighbors by σ-bonds. The remaining p-electron of each carbon atom joins with those at other sites to form an extended π-electron system whose properties govern SWNT low-energy electronic properties and optical spectroscopy. The available electronic states in this π-system reflect the unusual band structure of graphene combined with the constraint of an angular periodic boundary condition

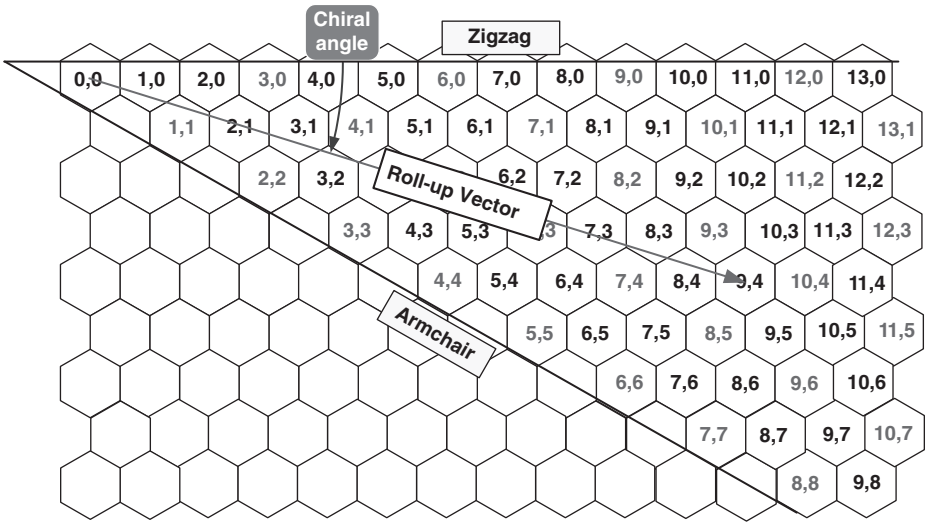

Fig. 1. Graphene sheet map illustrating possible single-walled nanotube structures that can be formed by wrapping the sheet to from a cylindrical tube. The resulting nanotube is labeled by the pair of integers in the cell that becomes overlapped with the origin cell. The nanotube's diameter is the length of the roll-up vector divided by π, and its chiral angle can lie between 0° (zigzag) and 30° (armchair).

for full rotation about the tube axis. Because this wavefunction boundary condition varies with the (*n*,*m*) values describing a nanotube's construction, each physical SWNT structure has its own characteristic electronic structure [1,3]. The diversity of electronic properties and their strong dependence on nanotube structure constitute one of the most remarkable and potentially useful features of SWNTs, which must be viewed as a family of related materials rather than a single substance such as C_{60}. It is found that SWNTs for which $n = m$ have a finite density of states at the Fermi energy and display metallic electronic behavior. These structures are called ''armchair'' nanotubes because of their pattern of bonds around the circumference. Other structures for which the quantity $n–m$ is evenly divisible by 3 are semimetallic, with band gaps smaller than $k_B T$ at room temperature. The remaining SWNT structures, in which $n–m$ does not divide evenly by 3, are semiconductors. The band gaps of these semiconducting SWNTs vary approximately inversely with nanotube diameter. Nanotubes with the same (*n*,*m*) identity but different lengths should have matching optical and electronic properties because SWNT electronic structure is governed by transverse structure. The quasi-one-dimensionality of nanotubes has an important electronic consequence for all (*n*,*m*) species: it introduces sharp spikes, called van Hove singularities, into the densities of states.

2. OPTICAL SPECTRA

Fig. 2 shows a band theory model density of states function for a semiconducting SWNT [4]. Each van Hove singularity belongs to a different sub-band, labeled with an integer representing the magnitude of those states' angular momentum projection along the nanotube axis. Within this model, optical absorption and emission are dominated by dipole-allowed transitions in which light polarized with its electric vector parallel to the tube axis promotes an electron from a valence sub-band to the corresponding conduction sub-band, conserving the angular momentum projection. In a one-electron model, these transitions are predicted to be most intense when the photon energy matches the energy difference between corresponding van Hove singularities. The absorption and emission spectra of a single (*n*,*m*) species of SWNT are therefore expected to consist mainly of a series of sharp features at energies E_{ii}, where i takes the values 1, 2, 3, … according to sub-band. These are illustrated in Fig. 2. For semiconducting SWNTs with diameters near 1 nm, the first three of these transitions will appear in the near-infrared, visible, and near-ultraviolet regions. Metallic or semimetallic SWNTs of similar diameter will have their lowest energy optical transitions at visible wavelengths falling between the semiconducting nanotubes' E_{22} and E_{33} features. In addition, semimetallic nanotubes also have much lower energy absorptions in the far-infrared at wavelengths near 100 μm [5,6]. These correspond to transitions across the small, diameter-dependent band gaps (in the range of 10 meV) that are induced by s–p hybridization associated with the nanotubes' cylindrical curvature [7]. Apart from the nondispersive interband optical transitions in the infrared and visible that are characteristic of nanotube diameter and chiral angle, SWNT samples also

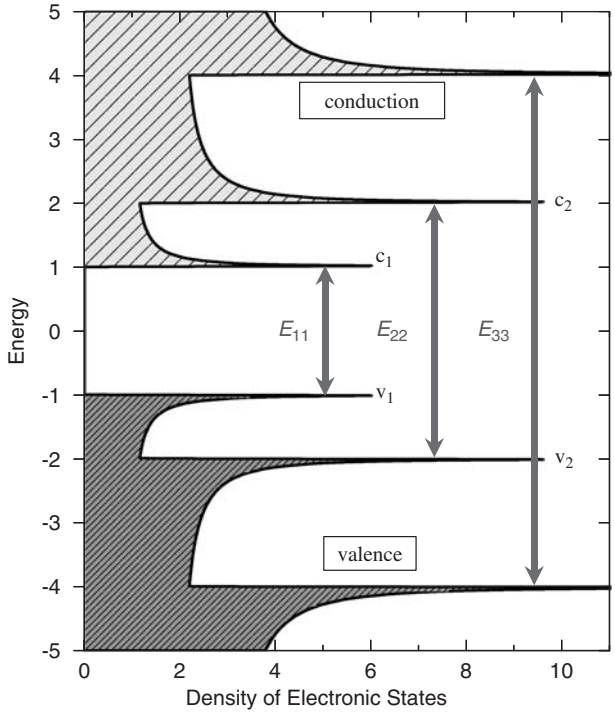

Fig. 2. Schematic density of states diagram for a semiconducting single-walled carbon nanotube, in a simple band theory model. Allowed optical transitions are illustrated as vertical arrows.

display dispersive, intense near-ultraviolet absorptions at 4.5 and 5.2 eV that have been assigned to collective plasmon excitations of their π-electrons [8,9].

The near-infrared and visible transitions of SWNTs would be expected to be quite useful in distinguishing different structural species from one another. However, it was found that spectra of samples containing many species typically showed broad, undifferentiated optical absorption features arising from strongly overlapped transitions of those species, rather than sharp, resolved absorptions. In addition, no emission was observed that could be assigned to van Hove interband transitions. A breakthrough in nanotube spectroscopy occurred with the 2002 report of structured absorption from samples of SWNTs that had been prepared with special processing to counteract their strong tendency to form bundles of parallel nanotubes held together by van der Waals forces. To obtain these disaggregated samples, raw and unpurified product from the HiPco process was first mechanically dispersed into an aqueous solution of a surfactant such as SDS (sodium dodecylsulfate). Then intense ultrasonic agitation was applied to free many individual nanotubes from bundles. Once freed, the nanotubes became surrounded by a micelle-like layer of surfactant molecules that prevented their

reaggregation into bundles. Finally, the sample was subjected to ultracentrifugation, which allowed significant physical separation of suspended individual nanotubes from the slightly denser suspended bundles. Decanted portions of such processed samples showed notably complex and sharpened near-infrared absorption spectra with structure extending from approximately 900 to 1600 nm, as shown in Fig. 3. D_2O was used in preference to H_2O as the solvent for spectroscopic studies because of its superior near-infrared transparency. The isotopic frequency shift of the O–H stretching overtone increases the long wavelength cut-off of D_2O to ca. 1900 nm from 1350 nm in H_2O.

Remarkably, these aqueous samples enriched in individual surfactant-suspended SWNTs also displayed near-infrared photoluminescence. As illustrated in Fig. 4, their highly structured emission spectra show a series of peaks nearly coincident with those in the absorption spectrum. The emission red-shifts are only approximately 4 meV (30 cm^{-1}). This similarity of absorption and emission spectra differs strikingly from the ''mirror-image'' relation that is common in molecular photophysics [10]. The data show that the sample contains many emitting species, with each displaying one dominant transition in this spectral range and a very small Stokes shift between its absorption and emission peaks. In accord with the predictions of Kasha's Rule that molecular electronic luminescence originates entirely from the lowest-lying electronic state within a spin multiplicity manifold [11], SWNT emission is observed exclusively for E_{11} transitions and not for E_{22} or higher transitions. Clearly, the many distinct spectral features in the E_{11} region correspond to different (n,m) species of semiconducting single-walled nanotubes in

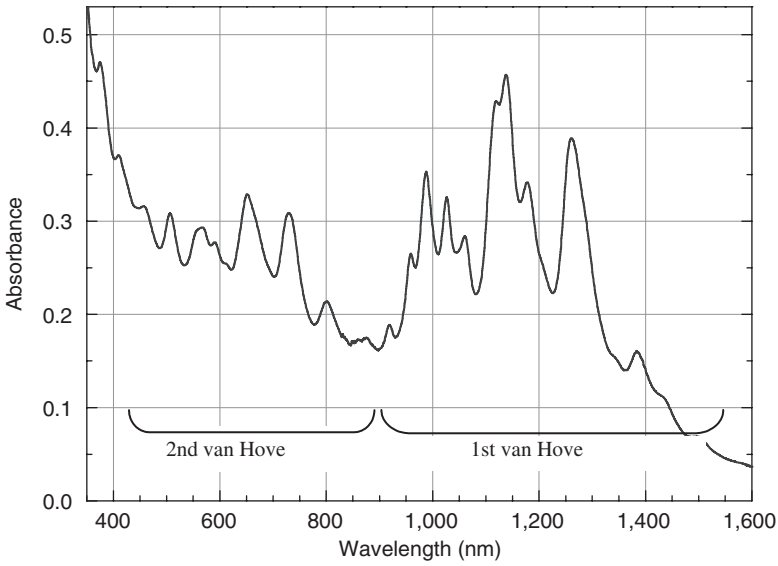

Fig. 3. Optical absorption spectrum of a sample of HiPco single-walled carbon nanotubes suspended in D_2O by SDS surfactant at 276 K.

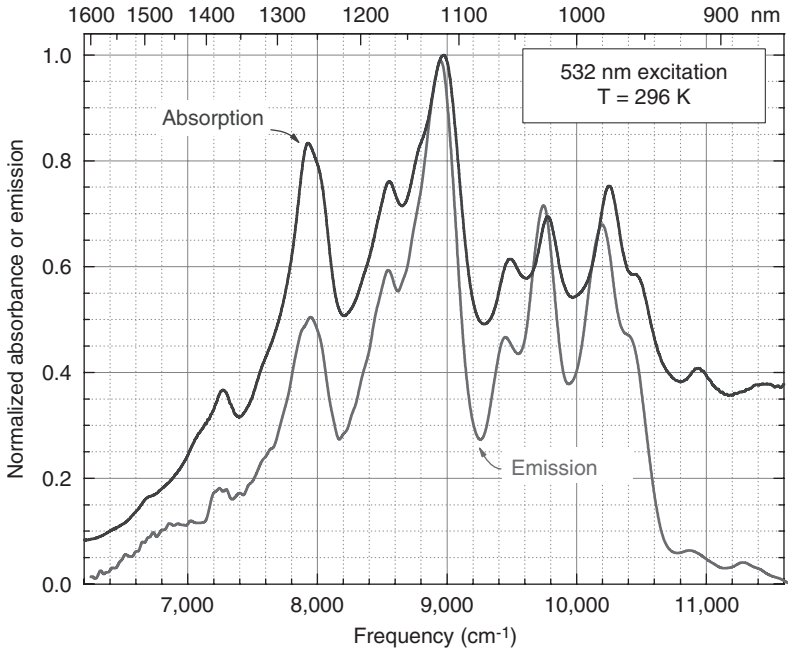

Fig. 4. Overlaid absorption and emission spectra of a sample of HiPco nanotubes in SDS/D_2O suspension. The emission was excited by a pulsed laser at 532 nm.

the structurally heterogeneous sample. Precise values of photoluminescence quantum yields are difficult to measure, in part because of overlapping transitions in mixed samples. However, initial estimates suggest quantum yields that are near 10^{-3} and vary somewhat as the nanotube's environment is altered by the presence of different surfactants. It will be of significant interest to quantify the dependence of this yield on nanotube diameter, chiral angle, and extrinsic factors.

Lifetime studies on SWNT optically excited states have been reported by several laboratories [12–16]. Despite some inconsistencies among the measured values, the excited state lifetime of ca. 10^{-10} s can be combined with the emissive quantum yield near 10^{-3} to deduce that the emitting state has a radiative rate constant consistent with a spin-conserving optical transition. Using the terminology of molecular photophysics, nanotube photoluminescence is therefore classified as fluorescence rather than phosphorescence. In the remainder of this chapter, SWNT photoluminescence will be referred to as fluorescence.

3. SPECTROSCOPIC ASSIGNMENT

Once the structured near-infrared emission had been discovered and identified as fluorescent band-gap transitions from a variety of semiconducting SWNT species,

the crucial next task was spectroscopic assignment: identifying the specific nanotube structure responsible for each peak. The key experimental method used for this task was spectrofluorimetry. Here the emission intensity of a sample was measured as a function of two variables: excitation wavelength and emission wavelength. The excitation source's wavelength was scanned over the range of E_{22} transitions, and when the photon energy matched the second van Hove transition energy of one of the SWNT species in the sample, the resulting optical absorption generated a hole in its second valence sub-band and an electron in its second conduction sub-band. The electrons and holes relaxed through phonon emission to the first sub-bands. Then a small fraction of the excited nanotubes emitted E_{11} near-infrared fluorescence through radiative electron–hole recombination across the semiconducting band gap. The wavelength of this emission was characteristic of the nanotube species that had undergone resonant E_{22} excitation. Fig. 5 displays the results from this experiment in the form of a surface plot, where height corresponds to emission intensity and the two other axes represent excitation and emission wavelengths. A rich structure of "mountain peaks" is clearly evident for excitation in the E_{22} range between ca. 500 and 800 nm. Each of these peaks arises from a distinct (n,m) species of semiconducting nanotube. The unique E_{11} and E_{22} transition energies of each species may be simply found from the wavelength coordinates of its peak.

The data shown in Fig. 5 immediately provided a valuable correlation of E_{11} and E_{22} values for many different nanotube species. However, assignment to the correct (n,m) values required extensive further analysis. Fig. 6 shows a plot of experimental E_{22}/E_{11} ratios as a function of excitation wavelength (inversely proportional to E_{22}). The data points appear to form a systematic splay pattern, as illustrated by the solid lines. This remarkable, regular pattern of spectral data must reflect the systematic pattern of nanotube structures present in the sample. The connection between structural and spectral patterns was found by comparing the experimental findings with a similar plot of results from an extended tight-binding model computation. Although there was no quantitative match of ratios or excitation wavelengths between this model and experiment, the model revealed a qualitatively similar splay pattern. In this pattern, points on a given line share the same value of $n–m$, and both n and m increase by one from left to right between adjacent points along any splay line. We take the value of $n–m$ to define a "family" of nanotube structures. Note that because only semiconducting SWNTs emit fluorescence, no points or lines are present for $n–m$ family values of 0, 3, 6, 9, …, which correspond to metallic or semimetallic species. The quantitative changes in n and m along a dotted line path connecting adjacent splay lines were also deduced by comparison with the model calculations. In this way, the connectivity pattern determining relative n and m values for the entire network of experimental spectroscopic points was deciphered. However, additional work was needed to assign absolute values of n and m.

The range of "anchoring" choices to define absolute (n,m) values was limited to a handful of plausible candidates by considerations such as the distribution of nanotube diameters that had previously been found from TEM analysis of the measured SWNT sample. Raman spectroscopy was then used to select the correct

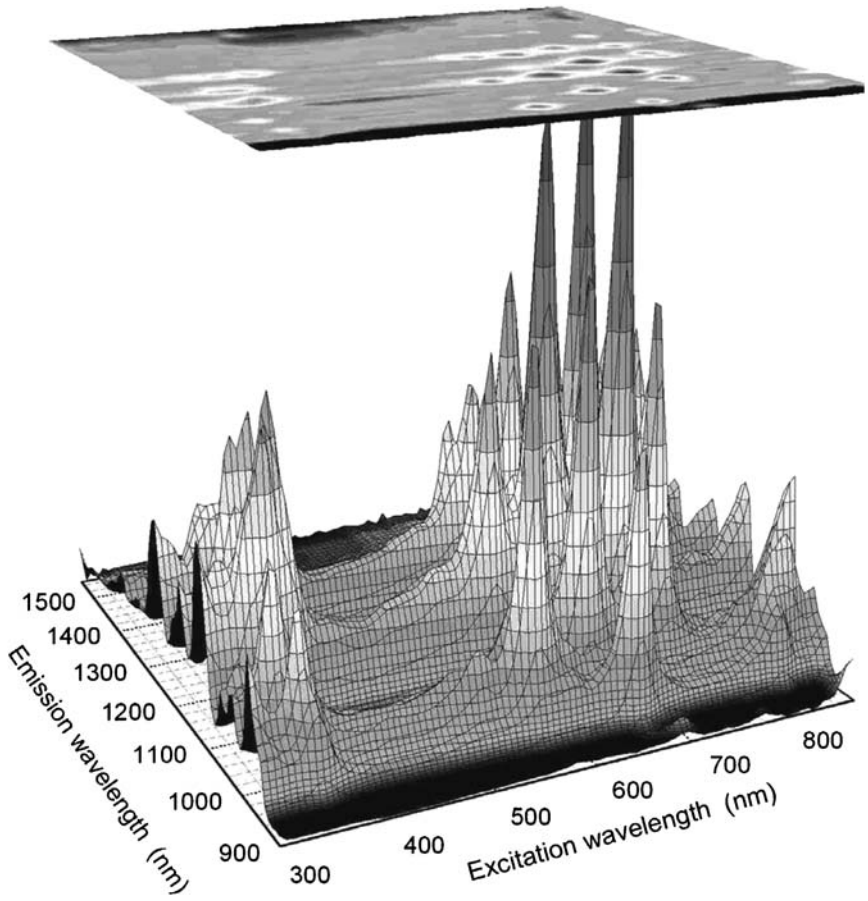

Fig. 5. Surface plot showing emission intensity from a sample of HiPco SWNT in SDS/D_2O suspension as a function of excitation and emission wavelengths. Each distinct peak arises from a specific (*n*,*m*) species of semiconducting nanotube.

choice from among these candidates. Prior experimental and theoretical studies had found that the low-frequency radial breathing vibrational mode (RBM) is strongly resonance enhanced in SWNT Raman spectra, and that its frequency is inversely related to nanotube diameter [17–20]. Raman spectroscopy was performed using a variety of laser wavelengths that provided resonance with ten different E_{22} transitions of semiconducting nanotubes in the surfactant-suspended SWNT sample. This gave a set of experimental RBM frequencies correlated with E_{22} transition wavelengths. Each candidate anchoring choice assigned different (*n*,*m*) values, and therefore different diameters, to the ten species in this set on the basis of their optical transitions. For each candidate anchoring choice, the experimental RBM frequencies were plotted versus those purported inverse diameters. These

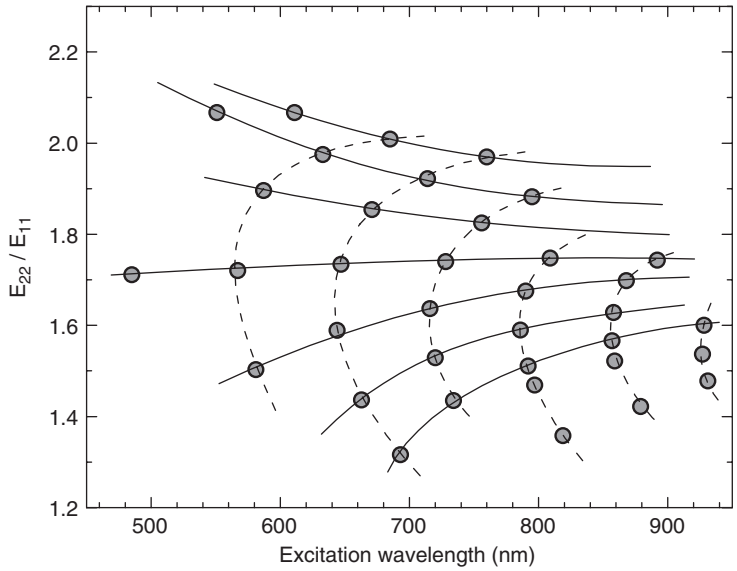

Fig. 6. Plot of the experimental photon energy ratios for excitation compared to emission as a function of excitation wavelength. The sample contained HiPco nanotubes in aqueous suspension. Points are measured values; lines indicate systematic patterns in the data.

plots were then compared for linearity. One choice was clearly superior in satisfying the expected linear relation between RBM frequency and inverse nanotube diameter, and that choice was therefore identified as the correct spectral assignment. Once the assignment was deduced, the (*n*,*m*) identities of all 33 observed peaks in Fig. 5 were immediately revealed. This provided precise experimental E_{11} and E_{22} transition energies for a large set of semiconducting nanotube species spanning a substantial range of diameters and chiral angles. Fig. 7 shows the identified and labeled E_{11} and E_{22} wavelengths for SWNTs in aqueous SDS suspension.

4. FURTHER OBSERVATIONS

The discovery and structural assignment of nanotube fluorescence has triggered a large wave of spectroscopically based studies of SWNT physical and chemical properties. Not surprisingly, these further investigations have revealed greater complexity than is implied by the simple model presented above. For example, the electron and hole formed by optical excitation are not independent, as implied by the single-particle band structure sketch of Fig. 2. Instead, they remain spatially associated as an exciton with a binding energy that is much larger than would be expected in a comparable three-dimensional material. This excitonic character of nanotube optically excited states, which has a parallel in the electronic excitations

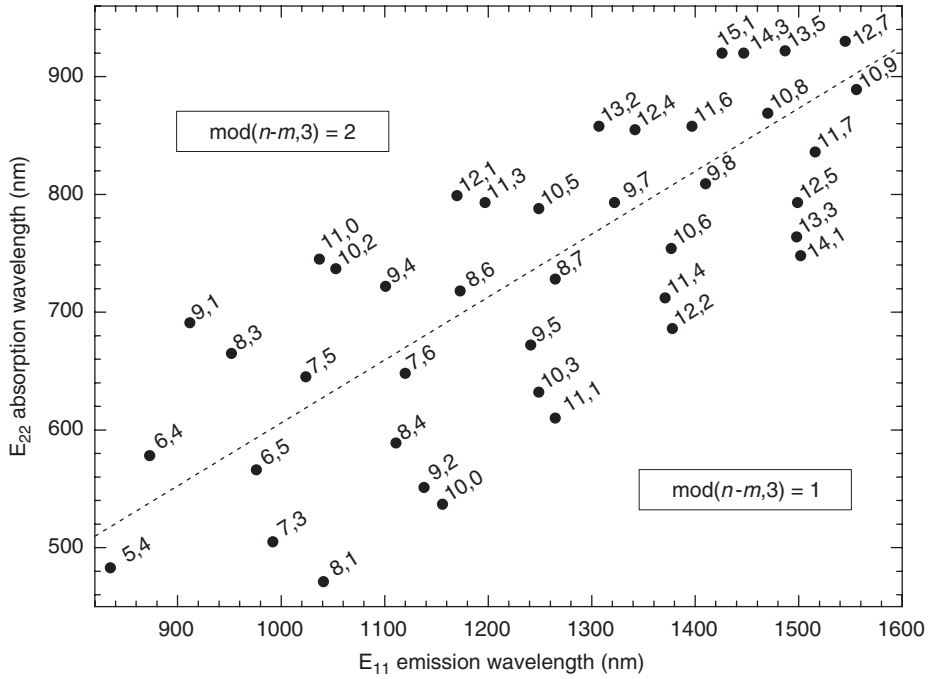

Fig. 7. Plot showing E_{22} absorption wavelengths and E_{11} emission wavelengths for a variety of SWNT in SDS aqueous suspension. Values are based on experimental measurements. The dashed line separates regions of "mod 2" and "mod 1" species.

of "zero-dimensional" molecular systems, has been predicted and modeled in several theoretical studies [21–29]. Early experimental evidence of nanotube excitons was seen in the shape of fluorescence excitation features, which are nearly symmetric Lorentzians rather than the asymmetric profiles expected from the joint density of one-electron states in a one-dimensional system [4,30]. A number of subsequent experimental studies have provided clear corroboration and much more detailed information about SWNT excitons [12,15,31–36]. Theoretical predictions of exciton binding energies that approach 40% of the tight-binding energy gap [23] seem to be supported by experimentally deduced binding energy values near 0.4 eV for smaller diameter species [34,35]. It therefore seems surprising that one-electron band theory models, which neglect excitonic effects, are fairly successful in describing nanotube optical transition energies. This success apparently reflects the approximate cancellation of two large but opposing many-body effects: electronic self-energy and exciton binding energy [26,27]. In addition, the van Hove-dominated interband optical transitions that are expected from a band theory picture and illustrated in Fig. 2 are transformed by inclusion of excitonic effects into a single dominant transition for each matching pair of sub-bands in a given (n,m) species. Thus, the use of E_{ii} labels to classify optical transitions and the simple

correspondences between species and transition wavelengths remain valid in excitonic treatments of nanotube spectroscopy.

Another example of spectral complexity is the presence of low-intensity absorption or emission features that are distinct from a nanotube species's dominant van Hove transitions. Some of these secondary features can be assigned to transitions with simultaneous changes in a nanotube's electronic and vibrational states, equivalent to vibronic transitions in molecules or phonon side-bands in solid state spectroscopy [15,37]. Others may reflect transitions to higher-energy excitonic states [15,35]. Energy transfer between different species of semiconducting nanotubes can give emission at the acceptor's wavelength following excitation of a transition in the energy donor. Finally, some weak optical features may also be assignable to E_{ij} cross-transitions between different sub-bands [38]. In contrast to the dominant E_{ii} features, selection rules for such cross-transitions require the light to be polarized perpendicular to the nanotube axis. The systematic observation and assignment of cross-transitions will provide important new insights into nanotube band structure and many-body effects.

Fluorescence appears to be the optical property of nanotubes that is most sensitive to sample condition. The most obvious example of this is the virtual absence of near-IR emission from nanotubes that have aggregated into bundles held together by van der Waals forces. It seems likely that this effect arises from efficient energy transfer within the bundle. Statistically, approximately one-third of the nanotubes in a raw sample are expected to be metallic. There is therefore a high probability that randomly formed bundles containing at least several nanotubes will include one or more metallic tubes. When a bundled semiconducting SWNT absorbs light, electronic coupling with its neighbors causes excitation transfer to species with smaller band gaps and eventually to a metallic nanotube, in which the excitation must relax nonradiatively. This efficient fluorescence quenching process allows one to use emissive yield as a sensitive monitor of SWNT aggregation.

Variations of fluorescence quantum yield with temperature reflect the combined temperature dependencies of competing radiative and nonradiative decay channels. In nanotubes, these channels include nonradiative relaxation from the optically excited state (generally E_{22} or higher) to the E_{11} excited state, and subsequent decay of the E_{11} excitation through either radiative emission or nonradiative relaxation. Recent considerations of "dark" nanotube exciton states, which have optical transitions to the ground state that are forbidden by symmetry selection rules or by triplet spin character, suggest that both radiative and nonradiative processes in nanotubes may depend strongly on phonon population, and therefore on temperature [39,40]. Experimentally, it has been reported that certain SWNT species show more than an order of magnitude intensification of their fluorescence emission as samples are cooled from ambient to cryogenic temperatures [41,42]. Further studies along these lines will surely prove important for basic and applied nanotube research.

Fluorescence efficiency can also be sensitive to chemical environment. The addition of acid to aqueous suspensions of pristine SWNT in ionic surfactants causes fluorescence quenching that can be reversed by the addition of base to

restore pH to a neutral or alkaline value [43–45]. Such quenching differs from the complete and essentially irreversible loss of near-infrared fluorescence caused by many oxidative acid treatments that are commonly applied to raw SWNT material to remove residual metallic catalysts. (This is why nanotube fluorescence was discovered only through the use of "unpurified" samples.) In addition, many chemical reactions that derivatize nanotube sidewalls inhibit fluorescence. It seems likely that the perturbation of a nanotube's π-electron system by the chemical conversion of scattered carbon atoms from sp^2 to sp^3 hybridization produces sites for efficient nonradiative recombination of excitons. Although such chemical derivatization also leads to the characteristic D-band in Raman spectra and the loss of van Hove structure in electronic absorption spectra, fluorescence is lost significantly before the onset of these other spectroscopic symptoms. This high sensitivity of fluorescence quantum yield to sidewall defects may reflect the mobility of excitons along the tube axis. Through such motion the electronic excitation can visit relatively large segments of a nanotube during its lifetime and undergo efficient quenching by sparse defect sites.

Another important effect is the sensitivity to external environment of SWNT optical transition energies. With every carbon atom occupying a surface site, SWNTs more closely resemble molecules than solids in terms of exposure to surroundings. It is therefore not surprising that nanotubes should mimic the well-known spectral variations observed for a molecular solute dissolved in different solvents. One would expect E_{11} transitions to be more environmentally sensitive than the E_{22}, E_{33},... transitions, which involve deeper valence states that are analogous to core orbitals and interact more weakly with the surroundings. In fact, such a pattern seems to be present in the limited systematic observations reported to date. Data are available for E_{11} and E_{22} transitions of SWNT that are dissolved in polymeric films, or suspended in air between pillars over a silicon surface [46,47], or in water surrounded by various surfactants [48]. It appears that E_{11} transitions red-shift by ca. 28 meV and E_{22} transitions by ca. 16 meV in aqueous SDS suspension as compared to an air environment [46]. These represent relative transition energy changes of approximately -3% and -1% for E_{11} and E_{22}. When SDS or SDBS is replaced by other synthetic surfactants, E_{11} red-shifts of up to 3% are observed. Finally, when biopolymers such as proteins or DNA are used as aqueous suspending agents, SWNT E_{11} transitions shift still further to lower energies [49,50]. However, because these overall environmental spectral shifts are relatively small and seem to be fairly systematic, it is feasible to adapt the (n,m) assignments deduced from aqueous SDS suspensions to assign spectral features in other media. Furthermore, the limited magnitudes of environmental shifts provide confidence that spectral patterns revealed in studies of aqueous suspensions reflect the intrinsic electronic properties of SWNTs.

Nanotube environment also affects the observed emission line widths. The smallest full-widths at half-maximum normally found in bulk aqueous suspensions are approximately 22 meV with ionic surfactants SDBS and sodium cholate. Nonionic polymeric surfactants such as Pluronic broaden fluorescence features by ca. 35%, and biopolymers can give comparable or even greater broadening. The

SWNT emission profiles reflect both homogeneous (Lorentzian) and inhomogeneous (Gaussian) broadening components. Nearly Lorentzian emission profiles have been observed from individual nanotubes at ambient temperature [47,51]. Microscopic studies on dilute SWNT in polymeric films have recently revealed small (ca. 3 meV) differences in the emission peak position between opposite ends of a slightly bent single nanotube [52]. This illustrates that inhomogeneous spectral broadening can occur within a single nanotube, as different segments along the tube's axis act as independent fluorophores. Polarization-dependent measurements in the same report confirmed that optically generated excitons were not able to travel ca. 3 μm between the ends of a bent SWNT during their lifetime [52]. Studies at cryogenic temperatures have found complex spectral behavior, with SWNT emission line widths as narrow as 1 meV and multiple peak positions from a single-nanotube type [42,53]. This behavior may reflect the trapping of excitons along the tube axis because of reduced mobility at very low temperatures. Temperature-dependent studies of bulk SWNT suspensions have shown that cooling causes the pattern of transition frequencies shown in Fig. 6 to become even more splayed, with systematic, (n,m)-dependent changes in E_{11} and E_{22} [41]. These complex and reversible spectral shifts, in which some transition frequencies increase while others decrease, have been attributed to nonuniform nanotube strain induced by thermal contraction or expansion of the host medium. By contrast, the application of isotropic hydrostatic pressure at fixed temperature induces spectral displacements that vary with (n,m) but shift consistently to lower frequency [54].

5. SPECTROSCOPIC APPLICATIONS

5.1. SWNT Electronic Structure Eludication

Although the visible and near-infrared optical transitions of nanotubes in aqueous surfactant suspension are broad by the standards of gas phase molecular spectroscopy, their center frequencies can often be measured to a relative precision of ca. 0.2 or 0.1%, respectively. Fig. 8 shows measured transition wavelengths as a function of deduced nanotube diameter. The experimental precision is sufficient to reveal novel patterns in SWNT electronic structure and severely challenge many approximate theoretical models. For example, the experimental variations in transition energies with chiral angle significantly exceed the trigonal warping effects predicted from simple tight-binding modeling. Fig. 8 also shows the segregation of semiconducting SWNT families into two groups. In one of these groups the value of mod $(n–m,3)$ equals 1, while in the other group it equals 2. As expected, the E_{22}/E_{11} ratios found from spectral data vary with diameter, chiral angle, and mod $(n–m,3)$ group, but Fig. 9 shows that the measured ratios extrapolate to a value near 1.8 in the limit of armchair chirality, rather than to the value of 2 predicted by band theory models. This discrepancy, termed the "ratio problem" [22], has spurred incisive efforts to compute and understand the role of many-body effects in SWNT spectroscopy [22,26–28,55,56]. The spectroscopic findings are thus playing a

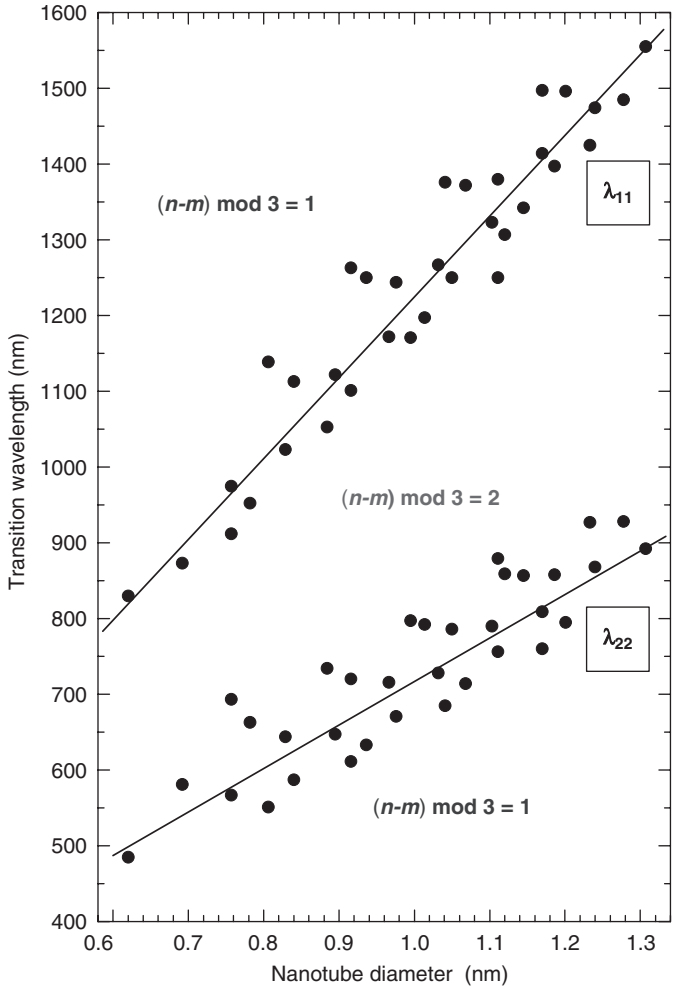

Fig. 8. Plot showing experimental wavelengths of E_{11} and E_{22} transitions in a sample of HiPco nanotubes in SDS/D_2O suspension. Solid lines separate regions of "mod 1" and "mod 2" species.

valuable role in stimulating and guiding the refinement of nanotube electronic structure theories.

5.2. SWNT Sample Characterization

The difficulty of sample characterization currently poses a serious obstacle to progress in nanotube basic research, applied research, and commercialization.

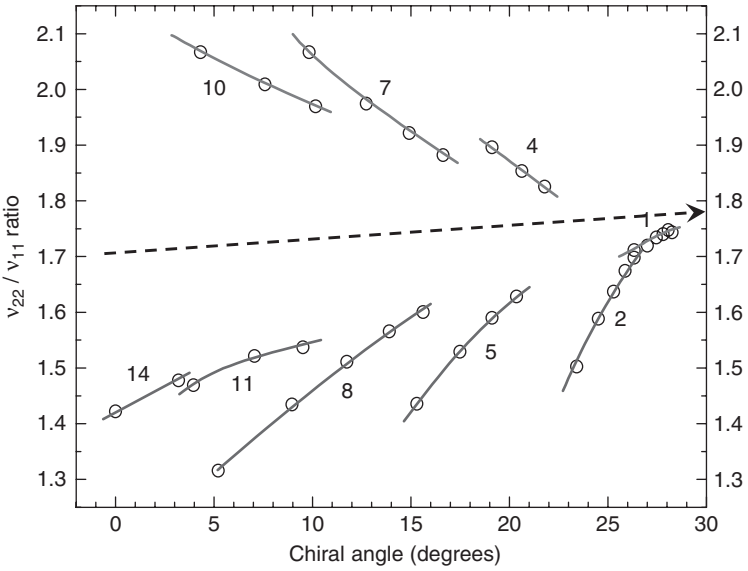

Fig. 9. Plot of the measured ratio of excitation to emission frequencies versus nanotube chiral angle for SWNT in SDS/D_2O suspension. The points show experimental data and the lines connect points for species in the same (*n–m*) family. Labels show those (*n–m*) values. The dashed line illustrates an extrapolation of the ratio trend to the armchair limit of 30°. A limiting ratio of approximately 1.8 is indicated.

In addition to their important use in elucidating basic nanotube physics, structure-assigned optical spectra have major value for such nanotube sample analysis. One of these applications involves the widespread use of resonance Raman spectroscopy as a characterization tool. In this method the Raman excitation laser must have a photon energy quite close to an E_{ii} optical resonance in order to generate conveniently intense scattering signals, so it is necessary to select laser wavelengths appropriate for the SWNT species of interest. Such matching of nanotube diameters to E_{ii} values has generally been guided by "Kataura plots" representing parameterized tight-binding model calculations. The spectroscopically determined transition energies have now been accurately fit to empirical functions of diameter and chiral angle to permit reliable extrapolation to a wide range of semiconducting species [57]. When these empirically based values for semiconducting E_{11} and E_{22} transitions are compared with Kataura plots based on simple tight-binding calculations, significant errors of ca. 15% are apparent, as can be seen from Fig. 10. The model plots seriously underestimate the E_{11} transition energies and the variation of those energies with chiral angle. The empirically based plot of E_{11} and E_{22} transition energies versus diameter therefore offers much more reliable guidance for many Raman nanotube investigations. It also serves as a reference for calibrating enhanced theoretical models that will be useful for predicting optical

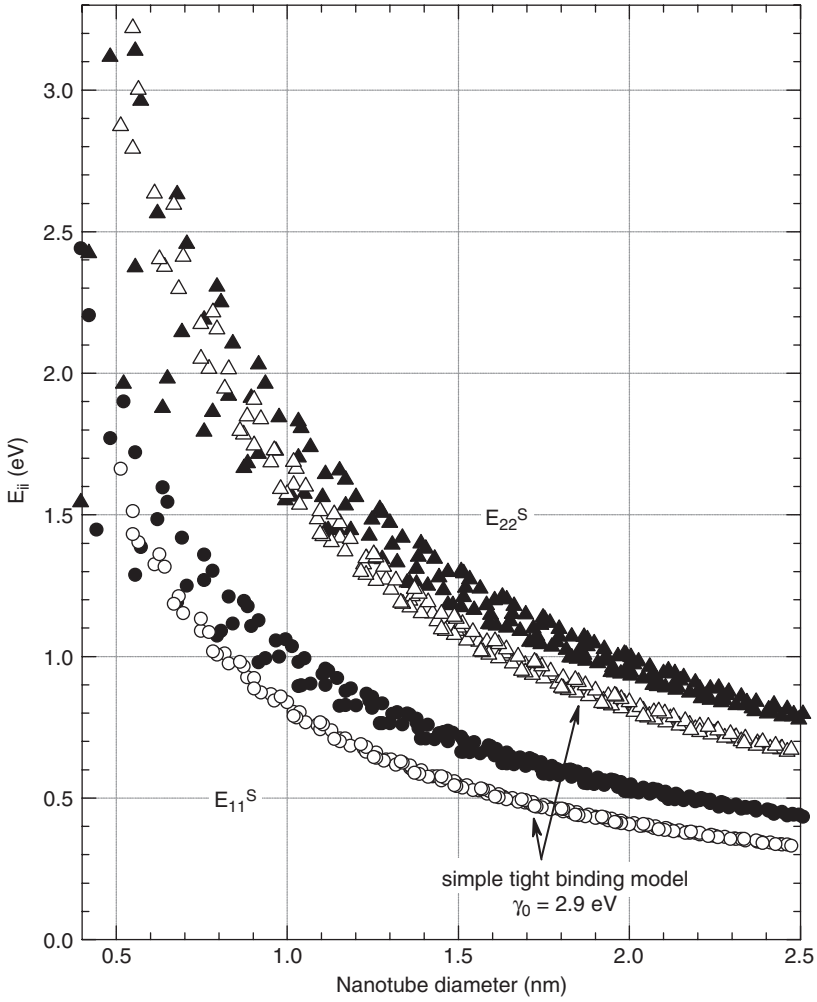

Fig. 10. Comparative "Kataura plots" showing optical transition energies as a function of nanotube diameter for the first and second van Hove transitions of semiconducting SNWT. Solid symbols are precise empirical extrapolations of experimental values, and open symbols are values computed using the simple tight-binding model. Adjustment of the γ_0 parameter cannot bring the model into agreement with experiment.

transitions of metallic nanotubes and higher van Hove transitions of semiconducting species.

The most powerful analytical application of structure-assigned optical spectra uses fluorimetry to deduce the detailed composition of SWNT samples. Recall that nearly all SWNT samples contain nanotubes with a variety of diameters and chiral angles. Following optical excitation in an E_{22} or higher transition, each

semiconducting species in a sample will emit near-infrared light at a wavelength characteristic of its (*n*,*m*) identity. By measuring this emission intensity as a function of excitation and emission wavelengths and using the optical assignment findings described above to identify the (*n*,*m*) species corresponding to each peak, one can compile an inventory of semiconducting nanotube species present in the sample.

In many applications, it is useful to have quantitative analyses in addition to a qualitative inventory. True quantitation is challenging because nanotube species may differ as to absorptivities in the excitation transition and quantum yields for E_{11} emission. However, if one assumes that these variations are minor over the range of structures present in a given sample, then the relative concentrations of (*n*,*m*) species may be directly deduced from their fluorescence intensities. This assumption is supported by the expectation that systematic variations in optical factors with structure will reverse sign between E_{11} and E_{22} transitions, giving partial cancellation of fluorimetric sensitivity variations for E_{22} excitation and E_{11} detection. We note that estimating a bulk sample's (*n*,*m*) composition from resonance Raman spectroscopy is much more challenging because of the need to use a wide variety of exciting laser wavelengths, the likelihood that Raman cross-sections depend strongly on diameter and chirality, and the double involvement of a single E_{ii} transition. An important near-term goal for the field of nanotube fluorimetry is to calibrate optical signal strengths against independently measured species concentrations so as to enable convenient quantitative (*n*,*m*)-level analyses.

Barriers to using fluorimetry as a routine tool for bulk sample characterization have included cumbersome instrumentation, relatively slow data collection, and manual data interpretation. Fortunately, these drawbacks have recently been overcome. Although a full two-dimensional scan of emission intensity as a function of excitation and emission wavelengths offers the most complete fluorimetric characterization, it is in fact practical to obtain nearly equivalent information from just two or three emission spectra excited by discrete, well-chosen wavelengths. This approach exploits the relatively large Lorentzian widths of nanotube E_{22} transitions to achieve off-resonance excitation of numerous species using a fixed monochromatic light source. Instrumentation designed for efficient fluorimetric analysis may contain diode lasers for E_{22} excitation and a near-IR spectrograph with multichannel detector for capturing emission spectra without wavelength scanning. The lasers provide excitation intensities several orders of magnitude higher than monochromated arc lamp sources, while occupying less much laboratory space. An instrument of this type can acquire very-high-quality emission spectra from typical aqueous SWNT dispersions quite quickly. Fig. 11 shows such a fluorescence spectrum measured with an acquisition time of only 500 ms.

Because the monochromatic diode lasers excite a variety of (*n*,*m*) species, sample emission spectra show complex superpositions of peaks representing the E_{11} fluorescence of many semiconducting nanotube structures. To interpret such spectra, one applies prior spectroscopic knowledge of the E_{11} peak emission frequencies for those (*n*,*m*) species that may be present in the sample. Using additional information about the typical Voigt emission line profiles, a measured

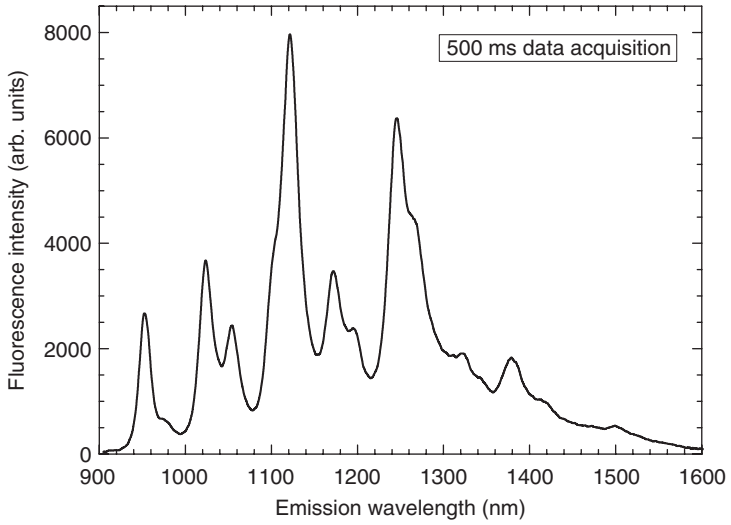

Fig. 11. Emission spectrum measured from a suspension of HiPco nanotubes in aqueous SDBS suspension using 658 nm excitation. The data were collected in 500 ms using an instrument designed for efficient fluorimetric analysis of nanotube samples. (Figure courtesy of Applied NanoFluorescence, LLC.)

spectrum may be quickly computer-simulated as a sum of individual species components to obtain the sample's (*n*,*m*) inventory. Relative amplitudes deduced in this fitting will not match those from peaks in full two-dimensional spectrofluorimetry until they have been adjusted by factors reflecting the mismatch between the laser wavelength used for excitation and the peak E_{22} wavelengths of the (*n*,*m*) species. After applying such adjustment factors, however, one obtains a sample analysis comparable to that from two-dimensional data, except with much faster data collection. Moreover, both the data acquisition and spectral data analysis can be automated to allow routine, rapid sample characterization with minimal operator input or expertise. Because this method relies on SWNT fluorescence, it is not suitable for observing metallic or semimetallic SWNT species, bundled nanotubes, or nanotubes that have been substantially chemically damaged or derivatized. It is most effective for deducing the (*n*,*m*) content of samples containing smaller diameter SWNT (below ca. 1.2 nm), for which the average separation between E_{11} frequencies is large enough to avoid severe spectral congestion in emission. However, fluorescence analysis can also be used with larger diameter samples to deduce diameter distributions without resolving populations at the level of individual (*n*,*m*) species. It appears that the development of commercialized automated systems for fluorimetric SWNT analysis will provide a valuable new characterization tool for a wide range of laboratories engaged in nanotube basic research, applications development, or production quality control.

5.3. SWNT Detection and Imaging

An emerging application of SWNT fluorescence exploits near-infrared fluorescence to detect the presence of nanotubes and visualize their locations. Although the emissive quantum yield of nanotubes (as estimated from aqueous dispersions) seems to be only near 10^{-3}, their emission lies in a spectral region that is nearly free of luminescent background from natural materials. This absence of emissive background interference plus the characteristic spectral signature of SWNT fluorescence make it possible to selectively detect very small relative concentrations of nanotubes embedded in complex sample environments. Fluorescence detection is therefore an appealing approach to finding and quantifying trace amounts of pristine SWNTs in environmental or biological specimens. As the remarkable properties of SWNTs lead in the future to increased and possibly large-scale use in industrial products, concerns will arise about safe nanotube disposal and possible environmental impact. Effective methods of analysis will be needed to address such concerns. SWNT analytical methods will also be essential for studying the fate of nanotubes introduced into organisms through unintended exposure or through administration of nanotube-based medical agents.

Analytical options are quite limited for such specimens. Because of the high carbon content in the surroundings, SWNTs obviously cannot be determined by elemental analysis. High-resolution microscopies such as TEM, STM, and AFM are extremely useful for observing nanotubes in clean samples on specialized substrates, but they face the problem of finding a "carbon needle in a haystack" for specimens dense with complex organic components or biopolymers. Radiotracer methods would be effective but probably require the preparation of SWNT samples containing ^{14}C, a difficult task. Like fluorescence, resonance Raman spectroscopy offers sensitivity down to the single-nanotube level [58]. However, the resonance-enhanced Raman signals from tiny fractional concentrations of SWNT can be obscured by overlapping background fluorescence, intense elastic scattering, or nonresonant Raman scattering from other molecular species that comprise the bulk of the sample. By comparison, near-IR SWNT fluorescence is conveniently excited by E_{22} transitions, which typically lie ca. 5000 cm^{-1} above the E_{11} emission. Because of this large shift, which exceeds the fundamental Raman frequencies of any organic compound, there is no Raman scattering interference at the wavelengths used to detect SWNT fluorescence. Furthermore, endogenous or background luminescence from biological materials is extremely weak at the relevant detection wavelengths beyond ca. 1100 nm. These factors currently enable detection of SWNT emission with high signal-to-background ratios from cells and tissues that contain nanotubes at parts-per-million concentrations. Substantially improved sensitivity and selectivity will be attained in the future by using specially grown or sorted SWNT samples composed mainly of individual semiconducting (n,m) species [59]. With such samples, optical efficiency can be greatly enhanced through the use of resonant excitation wavelengths and narrow-band spectral filtering of emission.

A particularly exciting development is the use of near-infrared fluorescence microscopy to visualize the locations of pristine (underivatized) nanotubes in media

including solid films, liquid suspensions, and biological cells and tissues [50,52]. Because much of the SWNT emission lies at wavelengths beyond the range of silicon-based cameras, it is necessary to use relatively exotic imagers built from arrays of InGaAs photodiodes. These detectors have the disadvantages of high cost, low resolution, imperfections, and high dark current, but they provide high quantum efficiencies for detection within the 900–1600 nm range typical of many SWNT samples. A conventional optical microscope can be relatively simply adapted for SWNT microscopy by adding a diode laser suitable for sample excitation, appropriate filters and dichroic optics, and the near-IR imager. Fig. 12 is a near-IR fluorescence micrograph recorded from emission between 1125 and 1600 nm using such a modified microscope. The image shows nanotube fluorescence from a macrophage-like cell that had been incubated in a growth medium containing suspended SWNT [50]. Two significant findings are immediately evident. First, the luminescent nanotubes are not uniformly distributed throughout the cell's cytoplasm but are instead concentrated in a number of small intracellular structures. These are believed to be phagosomes. Second, areas of the cytoplasm outside of these structures appear as dark as the region surrounding the cell, indicating the very low level of endogenous fluorescence background in the observed spectral range and the resulting excellent contrast attained despite the low

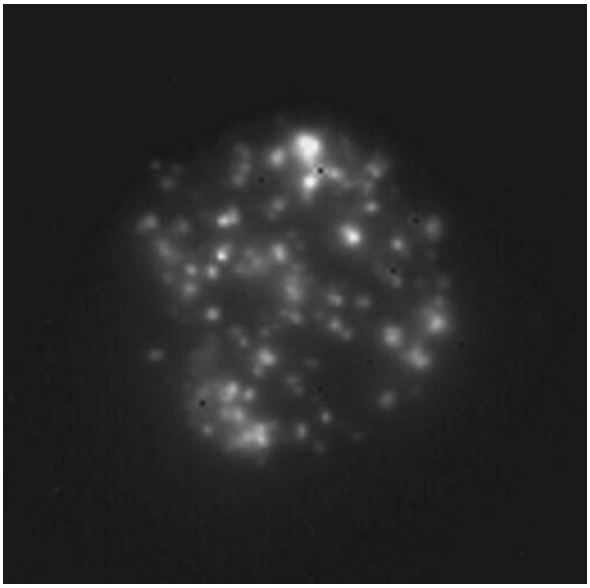

Fig. 12. Near-infrared fluorescence micrograph of a single macrophage-like cell that had been incubated in a growth medium containing suspended SWNT. The sample was excited at 658 nm and the image shows emission at wavelengths between 1125 and 1600 nm. The only significant emission under these conditions is from ingested nanotubes. The cell's diameter is approximately 25 μm.

quantum yield of SWNT emission. By adapting a confocal scanning microscope for near-IR nanotube detection, it should be possible in the future to improve spatial resolution by the ratio of emission to excitation wavelengths, a factor of approximately 2, although at some cost in data acquisition time.

Near-IR fluorescence imaging appears to be rapidly evolving into a practical method for visualizing the distributions of SWNTs inside biological cells, tissues, and even intact organisms. This application is favored by the reported steady fluorescence from nanotubes under conditions that cause rapid photobleaching of organic fluorophores or blinking between on and off states in inorganic quantum dots [51], and also by the weaker absorption and scattering in tissues of near-IR as compared to visible light. It should soon prove possible to monitor the location, orientation, and motions of single SWNTs in cells through in vitro near-IR fluorescence microscopy. If covalent or noncovalent derivatization methods can be developed that allow nanotubes to remain fluorescent after linkage to biological targeting agents such as antibodies or peptides, then SWNTs may form the basis for a new class of near-IR bio-markers useful in laboratory research. Targeted nanotubes may also have potential as near-IR fluorescent contrast agents that could be noninvasively detected or imaged from inside human patients to enable novel modes of medical diagnosis.

6. SUMMARY

SWNTs form a family of artificial nanomaterials with a rich, unusual, and useful array of optical spectroscopic properties. Each structural species of semiconducting nanotube displays not only a set of intense and distinct absorption transitions ranging from near-infrared to ultraviolet wavelengths, but also well-defined fluorescent band-gap photoluminescence in the near-infrared. The discovery of this fluorescence emission allowed the complex superposition spectra shown by structurally mixed nanotube samples to be dissected by spectrofluorimetric experiments and then deciphered by careful data analysis. A large set of absorption and emission features were thereby successfully assigned to specific structural species of nanotubes. The results provide a valuable body of precise experimental data that have led to greatly improved understanding of nanotube electronic structure and the role of many-body effects in their optically excited states. The secure assignment of spectral features to nanotube structures has also formed the basis for efficient optically based methods for deducing the detailed composition of bulk nanotube mixtures. These new analytical tools should support and accelerate progress in basic research, applied research, and commercial use of carbon nanotubes. Finally, the unusual near-infrared fluorescence wavelengths of semiconducting nanotubes enhance the value of emission methods for detecting and visualizing nanotubes in complex environmental and biological specimens. Active research projects underway in many laboratories are advancing nanotube chemical modification, near-infrared imaging instrumentation, and knowledge of nanotube–biological interactions. Supported by progress in these areas, the unique

optical properties of SWNT may eventually let them play important roles in medical research and clinical applications.

ACKNOWLEDGEMENTS

The author gratefully acknowledges the vital creative contributions of his co-workers and collaborators, and research support from National Science Foundation (grant CHE-0314270), Rice's NSF-supported Center for Biological and Environmental Nanotechnology (under grant EEC-0118007) and the Welch Foundation (grant C-0807).

REFERENCES

[1] R. Saito, G. Dresselhaus and M.S. Dresselhaus, *Physical Properties of Carbon Nanotubes* (Imperial College Press, London, 1998).
[2] M.S. Dresselhaus, G. Dresselhaus and P. Avouris (Eds), *Carbon Nanotubes: Synthesis, Structure, Properties, and Applications* (Springer-Verlag, New York, 2001).
[3] S. Reich, J. Janina and C. Thomsen, *Carbon Nanotubes: Basic Concepts and Physical Properties* (Wiley, New York, 2004).
[4] J.W. Mintmire and C.T. White, Universal density of states for carbon nanotubes, *Phys. Rev. Lett.* **81**, 2506–2509 (1998).
[5] A. Ugawa, A. Rinzler and D.B. Tanner, Far-infrared gaps in single-wall carbon nanotubes, *Phys. Rev. B* **60**, R11305–R11308 (1999).
[6] M.E. Itkis, S. Niyogi, M.E. Meng, M.A. Harmon, H. Hu and R.C. Haddon, Spectroscopic study of the Fermi level electronic structure of single-walled carbon nanotubes, *Nano Lett.* **2**, 155–159 (2002).
[7] C.L. Kane and E.J. Mele, Size, shape, and low energy electronic structure of carbon nanotubes, *Phys. Rev. Lett.* **78**, 1932–1935 (1997).
[8] T. Pichler, M. Knupfer, M.S. Golden, J. Fink, A. Rinzler and R.E. Smalley, Localized and delocalized electronic states in single-wall carbon nanotubes, *Phys. Rev. Lett.* **80**, 4729–4732 (1998).
[9] Y. Murakami, E. Einarsson, T. Edamura and S. Maruyama, Polarization dependence of the optical absorption of single-walled carbon nanotubes, *Phys. Rev. Lett.* **94**, 087402/1–087402/4 (2005).
[10] J.B. Birks, *Photophysics of Aromatic Molecules* (Wiley, London, 1970).
[11] M. Kasha, Characterization of electronic transitions in complex molecules, *Disc. Faraday Soc.* **9**, 14–19 (1950).
[12] Y.-Z. Ma, J. Stenger, J. Zimmerman, S.M. Bachilo, R.E. Smalley, R.B. Weisman and G.R. Fleming, Ultrafast carrier dynamics in single-walled carbon nanotubes probed by femtosecond spectroscopy, *J. Chem. Phys.* **120**, 3368–3372 (2004).
[13] G.N. Ostojic, S. Zaric, J. Kono, M.S. Strano, V.C. Moore, R.H. Hauge and R.E. Smalley, Interband Recombination Dynamics in Resonantly Excited Single-Walled Carbon Nanotubes, *Phys. Rev. Lett.* **92**, 117402/1–117402/4 (2004).
[14] S. Reich, M. Dworzak, A. Hoffmann, C. Thomsen and M.S. Strano, Excited-state carrier lifetime in single-walled carbon nanotubes, *Phys. Rev. B* **71**, 033402/1–033402/4 (2005).
[15] M. Jones, C. Engtrakul, W.K. Metzger, R.J. Ellingson, A.J. Nozik, M.J. Heben and G. Rumbles, Analysis of photoluminescence from solubilized single-walled carbon nanotubes, *Phys. Rev. B* **71**, 115426/1–115426/9 (2005).
[16] J.-P. Yang, M.M. Kappes, H. Hippler and A.-N. Unterreiner, Femtosecond transient absorption spectroscopy of single-walled carbon nanotubes in aqueous surfactant suspensions: Determination of the lifetime of the lowest excited state, *Phys. Chem. Chem. Phys.* **7**, 512–517 (2005).

[17] A.M. Rao, E. Richter, S. Bandow, B. Chase, P.C. Eklund, K.A. Williams, S. Fang, K.R. Menon, M. Menon, A. Thess, R.E. Smalley, G. Dresselhaus and M.S. Dresselhaus, Diameter-selective Raman scattering from vibrational modes in carbon nanotubes, *Science* **275**, 187–191 (1997).
[18] M.S. Dresselhaus, G. Dresselhaus, A. Jorio, A.G. Souza Filho and R. Saito, Raman spectroscopy on isolated single wall carbon nanotubes, *Carbon* **40**, 2043–2061 (2002).
[19] S. Bandow, S. Asaka, Y. Saito, A.M. Rao, L. Grigorian, E. Richter and P.C. Eklund, Effect of the growth temperature on the diameter distribution and chirality of single-wall carbon nanotubes, *Phys. Rev. Lett.* **80**, 3779–3782 (1998).
[20] G.S. Duesberg, W.J. Blau, H.J. Byrne, J. Muster, M. Burghard, L.J. Rothberg and S. Roth, Experimental observation of individual single-wall nanotube species by Raman microscopy, *Chem. Phys. Lett.* **310**, 8–14 (1999).
[21] T. Ando, Excitons in carbon nanotubes, *J. Phys. Soc. Jpn.* **66**, 1066–1073 (1997).
[22] C.L. Kane and E.J. Mele, Ratio problem in single carbon nanotube fluorescence spectroscopy, *Phys. Rev. Lett.* **90**, 207401/1–207401/4 (2003).
[23] T.G. Pedersen, Variational approach to excitons in carbon nanotubes, *Phys. Rev. B* **67**, 073401/1–073401/4 (2003).
[24] E. Chang, G. Bussi, A. Ruini and E. Molinari, Excitons in carbon nanotubes: An *ab initio* symmetry-based approach, *Phys. Rev. Lett.* **92**, 196401/1–196401/4 (2004).
[25] H. Zhao and S. Mazumdar, Electron–electron interaction effects on the optical excitations of semiconducting single-walled carbon nanotubes, *Phys. Rev. Lett.* **93**, 157402/1–157402/4 (2004).
[26] C.L. Kane and E.J. Mele, Electron interactions and scaling relations for optical excitations in carbon nanotubes, *Phys. Rev. Lett.* **93**, 197402/1–197402/4 (2004).
[27] C.D. Spataru, S. Ismail-Beigi, L.X. Benedict and S.G. Louie, Excitonic effects and optical spectra of single-walled carbon nanotubes, *Phys. Rev. Lett.* **92**, 077402/1–077402/4 (2004).
[28] V. Perebeinos, J. Tersoff and P. Avouris, Scaling of excitons in carbon nanotubes, *Phys. Rev. Lett.* **92**, 257402/1–257402/4 (2004).
[29] V. Perebeinos, J. Tersoff and P. Avouris, Electron–phone interaction and transport in semiconducting carbon nanotubes, *Phys. Rev. Lett.* **94**, 086802/1–086802/4 (2005).
[30] M. O'Connell, S.M. Bachilo, C.B. Huffman, V. Moore, M.S. Strano, E. Haroz, K. Rialon, P.J. Noon, W.H. Noon, C. Kittrell, J. Ma, R.H. Hauge, R.B. Weisman and R.E. Smalley, Band-gap fluorescence from individual single-walled carbon nanotubes, *Science* **297**, 593–596 (2002).
[31] C. Manzoni, A. Gambetta, E. Menna, M. Meneghetti, G. Lanzani and G. Cerullo, Intersubband exciton relaxation dynamics in single-walled carbon nanotubes, *Phys. Rev. Lett.* **94**, 207401/1–207401/4 (2005).
[32] S.G. Chou, F. Plentz, J. Jiang, R. Saito, D. Nezich, H.B. Ribiero, A. Jorio, M.A. Pimenta, G.G. Santos, A.P. Santos, M. Zheng, G.B. Onoa, E.D. Semke, G. Dresselhaus and M.S. Dresselhaus, Phonon-assisted excitonic recombination channels observed in DNA-wrapped carbon nanotubes using photoluminescence spectroscopy, *Phys. Rev. Lett.* **94**, 127402/1–127402/4 (2005).
[33] C.-X. Sheng, Z.V. Verdeny, A.B. Dalton and R.H. Baughman, Exciton dynamics in single-walled nanotubes: Transient photoinduced dichroism and polarized emission, *Phys. Rev. B* **71**, 125427/1–125427/11 (2005).
[34] Y.-Z. Ma, L. Valkunas, S.L. Dexheimer, S.M. Bachilo and G.R. Fleming, Femtosecond spectroscopy of optical excitations in single-walled carbon nanotubes: Evidence for exciton–exciton annihilation, *Phys. Rev. Lett.* **94**, 157402/1–157402/4 (2005).
[35] F. Wang, G. Dukovic, L.E. Brus and T.F. Heinz, The optical resonances in carbon nanotubes arise from excitons, *Science* **5723**, 838–841 (2005).
[36] X. Qiu, M. Freitag, V. Perebeinos and P. Avouris, Photoconductivity spectra of single-wall carbon nanotubes: Implications on the nature of their excited states, *Nano Lett.* **5**, 749–752 (2005).
[37] H. Htoon, M.J. O'Connell, S.K. Doorn and V.I. Klimov, Single carbon nanotubes probed by photoluminescence excitation spectroscopy: The role of phonon-assisted transitions, *Phys. Rev. Lett.* **94**, 127403/1–127403/4 (2005).

[38] Y. Miyauchi, M. Oba and S. Maruyama, Cross-polarized absorption of single-walled nanotubes by polarized photoluminescence excitation spectroscopy, *Phys. Rev. B* **74**, 205440/1–205440/6 (2006).
[39] C.D. Spataru, S. Ismail-Beigi, R.B. Capaz and S.G. Louie, Theory and *ab initio* calculation of radiative lifetime of excitons in semiconducting carbon nanotubes, *Phys. Rev. Lett.* **95**, 247402/1–247402/4 (2005).
[40] V. Perebeinos, J. Tersoff and P.H. Avouris, Radiative lifetime of excitons in carbon nanotubes, Los Alamos National Laboratory Preprint Archive, *Condens. Matter* 0506775/1–0506775/4 (2005).
[41] K. Arnold, S. Lebedkin, O. Kiowski, F.H. Hennrich and M.M. Kappes, Matrix-imposed stress-induced shifts in the photoluminescence of single-walled carbon nanotubes at low temperatures, *Nano Lett.* **4**, 2349–2354 (2004).
[42] J. Lefebvre, P. Finnie and Y. Homma, Temperature-dependent photoluminescence from single-walled carbon nanotubes, *Phys. Rev. B* **70**, 045419/1–045419/8 (2004).
[43] M.S. Strano, C.B. Huffman, V.C. Moore, M.J. O'Connell, E.H. Haroz, J. Hubbard, M. Miller, K. Kittrell, C. Kittrell, S. Ramesh, R.H. Hauge and R.E. Smalley, Reversible, band-gap-selective protonation of single-walled carbon nanotubes in solution, *J. Phys. Chem. B* **107**, 6979–6985 (2003).
[44] G. Dukovic, B.E. White, Z.Y. Zhou, F. Wang, S. Jockusch, M.L. Steigerwald, T.F. Heinz, R.A. Turro, N.J. Turro and L.E. Brus, Reversible surface oxidation and efficient luminescence quenching in semiconductor single-wall carbon nanotubes, *J. Am. Chem. Soc.* **126**, 15269–15276 (2004).
[45] R.B. Weisman, S.M. Bachilo and D. Tsyboulski, Fluorescence spectroscopy of single-walled carbon nanotubes in aqueous suspension, *Appl. Phys. A* **78**, 1111–1116 (2004).
[46] J. Lefebvre, J.M. Fraser, Y. Homma and P. Finnie, Photoluminescence from single-walled carbon nanotubes: A comparison between suspended and micelle-encapsulated nanotubes, *Appl. Phys. A* **78**, 1107–1110 (2004).
[47] J. Lefebvre, J.M. Fraser, P. Finnie and Y. Homma, Photoluminescence from an individual single-walled carbon nanotube, *Phys. Rev. B* **69**, 075403/1–075403/5 (2004).
[48] V.C. Moore, M.S. Strano, E.H. Haroz, R.H. Hauge and R.E. Smalley, Individually suspended single-walled carbon nanotubes in various surfactants, *Nano Lett.* **3**, 1379–1382 (2003).
[49] M. Zheng, A. Jagota, E.D. Semke, B.A. Diner, R.S. McClean, S.R. Lustig, R.E. Richardson and N.G. Tassi, DNA-assisted dispersion and separation of carbon nanotubes, *Nat. Mater.* **2**, 338–342 (2003).
[50] P. Cherukuri, S.M. Bachilo, S.H. Litovsky and R.B. Weisman, Near-infrared fluorescence microscopy of single-walled carbon nanotubes in phagocytic cells, *J. Am. Chem. Soc.* **126**, 15638–15639 (2004).
[51] A. Hartschuh, H.N. Pedrosa, L. Novotny and T.D. Krauss, Simultaneous fluorescence and Raman scattering from single carbon nanotubes, *Science* **301**, 1354–1356 (2003).
[52] D.A. Tsyboulski, S.M. Bachilo and R.B. Weisman, Versatile visualization of individual single-walled carbon nanotubes with near-infrared fluorescence microscopy, *Nano Lett.* **5**, 975–979 (2005).
[53] H. Htoon, M.J. O'Connell, P.J. Cox, S.K. Doorn and V.I. Klimov, Low temperature emission spectra of individual single-walled carbon nanotubes: Multiplicity of subspecies within single-species nanotube ensembles, *Phys. Rev. Lett.* **93**, 027401/1–027401/4 (2004).
[54] J. Wu, W. Walukiewicz, W. Shan, E. Bourret-Courchesne, J.W. Ager III, K.M. Yu, E.E. Haller, K. Bachilo, S.M. Bachilo, R.B. Weisman and R.E. Smalley, Structure-dependent hydrostatic deformation potentials of individual single-walled carbon nanotubes, *Phys. Rev. Lett.* **93**, 017404/1–017404/4 (2005).
[55] C.D. Spataru, S. Ismail-Beigi, L.X. Benedict and S.G. Louie, Quasiparticle energies, excitonic effects and optical absorption spectra of small-diameter single-walled carbon nanotubes, *Appl. Phys. A* **78**, 1129–1136 (2004).
[56] T. Ando, Excitons in carbon nanotubes revisited: Dependence on diameter, Aharonov–Bohm flux, and strain, *J. Phys. Soc. Jpn.* **73**, 3351–3363 (2004).

[57] R.B. Weisman and S.M. Bachilo, Dependence of optical transition energies on structure for single-walled carbon nanotubes in aqueous suspension: An empirical Kataura plot, *Nano Lett*. **3**, 1235–1238 (2003).
[58] M.S. Dresselhaus, G. Dresselhaus, A. Jorio, A.G. Souza Filho, M.A. Pimenta and R. Saito, Single nanotube Raman spectroscopy, *Acc. Chem. Res*. **35**, 1070–1078 (2002).
[59] M. Zheng, A. Jagota, M.S. Strano, A.P. Santos, P.W. Barone, S.G. Chou, B.A. Diner, M.S. McIean, R.S. McIean, G.B. Onoa, G.G. Samsonidze, E.D. Semke, M.L. Usrey and D.J. Walls, Structure-based carbon nanotube sorting by sequence-dependent DNA assembly, *Science* **302**, 1545–1548 (2003).

This page intentionally left blank

Chapter 6
STRUCTURAL PROPERTIES AND NANOELECTROMECHANICAL SYSTEMS APPLICATIONS

J. W. Seo and L. Forró

1. INTRODUCTION

Carbon nanotubes (CNTs) were originally discovered by S. Iijima in 1991 as a by-product of fullerene research [1]. CNTs are unique nanostructures with remarkable electronic and mechanical properties and have attracted tremendous interest worldwide. Interest from the research community first focused on their exotic electronic properties, since nanotubes can be considered as prototypes for a one-dimensional quantum wire applicable in nanometer-sized electronics. As other useful properties have been discovered, particularly strength, interest has grown in potential applications that exploit both the electronic and mechanical properties, e.g., nanomechanical and nanoelectromechanical systems (NEMS) such as nanotweezers, memory, sensors, actuators, and switches. These results have demonstrated that CNTs hold great promise for NEMS applications.

Meanwhile, researchers have made remarkable progress in synthesizing CNTs since their initial discovery [2]. Today CNTs can mainly be produced using electric arc-discharge, laser ablation, and catalytic chemical carbon vapor deposition (CVD). In all these techniques, carbon vapor condenses into tubular structures. By adding appropriate metal catalysts, which are commonly transition metals, CNTs with one single wall (single-walled carbon nanotubes, SWCNTs) or with multiple walls (multi-walled carbon nanotubes, MWCNTs) can be preferentially grown depending on the applied growth conditions.

SWCNTs preferentially bundle (Fig. 1) mostly in the form of closely packed hexagonal arrays, where individual nanotubes are held together via van der Waals interaction with a typical intertube distance of 0.33 nm. SWCNTs can also be considered as the fundamental cylindrical structure which forms the building blocks

Contemporary Concepts of Condensed Matter Science
Carbon Nanotubes: Quantum Cylinders of Graphene

ISSN: 1572-0934/doi:10.1016/S1572-0934(08)00006-1

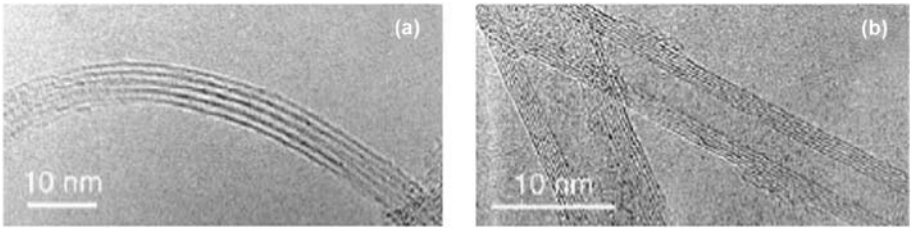

Fig. 1. TEM micrographs of (a) SWCNT bundles and (b) MWCNTs.

of MWCNTs. Hence, a MWCNT can be thought as a stack of SWCNTs with different diameters (Fig. 1). The number of cylindrical shells can vary from a double- or triple-walled CNTs with $N = 2$ or $N = 3$ up to several tens. The spacing between concentric shells can vary from 0.342 to 0.375 nm depending on the diameter and number of shells comprising the tube [3]. The interaction between the individual shells is governed by the weak van der Waals force, which makes for instance sliding of shells without friction possible. As illustrated in Section 5 this property is one of the key elements that has been exploited in several NEMS devices.

2. PREPARATION

For the growth of MWCNTs a catalyst is not necessarily required, SWCNTs can only be grown with a catalyst. However, the detailed mechanisms responsible for growth are not yet well understood. Transition metals (Fe, Co, Ni) are the most commonly used catalysts for CNT growth. The width and peak of the diameter distribution depends on the composition of the catalyst, the growth temperature, and various other growth conditions. Great efforts are now being made to produce narrower diameter distributions with different mean diameters, and to gain better control of the growth process.

The most widely used methods for CNT production are: arc-discharge, laser ablation, and synthesis by chemical CVD. All techniques are able to produce SWCNTs as well as MWCNTs.

2.1. Arc-Discharge Method

The arc-discharge method has initially been used for the production of C_{60}. This method creates nanotubes through arc-vaporization of two carbon-rod electrodes, separated by approximately 1 mm, in an enclosure that is usually filled with inert gas (usually helium or argon) at low pressure (between 50 and 700 mbar). Investigations have shown that it is also possible to create nanotubes with the arc method in liquid nitrogen [4]. A direct current (50 up to 100 A driven by

approximately 20 V) creates a high temperature discharge between the two electrodes. The discharge vaporizes one of the carbon rods and forms a deposit on the other rod. Nanotubes self-assemble from the resulting carbon vapor. The arc-discharge method yields highly graphitized tubes with structural perfection, because the manufacturing process occurs at a very high temperature (around 3000°C).

SWCNTs are mainly found in the arc chamber soot whereas MWCNTs are found in the cathode deposit. Therefore, an AC arc discharge can produce a higher yield of SWCNTs because both electrodes evaporate alternately [5]. Generally, aligned CNTs can hardly be obtained by arc discharge, although partial alignment of SWCNTs has been achieved by convection [6] or directed arc plasma [7]. In order to produce SWCNTs, the graphite-rod anode has to be doped with metal catalysts. The activity of various types of metal catalysts has been investigated [8]. The addition of S could also increase the catalytic effect of other metal catalysts [9,10].

Producing nanotubes in high yield strongly depends on the uniformity of the plasma arc and the temperature of the deposit on the carbon electrode [11]. Unfortunately, the growth by-products are usually a large amount of carbonaceous materials, such as amorphous carbon, nanoparticles, and fullerenes, which need to be removed during an appropriate purification procedure.

2.2. Laser-Vaporization Methods

The synthesis of CNTs by laser vaporization was reported in 1995 from R.E. Smalley's group at Rice University. A pulsed or continuous laser is used to vaporize a graphite target in an oven at 1200°C. The oven is filled with helium or argon gas in order to keep the pressure at 500 Torr. Upon a laser pulse, a very hot vapor plume forms, then expands and cools rapidly. As the vaporized species cool, small carbon molecules and atoms quickly condense to form larger clusters, possibly including fullerenes [12–14]. Moreover, a catalyst – supplied by doping the graphite target with the catalyst material – helps the growth of the nanotubes, presumably because it prevents the ends from being closed during synthesis, and about 70–90% of the carbon target can be converted to single-wall nanotubes [15].

The produced SWCNTs are mostly in the form of bundles consisting of several CNTs closely packed in hexagonal lattice and held together by van der Waals interactions, with a typical intertube distance of 0.33 nm.

2.3. Chemical Vapor Deposition

CVD process applies a carbon source in the gas phase through a heated tube furnace over a catalyst material. Compared with arc-discharge and laser methods, CVD is a simple and economic technique for synthesizing CNTs at low temperature (600–1200°C) and ambient pressure. It is versatile and can utilize a variety of carbon sources in any state (solid, liquid, or gas), enables the use of various

substrates, and allows CNT growth in a variety of forms, such as powder and films. Thus, CVD provides the possibility of growing CNTs from controlled surface sites by catalyst patterning on a desired substrate [16,17] for specific applications, which is not feasible by arc or laser methods. Therefore this technique is ideally suited for producing arrays of individual or a mat of aligned CNTs, e.g., for field-emission displays [18], as well as for a desired architecture of a nanotube device. CNTs have also been grown on probe tips of scanning probe microscopes (SPM).

Commonly used gaseous carbon sources have been methane, acetylene, and carbon monoxide. In the case of liquid carbon sources, an alcohol, such as methanol and ethanol, is heated in a flask and purged with an inert gas in order to carry the vapor into the reaction furnace. This alcohol-assisted growth has yielded SWCNTs at a relatively low minimum temperature of about 550°C [19].

The first CNTs produced by CVD method were multi-walled from pyrolisis of benzene at 1100°C [20]. SWCNTs were produced by Dai et al. [21] from disproportionation of CO at 1200°C, catalyzed from Mo catalyst particles. Later SWCNTs were also grown from different carbon sources, such as acetylene, methane etc., by using various catalysts. General observation is that low-temperature (600–900°C) yields MWCNTs, whereas a higher temperature (900–1200°C) is required for SWCNT growth. Therefore, MWCNTs are in general also easier to grow from most hydrocarbons compared to SWCNTs, which can only be grown from selected hydrocarbons stable at a high temperature range (e.g., CO, CH_4). Double-wall CNTs (DWCNTs) grown by CVD were first obtained by Dai et al. [21] in the soot of SWCNTs produced from disproportionation of CO. DWCNTs have currently attracted much attention because they can be considered as nano coaxial cable, when the internal tube is metallic while the outer tube is insulating [22]. A high proportion (70%) of DWCNTs has been obtained during selective reduction of $Mg_{1-x}Co_xO$ powder and addition of a Mo promoter [22,23]. Very uniform and clean DWCNTs with a narrow diameter distribution have also been prepared by using catalysts of Co loaded on porous MgO nanoparticles [24].

For CVD, the diameter of produced CNTs is strongly governed by the size of the catalyst particles. Solid organometallocenes, such as ferrocene, cobaltocene, and nickelocene, have been used in order to control the diameter distribution [25,26]. Thermal annealing generally results in cluster formation therefore the choice of the supporting material is also critical for the scalable CVD process [27–30]. In particular, recent results based on silicagel- or zeolite-supported catalysts made evident that porous materials are excellent supports in catalytic nanotube production. Al_2O_3 supports have resulted in significantly higher yields of CNTs due to their strong catalyst–support interaction, which allows high metal dispersion and, thus, a high density of catalytic sites [31,32]. Such interactions prevent metal species from aggregating and forming undesirable large clusters that lead to graphite particles or carbon fibers. MgO [30,33] and $CaCO_3$ [31,34,35] were also found to be eminent supports for high quality CNT growth and can easily be removed in a mild purification step.

Beside the most popular thermal CVD technique, many other techniques have been developed in order to improve the purity, yield, and directivity, for instance

plasma-enhanced CVD, laser-assisted CVD, and vapor phase growth. In particular, plasma-enhanced CVD has the advantage of low temperature synthesis over thermal CVD. Highly controlled growth, in terms of height, diameter, placement, and alignment of CNTs has been achieved at around 700°C and lower. For the alignment of CNTs, additional application of an electric [36] or a magnetic field [37] during synthesis was found to result in directed growth.

CVD is a well-established industrial process and offers uncomplicated control over growth parameters. Therefore, it is currently considered to be the most promising in terms of large-scale production, due to the relative ease for up-scaling the production and the purification methods. Very recently, Hata et al. [38] achieved a breakthrough in growing SWCNTs with a high efficiency and high yield by stimulating the catalytic activity by water. They obtained extraordinary dense and vertically aligned SWCNT forests with carbon purity above 99.98% when separated from the substrate. This approach is applicable for the mass production of SWCNTs as well as for realization of arrays of CNT structures in any shape and form. Therefore, it represents a significant advance toward industrial application of CNTs.

3. STRUCTURAL PROPERTIES

Intuitively, a SWCNT can be described as rolling up a graphene sheet by connecting two crystallographically equivalent sites. The circumference is given by the chiral vector $\vec{C}_h = n\vec{a}_1 + m\vec{a}_2$, where n and m are integers and $\vec{a}_1$ and $\vec{a}_2$ are unit vectors of the hexagonal honeycomb lattice of the graphene sheet (Fig. 2). Hence, the pair of integers (n, m) fully describe the tube geometry. Based on (n, m), three distinct types of CNTs can be generated: Two highly symmetrical configurations

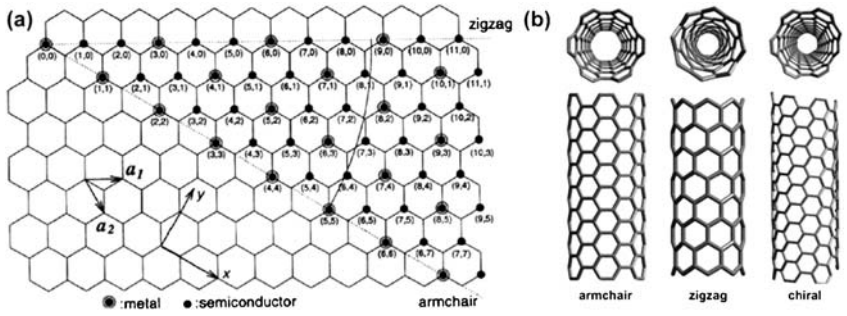

Fig. 2. (a) Schematic of the indexing method for SWCNTs [2]. A nanotube is made by folding the two-dimensional hexagonal lattice shown and matching the lattice point (n, m) with the origin. All nanotubes are uniquely defined by the (helical) angle θ and the distance from the origin to the selected lattice point. (b) Molecular models of SWCNTs exhibiting different chiralities: armchair, zigzag, and chiral arrangement. Reprinted with permission from Ref. [49]. Available at www.annualreviews.org

with $n = 0$ (or $m = 0$) and $n = m$, which correspond to zigzag- and armchair-type nanotubes with chiral angles of $\theta = 0$ and 30°, respectively. These nanotubes have a mirror plane and therefore are considered as achiral. All other nanotubes with angle $0^\circ < \theta < 30^\circ$ are chiral. The diameter of the nanotubes is given by $d = |\vec{C}_h|/\pi = (a_{c-c}/\pi)\sqrt{3(m^2 + mn + n^2)}$, where a_{c-c} is the carbon–carbon bond length. The choice of n and m determines whether the nanotube is metallic or semiconducting. In general, CNT is metallic when $n - m = 3l$, where l is an integer. Hence, all armchair nanotubes are metallic whereas two-third of all possible zigzag nanotubes are semiconducting. MWCNTs are generally metallic because the band gap in semiconducting nanotubes is inversely proportional to the tube diameter.

3.1. CNTs and Defect Structures

CNTs have been observed with a diameter down to 0.4 nm and many microns in length. The most common techniques to investigate the structure and to characterize the morphology of CNTs have been: transmission electron microscopy (TEM), scanning electron microscopy (SEM), and scanning tunneling microscopy (STM). In particular, electron diffraction (ED) has proven useful in determining the (n, m) geometric structure. Analytical techniques, such as electron energy-loss spectroscopy (EELS), associated with high-resolution TEM became a valuable and powerful tool to determine the stoichiometry of individual nanotubes, as well as the nature of the chemical bond.

Basically, sidewalls of CNTs consist of a perfect network of carbon hexagons. The most frequently observed defects are point- or planar defects, whose density strongly depends on the growth condition. A defective structure can easily be created by replacement of hexagons with pentagons or heptagons. A pentagon gives rise to a positive 30° disclination whereas a heptagon results in a negative 30° inclination. Hence, the presence of defects frequently results in bending of CNTs or in closure of walls unless pentagon–heptagon pairs are formed, which annihilate the inclinations. A nanotube relaxes its excess strain via the Stone–Wales transformation [39], which involves a 90° rotation of the C–C bond around its center (Fig. 3) and produces two pentagons and two heptagons coupled in pairs (5-7-7-5).

It is generally assumed that the growth of CNTs ends as the number of introduced pentagons and heptagons increases forming a cap, which fits continuously on the end of the long cylinder. As pentagons and heptagons are introduced under certain circumstances in a "controlled" way, special structures that will have other properties than their original forms can be created. For instance various new structures such as L-, Y-, T-branches or CNT junctions have been obtained, which are in particular of interest as electronic junctions [40]. As the defect incorporation occurs in a regular way, spirals [27,41–43] or bamboo-shaped CNTs [44–46] can be formed. Coiled tubes, which look like miniature telephone cables, do not appear when an arc-discharge or laser-vaporization process is used, therefore they are a unique feature of the catalytic CVD route. The curvature is

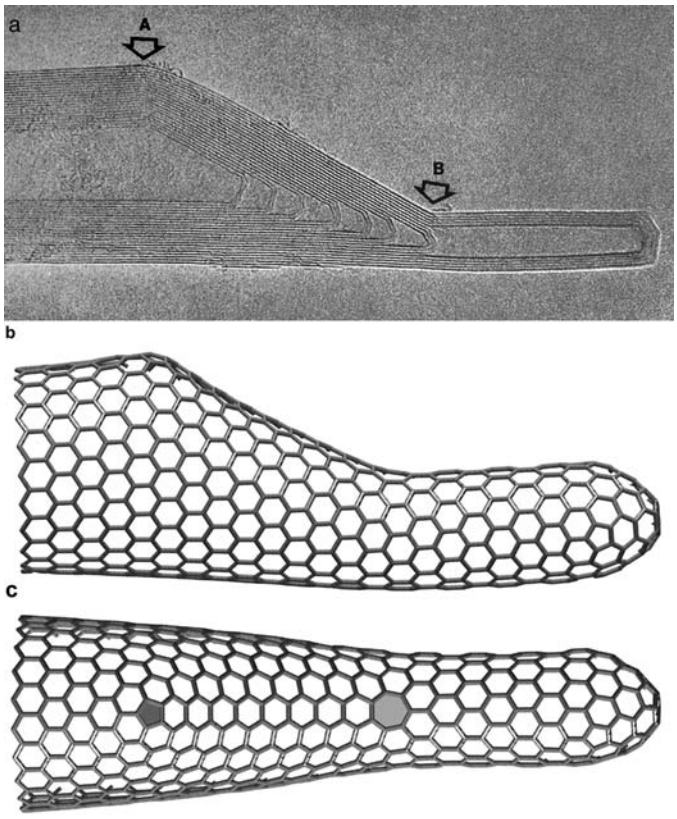

Fig. 3. (a) A nanotube structure showing curvature induced by the presence of a pentagon–heptagon pair: the $+30^\circ$ pentagon declination (marked by A) cancels the -30° heptagon inclination (marked by B). (b) and (c) Molecular model of a nanotube containing a pentagon–heptagon pair resembling the image shown in (a). Reprinted with permission from Ref. [49]. Available at www.annualreviews.org

achieved either by the formation of pentagon–heptagon pairs in the predominantly hexagonal carbon framework [47–49], as shown in Fig. 4, or by plane buckling [43]. It is assumed that helical tubes start to grow as a result of differences in local hydrocarbon decomposition rate, which originate from the asymmetry in the spherical catalyst particle. Hernadi et al. [43] have shown that the growth of coiled nanotubes can directly be tuned by the pH of the metal–salt solution during catalyst impregnation, which affects the size and the shape of the deposited catalyst particles.

Because of their unique 3D structure, CNT spirals have potential applications as mechanical components [50] such as resonating elements and nanosprings or as a novel reinforcement in high-strain composites. Other potential applications are as nanosolenoids and electromagnetic wave absorbers. Measurement of the elastic

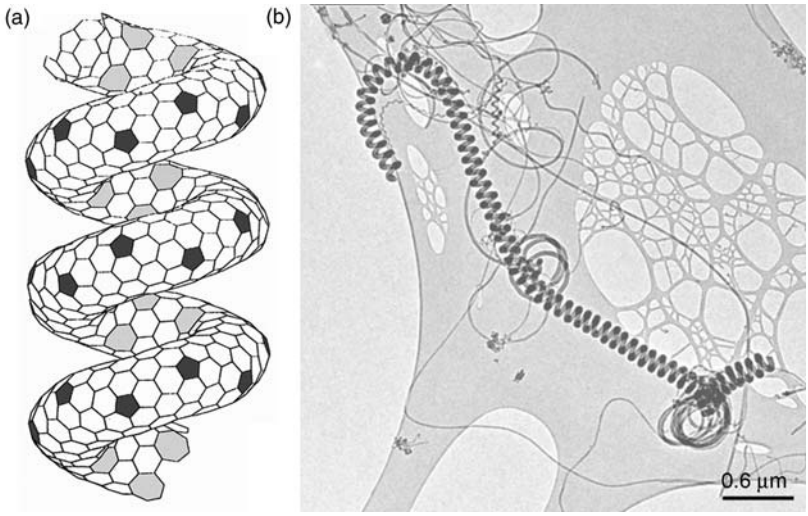

Fig. 4. (a) Molecular model of a SWCNT piral, constructed by insertion of pentagons and heptagons within the hexagonal network. Reprinted with permission from Ref. [49]. Available at www.annualreviews.org (b) coil-shaped MWCNT produced by decomposition of acetylene over Co supported on silicagel [43].

properties of coiled CNTs revealed Young modulus comparable to the very high Young modulus of hexagonal graphene sheets [51]. Hayashida et al. [52] reported a conductivity of 100–180 S/cm and Young modulus of 0.1 TPa. Motojima et al. [41] found that the coiled filaments could be elastically extended up to about three times versus the original coil length. These results suggest that carbon nanocoils have good conductivity and mechanical strength, which enable them to be applied to nanosized electronic and/or mechanical devices.

The bamboo-shaped CNTs were found first by Saito and Yoshikawa [44] in the course of encapsulation experiments by using the transition metals in arc-reactor. These graphitic tubes contained a regular series of hollow compartments and exhibited a needle-shaped catalyst particle at their ends (Fig. 5). In CVD process bamboo-structure occurs when the growth was carried out at relatively low temperature [53,54]. Numerous papers attempted to investigate the growth mechanism by examining this regular structure, which suggests a continual growth and renucleation mechanism taking place simultaneously. The distance between compartments is interpreted as indicator of the time lag between renucleation events [45].

The bamboo structure has also been found to be a characteristic feature in CNTs doped with N [55,56]. EELS and XPS measurements have revealed that two types of bonding of the N and C exist within the hexagonal network [55,57]: double and trigonally bonded N. Accordingly, pyridine-like N sites (double-bonded N) are responsible for the disorder in the graphite sheets and for interlinked morphologies, whose number increases as the overall N concentration increases [55,58,59]. In contrast, trigonally bonded N atoms are supposed to remain in plane within the

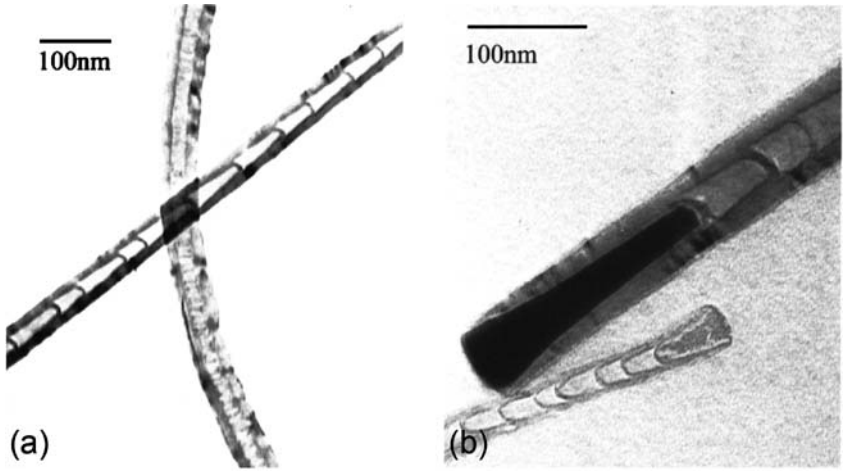

Fig. 5. (a) TEM image of bamboo-like CNT structures containing regular compartments and (b) needle-shaped Ni particle at the end of carbon nanotube. Reprinted with permission from Ref. [142]. Copyright 2000, American Institute of Physics.

hexagonal framework and constitute a stable form of carbon-nitride. Doping with B has also been found to lead to defective structures, in particular to ill-formed caps that contain a high concentration of B [60].

In contrast, BN forms nanotubes, comparable to C nanotubes [61]. They are semiconductors with a uniform large gap regardless of the radius, chirality, or the number of walls of the tube. Chopra and Zettl [62] measured the Young's modulus of BN nanotubes and found 1.22 ± 0.24 TPa. This makes BN nanotubes particularly useful for applications where a high-strength fiber of uniform electronic structure is desired.

3.2. Filled CNTs

Due to their high aspect ratio with the empty core, CNTs reveal a unique capillary behavior [63]. In the SWCNT production using laser-vaporization and arc-discharge techniques, C_{60} molecules can also be created and trapped in SWCNTs forming the so-called carbon "peapods," which was first observed by Smith et al. [64] in SWCNTs produced by laser vaporization and a short time after by Zhang et al. [65] in arc-discharge-grown SWCNTs. Upon high temperature annealing, encapsulated C_{60} molecules within the hollow core of the SWCNT are found to coalesce into interior tubes with a structural perfection and a diameter of 0.7 nm, forming a DWCNTs, while the surrounding SWCNT acts as a reaction container. Because of different nanotube diameters of the inner and outer tubes of the DWCNTs and the relatively weak coupling between tubes, DWCNTs represent ideal model systems for detailed studies of tube–tube interactions [66]. Peapods can

also be produced in high yield by opening the tubes ends and/or by creating sidewall defects, which represent entrances for C_{60} in vapor phase (Fig. 6) [67]. Meanwhile, not only endohedral fullerenes can be encaged in SWCNTs but also more complex materials, such as endohedral metallofullerenes Gd@C82 (Fig. 6) [68,69] and Dy@C82 [70] as well as KI crystals [71].

Usually, catalyst particles are very often found incorporated in CNTs. Ajayan and Iijima [72] could exploit this property and could successfully open and fill CNTs by heating them in presence of molten Pb. Many other works have followed soon. Currently, one can distinguish two different routes to obtain the filling. The first route involves, as pioneered by Ajayan and Iijima [72], opening pre-existing CNTs and filling them subsequently by physical or chemical methods. CNTs readily open by heating in air at 800°C [73] due to the oxidation reaction mainly occurring at the tips of the tubes. In the physical method, the capillary forces of a molten material which has a low surface tension such as S, Cs, Rb, Se, oxides (PbO, Bi_2O_3, V_2O_5, MoO_3) or metal salts of Ag, Co, Pb have been used [74]. In the chemical method, wet chemistry resulted in high yield of filled CNTs but the filling obtained rather showed discrete crystals than homogenous filling [75].

The second route involves producing CNTs and the filling simultaneously. The most successful method for synthesis within this approach has been a modified

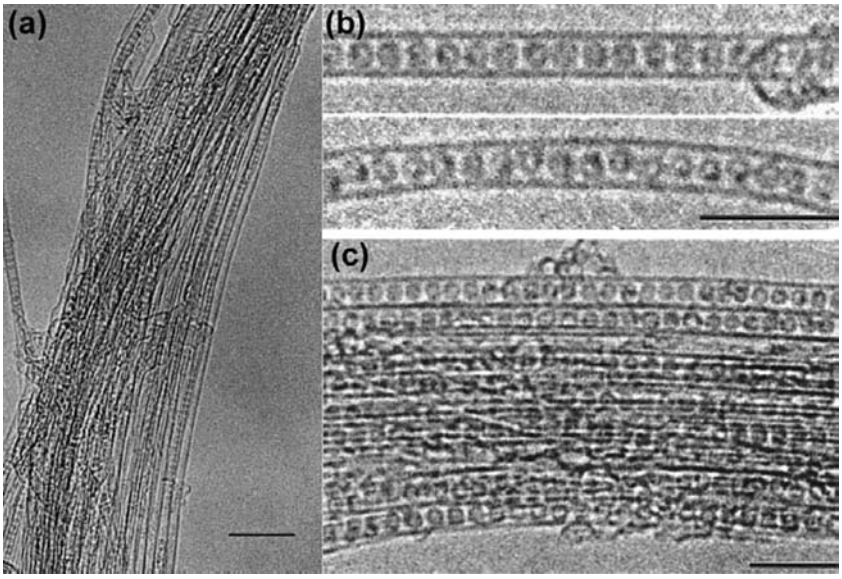

Fig. 6. (a) A bundle of nanotubes containing incorporated C_{60} (scale bar corresponds to 10 nm). Reprinted from Ref. [67], with permission from Elsevier. (b, c) HRTEM images of an isolated and bundled SWCNTs containing the Gd@C82 fullerenes. Dark spots seen on most of the fullerene cages correspond to the encapsulated Gd atoms (scale bar 5 nm). Reprinted figures with permission from Ref. [68]. Copyright 2000 by the American Physical Society.

arc-discharge method in which the anode is doped with the element to be filled into the CNTs [76]. Most of the nanotubes obtained by this method contained a filling of carbides, such as yittrium carbide [77], lanthanum carbide [78], and other carbides [55] (Ce, Gd, Ti, V, Zr, Ta, Hf, Fe, Ni, Cr, Dy, and Yb). Only a few metals such as Mn [79], Co, and Cu [80] and semiconducting elements such as Se [81], Ge, and Sb [81] have been inserted into nanotubes without carbide formation.

The parameters, which affect whether or not particular elements can be encapsulated, are still under discussion. It has been suggested that the vapor pressure of the encapsulated elements may be important by taking into account that the rare-earth metals capable of being encapsulated belong to the group of relatively low vapor pressure metals. However, Seraphin and co-workers [77] have pointed out that this criterion does not hold for transition metals, such as V, Cr, Mn, and Y, which have high vapor pressures but have been successfully encapsulated. They have rather suggested that the tendency of an element to form a carbide might be crucial, although exceptions also occur to this criterion. Loiseau and co-workers have proposed that the electronic structure of the metals may be important. They also observed that the addition of sulfur to metals (such as Cr) promotes the formation of long encapsulated nanotubes [76].

In any case, the critical parameter in the filling of nanotubes is the wetting characteristics of nanotubes, which is determined by the contact angle between the wetting liquid and the solid surface smaller than 90°. It was found that the main determining parameter is the surface tension of the wetting liquid. According to the calculation [82], no capillary action is expected for liquids with surface tensions higher than 200 mN/m, which is in agreement with the original compounds found to fill nanotubes such as lead oxides and bismuth oxides, have surface tensions that match this criteria.

CNTs have shown great potential for creating artificial materials and composites by exploiting the capillarity and template ability of their hollow interior. One direct application of the capillarity of CNTs has been demonstrated by the nanothermometer, which was developed by Gao and Bando [83]. In this nanothermometer, a CNT is filled with liquid Ga (up to about 10 μm long and 75 nm in diameter), and its height varies linearly and reproducibly in the temperature range 50–500°C, with an expansion coefficient that is the same as for Ga in the macroscopic state. In addition, the ability to encapsulate a material in a nanotube has proven to offer new possibilities for investigating dimensionally confined phase transitions, where the CNT acts as a reaction container [84,85].

At present, it is not clear if the capillarity and filling of CNTs can be useful for NEMS applications. However, mechanical properties of filled CNTs can be very different from the original carbon material. Moreover, filling provides for instance the possibility to deliver materials by using the capillary hollow core as conduit. Demonstration of this idea – by rather using the outer surface than the hollow core – was very recently reported by Regan et al. [86]. A controllable, reversible atomic scale mass transport along CNTs has been obtained by using indium metal particles decorating the outer surface of CNTs. This transport process is induced by an electrical circuit established by means of a nanomanipulator operated inside

a TEM. The current through the subject tube, which leads to thermal energy via Joule heating, can increase the local temperature past the melting point of the indium particles. Manipulation of the applied voltage produces mass transport between these nanoparticles, which serve as mass reservoirs, whereas the tube acts as nanoscale mass conveyors.

3.3. Chemical Functionalization of CNT Sidewalls

To make CNTs more accessible for the fabrication of arrays and architecture of NEMS, functionalization of the CNT surface is an important issue, for instance in order to align and attach CNTs on a substrate or to achieve local chemical activation.

The chemical reactivity of CNTs is assumed to be slightly higher than that of graphite, which is considered as chemically inert. The small difference in their chemical reactivity is due to the tip structure and the curvature of the graphene sheets [87]. Considerable effort has been devoted to the chemical modification of CNTs [88,89], which would not only assist in composite preparation [90] but also open new prospects in aligning and forming molecular devices [91] as well as generating nanoscale architectures [92]. First attempts at functionalization of CNTs were limited to a few reactions of oxidation with different oxidants [93–95], which resulted in the opening and shortening of nanotubes. After so-called ''acidic treatment,'' carboxylic groups are found on the open edges and also on places where pentagons or heptagons existed before oxidation [94]. With further functionalization of carboxylic groups, the dispersability of CNTs in different solvents was considerably improved [93–95], but in order to achieve effective incorporation of modified CNTs into the polymer matrix, the functional moieties have to be more uniformly attached to the sidewalls of the CNTs.

So far several derivatization approaches on the sidewalls of SWCNTs have been successful, such as hydrogenation via Birch reduction [96], fluorination [97], 1,3-dipolarcyclo addition of azomethine ylides [98], ozonization [99], and electrochemical reduction of aryl diazonium salts [100]. Addition of radicals generated in situ from diazonium salts also yielded functionalized SWCNTs [101]. Recently a new approach for functionalization of SWCNTs with carbon radicals was reported [102]. The approach is very promising for large-scale functionalization of SWCNTs since the reaction is performed without any solvent. Carbon radicals are highly reactive species and can be in general generated in three different ways: photochemically, thermally, and in oxidation–reduction reactions. Functionalization of SWCNTs by radical addition is a relatively simple but an efficient technique for attaching alkyl or aryl groups on sidewalls of SWCNTs [103]. Therefore, it is currently one of the most promising functionalization techniques. Moreover, functionalization with alkyl or aryl chains allows additional insertion of different functional groups onto these chains. Hence, this approach will enable adjustable modification of the chemical properties of SWCNTs with respect to their applications.

4. MECHANICAL PROPERTIES

4.1. Measurement of Mechanical Properties

CNTs are expected to have exceptionally good mechanical properties because strong sp^2-hybridized in-plane C–C bonds give them a remarkably high Young's modulus. Theoretical [104] and experimental studies [105,106] have shown that Young's modulus reaches values of about 1 TPa, which makes CNTs one of the stiffest material available. On the other hand, the mechanical properties strongly depend on the degree of structural disorder in CNTs. First direct measurements of the mechanical properties, which were based on measuring the amplitude of thermally induced vibration inside a TEM [107], were carried out on MWCNTs produced by laser vaporization and revealed Young modulus in the 0.4–4 GPa range. For SWCNTs an average value of 1.25 ± 0.35 TPa was obtained [108]. Poncharal et al. [105] measured Young modulus of arc-produced MWCNTs and found a sharp decrease from about 1 to 0.1 TPa with increasing diameter from 8 to 40 nm.

Another possibility to measure directly Young's modulus of nanotubes was pioneered by Salvetat et al. [106] and uses the tip of an atomic force microscope to apply a force and to detect the resulting deflection of the CNT. In this so-called "Swiss cheese" method, CNTs are dispersed in a solvent, for example in ethanol, and deposited on the surface of a porous alumina membrane (Fig. 7). CNTs stick to the surface due to van der Waals interaction. Occasionally they lie over a hole with a short section of their entire length so that the major part of CNTs is held by the contact with the membrane surface. The deflection versus force measurement allows the estimation of the Young's modulus (Fig. 8).

Salvetat et al. compared Young's modulus of arc-produced MWCNTs with that of CVD grown CNTs and found that the modulus is an order of magnitude smaller for CVD grown tubes whereas in the case of arc-discharge CNTs it is close to that of graphite (Fig. 9) [109,110]. This difference was explained by the presence of structural defects in CVD grown CNTs, in particular misalignment of the graphitic planes with the tube axis (Fig. 10). Indeed, Lukic et al. [111] have shown very

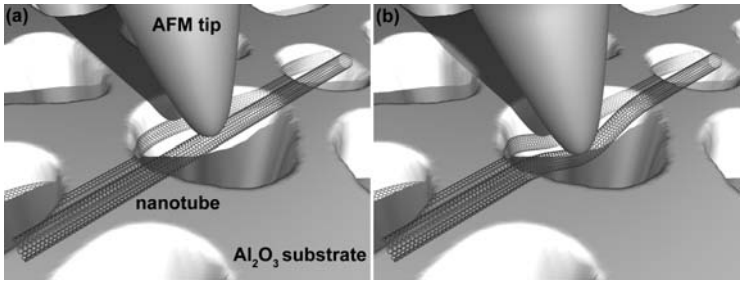

Fig. 7. (a) Schematic drawing of a carbon nanotube deposited on a porous Al_2O_3 substrate. (b) The tube deforms under an applied normal force and this deformation is recorded [143] (courtesy of A. Kis).

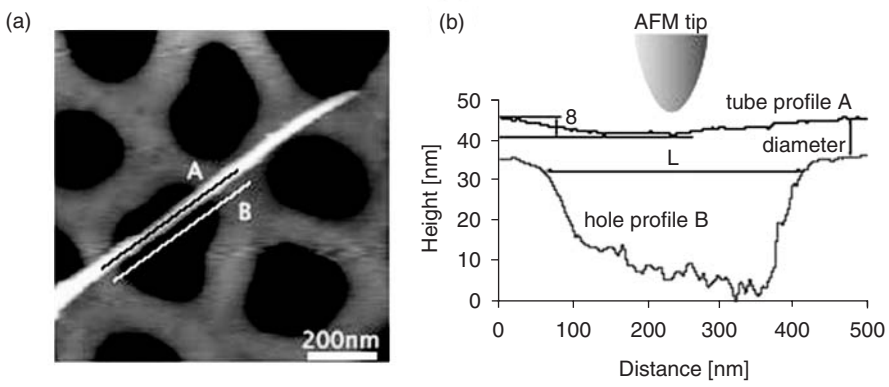

Fig. 8. (a) Three-dimensional rendering based on the AFM image of a CNT rope spanning two holes. (b) Subsequent analysis of linescans over the tube and the hole yields the nanotube's physical dimensions together with the deflection in the middle [143] (courtesy of A. Kis).

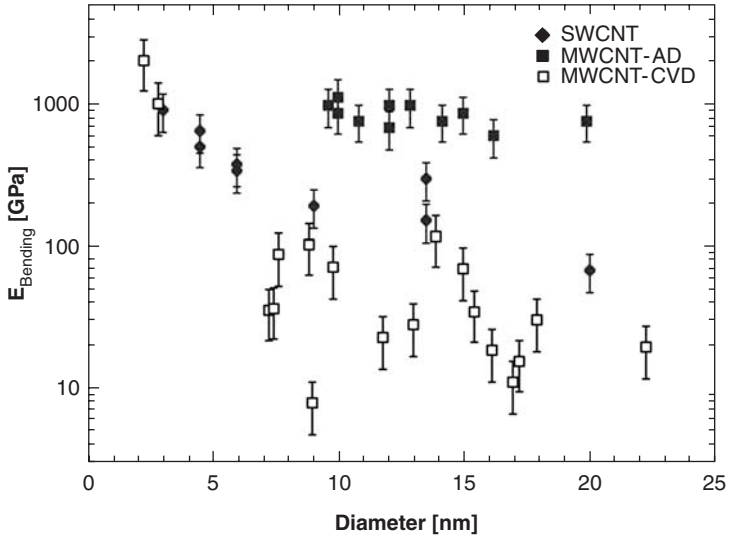

Fig. 9. Mechanical measurements of SWCNT bundles (full circles) [106] and MWCNTs grown by arc-discharge (full squares) [110] and CVD methods (open squares) [112] as a function of the CNT diameter. The measured bending modulus strongly depends on the diameter. For MWCNTs the bending modulus also depends on the growth methods.

recently that CVD grown MWCNTs have low Young modulus below 100 GPa independently of their growth conditions. Additional subsequent high-temperature treatment failed to improve the mechanical properties. These results have also shown that misalignment alone cannot explain the obtained low values of Young

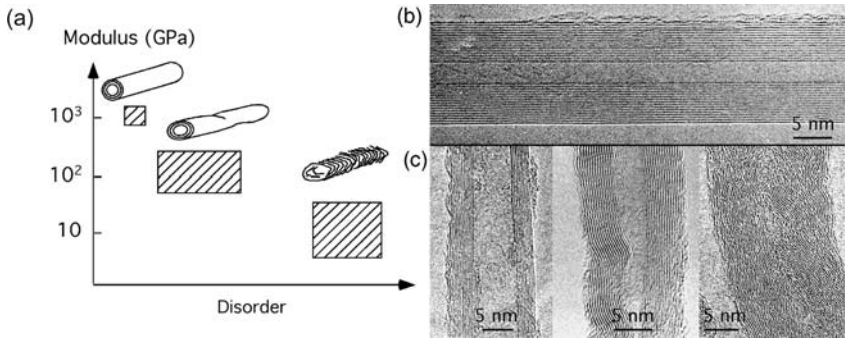

Fig. 10. (a) A map of the Young's modulus of MWCNTs depending on the amount of the structural disorder. For low-quality nanotubes Young's modulus decreases down to 10 GPa. TEM images of (b) an arc-discharge grown CNT and (c) CVD grown CNTs of different structural disorder. With kind permission from Ref. [109]. Springer Science and Business Media.

modulus, and their origin must lie in the number of structural defects (e.g., pentagon–heptagon pairs (Fig. 3), vacancies, point defects, dislocations, etc.). The growth mechanism for the CNTs produced by catalytic CVD is very different compared with arc-discharge or laser-vaporization CNTs. In particular, the temperature involved during processing reaches more than 3000°C in the latter techniques, in contrast to CVD where typically a temperature below 1000°C is applied. Hence, CVD process generally leads to incorporation of high density of structural defects, which cannot be recovered by high-temperature annealing.

However, the very recent results indicate that CVD grown CNTs can have a Young's modulus of 1 TPa in case CNTs contain a few walls (Fig. 9) [112]. These results indicate that the observed difference in the Young's modulus for the catalytically grown CNTs with high and low numbers of walls is probably related to the growth mechanism of CNT. For CVD grown CNTs, the growth rate is inversely proportional to the CNT diameter, thus, most presumably more defects get incorporated in MWCNTs with a high number of walls and a large diameter compared to CNTs with a few walls.

In the case of SWCNTs, the measurement is more difficult due to the small diameters and because they tend to form bundles, where individual CNTs are held together via the weak van der Waals interaction. As a consequence, when exposed to forces bundles behave as an assembly, and the contribution of the shearing between CNTs becomes larger as the bundle diameter increases (Fig. 9) [106,113]. An extremely low shear modulus in the order of 1–10 GPa has been measured. This low shear modulus is a serious weakness of CNTs because the mechanical strength of a macroscopic CNT fiber is strongly dominated by their shear modulus and not by their Young's modulus and, consequently, the distinctive high Young modulus of individual SWCNTs is not exploitable. In order to avoid the slide process crosslinks between CNTs have to be generated; irradiation is one of the possible routes.

As observed during observation in TEM, CNT wall structures are sensitive to the electron beam during observation in TEM. The most probable mechanism of irradiation damage is by direct knock-on collisions of incoming electrons with the carbon atoms, which break the carbon–carbon sp^2 bonds. The threshold energy strongly depends on the direction of the incoming electron. Obviously, the smallest value is expected for the radial displacement in the direction perpendicular to the nanotube surface, and highest for in-plane displacements. According to molecular dynamics calculations performed by Crespi et al. [114] ejection in the radial direction requires an energy transfer of about 17 eV while tangential ejection requires 30–50 eV. Using these values, Smith and Luzzi have calculated that an isolated nanotube will damage preferentially on surfaces that lie normal to the electron beam, and minimum incident electron-beam energy of 86 keV is required to remove a carbon atom by a knock-on collision [115]. Kis et al. [113] have shown recently that electron irradiation can indeed generate efficiently crosslinks and avoid sliding. They obtained a 30-fold increase of the bending modulus by electron irradiation (Fig. 11). In addition to linking the nanotubes by covalent bonds, irradiation has experimentally demonstrated to provide the possibility of complete welding and coalescence of nanotubes. The basis for these structural transformations was found in the formation of vacancies with chemically reactive dangling bonds followed by reconstruction of the damage in which the bonds were saturated [113].

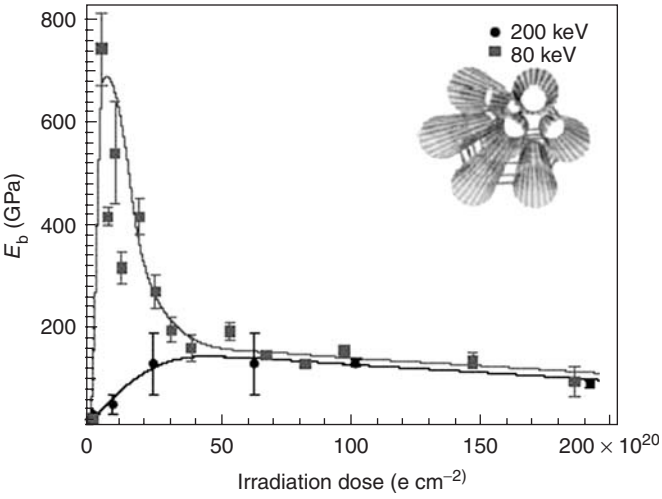

Fig. 11. Dependence of bending modulus E_b of different CNT ropes as a function of received dose for two incident electron energies. For 200 keV, the bending modulus increases on short exposures due to crosslinking and degrades at higher exposures because of structural damage. The rope irradiated with 80-keV electrons shows a much stronger and sharper increase of the bending modulus. Reprinted by permission from Ref. [113]. Copyright 2004, Macmillan Publishers Ltd.

4.2. Application of Mechanical Properties: Macroscopic Fibers

With the tremendous progress in synthesis and purification of CNTs, processing CNTs in macroscopic scale becomes more and more realistic. In particular, recent progress has shown the possibility to assemble CNTs into long macroscopic fibers. Very recently, Dalton et al. [116] have shown that 100-m-long CNT composite fibers can be produced, which can be woven into textiles. Due to simple macroscopic handling, CNT fibers are very good candidates for microelectromechanical systems (MEMS) applications.

For the preparation of macroscopic fibers one of the most critical issues is to disperse CNTs homogeneously. Vigolo et al. [117] dispersed CNTs in a surfactant solution (aqueous solution of sodium dodecyl sulfate (SDS)) and recondensed the nanotubes in the stream of a polymer solution containing polyvinylalcohol (PVA). A better alignment of CNTs within fibers was obtained when CNTs were stretch-aligned [119] or dispersed in a solvent, such as dimethylformamide (DMF) or in a solution of the polymer poly(*m*-phenylenevinylene-co-2,5-dioctyloxy-*p*-phenylenevinylene) (PmPV) in toluene and pulled out from the suspension containing CNTs by means of a carbon fiber mounted on a motor-driven translation stage [118].

Recently it was reported that the use of the solution of PmPV in toluene instead of the solvent DMF improved the pulling procedure of CNT fibers [120]. PmPV is a polymer well known for the high dispersability of CNTs in organic solvents and therefore has been frequently used in the synthesis of polymer-CNT-composites. Applied to fiber assembly, the pulling procedure was found to be more stable. In general, the assembly of MWCNTs into fibers is rather difficult since MWCNTs are not as straight as SWCNTs and they contain a high density of structural defects. Using DMF, only SWCNT fibers could be successfully pulled together whereas using PmPV fibers consisting of MWCNTs could also be obtained.

The mechanical strength of these fibers is not as high as expected, which is due to weak interaction between the individual nanotubes and bundles within the fiber. CNTs can easily slide along their axis leading to lower shear modules. Very recently, it has been shown that electron irradiation can create crosslinks between individual tubes inside a CNT bundle and results in a considerable increase of Young's modulus and enhanced conductivity of a CNT rope [121].

5. NANOELECTROMECHANICAL SYSTEMS APPLICATION

5.1. Linear Actuators

CNT is an attractive material for NEMS applications because of its small size, low density, structural perfection, as well as excellent electronic and mechanical properties. NEMS are considered to be one of the key elements to assemble and manipulate atoms and molecules for instance to build machines in the nanoscale as well as to detect extremely small force and replacements. The first demonstration of

CNTs applied in NEMS has been nanotweezers by attaching two CNTs onto two independent metal electrodes deposited onto tapered glass micropipettes [122]. The arms of the tweezers were about 4 μm long and 50 nm in diameter. By applying a voltage from 0 to 8.5 V, the tweezer arms could be bent from the initial open position (at 0 V) to about 50% closure at 8.3 V and finally to sudden closure exceeding 8.5 V. The opening and closing process was reproducible with the same displacement each time and could be repeated many times. The mechanical capabilities of the nanotweezers were demonstrated by gripping and manipulating submicron clusters (Fig. 12) and nanowires (Fig. 13).

Manipulation of even smaller nano-objects allowed the nanotweezer developed by Akita et al. [123], which operates in an atomic force microscope (AFM) by using two CNTs attached on the metal electrodes patterned on a conventional AFM Si tip. The CNT arms bend and the distance between them decreases with increasing the applied voltage from 0 to 4.5 V. For $V > 4.5$ V, an abrupt closure of the arms was obtained, and the motion could be repeated many times without any plastic deformation.

The bending effect of the tweezer arms can be described by a total energy E_{Total} given by $E_{\text{Total}} = E_{\text{elast}} + E_{\text{el.stat}} + E_{\text{vdW}}$, where E_{elast} is the elastic energy, $E_{\text{el.stat}}$ the electrostatic energy, and E_{vdW} the van der Waals energy between two CNTs. Calculations indicated that the sudden closing is caused by losing the balance between the attractive electrostatic and van der Waals forces and the bending moment of the CNT arms.

The open and close states of a nanotweezers can be used as "On" and "Off" states of a nanoswitch. A simple design of a modified nanotweezer consists of one single CNT actuated toward a metal electrode. For instance Ke and Espinosa [124]

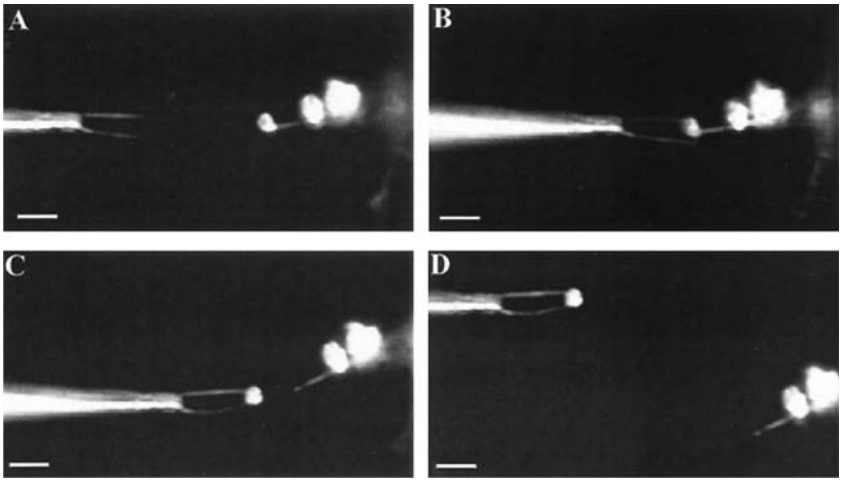

Fig. 12. Dark-field optical micrographs showing the manipulation of the nanotweezers demonstrated by Kim and Lieber [122], reprinted with permission from AAAS. By (a) approaching, (b) opening, and (c) closing the nanotweezer arms, a fluorescent polystyrene nanobead of 310 nm diameter is (d) moved away from the sample support.

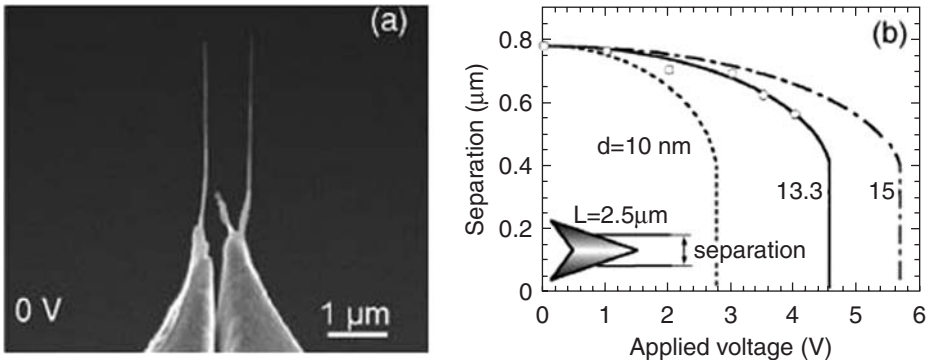

Fig. 13. (a) SEM image of the CNT nanotweezer developed by Akita et al. [123] with open arms by applying zero voltage. (b) Applied voltage dependence of the separation between the CNT nanotweezer arms for three different diameters of CNTs. Reprinted with permission from Ref. [123]. Copyright 2001, American Institute of Physics.

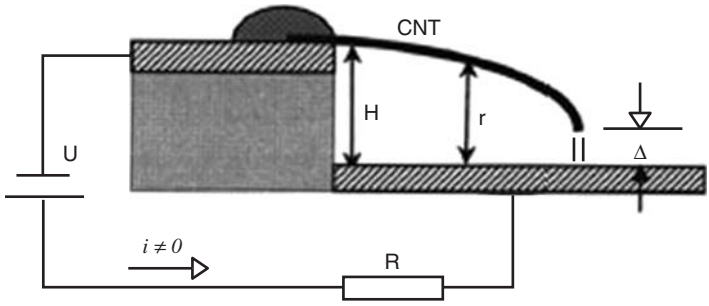

Fig. 14. Schematic drawing of the CNT-based cantilever nanoswitch suggested by Ke and Espinosa [124]. H is the initial step height, defining the "Off" state and Δ is the gap between the deflected tip and bottom electrode. Reprinted with permission from Ref. [124]. Copyright 2004, American Institute of Physics.

suggested a nanoswitch containing one single CNT attached to a cantilever, freestanding above a conducting substrate (Fig. 14). The theoretical concept of such a tunable nanocantilever device was also demonstrated experimentally [125]. In this device, when the applied electrostatic force becomes larger than the elastic force, the CNT is deflected toward the electrode defining the "up" and "down" positions of the CNT, which correspond to "ON" and "OFF" states of the nanoswitch (Fig. 15). It was found that in this device the concentration of charge at the end of the cantilever plays the most dominant role for the electrostatical interaction.

Another type of nanoelectromechanical switch was realized by Cha et al. [126] by using a suspended nanotube and self-aligned electrodes in triode structure, as shown in Fig. 16. Source and gate electrodes are positioned at both sides normal to

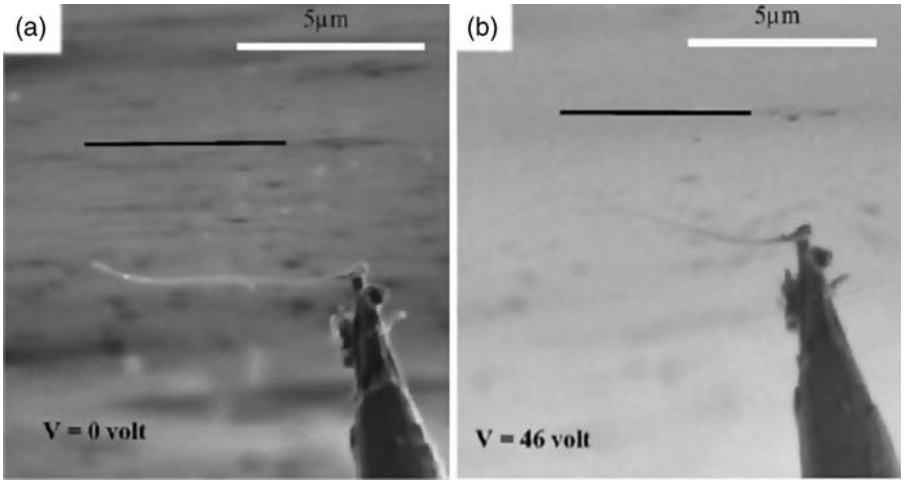

Fig. 15. SEM images of a CNT attached to a cantilever deflected at two different biased voltages, which define (a) the "On" and (b) "Off" states of the nanoswitch [125].

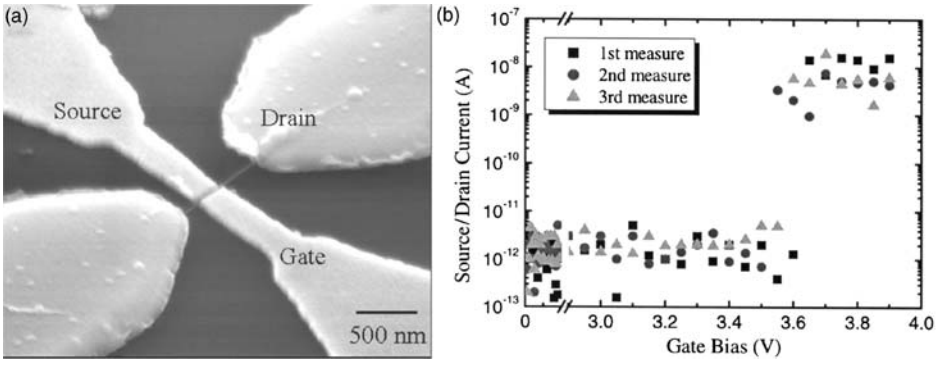

Fig. 16. (a) SEM image of the triode-structure nanoelectromechanical switch fabricated by Cha et al. [126], (b) the On and Off states of the nanoswitch are achieved by changing the gate bias voltage below and above 3.6 V. Reprinted with permission from Ref. [126]. Copyright 2005, American Institute of Physics.

the axis of the suspended CNT with drain contacts. The ON and OFF states are by the change of gate voltage leading to deflection of the CNT to make electrical contact with the source electrode.

Very recently, electromechanical switching devices were fabricated by employing vertically grown MWCNTs from catalyst dots on patterned device electrodes [127]. The device consists of three MWCNTs grown from predefined positions on

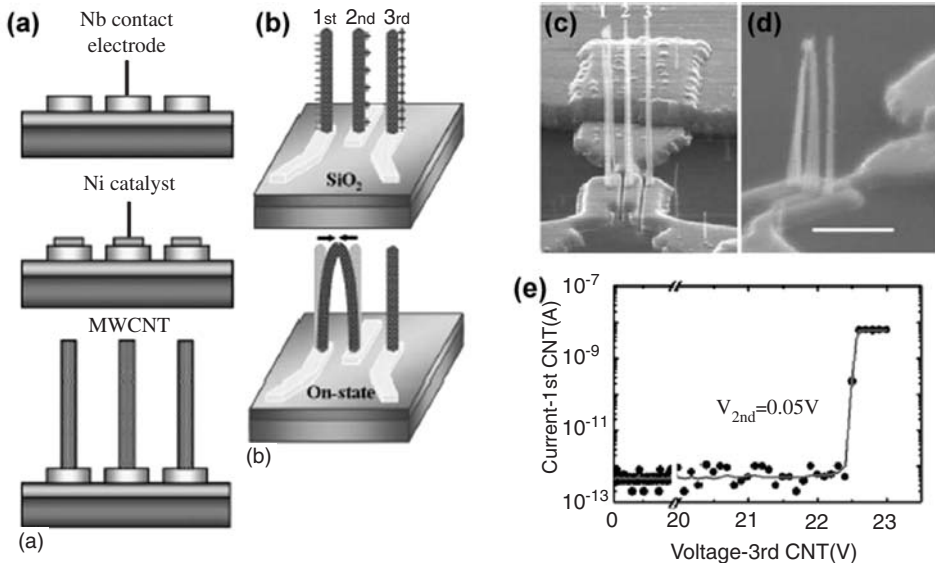

Fig. 17. (a, b) Schematic of the fabrication procedure of the nanoelectromechanical switch consisting of vertically grown MWCNTs fabricated by Jang et al. [127]. (c, d) SEM images shows the three MWCNT arms of the switch (the scale bar corresponds to 1 μm) at On and Off states. (e) Current–voltage characteristics of switching action indicates the On and Off states, which are obtained by varying the voltage of the third MWCNT below and above 22.5 V, whereas between the first and second a low voltage of 0.05 V is applied. Reprinted with permission from Ref. [127]. Copyright 2005, American Institute of Physics.

patterned Nb electrodes as illustrated in Fig. 17. The first MWCNT is electrically connected to the ground and acts as a negative electrode whereas the second and the third MWCNTs are connected to a positive voltage. Positive charges build up in the second and the third MWCNTs, and the second MWCNT is pushed toward the first MWCNT, due to electrostatic attraction and repulsion caused by the first and third CNT, respectively. Above a threshold bias – which is determined by the balance of the electrostatic force, the elastic force, and the van der Waals force involved – the second MWCNT makes electrical contact to the first MWCNT, establishing "On" state. A significant advantage of this design is that the voltage between the first and second MWCNT can be kept low (0.05 V), avoiding possible damages caused by large driving voltages. The off state can be re-established when the second MWCNT is connected to a floating ground. The gate voltage bias to the third MWCNT, swept between 20 and 25 V, will give rise to an attractive force to the second MWCNT and pull it back. Moreover, it was found that the re-opening of the close state strongly depends on the MWCNT length, since the elastostatic force is determined by $F_{\text{elast}} = 8Eld/L^3$ where E is the Young's modulus, I the moment of inertia, d the distance between two CNTs, and L the length of the CNT.

Hence, by tuning the MWCNT length the authors show the possibility to fabricate volatile and nonvolatile nanoswitches.

Two crossing CNTs can also be used to build a nanoswitch: At their crosspoint, the upper CNT can exist in either the separated state (Off state) or in contact (On state) with the perpendicular lower nanotube. Rueckes et al. [128] demonstrated that indeed dispersed crossed CNT devices can be fabricated and can be operated as a bistable nanoswitch. They also suggested fabricating a CNT-based nonvolatile random access memory (RAM) by formation of an array of CNT junctions as a network of bistable nanoswitches (Fig. 18). The viability of the concept was demonstrated by the experimental realization of a reversible bistable nanotube-based bit (Fig. 19). The authors emphasized the extreme high integration level of the CNT-based bit approaching 10^{12} elements/cm^2 and an element operation frequency in the order of 100 GHz. In addition, in this design the addressability of many devices is given by the long CNTs (several micrometers) and interconnects placed at the ends of long CNTs can address many individual junction elements. Also with respect to power consumption and heat dissipation CNT-based nonvolatile RAM are promising compared to dynamic RAMs, which must be continually refreshed.

The nanotechnology company Nantero (www.nantero.com), co-founded by Rueckes, is currently developing high density nonvolatile RAMs based on this idea. Nantero fabricated prototype devices including an array of ten billion nanotube junctions on single silicon wafer. Nantero claims that their CNT-based RAM (called NRAM™) will be considerably faster and denser than dynamic random access memory (DRAM), have substantially lower power consumption than DRAM or flash, be as portable as flash memory, and be highly resistant to environmental forces (e.g., heat, cold, magnetism).

Another important NEMS components are resonators. A room-temperature, self-detecting and tunable CNT resonator has been demonstrated that is based on the electrical actuation and sensing of the oscillation modes of doubly clamped

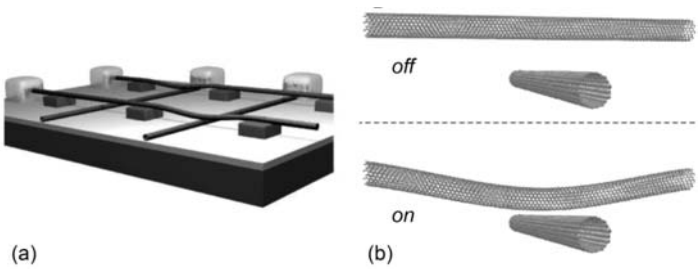

Fig. 18. (a) Schematic drawing of the device architecture of the non-volatile RAM suggested by Rueckes et al. [128]. The device consists of a suspended crossjunction array of CNTs. (b) The On and Off states are defined by the separation of the CNTs at cross-points. Reprinted with permission from Ref. [128]. AAAS.

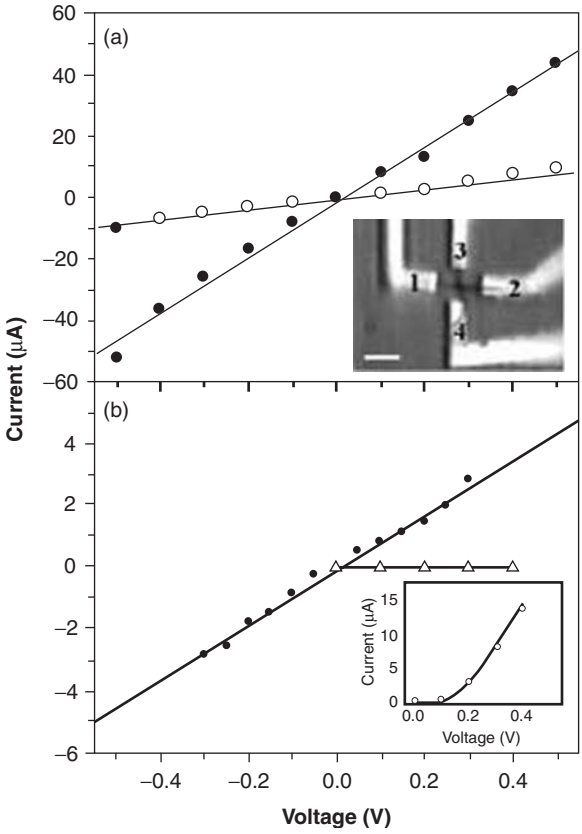

Fig. 19. (a) Current–voltage characteristics of two crossing CNTs (solid circles: electrodes 1 and 2, open circles: electrodes 3 and 4), which form the basic element of the CNT-based nonvolatile RAM suggested by Rueckes et al. [128], (b) I–V curves of the CNT junction in Off (open triangles) and On (solid circles) states measured between electrodes 2 and 3. The junction can be switched from Off to On at 2.5 V. Reprinted with permission from Ref. [128]. AAAS.

nanotubes [129]. Single or few-walled nanotubes are suspended over a 1.2–1.5 μm wide trench between two metal electrodes (Fig. 20). The nanotube motion was actuated and detected by using the electrostatic interaction between the tube and the gate electrode underneath. A DC gate voltage yields a static force on the CNT and can control its tension whereas a AC voltage results in a periodic electric force and actuates the CNT. The vibrational motion of the CNT is detected by the change in conductance, which is proportional to the change in the induced charge on the CNT. The resonance frequency can be widely tuned and the devices can be used to transduce very small forces (Fig. 21). The ultimate limit on force sensitivity is given by the thermal vibrations of the CNT and can be estimated to 20 $aNHz^{-1/2}$.

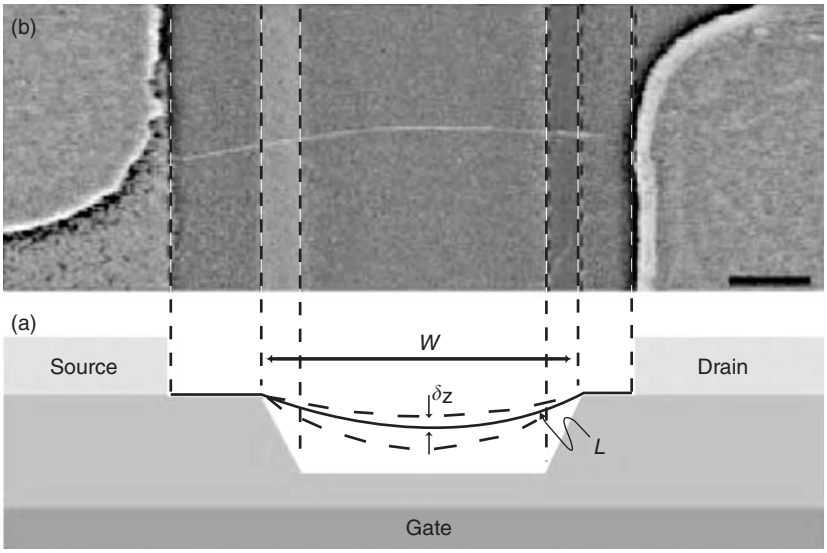

Fig. 20. (a) Schematic view of the resonator demonstrated by Sazanova et al. [129]. (b) A false-color SEM image shows the suspended nanotube bridging the trench and connecting two metal electrodes. The scale bar corresponds to 300 nm. Reprinted with permission from Ref. [129]. Copyright 2004, Macmillan Publishers Ltd.

5.2. Rotary Actuators

The first NEMS device that used the perfectly nested cylindrical shells of a MWCNT as the key element was developed in Alex Zettl's group at UC Berkeley. By using a manipulator inside a high-resolution TEM, this group was able to peel off a few outer layers of an MWCNT fixed at one end [130]. Fig. 22 shows a series of TEM micrographs presenting a MWCNT being peeled off and sharpened. By attaching the nanomanipulator to the core shells they could telescope the nanotube repeatedly (Fig. 23) and found that the system operates as an ideal low-friction and low-wear nanobearing [131]. This experimental result was in perfect agreement with the theoretical prediction made for the low translation and rotational barriers in multilayered CNTs by Charlier and Michenaud already in 1993 based on their density functional calculation [132]. Meanwhile, the low friction enabling easy intershell sliding has also experimentally been observed by other groups [133], and theory [134–136] confirmed that the actuator indeed operates as a constant-force spring.

Cumings and Zettl [131] also suggested to use bamboo configuration, where the inner nanotube sections do not extend along the entire length of the CNT, as a short ultralow-friction linear or rotational bearings that are firmly embedded in a common long, stiff CNT cylindrical housing (Fig. 24). When the extracted inner tubes are released, they are retracted by the attractive van der Waals force within on

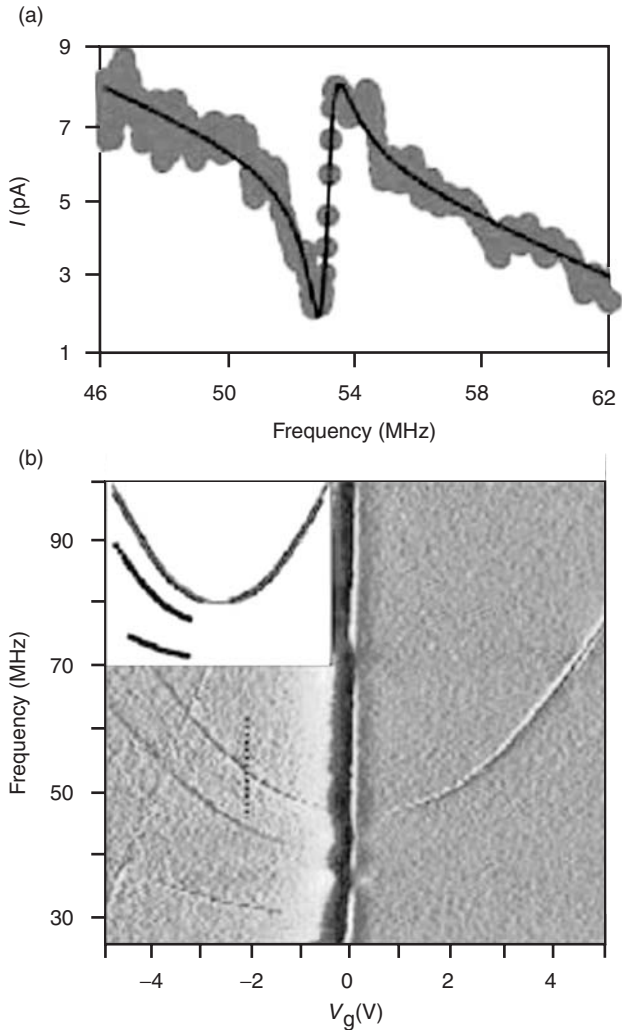

Fig. 21. (a) Resonant response of the resonator: detected current as a function of driving frequency taken at $V_g = 2.2$ V. (b) Detected current (plotted as a derivative in color scale) as a function of gate voltage and frequency. Reprinted with permission from Ref. [129]. Copyright 2004, Macmillan Publishers Ltd.

the order of 10^{-9} s. Molecular dynamics simulation revealed that telescopic extension and retraction movements are possible for a large variety of tube diameters and types [137]. However, sustained oscillations are only possible when the difference in tube diameter is of 3.4 Å independently of tube type. These gigahertz scale oscillations are found to be stable up to 400 K. Hence these MWCNT-based devices open the door for a new generation of NEMS [138] and is

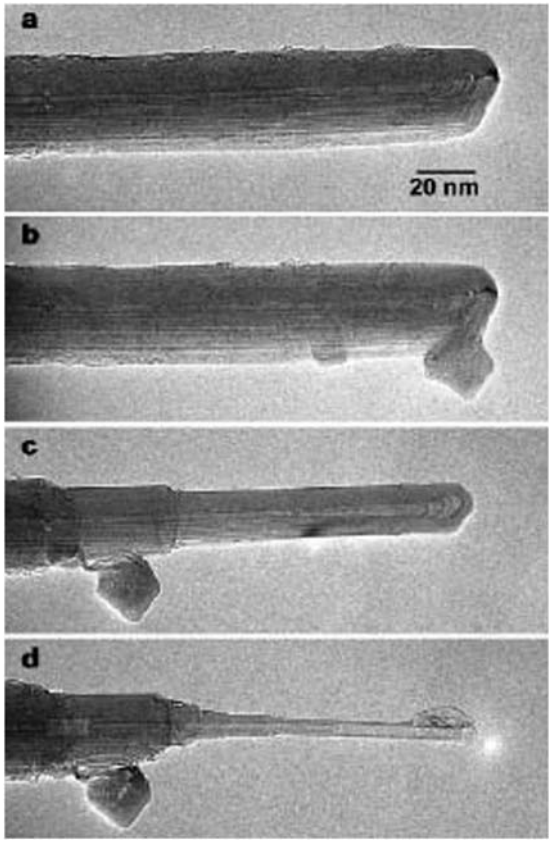

Fig. 22. TEM images of a MWCNT being peeled off and sharpened by a manipulator. Reprinted with permission from Ref. [130]. Copyright 2000, Macmillan Publishers Ltd.

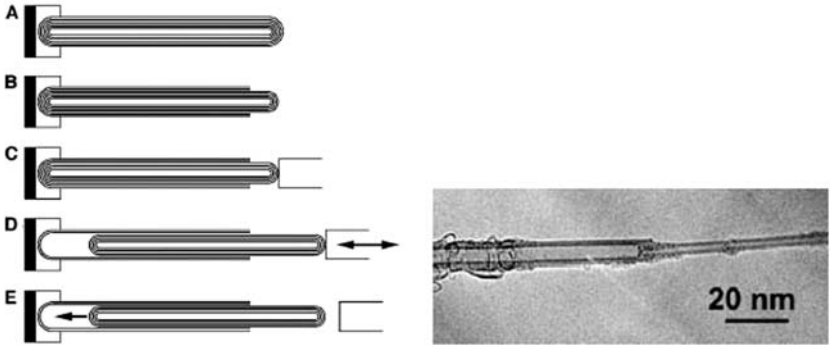

Fig. 23. (Left) Schematic illustration of the experiments performed by Cumings and Zettl [131] inside a TEM by using a manipulator. The end of a MWCNT is opened (A to B) and the exposed core tubes are attached to the manipulator (C). The inner tubes are telescoped repeatedly (D). When released (E), the core tubes are pulled into the outer shell housing by van der Waals force. (Right) A TEM image of a CNT with telescoped core shells. Reprinted with permission from Ref. [128]. AAAS.

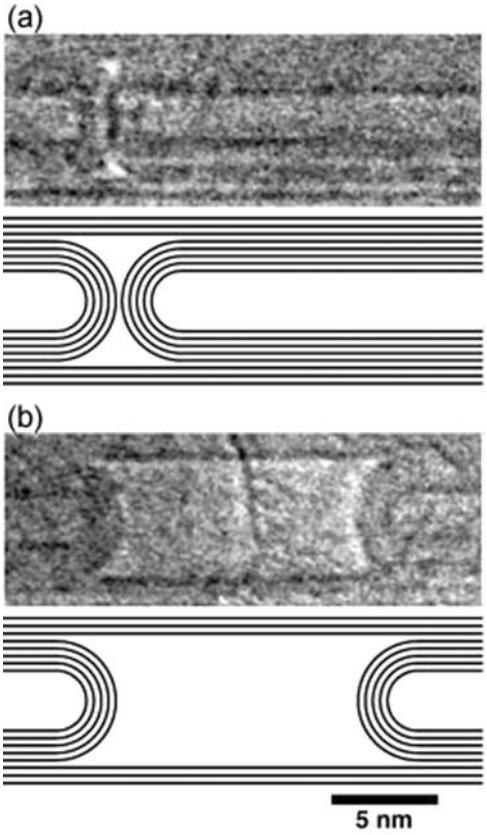

Fig. 24. (a) TEM image of a bamboo section of a MWCNT. (b) The same area after the core tubes on the right has been telescoped outward. Bamboo sections slide independently inside the CNT housing [131]. The schematic representations clarify both cases of the initial and telescoped bamboo structures. Reprinted with permission from Ref. [128]. AAAS.

exactly the structure envisaged by Drexler as the most efficient bearing for nanomechanical needs [139].

Based on the experimental breakthroughs of Zettl's group [130,131], Fennimore et al. [140] realized a rotational nanomotor, which represents the first really true CNT-based NEMS, fully integrating electronic control and mechanical response. The bearing is about 10 nm in diameter and the rotational motion of the rotor is activated electrostatically through three stator electrodes (Fig. 25). The overall size of the actuator is about 300 nm and its components are integrated on a silicon chip. Externally applied voltages precisely control the speed and position of the rotor plate without any indication of wear or fatigue. Very recently, a modified layout of the electromechanical rotational actuator with a better defined motion of the shells was presented by Bourlon et al. [141]: The rotating plate is attached to an inner MWCNT shell that turns inside whereas outer shells are fixed to two anchor pads

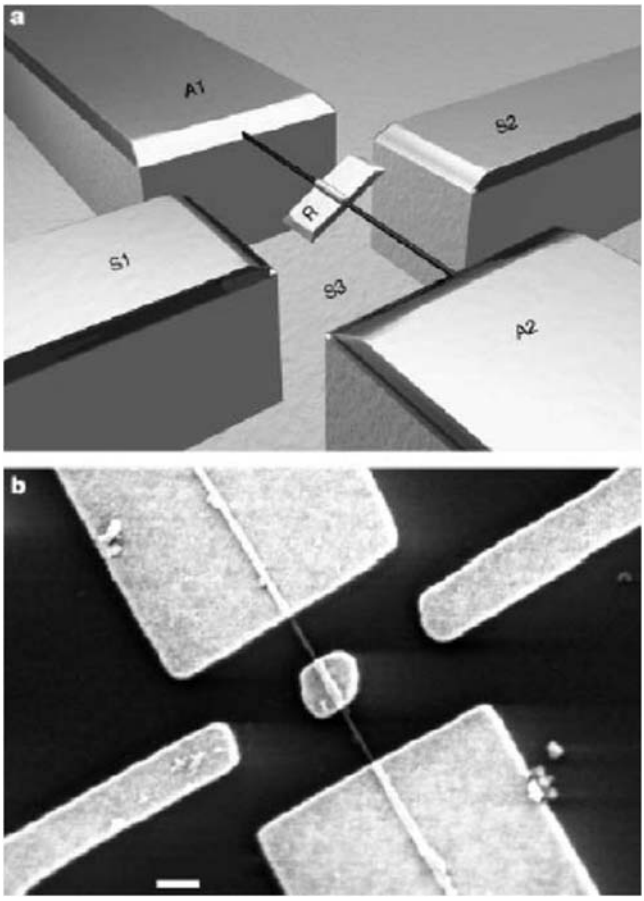

Fig. 25. (a) Schematic drawing of the nanoactuator developed by Fennimore et al. [140]. A metal plate rotor, marked by *R*, is attached to a MWCNT, which is anchored to electrodes A1 and A2 on both sides. Three stator electrodes, S1, S2, and S3 control the rotation by additional voltage. (b) SEM image of nanoactuator prior HF etching (scale bar corresponds to 300 nm). The actuator elements can clearly be seen. Reprinted with permission from Ref. [140]. Copyright 2003, Macmillan Publishers Ltd.

(Fig. 26). This device design also allows a second plate or a long molecule attached to the rotating inner shells which would enable the mechanical transfer of rotation.

The advantages of the MWCNT-based rotational nanomotors compared to existing chemically bio-actuators and bio-motors are that this type of actuators operates over a wide range of frequency, temperature and environmental condition, including high vacuum and harsh chemical environments. Moreover, the MWCNT systems yield about three times smaller upper-limit frictional forces compared to the friction measured in conventional materials.

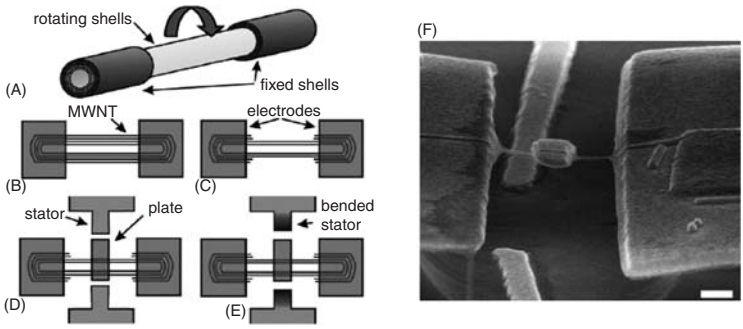

Fig. 26. An improved concept of the nanoactuator developed by Bourlon et al. [141]: Inner shells turn freely inside of fixed outer shell housing (A). Several shells are removed (B–C) and the rotator plate is attached to the inner shells (D). Two stator electrodes are fabricated (D–E), which control the rotation of the plate. (F) SEM image of the rotor. The scale bar corresponds to 200 nm.

CNT-based NEMS devices promise to revolutionize excitation and detection of extremely small displacements and extremely weak forces. With surface nanomachining processes involving state-of-the-art nanolithography and nanomanipulation techniques, CNTs provide the possibility to build NEMS with cross-sections of about 10 nm and with masses approaching a few attograms. The small size and extremely low mass offers immense potential for new applications and fundamental measurements. Moreover, the ultralow power, low energy dissipation and low friction, being main objectives in small-scale systems, make CNT ideal for NEMS applications. However, in spite of the fast acceleration in the development of NEMS structures, there are three principal challenges which need to be addressed before the full potential of CNT-based NEMS can be exploited: communicating signals from the nanoscale to the macroscopic devices; understanding and controlling mesoscopic mechanics; and developing methods for reproducible and routine nanofabrication.

ACKNOWLEDGMENT

We thank the NCCR Nanoscale Science of the Swiss National Science Foundation and the Swiss National Science Foundation for financial support.

REFERENCES

[1] S. Iijima, Helical microtubules of graphitic carbon, *Nature* **354**, 56–58 (1991).
[2] M.S. Dresselhaus, G. Dresselhaus and P. Avouris, *Carbon nanotubes: Synthesis, structure, properties, and applications* (Springer-Verlag, Berlin Heidelberg, New York, 2001).
[3] C.H. Kiang, M. Endo, P.M. Ajayan, G. Dresselhaus and M.S. Dresselhaus, Size effects in carbon nanotubes, *Phys. Rev. Lett.* **81**, 1869–1872 (1998).

[4] J.H. Jung, M.R. Kim, S.H. Jeong, S.U. Kim, O.J. Lee, K.H. Lee, J.H. Suh and C.K. Park, High-yield synthesis of multi-walled carbon nanotubes by arc discharge in liquid nitrogen, *Appl. Phys. A: Mater. Sci. Proc.* **76**, 285–286 (2003).
[5] M. Ohkohchi, Synthesis of single-walled carbon nanotubes by ac arc discharge, *Jpn. J. Appl. Phys.* **38**, 4158–4159 (1999).
[6] X. Zhao, S. Inoue, M. Jinno, T. Suzuki and Y. Ando, Macroscopic oriented web of single-wall carbon nanotubes, *Chem. Phys. Lett.* **373**, 266–271 (2003).
[7] H. Huang, H. Kajiura, S. Tsutsui, Y. Hirano, M. Miyakoshi, A. Yamada and M. Ata, Large-scale rooted growth of aligned super bundles of single-walled carbon nanotubes using a directed arc plasma method, *Chem. Phys. Lett.* **343**, 7–14 (2001).
[8] M. Yudasaka, Y. Kasuya, F. Kokai, K. Takahashi, M. Takizawa, S. Bandow and S. Iijima, Causes of different catalytic activities of metals in formation of single-wall carbon nanotubes, *Appl. Phys. A: Mater. Sci. Proc.* **74**, 377–385 (2002).
[9] C. Liu, H.T. Cong, H.M. Cheng and B.L. Zhou, Semi-continuous synthesis of single-walled carbon nanotubes by hydrogen arc method, *Carbon* **37**, 1865–1868 (1999).
[10] Y. Ando, X. Zhao, K. Hirahara, and S. Iijima, Production of thick single-walled carbon nanotubes by arc discharge in hydrogen ambience, in *Nanonetwork Materials*, AIP Conference Proceedings, 590, 2001, pp. 7–10.
[11] T.W. Ebbesen and P.M. Ajayan, Large scale synthesis of carbon nanotubes, *Nature* **358**, 220–222 (1992).
[12] T. Guo, P. Nikolaev, A. Thess, D.T. Colbert and R.E. Smalley, Catalytic growth of single-walled manotubes by laser vaporization, *Chem. Phys. Lett.* **243**, 49–54 (1995).
[13] M. Yudasaka, R. Yamada, N. Sensui, T. Wilkins, T. Ichihashi and S. Iijima, Mechanism of the effect of NiCo, Ni and Co catalysts on the yield of single-wall carbon nanotubes formed by pulsed Nd:YAG laser ablation, *J. Phys. Chem. B* **103**, 6224–6229 (1999).
[14] W.K. Maser, E. Muñoz, A.M. Benito, M.T. Martinez, G.F. de la Fuente, Y. Maniette, E. Anglaret and J.L. Sauvajol, Production of high-density single-walled nanotube material by a simple laser-ablation method, *Chem. Phys. Lett.* **292**, 587–593 (1998).
[15] C.D. Scott, S. Arepalli, P. Nikolaev and R.E. Smalley, Growth mechanisms for single-wall carbon nanotubes in a laser-ablation process, *Appl. Phys. A: Mater. Sci. Proc.* **72**, 573–580 (2001).
[16] Z.H. Ren, Z.P. Huang, D.Z. Wang, J.G. Wen, J.W. Xu, J.H. Wang, L.E. Calvet, J. Chen, J.F. Klemic and M.A. Reed, Growth of a single freestanding carbon nanotubes on each nanonickel dot, *Appl. Phys. Lett.* **75**, 1086–1088 (1999).
[17] T.S.J.-M. Bonard, H. Kind and L.A. Nilsson, Field emission from carbon nanotubes: The first five years, *Solid State Electron.* **45**, 893–914 (2001).
[18] W.B. Choi, D.S. Chung, J.H. Kang, H.Y. Kim, Y.W. Jin, I.T. Han, Y.H. Lee, J.E. Jung, N.S. Lee, G.S. Park and J.M. Kim, Fully sealed, high-brightness carbon nanotube field-emission display, *Appl. Phys. Lett.* **75**, 3129–3131 (1999).
[19] Y. Murakami, Y. Miyauchi, S. Chiashi and S. Maruyama, Characterization of single-walled carbon nanotubes catalytically synthesized from alcohol, *Chem. Phys. Lett.* **374**, 53–58 (2003).
[20] M. Endo, The production and structure of pyrolytic carbon nanotubes (PCNTs), *J. Phys. Chem. Solids* **54**, 1841–1848 (1993).
[21] H. Dai, A.G. Rinzler, P. Nikolaev, A. Thess, D.T. Colbert and R.E. Smalley, Single-wall nanotubes produced by metal-catalyzed disproportionation of carbon monoxide, *Chem. Phys. Lett.* **260**, 471–475 (1996).
[22] R.R. Bacsa, E. Flahaut, C. Laurent, A. Peigney, S. Aloni, P. Puech and W.S. Bacsa, Narrow diameter double-wall carbon nanotubes: Synthesis, electron microscopy and inelastic light scattering, *New J. Phys.* **5**, 131.1–131.9 (2003).
[23] E. Flahaut, R. Bacsa, A. Peigney and C. Laurent, Gram-scale CCVD synthesis of double-walled carbon nanotubes, *Chem. Commun.* 1442–1443 (2003).
[24] W.Z. Li, J.G. Wen, N. Sennett and Z.F. Ren, Clean double-walled carbon nanotubes synthesized by CVD, *Chem. Phys. Lett.* **368**, 299–306 (2003).

[25] A. Ago, T. Komatsu, S. Ohshima, Y. Kuriki and M. Yumura, Dispersion of metal nanoparticles for aligned carbon nanotube arrays, *Appl. Phys. Lett.* **77**, 79–81 (2000).
[26] J.-M. Bonard, P. Chauvin and C. Klinke, Monodisperse multiwall carbon nanotubes obtained with ferritin as catalyst, *Nano. Lett.* **2**, 665–667 (2002).
[27] V. Ivanov, J.B. Nagy, P. Lambin, A. Lucas, X.B. Zhang, X.F. Zhang, D. Bernaerts, G. Van Tendeloo, S. Amelinckx and J. Van Landuyt, The study of carbon nanotubules produced by catalytic method, *Chem. Phys. Lett.* **223**, 329–335 (1994).
[28] K. Hernadi, A. Fonseca, P. Piedigrosso, M. Delvaux, J. Nagy, D. Bernaerts and J. Riga, Carbon nanotubes production over Co/silica catalysts, *Catal. Lett.* **48**, 229–238 (1997).
[29] K. Hernadi, A. Fonseca, J.B. Nagy, D. Bernaerts, A. Fudala and A.A. Lucas, Catalytic synthesis of carbon nanotubes using zeolite support, *Zeolites* **17**, 416–423 (1996).
[30] Q. Li, H. Yan, Y. Cheng, J. Zhang and Z. Liu, A scalable CVD synthesis of high-purity single-walled carbon nanotubes with porous MgO as support material, *J. Mater. Chem.* **12**, 1179–1183 (2002).
[31] N. Nagaraju, A. Fonseca, Z. Konya and J. Nagy, Alumina and silica supported metal catalysts for the production of carbon nanotubes, *J. Mol. Catal. A* **181**, 57–62 (2002).
[32] T. de los Arcos, M.G. Garnier, J.W. Seo, P. Oelhafen, V. Thommen and D. Mathys, The influence of catalyst chemical state and morphology on carbon nanotube growth, *J. Phys. Chem. B* **108**, 7728–7734 (2004).
[33] H. Ago, K. Nakamura, N. Uehara and M. Tsuji, Roles of metal–support interaction in growth of single- and double-walled carbon nanotubes studied with diameter-controlled iron particles supported on MgO, *J. Phys. Chem. B* **108**, 18908–18915 (2004).
[34] E. Couteau, K. Hernadi, J.W. Seo, L. Thien-Nga, C. Mikó, R. Gaál and L. Forró, CVD synthesis of high-purity multiwalled carbon nanotubes using $CaCO_3$ catalyst support for large-scale production, *Chem. Phys. Lett.* **378**, 9–17 (2003).
[35] A. Magrez, J.W. Seo, Cs. Mikó, K. Hernadi and L. Forró, Growth of carbon nanotubes using alkaline earth carbonates as support for mass production, *J. Phys. Chem. B* **109**, 10087–10091 (2005).
[36] Y. Zhang, A. Chang, J. Cao, Q. Wang, W. Kim, Y. Li, N. Morris, E. Yenilmez, J. Kong and H. Dai, Electric-field-directed growth of aligned single-walled carbon nanotubes, *Appl. Phys. Lett.* **79**, 3155–3157 (2001).
[37] R. Hatakeyama, G. Jeong, T. Kato and T. Hirata, Effects of micro- and macro-plasma-sheath electric fields on carbon nanotube growth in a cross-field radio-frequency discharge, *J. Appl. Phys.* **96**, 6053–6060 (2004).
[38] K. Hata, D.N. Futaba, K. Mizuno, T. Namai, M. Yumura and S. Iijima, Water-assisted highly efficient synthesis of impurity-free single-walled carbon nanotubes, *Science* **306**, 1362–1364 (2004).
[39] A.J. Stone and D.J. Wales, Theoretical-studies of icosahedral C_{60} and some related species, *Chem. Phys. Lett.* **128**, 501–503 (1986).
[40] B.I. Dunlap, Connecting carbon tubules, *Phys. Rev. B* **46**, 1933–1936 (1992).
[41] S. Motojima, M. Kawaguchi, K. Nozaki and H. Iwanaga, Growth of regularly coiled carbon filaments by Ni catalyzed pyrolysis of acetylene, and their morphology and extension characteristics, *Appl. Phys. Lett.* **56**, 321–323 (1990).
[42] D. Bernaerts, X.B. Zhang, X.F. Zhang, S. Amelinckx, G. Van Tendeloo, J. van Landuyt, V. Ivanov and J.B. Nagy, Electron-microscopy study of coiled carbon tubules, *Philos. Mag. A* **71**, 605–630 (1995).
[43] K. Hernadi, L. Thien-Nga and L. Forró, Growth and microstructure of catalytically produced coiled carbon nanotubes, *J. Phys. Chem. B* **105**, 12464–12468 (2001).
[44] Y. Saito and T. Yoshikawa, Bamboo-shaped carbon tube filled partially with nickel, *J. Cryst. Growth* **134**, 154–156 (1993).
[45] V.V. Kovalevski and A.N. Safronov, Pyrolysis of hollow carbons on melted catalyst, *Carbon* **36**, 963–968 (1998).

[46] N.A. Kiselev, J. Sloan, D.N. Zakharov, E.F. Kukovitskii, J.L. Hutchison, J. Hammer and A.S. Kotosonov, Carbon nanotubes from polyethylene precursors: Structure and structural changes caused by thermal and chemical treatment revealed by HREM, *Carbon* **36**, 1149–1157 (1998).
[47] S. Ihara, S. Itoh and J. Kitakami, Toroidal forms of graphitic carbon, *Phys. Rev. B* **47**, 12908–12911 (1993).
[48] S. Amelinckx, X.B. Zhang, D. Bernaerts, X.F. Zhang, V. Ivanov and J.B. Nagy, A formation mechanism for catalytically grown helix-shaped graphite nanotubes, *Science* **265**, 635–639 (1994).
[49] M. Terrones, Science and technology of the twenty-first century: Synthesis, properties, and applications of carbon nanotubes, *Annu. Rev. Mater. Res.* **33**, 419–501 (2003).
[50] X.Q. Chen, S.L. Zhang, D.A. Dikin, W.Q. Ding, R.S. Ruoff, L.J. Pan and Y. Nakayama, Mechanics of a carbon nanocoil, *Nano Lett.* **3**, 1299–1304 (2003).
[51] A. Volodin, M. Ahlskog, E. Seynaeve, C.V. Haesendonck, A. Fonseca and J.B. Nagy, Imaging the elastic properties of coiled carbon nanotubes with atomic force microscopy, *Phys. Rev. Lett.* **84**, 3342–3345 (2000).
[52] T. Hayashida, L. Pan and Y. Nakayama, Mechanical and electrical properties of carbon tubule nanocoils, *Phys. B Condens. Matter* **323**, 352–353 (2002).
[53] V.I. Merkulov, D.H. Lowndes, Y.Y. Wei, G. Eres and E. Voelkl, Patterned growth of individual and multiple vertically aligned carbon nanofibers, *Appl. Phys. Lett.* **76**, 3555–3557 (2000).
[54] M. Chhowalla, K.B.K. Teo, C. Ducati, N.L. Rupesinghe, G.A.J. Amaratunga, A.C. Ferrari, D. Roy, J. Robertson and W.I. Milne, Growth process conditions of vertically aligned carbon nanotubes using plasma enhanced chemical vapor deposition, *J. Appl. Phys.* **90**, 5308–5317 (2001).
[55] M. Terrones, W.K. Hsu, A. Schilder, H. Terrones, N. Grobert, J.P. Hare, Y.Q. Zhu, M. Schwoerer, K. Prassides, H.W. Kroto and D.R.M. Walton, Novel nanotubes and encapsulated nanowires, *Appl. Phys. A: Mater. Sci. Proc.* **66**, 307–317 (1998).
[56] R. Sen, B.C. Satishkumar, A. Govindaraj, K.R. Harikumar, G. Raina, J.P. Zhang, A.K. Cheetham and C.N.R. Rao, B-C-N, C-N and B-N nanotubes produced by the pyrolysis of precursor molecules over Co catalysts, *Chem. Phys. Lett.* **287**, 671–676 (1998).
[57] R. Sen, B.C. Satishkumar, S. Govindaraj, K.R. Harikumar, M.K. Renganathan and C.N.R. Rao, Nitrogen-containing carbon nanotubes, *J. Mater. Chem.* **7**, 2335–2337 (1997).
[58] M. Terrones, H. Terrones, N. Grobert, W.K. Hsu, Y.Q. Zhu, J.P. Hare, H.W. Kroto, D.R.M. Walton, P. Köhler-Redlich, M. Rühle, J.P. Zhang and A.K. Cheetham, Efficient route to large arrays of CN_x nanofibers by pyrolysis of ferrocene/melamine mixtures, *Appl. Phys. Lett.* **75**, 3932–3934 (1999).
[59] R. Czerw, M. Terrones, J.C. Charlier, X. Blase, B. Foley, R. Kamalakaran, N. Grobert, H. Terrones, D. Tekleab, P.M. Ajayan, W. Blau, M. Rühle and D.L. Carroll, Identification of electron donor states in N-doped carbon nanotubes, *Nano Lett.* **1**, 457–460 (2001).
[60] P. Redlich, J. Loeffler, P.M. Ajayan, J. Bill, F. Aldinger and M. Ruhle, B-C-N nanotubes and boron doping of carbon nanotubes, *Chem. Phys. Lett.* **260**, 465–470 (1996).
[61] N.G. Chopra, R.J. Luyken, K. Cherrey, V.H. Crespi, M.L. Cohen, S.G. Louie and A. Zettl, Boron nitride nanotubes, *Science* **269**, 966–967 (1995).
[62] N.G. Chopra and A. Zettl, Measurement of the elastic modulus of a multi-wall boron nitride nanotube, *Solid State Commun.* **105**, 297–300 (1998).
[63] M.R. Pederson and J.Q. Broughton, Nanocapillarity in fullerene tubules, *Phys. Rev. Lett.* **69**, 2689–2692 (1992).
[64] B.W. Smith, M. Monthioux and D.E. Luzzi, Encapsulated C_{60} in carbon nanotubes, *Nature* **396**, 323–324 (1998).
[65] Y. Zhang, S. Iijima, Z. Shi and Z. Gu, Defects in arc-discharge-produced single-walled carbon nanotubes, *Philos. Mag. Lett.* **79**, 473–479 (1999).
[66] R. Pfeiffer, H. Kuzmany, C. Kramberger, C. Schaman, T. Pichler, H. Kataura, Y. Achiba, J. Kurti, and V. Zolyomi, Unusual high degree of unperturbed environment in the interior of single-wall carbon nanotubes, *Phys. Rev. Lett.* **90**, 225501.1–225501.4 (2003).
[67] B.W. Smith and D.E. Luzzi, Formation mechanism of fullerene peapods and coaxial tubes: A path to large scale synthesis, *Chem. Phys. Lett.* **321**, 169–174 (2000).

[68] K. Hirahara, K. Suenaga, S. Bandow, H. Kato, T. Okazaki, H. Shinohara and S. Iijima, One-dimensional metallofullerene crystal generated inside single-walled carbon nanotubes, *Phys. Rev. Lett.* **85**, 5384–5387 (2000).
[69] K. Suenaga, T. Tence, C. Mory, C. Colliex, H. Kato, T. Okazaki, H. Shinohara, K. Hirahara, S. Bandow and S. Iijima, Element-selective single atom imaging, *Science* **290**, 2280–2282 (2000).
[70] P.W. Chiu, G. Gu, G.T. Kim, G. Philipp, S. Roth, S.F. Yang and S. Yang, Temperature-induced change from p to n conduction in metallofullerene nanotube peapods, *Appl. Phys. Lett.* **79**, 3845–3847 (2001).
[71] J. Sloan, M.C. Novotny, S.R. Bailey, G. Brown, C. Xum, V.C. Williams, S. Friedrichs, E. Flahaut, R.L. Gallender, A.P.E. York, K.S. Coleman, M.L.H. Green, R.E. Dunin-Borkowski and J.L. Hutchison, Two-layer 4:4 co-ordinated KI crystals grown within single walled carbon nanotubes, *Chem. Phys. Lett.* **329**, 61–65 (2000).
[72] P.M. Ajayan and S. Iijima, Capillarity-induced filling of carbon nanotubes, *Nature* **361**, 333–334 (1993).
[73] P.M. Ajayan, T.W. Ebbesen, T. Ichihashi, S. Iijima, K. Tanigaki and H. Hiura, Opening carbon nanotubes with oxygen and implications for filling, *Nature* **362**, 522–525 (1993).
[74] P.M. Ajayan, O. Stephan, P. Redlich and C. Colliex, Carbon nanotubes as removable templates for metal-oxide nanocomposites and nanostructures, *Nature* **375**, 564–567 (1995).
[75] S.C. Tsang, Y.K. Chen, P.J.F. Harris and M.L.H. Green, A simple chemical method of opening and filling carbon nanotubes, *Nature* **372**, 159–162 (1994).
[76] A. Loiseau, N. Demoncy, O. Stephan, C. Colliex, and H. Pascard, Filling carbon nanotubes using an arc discharge in science and application of nanotubes, in Science and Application of Nanotubes, edited by D. Tomanek and R.J. Enbody (Kluwer Academic/Plenum Publishers, New York, 2000).
[77] S. Seraphin, D. Zhou, J. Jiao, J.C. Withers and R. Loutfy, Yttrium carbide in nanotubes, *Nature* **362**, 503 (1993).
[78] M.Q. Liu and J.M. Cowley, Encapsulation of manganese carbides within carbon nanotubes and nanoparticles, *Carbon* **33**, 749–756 (1995).
[79] P.M. Ajayan, C. Colliex, J.M. Lambert, P. Bernier, L. Barbedette, M. Tence and O. Stephan, Growth of manganese filled carbon nanofibers in the vapor-phase, *Phys. Rev. Lett.* **72**, 1722–1725 (1994).
[80] J.Y. Dai, J.M. Lauerhaas, A.A. Setlur and R.P.H. Chang, Synthesis of carbon-encapsulated nanowires using polycyclic aromatic hydrocarbon precursors, *Chem. Phys. Lett.* **258**, 547–553 (1996).
[81] A. Loiseau and H. Pascard, Synthesis of long carbon nanotubes filled with Se, S, Sb and Ge by the arc method, *Chem. Phys. Lett.* **256**, 246–252 (1996).
[82] E. Dujardin, T.W. Ebbesen, H. Hiura and K. Tanigaki, Capillarity and wetting of carbon nanotubes, *Science* **265**, 1850–1852 (1994).
[83] Y.H. Gao and Y. Bando, Carbon nanothermometer containing gallium – Gallium's macroscopic properties are retained on a miniature scale in this nanodevice, *Nature* **415**, 599 (2002).
[84] D. Ugarte, A. Chatelain and W.A. deHeer, Nanocapillarity and chemistry in carbon nanotubes, *Science* **274**, 1897–1899 (1996).
[85] K. Koga, G.T. Gao, H. Tanaka and X.C. Zeng, Formation of ordered ice nanotubes inside carbon nanotubes, *Nature* **412**, 802–805 (2001).
[86] B.C. Regan, S. Aloni, R.O. Ritchie, U. Dahmen and A. Zettl, Carbon nanotubes as nanoscale mass conveyors, *Nature* **428**, 924–927 (2004).
[87] J. Aihara, Lack of superaromaticity in carbon nanotubes, *J. Phys. Chem.* **98**, 9773–9776 (1994).
[88] A. Hirsch, Functionalization of single-walled carbon nanotubes, *Angew. Chem. Int. Ed.* **41**, 1853–1859 (2002).
[89] J.L. Bahr and J.M. Tour, Covalent chemistry of single-wall carbon nanotubes, *J. Mater. Chem.* **12**, 1952–1958 (2002).
[90] P. Calvert, Nanotube composites: A recipe for strength, *Nature* **399**, 210–211 (1999).
[91] S. Banerjee and S.S. Wong, Synthesis and characterization of carbon nanotube-nanocrystal heterostructures, *Nano Lett.* **2**, 195–200 (2002).

[92] M. Sano, A. Kamino, J. Okamura and S. Shinkai, Ring closure of carbon nanotubes, *Science* **293**, 1299–1301 (2001).
[93] K.C. Hwang, Efficient cleavage of carbon graphene layers by oxidants, *J. Chem. Soc. Chem. Commun*. 173–174 (1995).
[94] C.N.R. Rao, A. Govindaraj and B.C. Satishkumar, Functionalised carbon nanotubes from solutions, *Chem. Commun*. 1525–1526 (1996).
[95] J. Liu, A.G. Rinzler, H. Dai, J.H. Hafner, R.K. Bradley, P.J. Boul, A. Lu, T. Iverson, K. Shelimov, C.B. Huffman, F. Rodriguez-Macias, Y.-S. Shon, T.R. Lee, D.T. Colbert and R.E. Smalley, Fullerene pipes, *Science* **280**, 1253–1256 (1998).
[96] S. Pekker, J.P. Salvetat, E. Jakab, J.M. Bonard and L. Forró, Hydrogenation of carbon nanotubes and graphite in liquid ammonia, *J. Phys. Chem. B* **105**, 7938–7943 (2001).
[97] E.T. Mickelson, C.B. Huffman, A.G. Rinzler, R.E. Smalley, R.H. Hauge and J.L. Margrave, Fluorination of single-wall carbon nanotubes, *Chem. Phys. Lett*. **296**, 188–194 (1998).
[98] V. Georgakilas, K. Kordatos, M. Prato, D.M. Guldi, M. Holzinger and A. Hirsch, Organic functionalization of carbon nanotubes, *J. Am. Chem. Soc*. **124**, 760–761 (2002).
[99] D.B. Mawhinney, V. Naumenko, A. Kuznetsova, J.T. Yates, J. Liu and R.E. Smalley, Infrared spectral evidence for the etching of carbon nanotubes: Ozone oxidation at 298 K, *J. Am. Chem. Soc*. **122**, 2383–2384 (2000).
[100] J.L. Bahr, J.P. Yang, D.V. Kosynkin, M.J. Bronikowski, R.E. Smalley and J.M. Tour, Functionalization of carbon nanotubes by electrochemical reduction of aryl diazonium salts: A bucky paper electrode, *J. Am. Chem. Soc*. **123**, 6536–6542 (2001).
[101] J.L. Bahr and J.M. Tour, Highly functionalized carbon nanotubes using in situ generated diazonium compounds, *Chem. Mater*. **13**, 3823–3824 (2001).
[102] C.A. Dyke and J.M. Tour, Solvent-free functionalization of carbon nanotubes, *J. Am. Chem. Soc*. **125**, 1156–1157 (2003).
[103] P. Umek, J.W. Seo, K. Hernadi, A. Mrzel, P. Pechy, D.D. Mihailovic and L. Forró, Addition of carbon radicals generated from organic peroxides to single wall carbon nanotubes, *Chem. Mater*. **15**, 4751–4755 (2003).
[104] J.P. Lu, Elastic properties of carbon nanotubes and nanoropes, *Phys. Rev. Lett*. **79**, 1297–1300 (1997).
[105] P. Poncharal, Z.L. Wang, D. Ugarte and W.A.D. Heer, Electrostatic deflections and electromechanical resonances of carbon nanotubes, *Science* **283**, 1513–1516 (1999).
[106] J.-P. Salvetat, G.A.D. Briggs, J.-M. Bonard, R.R. Bacsa, A.J. Kulik, T. Stöckli, N. Burnham and L. Forró, Elastic and shear moduli of single-walled carbon nanotube ropes, *Phys. Rev. Lett*. **82**, 944–947 (1999).
[107] M.M.J. Treacy, T.W. Ebbesen and J.M. Gibson, Exceptionally high young's modulus observed for individual carbon nanotubes, *Nature* **381**, 678–680 (1996).
[108] A. Krishnan, E. Dujardin, T.W. Ebbesen, P.N. Yianilos and M.M.J. Treacy, Young's modulus of single-walled nanotubes, *Phys. Rev. B* **58**, 14013–14019 (1998).
[109] J.-P. Salvetat, J.M. Bonard, N.H. Thomson, A.J. Kulik, L. Forró, W. Benoit and L. Zuppiroli, Mechanical properties of carbon nanotubes, *Appl. Phys. A* **69**, 255–260 (1999).
[110] J.-P. Salvetat, A.J. Kulik, J.-M. Bonard, G.A.D. Briggs, T. Stöckli, K. Méténier, S. Bonnamy, F. Béguin and L. Forró, Elastic modulus of ordered and disordered multiwalled carbon nanotubes, *Adv. Mater*. **11**, 161–165 (1999).
[111] B. Lukic, J.W. Seo, E. Couteau, K. Lee, S. Gradeçak, R. Berkecz, K. Hernadi, S. Delpeux, T. Cacciaguerra, F. Beguin, A. Fonseca, J.B. Nagy, G. Csanyi, A. Kis, A.J. Kulik and L. Forró, Elastic modulus of multi-walled carbon nanotubes produced by catalytic chemical vapour deposition, *Appl. Phys. A: Mater. Sci. Proc*. **80**, 695–700 (2005).
[112] B. Lukic, J.W. Seo, R.R. Bacsa, S. Delpeux, F. Beguin, G. Bister, A. Fonseca, J.B. Nagy, A. Kis, S. Jeney, A.J. Kulik and L. Forró, Catalytically grown carbon nanotubes of small diameter have a high young's modulus, *Nano Lett*. **5**, 2074–2077 (2005).
[113] A. Kis, J.P. Salvetat, T.N. Lee, E. Ljubovic, A. Kulik, W. Benoit, J. Brugger and L. Forró, Reinforcement of single-walled carbon nanotube bundles by intertube bridging, *Nat. Mater*. **3**, 153–157 (2004).

[114] V.H. Crespi, N.G. Chopra, M.L. Cohen, A. Zettl and S.G. Louie, Anisotropic electron-beam damage and the collapse of carbon nanotubes, *Phys. Rev. B* **54**, 5927–5931 (1996).
[115] B.W. Smith and D.E. Luzzi, Formation mechanism of fullerene peapods and coaxial tubes: A path to large scale synthesis, *Chem. Phys. Lett.* **321**, 169–174 (2001).
[116] A.B. Dalton, S. Collins, E. Muñoz, J.M. Razal, V.H. Ebron, J.P. Ferraris, J.N. Coleman, B.G. Kim and R.H. Baughman, Super-tough carbon-nanotube fibres, *Nature* **423**, 703 (2003).
[117] B. Vigolo, A. Penicaud, C. Coulon, C. Sauder, R. Pailler, C. Journet, P. Bernier and P. Poulin, Macroscopic fibers and ribbons of oriented carbon nanotubes, *Science* **290(5495)**, 1331–1334 (2000).
[118] H.H. Gommans, J.W. Alledredge, H. Tashiro, J. Park, J. Magnuson and G.A. Rinzler, Fibers of an aligned single-walled carbon nanotubes: Polarized Raman spectroscopy, *J. Appl. Phys.* **88**, 2509–2514 (2000).
[119] S. Badaire, V. Pichot, C. Zakri, P. Poulin, P. Launois, J. Vavro, C. Guthy, M. Chen and J.E. Fischer, Correlation of properties with preferred orientation in coagulated and stretch-aligned single-wall carbon nanotubes, *J. Appl. Phys.* **96**, 7509–7513 (2004).
[120] J.W. Seo, E. Couteau, P. Umek, K. Hernadi, P. Marcoux, B. Lukic, C. Mikó, M. Milas, R. Gaál, and L. Forró, Synthesis and manipulation of carbon nanotubes, *New J. Phys.* **5**, 120.1–120.22 (2003).
[121] C. Mikó, M. Milas, J.W. Seo, E. Couteau, N. Barisic, R. Gaál and L. Forró, Effect of electron irradiation on the electrical properties of fibers of aligned single-walled carbon nanotubes, *Appl. Phys. Lett.* **83**, 4622–4624 (2003).
[122] P. Kim and C.M. Lieber, Nanotube nanotweezers, *Science* **286**, 2148–2150 (1999).
[123] S. Akita, Y. Nakayama, S. Mizooka, Y. Takano, T. Okawa, Y. Miyatake, S. Yamanaka, M. Tsuji and T. Nosaka, Nanotweezers consisting of carbon nanotubes operating in atomic force microscope, *Appl. Phys. Lett.* **79**, 1691–1693 (2001).
[124] C.H. Ke and H.D. Espinosa, Feedback controlled nanocantilever device, *Appl. Phys. Lett.* **85**, 681–683 (2004).
[125] C.H. Ke, N. Pugno, B. Peng and H.D. Espinosa, Experiments and modeling of carbon nanotube-based NEMS devices, *J. Mech. Phys. Sol.* **53**, 1314–1333 (2005).
[126] S.N. Cha, J.E. Jang, Y. Choi, G.A. Amaratunga, D.-J. Kang, D.G. Hasko, J.E. Jung and J.M. Kim, Fabrication of a nanoelectromechanical switch using a suspended carbon nanotube, *Appl. Phys. Lett.* **86**, 083105.1–083105.3 (2005).
[127] J.E. Jang, S.N. Cha, Y. Choi, G.A.J. Amaratunga, D.J. Kang, D.G. Hasko, J.E. Jung and J.M. Kim, Nanoelectromechanical switches with vertically aligned carbon nanotubes, *Appl. Phys. Lett.* **87**, 163114.1–163114.3 (2005).
[128] T. Rueckes, K. Kim, E. Joselevich, G.Y. Tseng, C.-L. Cheung and C.M. Lieber, Carbon nanotube based nonvolatile random access memory for molecular computing, *Science* **289**, 94–97 (2000).
[129] V. Sazonova, Y. Yaish, H. Üstünel, D. Roundy, T.A. Arias and P.L. McEuen, A tunable carbon nanotube electromechanical oscillator, *Nature* **431**, 284–287 (2004).
[130] J. Cumings, P.G. Collins and A. Zettl, Peeling and sharpening multiwall nanotubes, *Nature* **406**, 586 (2000).
[131] J. Cumings and A. Zettl, Low-friction nanoscale linear bearing realized from multiwall carbon nanotubes, *Science* **289**, 602–604 (2000).
[132] J.C. Charlier and J.P. Michenaud, Energetics of multilayered carbon tubules, *Phys. Rev. Lett.* **70**, 1858–1861 (1993).
[133] M.F. Yu, B.I. Yakobson and R.S. Ruoff, Controlled sliding and pullout of nested shells in individual multiwalled carbon nanotubes, *J. Phys. Chem. B* **104**, 8764–8767 (2000).
[134] A.N. Kolmogorov and V.H. Crespi, Smoothest bearings: Interlayer sliding in multiwalled carbon nanotubes, *Phys. Rev. Lett.* **85**, 4727–4730 (2000).
[135] Y. Zhao, C.C. Ma, G. Chen and Q. Jiang, Energy dissipation mechanisms in carbon nanotube oscillators, *Phys. Rev. Lett.* **91**, 175504.1–175504.4 (2003).
[136] J. Servantie and P. Gaspard, Methods of calculation of a friction coefficient: Application to nanotubes, *Phys. Rev. Lett.* **91**, 185503.1–185503.4 (2003).

[137] S.B. Legoas, V.R. Coluci, S.F. Braga, P.Z. Coura, S.O. Dantas and D.S. Galvao, Molecular-dynamics simulations of carbon nanotubes as gigahertz oscillators, *Phys. Rev. Lett.* **90**, 55504.1–55504.4 (2003).
[138] L. Forró, Nanotechnology: Beyond Gedanken experiments, *Science* **289**, 560–561 (2000).
[139] K.E. Drexler, *Nanosystems: Molecular machinery, manufacturing and computation* (Wiley, New York, 1992).
[140] A.M. Fennimore, T.D. Yuzvinsky, W.-Q. Han, M.S. Fuhrer, J. Cumings and A. Zettl, Rotational actuators based on carbon nanotubes, *Nature* **424**, 408–410 (2003).
[141] B. Bourlon, C. Glattli, C. Mikó, L. Forró and A. Bachtold, Carbon nanotube based bearing for rotational motions, *Nano Lett.* **4**, 709–712 (2004).
[142] H. Cui, O. Zhou and B.R. Stoner, Deposition of aligned bamboo-like carbon nanotubes via microwave plasma enhanced chemical vapor deposition, *J. Appl. Phys.* **88**, 6072–6074 (2000).
[143] A. Kis, Mechanical properties of mesoscopic objects, Ph.D. Thesis, Ecole Polytechnique Fédérale de Lausanne, 2003.

Chapter 7
LOW-ENERGY ELECTRONIC STRUCTURE OF GRAPHENE AND ITS DIRAC THEORY

E. J. Mele and C. L. Kane

1. INTRODUCTION

Graphene is an extended two-dimensional (2D) sheet of carbon atoms bound by strong nearest neighbor sp^2 bonds and ordered in the form of a 2D honeycomb lattice. Stacked sheets of graphene occur naturally in the mineral graphite, an extremely well-studied form of carbon that historically has attracted attention because of its unique electronic and structural properties. Interest in the physical properties of single-layer graphene has been sparked by the recent discoveries of practical experimental methods for isolating macroscopic single- and few-layer samples [1–3]. Subsequent work has revealed a class of remarkable quantum electronic transport phenomena in ultrathin one- and few-layer samples [4–6] even at room temperature [7], although the related effects are quickly suppressed when the graphene layers are stacked to form a three-dimensional (3D) material [8]. It is possible that some of these phenomena might be harnessed to develop a new family of submicron electronic devices based on their 2D physics [9,10].

There has been significant progress in understanding many of these effects using a relatively simple model for the electronic structure. Indeed many of the unusual electronic phenomena observed in graphene arise from a particular topological property of its low-energy spectrum. The graphene ''nonbonding'' π electrons form its valence and conduction bands [11,12], and these bands meet at discrete critical points at the corners (conventionally labeled K and K') of its 2D Brillouin zone. The energy bands disperse linearly away from the touching points, so that the dispersion relation for the electrons(holes) is described by an isotropic cone that opens upward

Contemporary Concepts of Condensed Matter Science
Carbon Nanotubes: Quantum Cylinders of Graphene

ISSN: 1572-0934/doi:10.1016/S1572-0934(08)00007-3

(downward) near these critical points. This situation can be described by a long wavelength effective mass model in the form of the Dirac equation for a massless particle propagating in two space dimensions [13–15]. The topological structure of the eigenstates of this model are responsible for many of the interesting electronic effects observed at low energy.

Some of these effects reported in the recent literature have precedents in the assortment of rich electronic phenomena discovered in carbon nanotubes [17]. Indeed the nanotubes are *one dimensional* (1D) structures formed by seamlessly wrapping 2D sheets of graphene. It is known that single-walled nanotubes can be formed in semiconducting (gapped), metallic (gapless) and nearly metallic (nearly gapless) forms, where the distinction depends sensitively on the geometry of the wrapping [18,19]. This is now understood to arise from a subtle size quantization effect where the extreme sensitivity to wrapping arises from the point singularity in the spectrum of the parent graphene, the linear dispersion around this point, and phase coherent electron motion around the circumference of the cylinder.

Detailed reviews of the recent theoretical and experimental developments in the study of graphene and nanotubes are beginning to appear in the literature [15–17,20,21]. In this contribution to a volume on nanotube physics, we briefly highlight some of the novel quantum mechanical properties of electrons near the Dirac points in graphene, emphasizing their topological origin and relate them to some closely analogous phenomena that occur in the electronic physics of carbon nanotubes.

2. ATOMICALLY THIN GRAPHENES

Until quite recently attempts to isolate single layers of graphene were limited to chemical methods. Indeed the interplanar bonding in graphite is weak permitting the chemical insertion of donor or acceptor species between the layers, which both separates the layers and modifies the electronic properties of the composite. These intercalated graphites attracted great interest because of their relatively high conductivities and because the plasma edge in their reflectance spectra occurs at optical frequencies. However, intercalated graphites remain essentially anisotropic 3D materials.

Attempts to chemically grow isolated ultrathin graphene layers on a substrate, either by chemical vapor deposition or by chemical decomposition of SiC are generally limited by the difficulty of finding a lattice matched substrate that permits coherent growth of a graphene layer, and of developing a controlled synthesis that can produce a single layer, although there has been significant progress in this direction [9,10]. Practical applications of graphite in nanoelectronics will likely require refinements of this strategy.

To date the most successful methods for producing isolated one- and few-layer graphene sheets have instead focused on various forms of micromechanical cleavage

[1–3,21]. Early work employed repeated tapping of a graphite flake attached to stylus (e.g., an atomic force microscope tip) to deposit ultrathin graphene layers on a substrate [1]. This method of "writing" graphene samples turns out to be somewhat uncontrolled depositing multilayer samples as thin as 10 nm, but often thicker. An alternative, and now commonly used method is the inverse of writing – namely repeated *pealing* a thick (i.e., multilayer) graphitic sample with adhesive tape until ultrathin samples remain [2,21]. This method readily yields samples as small as a single atomic layer and with lateral dimensions up to 100 μm. Remarkably, samples produced by this method can be located and identified using phase contrast optical microscopy.

An important feature of these ultrathin samples is that they can be electrostatically doped n- or p-type to lateral carrier densities exceeding $10^{12}\,\mathrm{cm}^{-2}$ [2,5]. Indeed, this has been a critical ingredient in most transport measurements made to date, since nonmonotonic behavior in the charge transport as a function of gate voltage identifies the "charge neutrality point" in experimental samples, and allows one to carefully study the dependence of the conductivity and the mobility on the carrier density.

In fact, transport studies provide some of the clearest indications that few-layer films produced by this method are of very high quality. Near the charge neutrality point, the conductivity shows an approximately linear increase with the carrier density, from a minimum value $\sigma \approx 4e^2/h$ at the charge neutrality point [2] as shown in Fig. 1. Away from this minimum, normalizing to the carrier density suggests a mobility $\mu \approx 10^4\mathrm{cm}^2/\mathrm{Vs}$ at 1.7 K, with a weak density and temperature dependence at high carrier density, indicating a mean free path $\sim 0.3\,\mu\mathrm{m}$ even at room temperature. The interpretation of the bulk mobility is problematic in the limit of vanishing carrier concentration where the conductivity remains finite. Physically this may reflect charge inhomogeneity in the graphene sheets or some other nonextensive effect that controls the carrier transport in this regime.

Samples produced by these methods show a striking quantization of the Hall conductance, and oscillations in their longitudinal magnetoresistance [4,5]. Fig. 2 clearly shows the quantized plateaus in the Hall conductance $R_{xy}^{-1} = \pm 4(n + 1/2)e^2/h$ on either side of its charge neutrality point in a magnetic field of 9 T and a temperature 1.6 K [5]. Significantly, at much larger fields $\sim 30\,\mathrm{T}$, these quantum oscillations can be detected even at room temperature [7], extending by a factor of ten the temperature range for observing the effects of Landau quantization in two dimensions.

The high quality of 2D crystalline samples of graphene can be rationalized by invoking the intrinsic strength of interatomic bonding between carbon atoms *and* by the fact that experiments are actually carried out on samples that are attached to a 3D substrate [22]. Indeed, for freely suspended graphene sheets, one observes significant deviations from planarity (~ 1 nm), possibly stabilizing their crystalline order within the tangent plane through anharmonic couplings between their bending and stretching degrees of freedom [22]. The mobility is believed to be

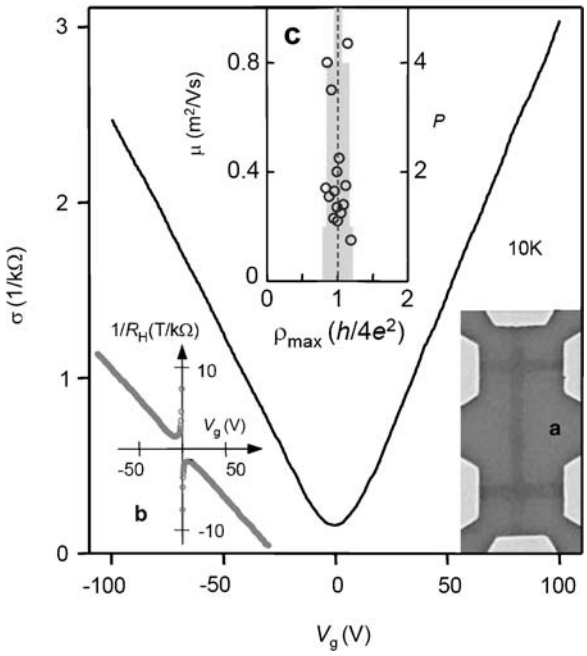

Fig. 1. The variation of the conductivity of single-layer graphene as a function of the potential of an electrostatic gate, which varies the carrier concentration. These samples shows a nonzero minimum conductivity at its charge neutrality point and an approximately linear increase with carrier concentration. The insets show the observed minimum conductivity near the value $4e^2/h$ for several different samples and the Hall conductance as a function of the gate voltage. (Reprinted by permission from MacMillan Publishers Ltd. [21].)

limited by long-range scattering from impurities near the graphene and its unexpectedly high value may reflect a suppression of long-range scattering due to the quantum character of its charge carriers [23,24].

3. EFFECTIVE MASS THEORY FOR MASSLESS ELECTRONS

The graphene honeycomb lattice is a triangular Bravais lattice containing two atomic sites (conventionally labeled the A and B sites) in its primitive cell. The π electrons are responsible for its low-energy electronic properties, and their Bloch states can be represented by two-component (spinor) wavefunctions where the two components are the complex amplitudes for an electron to reside in the π orbitals centered on the A and the B sublattice sites. Expanding the Hamiltonian to linear order in the crystal momenta $\vec{k}$ near a Brillouin zone corner (K) where the

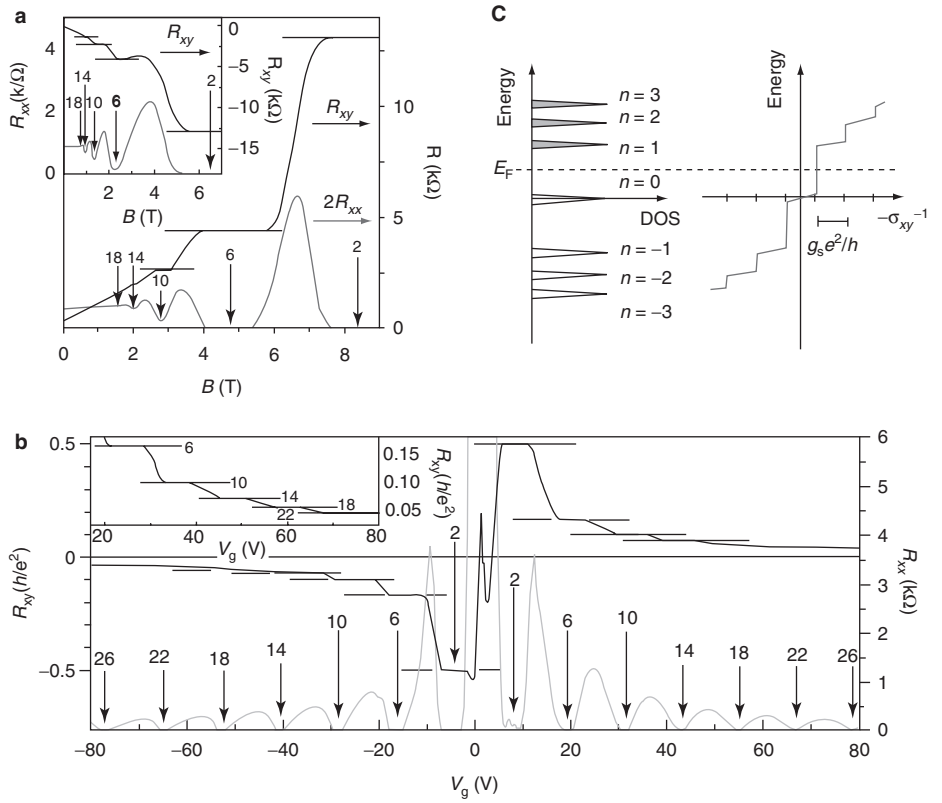

Fig. 2. The quantized Hall resistance R_{xy} and the longitudinal magnetoresistance R_{xx} measured as a function of gate potential which controls the carrier concentration in single-layer graphene in a magnetic field of 9 T and at $T = 1.6$ K. The inverse Hall resistance is quantized to the integer values $(n+1/2)4e^2/h$, accompanied by a minima in the longitudinal resistance. Complex structure is seen in the Hall resistance when it changes sign at the charge neutrality point and in the longitudinal resistance near this point. Panel (c) shows the particle–hole symmetric Landau quantization for a massless Dirac particles and a schematic of the variation of the Hall conductance with the chemical potential. (Reprinted by permission from MacMillan Publishers Ltd. [5].)

conduction and valence bands just touch, one finds that this spinor is an eigenfunction of a 2×2 matrix effective mass Hamiltonian.

$$\hat{H}_K(k_x, k_y)\begin{pmatrix} u \\ v \end{pmatrix} = \hbar v_F \begin{pmatrix} 0 & k_x - ik_y \\ k_x + ik_y & 0 \end{pmatrix}\begin{pmatrix} u \\ v \end{pmatrix} = E(k_x, k_y)\begin{pmatrix} u \\ v \end{pmatrix} \qquad (1)$$

This Hamiltonian describes a massless Dirac particle with an internal "pseudospin" 1/2 propagating in two dimensions with an isotropic dispersion

relation $E(\vec{k}) = \pm\hbar v_F|\vec{k}|$ [13,14]. Here the Fermi velocity $\sim 10^6$ m/s plays the role of the speed of light in the ordinary Dirac Hamiltonian. The two pseudospin degrees of freedom do not represent the physical spin polarizations, but rather the A and B sublattice amplitudes. The low-energy electronic states are then characterized by quantum numbers labeling their pseudospin (sublattice) amplitudes, their physical spin polarization, and a two-component isospin degree of freedom, which is a valley index arising from the degeneracy of the electronic states associated with the two inequivalent K and K' zone corners (Fig. 3).

An important property of the Hamiltonian in Eq. (1) is its *chirality*: the energy spectrum of Eq. (1) is isotropic, but the relative phases of the two components of its spinor eigenstates *rotate* with the propagation direction [13,14]. This can be seen by rewriting Eq. (1) in the form $H_K = \hbar v_F|\vec{k}|\vec{\sigma}\cdot\hat{k}$ where σ_i are the 2×2 Pauli matrices. This demonstrates that the positive(negative) energy solutions of Eq. (1) align their pseudospins parallel (antiparallel) to the propagation direction $\hat{k}$. Of course, the honeycomb latttice is not a chiral crystal structure, and the spinor eigenstates obtained near the K' point show precisely the complementary behavior. There the positive(negative) energy eigenstates align their pseudospins antiparallel (parallel) to the related director $\hat{k}^* \equiv (k_x - ik_y)/|k|$; this conjugate director *counter-rotates* relative to the propagation direction.

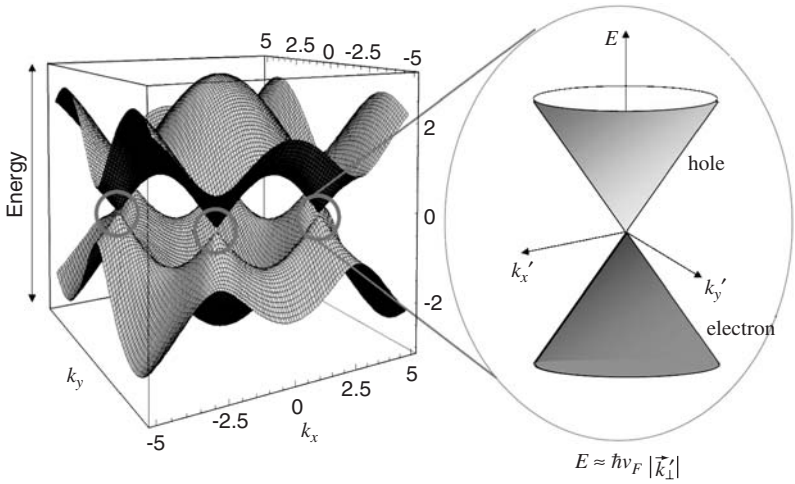

Fig. 3. The dispersion of the π electronic bands in graphene as a function of crystal momentum near the zone corners has an isotropic conical dispersion relation that provides a solid-state analog of the dispersion for a 2D relativistic particle. The valence and conduction bands just touch at two critical points (labeled K and K') at the Brillouin zone corners. The linearized Hamiltonians near these two points are separately chiral, but have opposite handedness. The Bloch waves of this spectrum are two-component spinors, describing a pseudospin 1/2 particle, and reflecting the two-sublattice structure of the underlying honeycomb lattice. (Graphic courtesy of P. Kim, unpublished.)

The pseudospin is an essential internal degree of freedom because it encodes important phase relations for the electron amplitudes on the two sublattices. In early work, it was appreciated that the existence of the internal pseudospin requires an anomalous quantization of the total orbital angular momentum of the electronic states to *half-integral* values [13], describing a change of sign of the two-component spinor under rotation of its coordinate system by 2π. This anomaly can be traced to the effect of a Berry's phase of π [5] for an electron that evolves adiabatically on a phase space trajectory that encloses the point of degeneracy at $k = 0$.

When graphene is undoped, its Fermi surface consists of just the two singular points at which the valence and conduction bands meet. Because of the linear dispersion of these bands away from these points, the electronic density of states vanishes $\propto |E|$ at low energy, yielding a prototypical model for a 2D semimetal. This system is poised precisely in between conducting and insulating behavior: it has a Fermi surface, but one that is nonextensive (i.e., it is collapsed to Fermi *points* instead of lines), and it has a direct gap almost everywhere in the Brillouin zone except at the touching points. When the Fermi energy is located precisely at the charge neutrality point, the density of thermally excited free carriers also vanishes as $T \to 0$. The implications of this situation for electrical transport in *intrinsic* graphene are subtle and unconventional [25], and require a careful treatment of the effects of scattering on the electronic states near the contact point. It has been emphasized that intrinsic graphene may be an abstraction, of theoretical interest only, since transport measurements on graphene inevitably involve the motion of *extrinsic* carriers in the presence of a background potential from an ensemble of self consistently screened charged impurities [24,26].

The Dirac model for the low-energy spectrum, in its simplest form, requires elaboration to allow a comparison with experimental data. Prominently, its description of a "zero gap" semiconductor is modified by the effects of quantum confinement in experimental nanographenes of finite lateral extent. Illustrative calculations have been carried out for the cases of graphene nanoribbons with the high symmetry zigzag and armchair terminations at the edges [27,28]. These structures retain the translational symmetry of the parent graphene sheet along the length of the ribbon, but their low-energy spectra are changed by the quantization of the crystal momentum across its width. Within the simplest isotropic tight binding models one finds that ribbons with armchair terminations can be grouped into three families: one retains a branch in the electronic spectrum that extends to zero energy and two have size quantization gaps that are inversely proportional to the ribbon width [28]. A more complete theoretical description using the self-consistent pseudopotential method demonstrates that the isotropic approximation fails for armchair nanoribbons [28] due to the angular dependence of the intersite hopping amplitudes when the threefold symmetry of the parent graphene sheet is absent. As a consequence, all armchair ribbons are semiconductors and they can be grouped into three structural families where the bandgaps within family each are inversely proportional to the width [28]. These size quantization gaps can be substantial, or order 1 eV for ultranarrow graphenes with width of order 1 nm, reflecting the relatively large size of the Fermi velocity. Zigzag graphene

nanoribbons are also gapped, but the mechanism is different. For the zigzag termination, the twofold rotational symmetry of the parent graphene sheet is absent and the site diagonal potentials on the A and B sublattices are in general different. This induces an asymmetric site diagonal term in the Dirac model (a mass term) that gaps its low-energy spectrum. In addition the zigzag edge possess a low-energy surface band that crosses its charge neutrality point and leads to interesting physics as discussed further in Section 8.

Similar considerations arise in the theory of graphene bilayers. In a typical experiment, these structures are fabricated on substrates that render the two layers symmetry inequivalent, and in many cases this asymmetry can be further tuned by an electric field from a gate electrode positioned below the bilayer graphene. There has been particular interest in the experimentally important case of Bernal stacking of the layers, in which half of the bilayer atoms are stacked above atoms and half over sixfold hollows [29,30]. In the absence of any perpendicular asymmetry, these two layers are symmetry equivalent and the system retains a point zero in its electronic dispersion, but interestingly with a *quadratic* dispersion away from its Fermi point. A perpendicular electric field produces an asymmetry between the site diagonal potentials on the two layers. This disproportionates the charge between the two layers, displacing their respective low-energy Dirac cones in energy and leading to avoided crossings between these bands at the bilayer charge neutrality level. The scale of the residual gap produced by this mechanism is significant, of order 100 meV for experimentally achievable perpendicular fields strengths [29,30].

A carbon nanotube is a rolled sheet of graphene [17], and for all but the smallest radius tubes the graphene model provides a good starting point for understanding their electronic properties as well. The wrapping of the graphene sheet imposes periodic boundary conditions on its Bloch wavefunctions, quantizing their crystal momenta in the circumferential direction while retaining their free running wave character along the tube axis [18]. The allowed electronic states for the nanotube become kinematically confined to parallel lines mapped into graphene's 2D Brillouin zone as illustrated in Fig. 4. Measured relative to the Brillouin zone center, these transverse momenta are quantized to the elementary values $k_m = m/R$ where R is the tube radius. However, when analyzing the low-energy electronic behavior it is generally more useful to translate this kinematical constraint into a boundary condition on the effective mass wavefunctions, i.e., the eigenfunctions of Eq. (1). These envelope functions describe long wavelength spatial modulations the Bloch wavefunctions at the zone *corners*, which are actually the $\sqrt{3} \times \sqrt{3}$ standing waves of the honeycomb lattice. To describe a single valued electronic wave, one therefore requires an anomalous *fractional* quantization of the envelope function. One finds that the appropriate boundary condition on the envelope field quantizes their crystal momenta to the one-third fractional values $k_n = (n + \nu/3)/R$ where the chiral index ν can take the values 0, ± 1 depending on the circumferential wrapping vector for the tube in question [18,19]. One immediately concludes that the critical semimetallic character of the parent graphene structure leads to distinct conducting or semiconducting behavior in three nanotube families, labeled by the value of the chiral index ν. A zero energy state is possible only for the special case of $\nu = 0$.

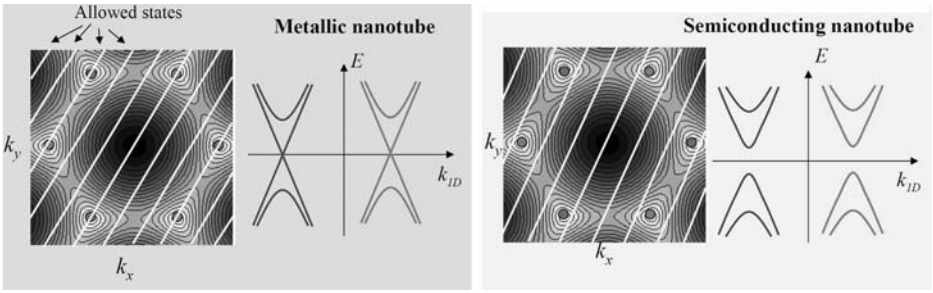

Fig. 4. On a carbon nanotube, the quantization of the circumferential component of the crystal momentum kinematically confines the allowed electronic states to parallel lines in the graphene Brillouin zone. When these lines pass through the Brillouin zone corners two branches cross $E = 0$ at each Dirac point and the tube is metallic. When no lines pass through the Dirac point the tube is a semiconductor characterized by a bandgap determined by the point of closest approach to the Dirac point. (Graphic courtesy of P. Kim, unpublished.)

Nonzero v induces a substantial semiconducting gap (~ 1 eV) for the range of tube radii produced in typical experiments. These gaps scale inversely with the tube radius R to leading order in $1/R$. Corrections to this leading order approximation arise from tube curvature and from the rehybridization of the electronic states and enter the theory proportional to $1/R^2$, with a strength that depends on the chiral angle (conventionally given by the angle between a bond and the circumferential direction) and with a sign that depends on the chiral index v [19]. Interestingly, curvature corrections *also* occur for the nominally metallic structures with $v = 0$ rendering most of them small bandgap (~ 10 meV) semiconductors [19]. These corrections turn out to vanish by symmetry for the so-called "armchair" structures with chiral angle $2\pi m/3$, with $m = 0, \pm 1$ which are the only intrinsically conducting species of single-walled carbon nanotube.

The valley degeneracy of the parent graphene sheet is also inherited by the carbon nanotube. Kinematically allowed states near the K and K' points of the nanotube are related by time-reversal symmetry and by a twofold rotational symmetry about an axis perpendicular to the tube axis. This implies that for semiconducting tubes the minimum offsets of the kinematically allowed crystal momenta from the K and K' points (and thus their gap parameters) are exactly "reversed" at the two valleys as shown in Fig. 4.

4. BERRY'S PHASE AND LANDAU QUANTIZATION

Perhaps the most spectacular manifestation of the Dirac character of the electronic structure in graphene is found in its Hall effect. For the 2D electron gas described by the *nonrelativistic* Schrödinger equation, an applied uniform magnetic field

collapses the spectrum to discrete Landau levels at quantized energies.

$$E_n = \left(n + \frac{1}{2}\right)\frac{e\hbar B}{mc} \tag{2}$$

Each of these levels has a macroscopic orbital degeneracy proportional to the flux Φ linking the sample $g = e\Phi/hc$ and the inverse Hall resistance is quantized to the values $R_{xy}^{-1} = ne^2/h$ when the chemical potential resides in the nth gap between Landau levels [31].

In contrast Landau quantization of massless relativistic fermions in a uniform magnetic field also produces a discrete electronic spectrum with a particle–hole symmetric nonuniform level spacing [14].

$$E_n = \sqrt{2e\hbar v_F^2\left(n + \frac{1}{2} \pm \frac{1}{2}\right)} \tag{3}$$

where the $\pm$ describes the two *pseudospin* degrees of freedom. For $n \geq 1$ theses levels carry a macroscopic degeneracy $4g$ accounting for the physical spin and isospin (valley degeneracy). Importantly, Eq. (2) also reveals that the spectrum contains a special zero energy state in which electrons reside on a single sublattice and the degeneracy is halved $g_0 = 2g$. Here, when the chemical potential is pinned in a gap between neighboring Landau levels, the inverse Hall resistance is quantized [32] to the values.

$$R_{xy}^{-1} = \pm 4\left(n + \frac{1}{2}\right)\frac{e^2}{h} \tag{4}$$

This demonstrates that the zero energy state does not contribute to the Hall effect in graphene, or equivalently that electrons and holes contribute equally (but in opposite directions) to the Hall effect in its lowest Landau level. The resulting quantization sequence to *half-integral* values then reflects the Berry's phase acquired by the pseudospin as the Dirac electrons orbit in a magnetic field. The quantized Hall conductance measured experimentally [4,5] shown in Figs. 2 and 5 provide a striking confirmation of this quantization rule.

For the Hall effect in graphene when the Fermi energy is pinned in a bulk gap between Landau levels, the quantized plateaus in the Hall conductance (as a function of electron density) are accompanied by minima in the longitudinal resistance (Fig. 5) [5], just as found in the quantum Hall effect of the ordinary 2D electron gas. As the electron density is tuned through the charge neutrality point the Hall conductance changes its sign and complex behavior is seen in its longitudinal conductance.

This situation undergoes a remarkable modification for bilayer graphene. For bilayer graphene with two graphene sheets stacked in the Bernal structure (with half the atoms above atoms and half above sixfold hollows), the low-energy Hamiltonian has the form of Eq. (1), but with off diagonal terms proportional to

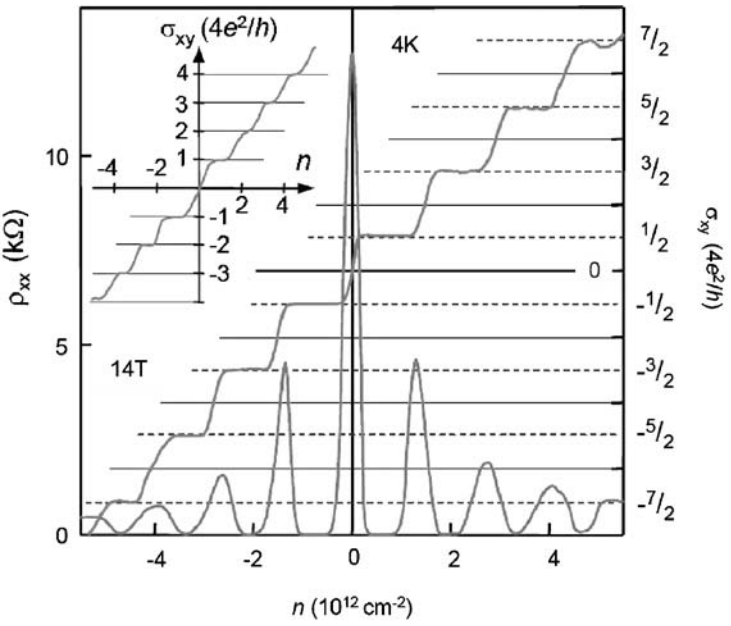

Fig. 5. The quantization of the Hall conductance for to single-layer graphene and for bilayer graphene (inset). In the former the electrons are described by massless Dirac particles and the Hall conductance is quantized to the integer values $(n+1/2)4e^2/h$. For the bilayer at low energy the electrons have a gapless particle–hole symmetric spectrum but with a quadratic dispersion. This yields plateaus in the Hall conductance at $4ne^2/h$ with a missing plateau at the charge neutrality point. The quantization arises from a Berry's phase of π for the spinor eigenstates of the single-layer graphene and 2π for the bilayer. (Reprinted by permission from MacMillan Publishers Ltd. [4].)

$(k_x \pm ik_y)^2$ [8,33]. Thus one has the rather peculiar situation of two *massive* Dirac bands that just touch and disperse quadratically in momentum space away from its charge neutrality point. Notably this also introduces a Berry's phase, but with value 2π, in the electronic spectrum [33]. The Landau level quantization for this system is

$$E_n = \sqrt{n(n-1)}\frac{e\hbar B}{mc} \tag{5}$$

The Hall conductance is quantized to integral values of $4e^2/h$ but, as shown in Fig. 5 with a *missing plateau* at zero energy, so that the step in the Hall conductance separating electron- and hole-like regions is twice as large as the quantized steps on either side of the charge neutral state. This anomaly at $E = 0$ can be removed by field effect doping, which has the effect of adding carriers *and* splitting the layer degeneracy of the zero energy Landau level producing two new steps in the Hall conductance, each of height $4e^2/h$.

5. INTRAVALLEY AND INTERVALLEY SCATTERING

The pseudospin and its accompanying Berry's phase in graphene turn out to control matrix elements that arise in the discussion of various scattering and transport processes. It is generally useful to treat separately the effects of impurity potentials that vary smoothly on the scale of a lattice constant (long-range scatterers) and those that vary on the scale of a lattice constant (short-range scatterers). The latter can mediate scattering processes between the K and K' points, while the former allow only for intravalley scattering near the K and K' points [25,34–36,37,38].

The situation where one treats only the effect of long-range scatterers is especially interesting. Because of the helicity of the electronic states, a scattering event that connects states with different momenta requires a rotation of the pseudospin polarization. *Backscattering* an electron from a state $\vec{k}$ to a state $-\vec{k}$ is described by the coherent superposition of amplitudes for multiple scattering events connecting the initial and final states *and* their conjugate amplitudes that connect the same initial and final states through the same scattering processes in the reverse time ordering [25,39,40]. The amplitudes for these "forward" and "backward" multiple scattering processes are equal in magnitude, but because of the pseudospin rotation they carry opposite signs and cancel. One concludes that there can be no backscattering from a static long-range impurity potential. The situation is analogous to the absence of backscattering in an ordinary metal in the presence of strong spin–orbit scattering, where the sign change arises from a rotation of the physical spin degree of freedom.

For short-range scatterers on the other hand, this argument fails for two reasons. First, a localized short-range scatterer, for example a point defect, generally has different strengths on the A and B sublattices and therefore it introduces an intravalley scattering process through a site asymmetric σ_z-type potential in the effective mass theory. Here the scattering states are no longer states of definite helicity, allowing a nonzero backscattering probability. Second, a short-range potential also allows for intervalley backscattering between the K and K' points and this process is not excluded by the pseudospin character of these states. In spite of these complications, the suppression of backscattering for slowly varying potentials remains an interesting and experimentally relevant feature of graphene's Dirac spectrum.

This interference phenomenon has a striking analog in transport phenomena observed in carbon nanotubes [41]. For an intrinsically conducting nanotube, the kinematically allowed lines of crystal momenta pass through the critical K, K' points, but are *offset* by a minimum crystal momentum $\delta k_\perp$ for the semiconducting tubes as shown in Fig. 4. Thus backscattering is a qualitatively different phenomenon for the two species. Backscattering an electron on a conducting tube requires an exact reversal of the crystal momentum near the K point (i.e., $k_\parallel \to -k_\parallel$) which is suppressed by its pseudospin symmetry, but for semiconducting tubes the momentum is not quite reversed ($\delta k_\perp + k_\parallel \to \delta k_\perp - k_\parallel$) and backscattering from long wavelength perturbations is allowed. Indeed one observes very different carrier mobilities in these two situations. For example, McEuen [41] et al.

estimate a mean free path $\ell \approx 1\mu$ on a conducting tube (a value that could be limited by the lengths of the tubes in their experiments), but only $l \approx 2\,\text{nm}$ for a comparable highly doped semiconducting tube, a reduction by nearly three orders of magnitude.

A Boltzmann treatment of the effect of impurity scattering on the conductivity in graphene gives a scattering rate that vanishes linearly in energy near the charge neutrality point [25]. Thus, in spite of the reduction of the number of charge carriers as one approaches the critical point, the Boltzmann conductivity remains constant *independent* of the carrier concentration; it is given by a nonuniversal value that depends on the scattering strength. The result highlights the fact that the $n \to 0$ limit is quite singular in this problem, and requires a more careful consideration of the effects of disorder on the states deep in the pseudogap of the Dirac cone.

In fact, this anomalous behavior is resolved at least in part by treating the effect of impurity scattering on the electronic spectrum using the impurity averaged self-energy calculated within the self-consistent Born approximation [23,25]. This approach predicts a continuous suppression of the conductivity near the charge neutrality point, limiting to a nonzero minimum value. For example, Shon and Ando [25] find $\sigma_{\min} = (4/\pi)(e^2/h)$ (this result includes a factor of two to account for the spin degeneracy). This value is curiously both independent of the impurity scattering strength (for sufficiently strong scatterers) and is a roughly a factor of three (possibly a factor of π!) smaller than the minimum conductivity actually observed experimentally. One should be cautious about a direct comparison of this prediction with measurements however, as it is widely believed that near its charge neutrality point, experimental graphene (at least samples presently available) is not a homogeneous structure at all, but instead actually contains compensating electron- and hole-rich puddles [24,26].

6. PSEUDOSPINTRONICS

The coupling between the electron momentum and its internal pseudospin degree of freedom has led to theoretical proposals for graphene-based nanostructures that control electronic motion by exploiting their pseudospin polarization. This idea has been dubbed *pseudospintronics* drawing a loose analogy to a theme in modern spintronics where one attempts to control charge currents by developing probes that couple to the ordinary spin degree of freedom.

An interesting family of proposals considers the ballistic motion of electrons through a graphene pn junction [42], a device that might be produced experimentally by patterning a pair of split conducting gates slightly below a single sheet of graphene [43,44]. Such a device is illustrated schematically in Fig. 6 and can be characterized by the length scale d giving the separation between the gates and by the potentials $\pm V_0/2$ on the two gates. One envisions a situation where the junction is made both straight and wide. Above either of the gates, the graphene sheet is electrostatically doped n- or p-type by the field effect. In this situation, conservation of momentum parallel to the junction leads to a region in the junction where

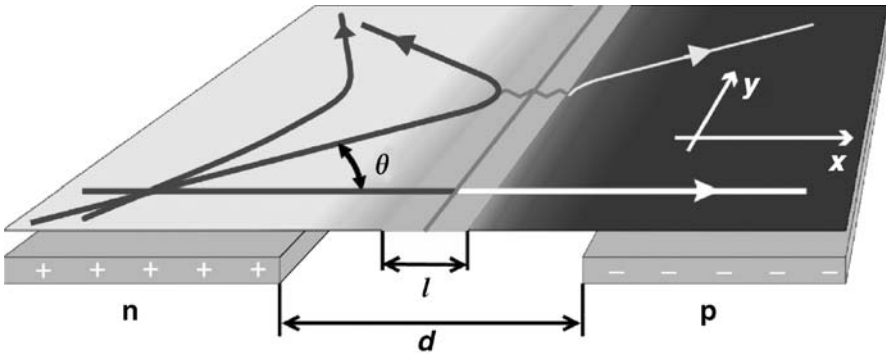

Fig. 6. Ballistic quasiparticle reflection and transmission at a pn junction in single-layer graphene. The p- and n-type regions are doped electrostatically by the split gates below the sheet. The transmission of an incident particle is governed by conservation of crystal momentum parallel to the junction and by matching of the pseudospins of the incident, transmitted and reflected waves. There is a classically forbidden barrier of width l between the doped regions. Because of the pseudospin constraint, there is perfect transmission for a particle at normal incidence. (Reprinted with permission from Ref. [42] ©(2006) by the American Physical Society.)

electron motion is classically forbidden. This barrier can be penetrated quantum mechanically, but the transmission coefficient is governed by a boundary condition that requires matching the *pseudospins* of the incident, reflected and transmitted waves in the barrier region. Indeed backscattering of a wave normally incident on the barrier requires a reversal of its pseudospin (a pseudospin flip), and this is a process that is strongly suppressed for any potential that varies smoothly on the scale of the lattice constant. This observation was quantified by Cheianov and Fal'ko [42] who calculate the barrier transmission probability $w(\theta)$ for any such smooth barrier.

$$w(\theta) = \exp(-\pi(k_F d)\sin^2(\theta)) \tag{6}$$

where k_F is the radius of the Fermi circle for the doped carriers. Interestingly, *independent* of the particle energy, there is a selective perfect transmission of Dirac electrons that are normally incident on a smooth barrier.

It is also intriguing that the on the Dirac cone, near the charge neutrality point the relation between the crystal momentum and the group velocity is reversed for its valence and conduction bands. Thus at an abrupt pn junction, phase matching of incident and transmitted waves along the interface *reverses* the group velocity parallel to the interface. This effect is reminiscent of the refraction of rays in classical optics at surfaces of left-handed materials characterized by a *negative* index of refraction [45,46]. As a consequence de Broglie waves that are injected at a point source on one side of the junction (this could be produced by a quantum point

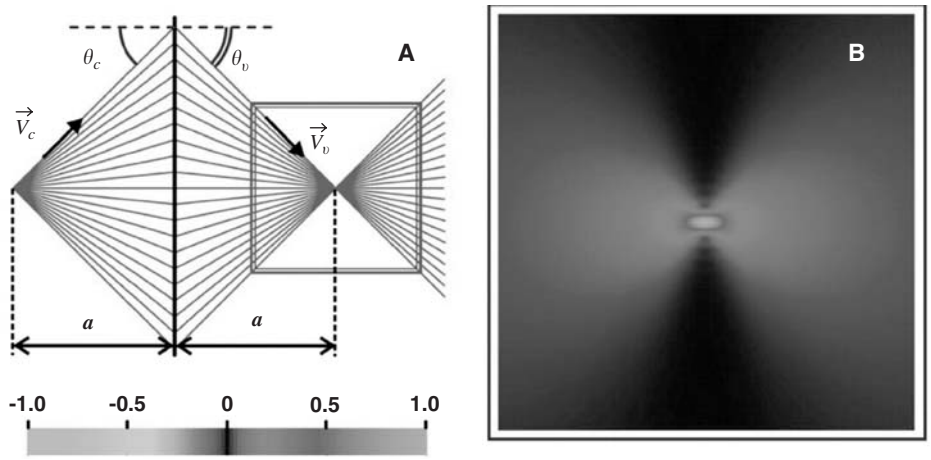

Fig. 7. Schematic for a proposal for lensing at a pn junction that refracts electron waves from a point source to a point focus. The lines are the classical rays illustrating the propagation from a point source on the left. The density plot on the right illustrates solution of the wave equation for the refraction of Dirac waves in the pn junction geometry, showing the lensing character of the junction. (Adapted from Ref. [47].)

contact) would refocus to a point on the other side [47] as shown in Fig. 7. Note that this situation requires an abrupt (on the scale of a lattice constant) pn junction to circumvent the pseudospin selection rules that restrict transmission through smooth junctions, and also requires ballistic propagation over the length scale of the experiment. In principle this scheme also permits the construction of a solid-state analog of a Veselago lens produced by successive refractions at a pnp junction.

The spinor character of the electron and hole states on the Dirac cone might also permit a solid-state realization of the Klein paradox of QED [48]. The Klein paradox arises when considering the penetration of a quantum mechanical particle (an electron) through a potential barrier that exceeds the rest energy $m_e c^2$ [49]. In this situation the transmission probability is predicted to depend only weakly on the barrier height and width in contrast to the nonrelativistic result where this transmission is exponentially suppressed. The physics underlying this effect involves resonant tunneling through the propagating (i.e., nonevanescent) *antiparticle* solutions inside the barrier that are brought into resonance with propagating free particle solutions outside the barrier by the repulsive potential. Ordinarily this would require an extraordinarily large energy barrier (of order the rest energy) changing over a very small width of order the Compton wavelength.

Remarkably, graphene provides a medium where these constraints can be relieved [48]. First, the effective particles and holes of graphene are *massless* particles; their spectrum extends to zero energy, and so there is no threshold barrier height to realize this effect. Second, unlike ordinary semiconductors, the electron and hole states share the same underlying spinor structure (described by their

pseudospins). Physically they are constructed from the same manifold of atomic π orbitals and can be efficiently coupled at such a hypothetical barrier. Indeed the prediction of perfect transmission of single-layer graphene electrons normally incident on a potential barrier is a manifestation of precisely this effect. Katsnelson et al. [48]. emphasize that this arises as a consequence of both the pseudospin structure of the underlying states *and* the linear dispersion relation on the Dirac cone. For example, in bilayer graphene, where the low-energy states are also described by two-component chiral spinor wavefunctions but the energy band disperse *quadratically* in momentum, electrons normally incident on a steep barrier would be nearly perfectly reflected.

7. PERTURBATIONS AS GAUGE FIELDS

Although the low-energy electronic structure of graphene provides a solid-state analog to phenomena in $(2+1)$-dimensional vacuum QED, its charge carriers are neither relativistic nor moving in a vacuum. It is important to identify and classify perturbations to ideal graphene that inevitably arise in experiments and can potentially change the description of its low-energy physics. One can classify potential scattering in graphene through its dependence on the internal spin, pseudospin, and isospin degrees of freedom.

Most relevant for experiments on graphene are potentials that vary slowly in space, so that they are smooth on the scale of a lattice constant. These potentials do not allow intervalley scattering, which is a large momentum scattering process [25,35], and therefore long-range potentials are diagonal in the isospin (valley) index. They can arise from many sources, including Coulomb scattering from remote charged impurities, from lattice strains [19,50] or from nonplanarity of a graphene sheet [51,52].

Intravalley disorder is represented by a spatially varying 2×2-matrix potential in the single valley effective mass model of Eq. (1) [34,35]. Such a potential can be represented by random scalar potential (diagonal and symmetric on the A and B sublattices), a random mass (diagonal and antisymmetric), and a random vector potential (off diagonal). A random mass would require a potential that varies on ultrashort length scales, and this can also be excluded for smooth potentials.

The random vector potential is particularly interesting. It arises from any local variations in the electronic hopping amplitudes, which occur in the presence of lattice strain or curvature of the graphene sheet [19,50–52]. This term shifts the zero of the Dirac cone in momentum space away from the Brillouin zone corner, but it does not eliminate the singularity. Formally the effect of this shift can be locally eliminated by a gauge transformation, and observable effects can only be associated with the gauge invariant Berry's curvature, which describes an effective magnetic field obtained from the 2D curl of this vector potential. Of course, the appearance of an effective magnetic field would explicity break the time-reversal symmetry of the model and this is a pathology of the valley polarized Hamiltonian. Time-reversal symmetry of the problem is recovered by a reversal of the related gauge

field that occurs in the valley polarized Hamiltonian at the K' point [53]. The electromagnetic vector potential breaks time-reversal symmetry and couples to the physical charge current with the same sign in the two valley polarized Hamiltonians [53].

Stronger lattice defects can allow for scattering between the K and K' points and tend to suppress the effects of chirality in the electronic spectrum. Importantly disclinations require the introduction of five- or seven-membered rings, which strongly mix K and K' point excitations [52,54]. Such effects can also be introduced, albeit more weakly, by the large momentum components of a spatially varying potential. Any such source of intervalley scattering introduces a characteristic valley coherence time τ_{iv} so that effects arising from the chiral structure of the underlying Fermions are accessible only when the dephasing time $\tau_\phi < \tau_{iv}$ [34,35].

8. CHIRAL EDGE MODES AND TOPOLOGICAL INSULATORS

If one neglects physical spin, the degeneracy at the Dirac point in graphene is topologically protected by parity and time-reversal symmetry. This can be seen by noting that these symmetries constrain the Berry's phase associated with any loop in momentum space to be either 0 or π. The π Berry's phase associated with the Dirac point can therefore not be removed by any perturbation respecting these symmetries. The degeneracy can be only lifted by symmetry breaking perturbations. The σ_z-type mass term would gap the spectrum by introducing a staggered sublattice on site potential, and this is odd under parity (here a twofold rotation of the 2D system about a perpendicular axis) [55]. Such a term does in fact arise in a long wavelength theory of the related III–V structure boron nitride [56], but it is symmetry forbidden in graphene. A possible mass term that is also odd in the isospin index $\sigma_z\tau_x$ is even under parity, but it explicitly breaks time-reversal symmetry that exchanges the K and K' points without sublattice exchange [57].

The above symmetry argument fails if the physical spin is taken into account because the time-reversal operation is no longer simply complex conjugation, but also flips the eigenvalue of the spin s_z. Remarkably, inclusion of the physical spin introduces a new term that respects all the lattice symmetries of the honeycomb lattice *and* produces a low-energy gap in the spectrum [55]. The relevant term is

$$H' = \Delta(\sigma_z\tau_z s_z) \tag{7}$$

H' is separately sublattice (σ), valley (τ), and spin (s) antisymmetric, but the product is invariant under all of the symmetry operations of the graphene lattice [55]. Physically, this term arises from the spin–orbit interaction in the low-energy Hamiltonian. However, the strength of the spin–orbit coupling for carbon is quite weak and the scale of this gap is expected to be extremely small [58,59].

Nonetheless, it is important to observe that the insulating state produced by H' differs fundamentally from the more conventional insulating state produced by a

symmetry breaking σ_z mass term. This is because Eq. (7) produces (spin-dependent) gaps with *opposite* signs at the two Dirac points a situation that has no simple strong coupling limit. The insulator produced by the mass term (7) has been named a *topological insulator* [60–62]. It behaves like an ordinary insulator with a gap to charge excitations in its bulk. However, unlike an ordinary insulator its boundaries support two counter-propagating spin polarized chiral edge modes [55] as shown in Fig. 8. Importantly in these topological edge states the direction of propagation is determined by the (physical) spin polarization of the electrons. Ballistic propagation in these edge channels provides a mechanism for the control and detection of spin currents by coupling to the scalar (electric) potential.

An analogous situation is encountered in the theory of the 2D electron gas in the quantum Hall regime [63,64]. In this system time-reversal symmetry is explicitly broken and the quantization of the Hall conductance arises from charge transport in a chiral edge mode that circulate around the boundary of this broken-T topological insulator [63]. The low-energy spectrum of graphene provides the first proof-of-principle that topological insulators can be realized in a family of T-invariant systems as well. Topological insulators and ordinary band insulators are

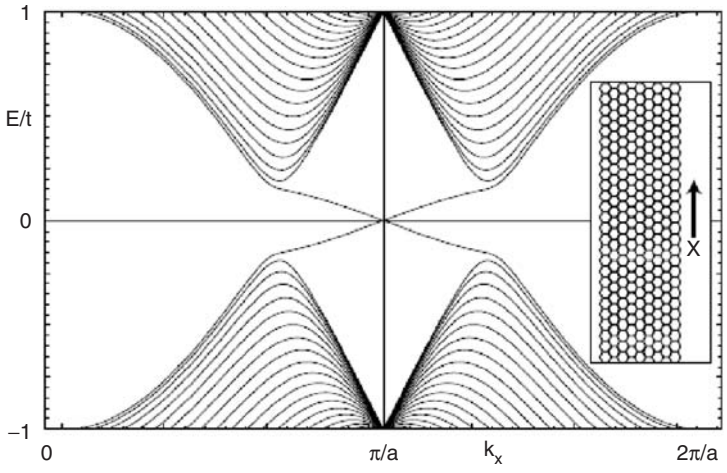

Fig. 8. Electronic bands calculated for a graphene ribbon, including the effect of its intrinsic spin–orbit coupling. The scale of the spin–orbit coupling is greatly exaggerated for clarity, but the topology of this band structure applies to experimental graphene. The left panel displays the bands for electrons with a single spin polarization perpendicular to the graphene sheet. The Dirac spectrum in the bulk of the ribbon is gapped by the spin–orbit interaction; nonetheless the low-energy spectrum contains two edge mode that propagate around the sample boundary with an upward propagating branch on the left edge and downward on the right. The spins with the opposite spin polarization have the same spectrum but with the propagation directions reversed for the two edge modes. Graphene is an example of a time-reversal invariant system exhibiting spin polarized chiral edge modes. (Adapted from Ref. [55].)

distinct phases of matter distinguishable by the presence or absence of a nonzero internal Z_2 topological index [60–62].

For graphene in a perpendicular magnetic field time-reversal symmetry is broken. In the quantum Hall regime with the Fermi energy pinned in a bulk gap between Landau levels, the particle–hole symmetry of the electronic spectrum implies an interesting structure to its own spectrum of edge modes [65–67]. In the bulk, the Landau level spectra obtained at the K and K' points are *identical* copies of each other, each containing a series of macroscopically degenerate states at energies $E_n = \pm\varepsilon_0\sqrt{|n|}$, with $\varepsilon_0 = \hbar v_F\sqrt{2e\mathbf{B}/\hbar c}$. Near an abrupt boundary (edge) the valley degeneracy is lifted. For example, explicit calculations for an atomically abrupt "armchair" edge shows that the reflection strongly mixes the K and K' point excitations, opening intervalley gaps in the Landau level spectrum near the surface [65,67] as illustrated in Fig. 9. For nonzero carrier density when the Fermi energy resides in a bulk gap, it must cross an *odd number* of these backscattering split Landau levels near the edge. Ballistic transport through the surface modes then quantizes the Hall conductivity to the values $\sigma_{xy} = 2(2n+1)e^2/h$ including a factor

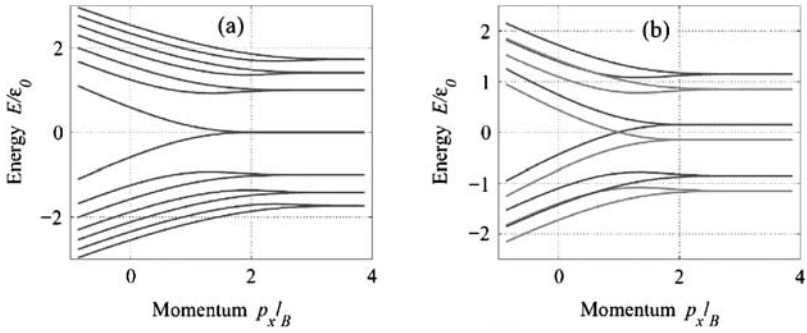

Fig. 9. The edge state spectra for a graphene sheet with an armchair edge in a perpendicular magnetic field without (left) and with (right) the Zeeman coupling of the electron spin to the magnetic field. The energy bands are plotted as a function of the component of crystal momentum parallel to the edge, which in the Landau gauge also determines the distance of the center of a Landau orbital from the edge. For large momenta, the states are confined to the interior of the sheet and show the level Landau quantization of a 2D Dirac particle, doubled to account for the valley degeneracy of the K and K' points. Reflection from the armchair edge mixes the K and K' Dirac states, removing the valley degeneracy of the Landau levels. When the Fermi energy is pinned in a bulk Landau level gap, it crosses an odd number of valley mixed edge modes near the surface, accounting for the anomalous integer quantization of the Hall conductance. Including the effect of the Zeeman coupling (right) the lowest bands are split both by the valley mixing and by the Zeeman interaction, which breaks the spin degeneracy of the spin down and spin up states. When the Fermi energy is pinned in the bulk Zeeman gap closest to its charge neutrality point, it crosses a single pair of counter-propagating edge modes that are nevertheless spin filtered. The edge modes provide channels for ballistic spin and charge transport at the boundary. Adapted from Ref. [67].

of two from the physical spin degeneracy, thus accounting for the anomalous quantization rule for the Hall conductance in graphene. The situation is similar to the quantum Hall effect of the nonrelativistic 2D electron gas, which can also be understood as a manifestation of edge state transport [63], but the Dirac form of graphene's Hamiltonian produces an unconventional counting rule for the edge modes.

The spin degeneracy is in fact lifted by a rather substantial Zeeman coupling that occurs in graphene, as shown the right-hand panel of Fig. 9. When the Fermi energy resides in the bulk Zeeman gap nearest the charge neutrality point, a similar construction shows that it necessarily crosses a *single pair* of Zeeman split and intervalley coupled edge modes near the surface [66]. These two edge modes are counter-propagating bands that carry different spin polarizations, i.e., they are spin filtered chiral edge modes. Although the bulk system supporting this edge state spectrum breaks time-reversal symmetry, its edge modes are similar to those obtained for the quantum spin Hall insulator (which preserves T). An important difference is that the Zeeman splitting responsible for the spin filtering in the quantum Hall regime can be large (and tunable by varying the strength of the magnetic field), possibly bringing spin polarized "quantum edge" transport into an experimentally accessible range.

It is important to distinguish between topological edge modes and the conventional surface states that can occur at the edges of graphitic nanoribbons. The edge modes of a topological insulator are surface modes that occur in a system that is *insulating* in its bulk, their existence requires a form of topological order of the supporting bulk insulating state [60–62]. Indeed because they are protected by the bulk order, these modes persist in the presence of disorder and weak electron–electron interactions. The spin–orbit interaction and coupling of the graphene electrons to an applied magnetic field provide two explicit mechanisms for realizing this state of matter.

The edges of a graphitic nanoribbon can also support a band of conventional surface states. These are known to exist for graphenes with a "zigzag" termination [27] where they occur at low energy in a sector of the surface Brillouin containing a projected bulk band gap. In fact scanning tunneling spectroscopy reveals that the tunneling current observed near the zigzag edges of nanographene samples at low bias is enhanced relative to the bulk [68] likely verifying the presence of these zigzag edge states. Importantly, the physics of these surface states is quite distinct from that of the topological edge modes. The zigzag surface states in graphene occur at the boundary of a system that is actually *gapless* in its bulk and indeed the existence of these surface states relies crucially on the conservation of crystal momentum parallel to the translationally ordered zigzag edge. These states are not protected by the topological order of the interior graphene sheet, and consequently they are sensitive both to disorder at the edge and to the effects of electron–electron interactions. For example, band calculations show that the surface states are absent even for a *translationally ordered* graphene strip with an armchair termination [27,28,65] and the situation for a general edge orientation is expected to be complex. Unlike the chiral edge modes of the topological insulator, the zigzag edge surface

states are also spin unpolarized neglecting the possibility of a broken symmetry ground state driven by electron–electron interactions. Notably, for the intrinsic graphene zigzag nanoribbon the Fermi energy falls in the middle of its weakly dispersive spin degenerate surface band, suggesting a strong tendency toward magnetic ordering driven by repulsive interparticle interactions. Indeed theory predicts that the ground state of the isolated zigzag edge realizes a form of "flat band" ferromagnetism, in which ferromagnetic ordering of the surface state spins completely gaps its electronic spectrum [28,69,70]. Calculations also suggest a residual weak antiferromagnetic interaction between the moments on parallel edges of a finite width zigzag ribbon [71]. This leads to the possibility of a novel Stark effect whereby a strong electric field applied across the edge of the zigzag ribbon and in its tangent plane produces a level crossing between electronic bands with the same spin polarization, but localized at opposite edges of the ribbon. The spillover of charge from one edge to the other produces a semimetallic electronic state that is also "half metallic", namely it is a conductor for carriers with one spin polarization and insulating for the other [71].

9. ELECTRON–ELECTRON INTERACTIONS ON THE DIRAC CONE

It is important to augment the low-energy Hamiltonian (1) to account for the effects of electron–electron interactions. Interacting electrons on the 2D Dirac cone are predicted to exhibit behavior intermediate between that of the 3D and 1D interacting electron fluids. In the former case the low-energy physics is controlled by its quasiparticle excitations near the Fermi surface which, in the Landau Fermi liquid theory, are renormalized analogs of the excitations of a noninteracting system [72]. By contrast the 1D interacting electron fluid is a Luttinger liquid, a strongly interacting state of matter where the low-energy physics is instead controlled by its long wavelength collective modes [73]. These contain distinct spin and charge modes, and are not smoothly connected to the excitations of the noninteracting degenerate Fermi sea.

Although the interacting 2D nonrelativistic electron fluid is known to exhibit Landau Fermi liquid behavior [74], the situation for 2D Dirac fermions is more subtle. In graphene, the phase space available for intraband quasiparticle excitations collapses in the limit of low (doped) particle densities, and the spectrum of interband excitations extends to low energy [75,76]. Importantly, the contribution of interband excitations to the screening of the Coulomb interaction turns out to be limited by the opposing pseudospin character of its valence and conduction band states [77,78].

In graphene the interaction strength is characterized by an effective fine structure constant $\alpha_g = e^2/\hbar v_F \sim 2.5$, giving the ratio of the interparticle potential energy to the single-particle kinetic energy. This bare coupling strength is screened both by the background dielectric constant $\kappa \approx 3$, and importantly by the frequency and wavevector dependent spectrum of intraband particle–hole excitations in a single

Dirac band (when the system is doped) *and* by its interband particle–hole excitations [24,75,77].

For intrinsic graphene the Fermi energy is located at its charge neutrality point and the screening from the intraband excitations is absent. Here the effects of interactions are most evident. Remarkably, in this case despite a vanishing of the interband gap, graphene screens the bare Coulomb potential $v(q) = 2\pi e^2/q$ like a conventional *3D* semiconductor characterized by a static dielectric constant $\alpha(q \to 0) = 1 + (\pi\alpha_g/2\kappa)$ [75]. Furthermore, by calculating the exchange self-energy from the screened Coulomb interaction one finds that in the intrinsic system the *slope* of its Dirac cone undergoes the nontrivial scale dependent renormalization [24,75].

$$\frac{1}{\hbar v_{\mathrm{F}}}\nabla_k E = 1 - \frac{5}{3\pi}\alpha_g + \frac{\alpha_g}{4}\log\left(\frac{\Lambda}{k}\right) \tag{8}$$

where Λ is an ultraviolet cutoff of order the inverse cell size. Eq. (8) demonstrates that the effective Fermi velocity is scale dependent and is enhanced at small momenta. The group velocity in Eq. (8) in fact diverges logarithmically as $k \to 0$ and thus the Coulomb interaction pinches the linear Dirac cone into a singular logarithmic cusp. The quasiparticles of this liquid inherit a lifetime that diverges at low energy proportional to $1/\omega$ identifying this state of matter as a 2D realization of the marginal Fermi liquid [24]. The situation for finite doping is much more conventional since these singular behaviors are ultimately regularized by the nonzero value of the Fermi momentum and the system retains the behavior an ordinary 2D interacting Fermi liquid, albeit with a renormalized and density dependent Fermi velocity.

There is strong evidence for such a scale dependent renormalization of the velocity from the photophysics of carbon nanotubes. Semiconducting tubes show strong optical absorption from excitonic states (bound states of excited electron hole pairs) that arise from their interband excitations [79,80]. Quantization of the circumferential crystal momenta leads to a quantized subband energy spectrum in which all excitation energies scale inversely with the tube radius. Instead, experimental data [81,82] that show that the absorption energies obey a nonlinear scaling law as a function of the inverse tube radius, even in the limit of large radius tubes, where one would expect the kinematical prediction to be most accurate [82]. This nonlinearity arises as an interaction effect and it can be traced to the physics of the singular velocity renormalization in graphene. One finds that on a nanotube, the quasiparticle self-energies acquires a $q\log(q)$ nonlinear contribution from the *short-range* part of the Coulomb interaction, i.e., by the interactions on a scale of order the tube radius. There is an additional, very strong contribution to the self-energy from the long-range part of the Coulomb interaction, which remains unscreened in the nanotube and introduces a sizeable renormalization (increase) of the bandgap. But this gap renormalization is compensated by a nearly equally strong electron hole attraction which produces the excitonic bound state; physically the cancellation reflects the fact that the exciton is a charge neutral excitation. This

near cancellation was observed in early theoretical work [79] and exposes the physics of the short-range interactions in the self-energies. Thus the q-nonlinear scaling of the exciton energy and its anomalous scaling with tube radius R is a feature inherited by the nanotube excitons as a remnant of the anomalous quasiparticle velocity in the parent graphene sheet. Indeed the logarithmic velocity renormalization provides a striking account of the nonlinear scaling law actually observed experimentally, and it yields a measure of the effective (screened) Coulomb coupling strength on carbon nanotubes [82].

Electron–electron interactions have also been associated with the appearance of additional plateaus observed in the Hall conductance for high mobility graphene samples in high magnetic fields ($B > 20$ T) [6]. These plateaus are observed for filling fractions near the charge neutrality point and show an additional structure in the quantization of the Hall conductance with plateaus $R_{xy}^{-1} = \nu e^2/h$ with $\nu = 0, \pm 1$ [6]. Naively, these plateaus correspond to situations for which the Fermi energy resides *within* the macroscopically degenerate (and ordinarily inert in the Hall response) $E = 0$ Landau level, and the appearance of the additional plateaus almost certainly signifies the onset of a new broken symmetry many body state [83–85]. In principle such a broken symmetry state could arise from ordering of the spin or isospin degrees of freedom driven by the interparticle interactions. There is a close analogy between this situation and the occurrence of quantum Hall ferromagnetism in bilayer 2D electron gas systems.

10. OUTLOOK

Perhaps the most exciting aspect of the "rise of grapheme" is that it has drawn attention to a class of nontrivial quantum electronic effects that are accessible in matter in ordinary experimental environments: at room temperature, in moderate external fields, and in samples that are not particularly clean. These discoveries will surely promote further work in cleaner samples in higher fields and at lower temperatures. It is quite possible that here graphene will bring still other surprising and beautiful quantum mechanical phenomena into focus.

ACKNOWLEDGMENTS

The authors acknowledge support from the National Science Foundation through the MRSEC program (DMR-00-79909), the Department of Energy (grant DE-FG-02-ER45118), and the American Chemical Society (grant PRF 4476-AC10) for their work cited in this review.

REFERENCES

[1] Y. Zhang, J.P. Small, W.V. Pontius and P. Kim, Fabrication and electric field dependent transport measurements of mesoscopic graphite devices, *Appl. Phys. Lett.* **86**, 073104 (2005).

[2] K.S. Novoselov, A.K. Geim, S.V. Morozov, D. Jiang, Y. Zhang, S.V. Dubonos, I.V. Grigorieva and A.A. Firsov, Electric field effect in atomically thin carbon films, *Science* **306**, 666 (2004).
[3] Y. Zhang, J.P. Small, M.E.S. Amori and P. Kim, Electric field modulation of the galvanomagnetic properties of mesoscopic graphite, *Phys. Rev. Lett.* **94**, 176803 (2005).
[4] K.S. Novoselov, A.K. Geim, S.V. Morozov, D. Jiang, M.I. Katsnelson, I.V. Grigorieva, S.V. Dubonos and A.A. Firsov, Two dimensional gas of massless fermions in graphene, *Nature* **438**, 197 (2005).
[5] Y. Zhang, Y.-W. Tan, H.L. Stormer and P. Kim, Experimental observation of the quantum Hall effect and Berry's phase in graphene, *Nature* **438**, 201 (2005).
[6] Y. Zhang, Z. Jiang, J.P. Small, M.S. Purewall, Y.-W. Tan, M. Fazlollahi, J.D. Chudow, J.A. Jaszczak, H.L. Stormer and P. Kim, Landau level splitting in graphene in high magnetic fields, *Phys. Rev. Lett.* **96**, 136806 (2006).
[7] K.S. Novoselov, Z. Jiang, Y. Zhang, S.V. Morozov, H.L. Stormer, U. Zeitler, J.C. Maan, G.S. Boebinger, P. Kim and A.K. Geim, Room temperature quantum Hall effect in graphene, *Science* **315**, 1379 (2007).
[8] J. Nilsson, A.H. Castro Neto, F. Guinea and N.M.R. Perez, Electronic properties of graphene multilayers, *Phys. Rev. Lett.* **97**, 266801 (2006).
[9] C. Berger, Z. Song, T. Li, X. Li, A.Y. Ogbazghi, R. Feng, Z. Dai, A.N. Marchenkov, E.H. Conrad, P.N. First and W.A. deHeer, Ultrathin expitaxial graphite: 2D electron gas properties and a route towards graphene based nanoelectronics, *J. Phys. Chem. B* **108**, 19912 (2004).
[10] E. Rollings, G.-H. Gweon, S.Y. Zhou, B.S. Mun, B.S. Hussain, A.V. Federov, P.N. First, W.A. deHeer, and A. Lanzara, Synthesis *and Characterization of Atomically Thin Graphite Films on a SiC Substrate* [arXiv:cond-mat/0512226v1].
[11] P.R. Wallace, The band theory of graphite, *Phys. Rev.* **71**, 622 (1947).
[12] J.C. Slonczewski and P.R. Weiss, The band structure of graphite, *Phys. Rev.* **109**, 272 (1958).
[13] D.P. DiVincenzo and E.J. Mele, Self consistent effective mass theory for intralayer screening in graphite intercalation compounds, *Phys. Rev. B* **29**, 1685 (1984).
[14] G.W. Semenoff, Condensed matter simulation of a 3-dimensional anomaly, *Phys. Rev. Lett.* **53**, 2449 (1984).
[15] N.M.R. Perez, F. Guinea and A.H. Castro Neto, Electronic properties of two dimensional carbon, *Ann. Phys.* **321**, 1559 (2006).
[16] M.I. Katsnelson, Graphene: Carbon in two dimensions, *Mater. Today* **10**, 20 (2006).
[17] R. Saito, G. Dresselhaus and M.S. Dresselhaus, *Physical Properties of Carbon Nanotubes* (Imperial College Press, London, 2000).
[18] N. Hamada, S. Sawada and A. Oshiyama, New one dimensional conductors graphitic microtubules, *Phys. Rev. Lett.* **68**, 1579 (1992).
[19] C.L. Kane and E.J. Mele, Size shape symmetry and low energy electronic structure of carbon nanotubes, *Phys. Rev. Lett.* **78**, 1932 (1997).
[20] J.-C. Charlier, X. Blase and S. Roche, Electronic and transport properties of nanotubes, *Rev. Mod. Phys.* **79**, 677 (2007).
[21] A.K. Geim and K.S. Novoselov, The rise of graphene, *Nat. Mater.* **6**, 183 (2007).
[22] J.C. Meyer, A.K. Geim, M.I. Katsnelson, K.S. Novoselov, T.J. Booth and S. Roth, The structure of suspended graphene sheets, *Nature* **446**, 60 (2007).
[23] K. Nomura and A.H. MacDonald, Quantum transport of massless Dirac fermions, *Phys. Rev. Lett.* **98**, 076602 (2007).
[24] S. Das Sarma, E.H. Hwang and W.K. Tse, Many body interaction effects in doped and undoped graphene: Fermi liquid versus non-Fermi liquid, *Phys. Rev. B* **75**, 121406(R) (2007).
[25] N.H. Shon and T. Ando, Quantum transport in two dimensional graphite system, *J. Phys. Soc. Jpn.* **67**, 2421 (1998).
[26] V.V. Cheianov, V.I. Fal'ko, B.L. Altshuler, and I.L. Aleiner, *Random Resistor Network of Minimal Conductivity in Graphene* [arXiv:0706.2968].
[27] K. Nakada, M. Fujita, G. Dresselhaus and M.S. Dresselhaus, Edge state in graphene ribons: Nanometer size effect and edge shape dependence, *Phys. Rev. B* **54**, 17954 (1996).

[28] Y.-W. Son, M.L. Cohen and S.G. Louie, Energy gaps in graphene nanoribbons, *Phys. Rev. Lett.* **97**, 216803 (2006).
[29] E. McCann, Asymmetry gap in the electronic bandstructure of bilayer graphene, *Phys. Rev. B* **74**, 161403 (2006).
[30] H. Min, B. Sahu, S.K. Banerjee and A.H. MacDonald, Ab initio theory of gate induced gaps in graphene bilayers, *Phys. Rev. B* **75**, 155115 (2007).
[31] R.B. Laughlin, Quantized hall conductivity in two dimensions, *Phys. Rev. B* **23**, 5632 (1981).
[32] V.P. Gusynin and S.G. Sharapov, Unconventional integer quantum Hall effect in graphene, *Phys. Rev. Lett.* **95**, 146801 (2005).
[33] E. McCann and V.I. Fal'ko, Landau level degeneracy and quantum Hall effect in a graphite bilayer, *Phys. Rev. Lett.* **96**, 086805 (2006).
[34] E. McCann, K. Kechedzhi, V.I. Fal'ko, H. Suzuura, T. Ando and B.L. Altshuler, Weak localization magnetoresistance and valley symmetry in graphene, *Phys. Rev. Lett.* **97**, 146805 (2006).
[35] A.F. Morpurgo and F. Guinea, Intervalley scattering, long range disorder and effective time reversal symmetry breaking in graphene, *Phys. Rev. Lett.* **97**, 196804 (2006).
[36] D.S. Novikov, *Scattering Theory and Transport in Graphene* [arXiv: 0706:1391v2].
[37] H. Sakai, H. Suzuura and T. Ando, Effective mass theory of electron correlations in band structure of semiconducting carbon nanotubes, *J. Phys. Soc. Jpn.* **72**, 1698 (2003).
[38] T. Ando, Theory of electronic states and transport in carbon nanotubes, *J. Phys. Soc. Jpn.* **74**, 777 (2005).
[39] T. Ando, T. Nakashini and R. Saito, Berry's phase and absence of backscattering in carbon nanotubes, *J. Phys. Soc. Jpn.* **67**, 2857 (1998).
[40] T. Ando, T. Nakashini and R. Saito, Impurity scattering in carbon nanotubes: Absence of backscattering, *J. Phys. Soc. Jpn.* **67**, 1704 (1998).
[41] P.L. McEuen, M. Bockrath, D.H. Cobden, Y.G. Yoon and S.G. Louie, Disorder, pseudospins and backscattering in carbon nanotubes, *Phys. Rev. Lett.* **83**, 5098 (1999).
[42] V.V. Cheianov and V.I. Fal'ko, Selective transmission of Dirac electrons and ballistic magnetoresistance of pn junctions in graphene, *Phys. Rev. B* **74**, 041403(R) (2006).
[43] B. Huard, J.A. Sulpizio, N. Stander, K. Todd, B. Yang and D. Goldhaber Gordon, Transport measurements across a tunable potential barrier in graphene, *Phys. Rev. Lett.* **98**, 236803 (2007).
[44] J. R. Williams, L. DiCarlo, and C.M. Marcus, *Quantum Hall Effect in a Graphene pn Junction* [arXiv:0704.3487].
[45] V.G. Veselago, Electrodynamics of substances with simultaneously negative values of σ and μ, *Sov. Phys. Usp.* **10**, 509 (1968).
[46] J.B. Pendry, Negative refraction makes a perfect lens, *Phys. Rev. Lett.* **85**, 3966 (2000).
[47] V.V. Cheianov, V. Fal'ko and B.L. Altshuler, The focusing of electron flow and a Veselago lens in graphene p–n junctions, *Science* **315**, 1252 (2007).
[48] M.I. Katsnelson, K.S. Novoselov and A.K. Geim, Chiral tunneling and the Klein paradox in graphene, *Nat. Phys.* **2**, 620 (2006).
[49] P. Krekora, Q. Su and R. Grobe, Klein paradox in spatial and temporal resolution, *Phys. Rev. Lett.* **92**, 040406 (2004).
[50] K. Sasaki, S. Murakami and R. Saito, Gauge field for edge states in graphene, *J. Phys. Soc. Jpn.* **75**, 074713 (2006).
[51] A. Cortijo and M.A.H. Vozmediano, Electronic properties of curved graphene sheets, *Europhys. Lett.* **77**, 47002 (2007).
[52] A. Cortijo and M.A.H. Vozmediano, Effects of topological defects and local curvature on the electronic properties of planar graphene, *Nucl. Phys. B* **763**, 293 (2007).
[53] D.A. Abanin, P.A. Lee and L.S. Levitov, Randomness-induced XY ordering in a graphene quantum Hall ferromagnet, *Phys. Rev. Lett.* **98**, 156801 (2007).
[54] P.E. Lammert and V.H. Crespi, Graphene cones: Classification by fictitious flux and electronic properties, *Phys. Rev. B* **69**, 035406 (2004).
[55] C.L. Kane and E.J. Mele, Quantum spin Hall effect in graphene, *Phys. Rev. Lett.* **95**, 226801 (2005).

[56] E.J. Mele and P. Kral, Electric polarization of heteropolar nanotubes as a geometric phase, *Phys. Rev. Lett.* **88**, 056803 (2002).
[57] F.D.M. Haldane, Model for quantum Hall effect without Landau levels: Condensed matter realization of the parity anomaly, *Phys. Rev. Lett.* **61**, 2015 (1988).
[58] H. Min, J.E. Hill, N.A. Sinitsyn, B.R. Sahu, L. Kleinman and A.H. MacDonald, Intrinsic and Rashba spin–orbit interactions in graphene sheets, *Phys. Rev. B* **74**, 165310 (2006).
[59] J.C. Boettger and S.B. Trickey, First principles calculation of the spin orbit splitting in graphene, *Phys. Rev. B* **75**, 121402 (2007).
[60] C.L. Kane and E.J. Mele, Z(2) Topological order and the quantum spin Hall effect, *Phys. Rev. Lett.* **95**, 146802 (2005).
[61] L. Fu and C.L. Kane, Time reversal polarization and a Z(2) adiabatic spin pump, *Phys. Rev. B* **74**, 195312 (2006).
[62] T. Fukui and Y. Hatsugai, Topological aspects of the quantum spin Hall effect in Graphene: Z(2) topological order and spin Chern number, *Phys. Rev. B* **75**, 121403 (2007).
[63] B.I. Halperin, Quantized Hall conductance, current carrying edge states and the existence of extended states in a two dimensional disordered system, *Phys. Rev. B* **25**, 2185 (1982).
[64] D.J. Thouless, M. Kohmoto, M.P. Nightingale and M. DenNijs, Quantized Hall conductance in a two dimensional periodic potential, *Phys. Rev. Lett.* **49**, 405 (1982).
[65] L. Brey and H.A. Fertig, Electronic state of graphene nanoribbons studied with the Dirac equation, *Phys. Rev. B* **73**, 235411 (2006).
[66] D.A. Abanin, P.A. Lee and L.S. Levitov, Spin filtered edge states and quantum Hall effect in graphene, *Phys. Rev. Lett.* **96**, 176803 (2006).
[67] D.A. Abanin, P.A. Lee, and L.S. Levitov, *Charge and Spin Transport at the Quantum Hall Edge of Graphene* [arXiv:0705.2882].
[68] Y. Kobayashi, K. Fukui, T. Enoki and K. Kusakabe, Edge state on hydrogen terminated graphite edges investigated by scanning tunneling microscopy, *Phys. Rev. B* **73**, 125415 (2006).
[69] S. Okada and A. Oshiyama, Magnetic ordering in hexagonally bonded sheets with first row elements, *Phys. Rev. Lett.* **87**, 146803 (2001).
[70] H. Lee, Y.-W. Son, N. Park, S. Han and J. Yu, Magnetic ordering at the edges of graphitic fragments: Magnetic tail interactions between the edge localized states, *Phys. Rev. B* **72**, 174431 (2005).
[71] Y.-W. Son, M.L. Cohen and S.G. Louie, Half metallic graphene nanoribbons, *Nature* **444**, 347 (2006).
[72] G. Baym and C. Pethick, *Landau Fermi liquid theory: Concepts and applications* (Wiley and Sons, New York and Toronto, 1992).
[73] T. Giamarchi, *Quantum Physics in One Dimension* (Clarendon Press, Oxford, 1992).
[74] R. Shankar, Renormalization group approach to interacting fermions, *Rev. Mod. Phys.* **66**, 129 (1994).
[75] J. Gonzales, F. Guinea and M.A.H. Vozmediano, Marginal Fermi liquid behavior from two dimensional coulomb interaction, *Phys. Rev. B* **59**, R2474 (1999).
[76] J. Gonzales, F. Guinea and M.A.H. Vozmediano, Electron–electron interactions in graphene sheets, *Phys. Rev. B* **63**, 134421 (2001).
[77] Y. Barlas, T. Pereg-Barnea, M. Polini, R. Asgari and A.H. MacDonald, *Chirality and Correlations in Graphene*, [arXiv:cond-mat/0701257].
[78] M. Polini, R. Asgari, Y. Barlas, T. Peref-Barnea, and A.H. MacDonald, *Graphene: A Pseuochiral Fermi Liquid*, [arXiv:0704.3786].
[79] T. Ando, Excitons in carbon nanotubes, *J. Phys. Soc. Jpn.* **66**, 1066 (2001).
[80] C.D. Spataru, S. Ismail-Beigi, L.X. Benedict and S.G. Louie, Excitonic effects and optical spectra in single wall carbon nanotubes, *Phys. Rev. Lett.* **92**, 077402 (2004).
[81] S.M. Bachilo, M.S. Strano, C. Kittrell, R.H. Hauge, R.E. Smalley and R.B. Weisman, Structure assigned optical spectra of single wall carbon nanotubes, *Science* **298**, 2361 (2002).
[82] C.L. Kane and E.J. Mele, Electron interactions and scaling relations for optical excitations in carbon nanotubes, *Phys. Rev. Lett.* **93**, 197402 (2004).

[83] K. Nomura and A.H. MacDonald, Quantum Hall ferromagnetism in graphene, *Phys. Rev. Lett.* **96**, 256602 (2006).
[84] J. Alicea and M.P.A. Fisher, Graphene integer Hall effect in the ferromagnetic and paramagnetic regimes, *Phys. Rev. B* **74**, 075422 (2006).
[85] V.P. Guzynin, V.A. Miransky, S.G. Sharapov and I.A. Shovkovy, Excitonic gap, phase transition and quantum Hall effect in graphene, *Phys. Rev. B* **74**, 195429 (2006).

This page intentionally left blank

AUTHOR INDEX

SUBJECT INDEX